PROGRAMA DE DOCTORADO EN FÍSICA

TESIS DOCTORAL:

Dynamic Properties of Liquid Metals and their Free Surface with First Principles Molecular Dynamics.

**Presentada por Beatriz González del Río para optar al grado de
Doctor/a por la Universidad de Valladolid**

**Dirigida por:
Luis Enrique González Tesedo**

UVa
Secretaría Administrativa. Escuela de Doctorado. Casa del Estudiante. C/ Real de Burgos s/n. 47011-Valladolid. ESPAÑA
Tfno.: + 34 983 184343; + 34 983 423908; + 34 983 186471 - **Fax** 983 186397 - **E-mail**: seccion.tercer.ciclo@uva.es

CONTENTS

1

INTRODUCTION

1.1 THE SIMULATION OF THE LIQUID STATE.

At present, three major research fields can be distinguished in Physics: Particle and High Energy Physics which deal with very small bodies; Cosmology, dealing with the very big; and Non-Linear Physics and Nanophysics, which deal with complex behaviors. This thesis corresponds to this last field in which we will study liquid metals through *ab initio* simulation techniques based on Density Functional Theory [1–3].

One of the major difficulties in describing liquid systems, is the lack of ideal models like those of the ideal gas or the harmonic solid which can be exactly solved. Nevertheless, there have been various models which have attempted to describe, in a more or less accurate way, the behavior of liquid systems of diverse nature. An example is the *lattice model*, in which the similarity between liquids and solids is exploited; or the *perturbative model* where a similar philosophy to other fields in Physics is followed in the sense that liquid systems are described in terms of perturbations of a reference system whose properties are known.

A different approach for the study of the behavior of liquid systems is through computer simulation techniques; in particular, Molecular Dynamics (MD). In fact, MD methods are an extremely useful tool to investigate the behavior of both macroscopic and low dimension systems since it not only allows to compare the reliability of different theoretical models but also provides information which would be very difficult (or even impossible) to acquire experimentally. The computation power to perform complex calculations, enables to solve the equation of motion of a group of particles in time with an almost total control over the conditions of the system either thermodynamic (pressure, external fields) or microscopic (interactions, composition). In other words, the liquid state can be simulated in a precise way obtaining exact results given the level of approximations used in the simulation.

The first MD study was performed by Alder and Wainwright in 1957 [4]. They studied the solid-liquid phase transitions of a system of particles interacting through a hard-spheres potential,

$$V(r) = \begin{cases} \infty & r \leqslant \sigma \\ 0 & r > \sigma \end{cases} \tag{1}$$

Later, in 1959, they published a work where they detail the purpose, methodology, and applications and limitations of MD [5]. In 1964, in a study which became a milestone in the development of this technique, Rahman [6] presented a simulation with 864 argon atoms at 94.4 K and a density of 1.374 g cm^{-3} with a Lennard-Jones (LJ) potential:

$$V(r) = 4\epsilon[(\sigma/r)^{12} - (\sigma/r)^6]$$

The final results enabled the calculation of different microscopic correlation functions. For this particular study and his whole career in general, Rahman is considered as one of the pioneers in the application of computational methods for the study of physical problems, and many of the codes used nowadays are inheritors of the ones developed by him in this period. Following this line of work, between 1967 and 1968, Verlet performed simulations of LJ systems calculating different thermodynamic [7] dynamic and structural properties [8], improving technical aspects like the algorithm for propagating the coordinates, which ended up as the Verlet algorithm. A review of the most relevant work performed in the mid 70's can be found in Ref. [9].
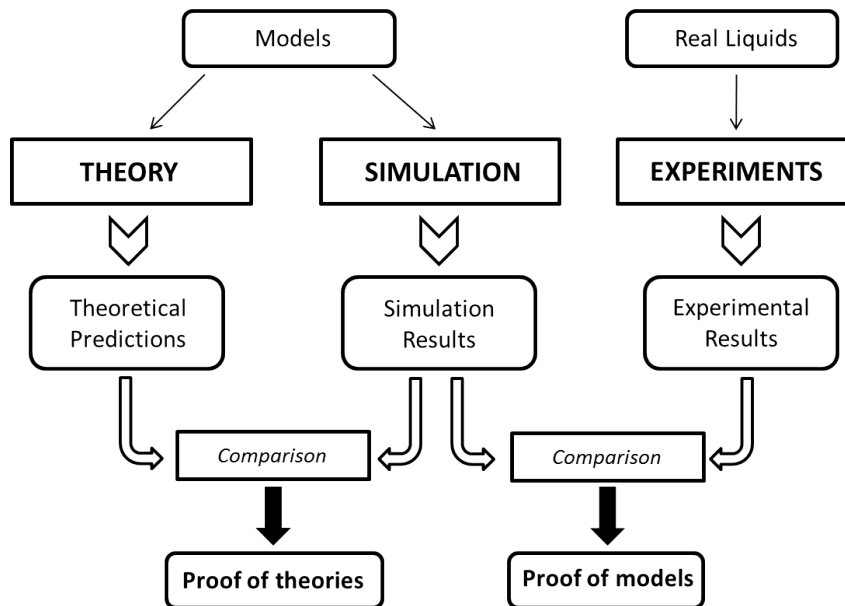
FIGURE 1.1: Relationship between experimentation, theory and simulation; and how this last one acts as a bridge between the former two [10].

In the 70s, when computational simulation was widely used by the scientific community, a question arose of whether simulation techniques belonged to theory or experimentation. Even though it may seem just a nominal problem, behind it lay important conceptual aspects. The simulated systems are not real but mere numeric calculus used to described a specific case. However, the method shares several points with experiments: simulation as well as experiments are prepared, are set to run, data is generated, and these are finally analyzed, while theoretical work follows other paths based on reductionism, mathematical formulae and the prevision of new phenomena. How was this dilemma solved? It is accepted that simulations conform a field of its own, playing a fundamental role connecting theory and experiment, figure 1.1.

In the 80s an important step in the simulation methods was taken by including explicitly the electrons in the calculation. Before then, the interaction was modeled by pair potentials whose parameters were adjusted to experimental data. From the first simulations of argon by Rahman and Verlet, where a LJ potential was used, more sophisticated models were introduced to describe very different systems. For example, potentials to describe the interaction in water [11], proteins [12] or liquid metals [13]. However, apart from the success of these type of methods called Classical Molecular Dynamics (CMD), they faced some important limitations (for example, the problem of transferability of the interaction potential), which did not allow a precise general description of the systems able to reproduce the experimental results.

In 1985, Car and Parrinello published a revolutionary work [14] where they described a method which included the electrons in the simulation, creating what is called *ab initio* Molecular Dynamics (AIMD), or "first principles" MD. In this method the forces were obtained through calculations of the electronic structure in each step of the generated trajectory in the simulation. Therefore, the interactions were treated in a more fundamental level than CMD. Complex phenomena, like distortion and polarization of the water molecule, as well as bonds being formed [15], emerged from the simulation. As a counterpart, the *ab initio* methods are much more complex and demanding in computational terms.

With the development of new computers and computational algorithms, AIMD methods have been incorporated into the field of research to become nowadays a very powerful tool to describe the behaviour of various physical phenomena [16, 17].

1.2 LIQUID METALS AND THEIR APPLICATION

Liquid metals are a great example of systems which combine a relevance both in industrial applications and basic science. Research in liquid metals has increased in recent years due to their numerous applications in diverse fields: fusion energy, as plasma facing components [18]; medicine, for tumor therapy, bone disease repair and nerve connections [20]; nanoelectronics, for low dimension circuits [21]; and soft robotics, for wearable technology [22].

Fusion energy could be the solution to many energetic and environmental challenges being faced today by human kind. That is why many research is focused in developing the technology required to maintain plasma at such high temperature without destroying the machinery containing it. Liquid metals have become a promising plasma facing component because their properties will not be modified by the displacement of atoms by their collision with particles escaping from plasma. Moreover, they can withstand the high temperatures inside the fusion reactor. The most favorable materials are liquid lithium (Li) and liquid tin (Sn). Some experiments have already been carried out to study their performance at high temperatures. However, computer simulations would be of great help in understanding the properties and behavior at different situations.

For biomedical applications, all the compounds must have specific thermal and electrical properties, fluidic features, plasticity, chemical stability, mechanical performance, biocompatibility and low cost. Promising candidates for alloying are: gallium (Ga), indium (In), Sn, bismuth (Bi), cadmium (Cd), and zinc (Zn). All these elements can be potentially described with computer simulations, as well as their liquid binary and ternary alloys.

On the other hand, liquid metals, in particular the monatomic, have been recognized for many years as the prototype of simple liquids, since they englobe most of the physical properties of real fluids without the complications that can be present in each system in particular [23]. MD simulations with realistic ionic potentials are a very useful tool for the investigation of liquids at a microscopic level since they provide information on the atomic trajectories which complement the information obtained from experiments, providing access to some dynamic properties which are very difficult (or even impossible) to obtain experimentally.

In the present thesis several liquid metal systems either in bulk or slab configuration have been studied with AIMD simulations, either in the Kohn-Sham or the Orbital-Free implementations. The thesis is organized as follows: Chapters 2 and 3 present a theoretical introduction to liquid properties calculation and modeling; in Chapter 4 the computational method is described; and the next five chapters include all the results obtained in our research. The development of a new method for the construction of accurate ionic pseudopotentials for liquids and solids is described in Chapter 5. Chapter 6 includes the results obtained in our study of bulk liquid nickel (Ni), titanium (Ti), palladium (Pd) and platinum (Pt). The study of complex collective dynamics through mode coupling theory in liquid Zn and liquid Sn is presented in Chapter 7. In Chapter 8 we turn to study liquid silver (Ag)-Sn alloy. Finally, Chapter 9 presents work performed on different elements in the slab configuration: liquid Ag; a new perspective on the reflectivity calculation through the intrinsic density profile applied to mercury (Hg), lead (Pb) and bismuth (Bi); and the study of collective dynamics at different depths in the free liquid surfaces of Sn and In.

2

THEORY OF SIMPLE LIQUIDS: AN INTRODUCTION

2.1 STATISTICAL MECHANICS

This section is devoted to a brief summary of the principles of classical mechanics and to the discussion of the connection between statistical mechanics and thermodynamics. Consider an isolated, macroscopic system consisting of N identical particles, each of which has three translational degrees of freedom. The dynamical state of the system at a given time is completely identified by the 3N coordinates, $\vec{r}_i$, and 3N momenta, $\vec{p}_i$, of the particles. The values of these variables define a *phase point*, ξ, in a 6N-dimensional *phase space*, Γ,

$$\Gamma \equiv \{\vec{r}_i(t), \vec{p}_i(t)\} \quad , \quad i = 1...N \tag{2}$$

and $\xi = (\vec{r}_1, \vec{p}_1, ..., \vec{r}_N, \vec{p}_N)$. The evolution of the phase point will describe a curve or *phase trajectory* in the phase space, $\xi(t)$, determined by Hamilton's equations,

$$\frac{\partial \vec{r}_i}{\partial t} = -\frac{\partial H}{\partial \vec{p}_i} \quad , \quad \frac{\partial \vec{p}_i}{\partial t} = \frac{\partial H}{\partial \vec{r}_i} \tag{3}$$

where $H = H(\vec{r}_i, \vec{p}_i; t)$ is the Hamiltonian of the system. In principle, the trajectory could be calculated directly from equation 3, but in a thermodynamic system the dimension of Γ is of the order of the Avogadro's number, making the task impossible. Therefore, a statistical treatment is necessary.

The aim of equilibrium statistical mechanics is to calculate observable properties of the system either as averages over a phase-space trajectory or as averages over an ensemble of systems, each of which is a replica of the system of interest. An ensemble is an arbitrarily large collection of imaginary systems, all of which are replicas of the system of interest insofar as they are characterized by the same macroscopic parameters. The systems of the ensemble differ from each other in the assignment of the coordinates and momenta of the particles, and the ensemble is represented by a cloud of phase points whose distribution is described by a phase-space *probability density* $f(\Gamma) = f(\vec{r}_i, \vec{p}_i; t)$. The quantity $f(\xi)d\Gamma$ is the probability that at time t the physical system is in a microscopic state represented by the phase point ξ inside the volume $d\Gamma$, representing,

$$d\Gamma = \prod_{i=1}^{N} d\vec{r}_i d\vec{p}_i \tag{4}$$

The probability density $f(\Gamma)$ must be normalized, meaning its integral over the entire phase space must be unity. Given a complete knowledge of the probability density, it would be possible to calculate the average value of any function of the coordinates and momenta. The explicit form of the equilibrium probability density depends on the macroscopic parameters chosen to characterize the ensemble. A particularly simple case is one where the systems of the ensemble are assumed to have the same number of particles, same volume and same total energy. An ensemble constructed this way is called *microcanonical* ensemble. When the temperature is kept constant instead of the total energy, the ensemble is called *canonical*.

Thermodynamic properties of a system, with some exceptions, can be represented as averages of certain functions of the coordinates and momenta of the constituent particles called dynamic variables, $A(\vec{r}_i, \vec{p}_i)$. These dynamic variables can be averaged over the ensemble to obtain the associated thermodynamic property, $\langle A \rangle$,

$$\langle A \rangle = \int_{\Gamma} d\Gamma f(\vec{r}_i, \vec{p}_i) A(\vec{r}_i, \vec{p}_i) \tag{5}$$

Another alternative to calculate the statistical average of $A(\vec{r}_i, \vec{p}_i)$ is as a time average over the dynamical evolution through the phase space. After a suitable lapse of time the system will have sampled the space Γ accordingly to the conditions imposed by the force field, and its mean value will be given by,

$$\bar{A} = \lim_{T \to \infty} \frac{1}{T} \int_0^T dt A(\vec{r}_i, \vec{p}_i; t) \tag{6}$$

It is reasonable to suppose that the phase trajectory of the system will pass more frequently through phase points with a higher probability while those with a zero probability will never be visited. Therefore, for reasonable long times, the trajectory of $A(t)$ will have sampled the entire ensemble, and the ensemble average and time average will coincide,

$$\langle A \rangle = \bar{A} \tag{7}$$

This result, introduced by Boltzmann, is known as the *ergodic hypothesis*, and is essential for the development of MD.

2.2 TIME-CORRELATION FUNCTIONS

In a thermodynamic system in equilibrium, the value of a dynamic variable $A(t)$ will be constant [1]. However, if the scale is reduced so is the statistics over which the study is made, and $A(t)$ starts to fluctuate around its mean value. These microscopic spontaneous fluctuations which move away the system from its equilibrium state conform the main object in the description of the dynamical properties of the system [24, 25].

A crucial aspect about these fluctuations in the system comes through the *fluctuation-dissipation theorem*, which indicates that the laws and mechanisms describing the behavior of the fluctuations are the same as those that manifest in the system's response to an external perturbation. The connection between these different aspects is enormously meaningful: on one hand, it establishes the possibility to analyze the behavior of a system in a non-equilibrium state from the information obtained from equilibrium; moreover, it connects directly with the experiment, whose methodology consist in analyzing the reaction of a system to perturbations at certain conditions.

The fluctuations of a given space-time variable $A(\vec{r}, t)$ are treated through the *correlation functions*. These magnitudes are defined as the statistical average of the product of the dynamic variable in two different space-time points:

$$C_A(\vec{r}_1, t_1, \vec{r}_2, t_2) \equiv \langle A(\vec{r}_1, t_1) A(\vec{r}_2, t_2) \rangle \tag{8}$$

where $\langle \ldots \rangle$ stands for the ensemble average. C_A is an autocorrelation function; a correlation function can connect, in general, two different dynamic variables. Some of their main properties are:

- If the system is in equilibrium, the behavior of C_A cannot depend on the choice of the time origin, therefore:

$$C_A(t_1, t_2) = C_A(t_1 + \tau, t_2 + \tau) \tag{9}$$

With the choice $\tau = -t_2$ the time dependency simplifies:

$$C_A(t_1 - t_2) = \langle A(t_1 - t_2) A(0) \rangle \tag{10}$$

If the system is homogeneous and isotropic, C_A will only depend on the distance between points, $|\vec{r}_1 - \vec{r}_2|$:

$$C_A(|\vec{r}_1 - \vec{r}_2|) = \langle A(|\vec{r}_1 - \vec{r}_2|) A(0) \rangle \tag{11}$$

---

1 The thermodynamic limit is defined by the conditions $N \to \infty$, $V \to \infty$, with N/V, the number density, constant.

- Applying Schwartz's inequality, the time correlation function has an upper limit of its initial values:

$$C_A = \langle A(t)A(0) \rangle \leqslant \sqrt{\langle A(t)A(t) \rangle \langle A(0)A(0) \rangle} =$$
$$= \langle A(0)A(0) \rangle = C_A(0) \tag{12}$$

The normalization of $C_A(t)$ is performed by its initial value.

- For long times, $A(t)$ will be completely uncorrelated to its initial value $A(0)$:

$$C_A \xrightarrow{t \to \infty} \langle A(0) \rangle^2 \tag{13}$$

- To study time fluctuations, it is more appropriate that the value taking part in the correlations is the fluctuation itself with respect to the mean value:

$$\delta A(t) = A(t) - \langle A \rangle \tag{14}$$

Therefore, the correlation function decays, in a more proper way, to zero.

- Transforming again $\delta A \to A$ following the previous definition, the spectrum of the time correlation function can be defined, $C_A(\omega)$, through the Fourier Transform (FT):

$$C_A(\omega) = \frac{1}{2\pi} \int_{-\infty}^{+\infty} dt e^{i\omega t} C_A(t) \tag{15}$$

Many experimental techniques, as neutron scattering (NS), inelastic neutron scattering (INS) or X-Ray scattering (XRS), consist of spectroscopic readings, or spectrum measurements like $C_A(\omega)$.

- It is useful to consider the transformation between position and time spaces:

$$C_A(q) = \int d\vec{r} e^{-i\vec{q} \cdot \vec{r}} C_A(r) \tag{16}$$

Working in r space the spatial correlations are analyzed directly (distances, angles); however, q space is more appropriate for the study of collective phenomenons and for comparison with actually measured quantities.

2.3 FUNDAMENTAL PROPERTIES

The main dynamic variables in the study of the thermal movement are the number density, defined as:

$$\rho(\vec{r}, t) = \sum_{i=1}^{N} \delta(\vec{r} - \vec{R}_i(t)) \tag{17}$$

where $\delta(\vec{r})$ represents the Dirac delta and $\vec{R}_i(t)$ is the position of the i-th particle, and the density current due to the overall motion of the particles:

$$\vec{J}(\vec{r}, t) = \sum_{i=1}^{N} \vec{v}_i(t) \delta(\vec{r} - \vec{R}_i(t)) \tag{18}$$

where $\vec{v}_i$ is the velocity of the i-th particle. The mean ionic density is denoted by ρ. The relevant properties are divided into static and dynamic. The last case can be separated into single particle, named *self*, and collective. Down below, some basic functions which will be used in this work are presented (a more detailed description may be found in Hansel and McDonald's book [26])

2.3.1 *Structural properties*

The interaction among particles in a liquid system produces correlations between its positions making their space distribution neither perfectly homogeneous nor purely disordered, but characteristic of the peculiarities of their interactions. The *radial distribution function*, $g(\vec{r})$, takes into account the spatial correlations appearing in a real system due to the interaction potential. In particular, $\rho g(\vec{r})$ is the probability density of finding a particle at a certain distance r from a particle at the origin. In a simulation, it is calculated from the distance of each atom of the system to all its neighbours. An histogram is made from the results, in such a way that the integration of $\rho g(\vec{r})$ in a sphere of any radius results in the same number of neighbours as an atom has inside that sphere. $g(\vec{r})$ can be understood as a function which adjusts locally the numeric density. In isotropic systems the radial dependency is simplified: $g(\vec{r}) = g(r)$.

The general shape of $g(r)$ for a dense monatomic liquid shows some distinctive characteristics. At small r it is almost zero due to the high energies required to force atoms to overlap. The $g(r)$ shows a pronounced peak at $r = r_{max}$ which is close to the atomic diameter and is identified as the nearest neighbour distance; moreover it also characterizes the sphere of nearest neighbours. Beyond this region, the presence of several oscillations indicates that the average arrangement of particles around an arbitrary atom proceeds through 'clusters' resembling the shells of neighbours occurring in a crystal. The analogy is however incomplete, both because of the inherent isotropy of the liquid and for the ill-defined character of the shells, which are considerably broader than those of a crystal at finite temperatures. These oscillations decrease in amplitude with increasing r, and eventually $g(r)$ approaches the (unit) mean density of the system and the system effectively behaves as a structureless continuum.

The radial distribution function is defined through the following averages:

$$\rho g(\vec{r}) = \frac{1}{N} \left\langle \sum_{i \neq j} \delta(\vec{r} - \vec{R}_{ij}) \right\rangle, \quad \rho^2 g(\vec{r} - \vec{s}) = \left\langle \sum_i \delta(\vec{r} - \vec{R}_i) \sum_{j \neq i} \delta(\vec{s} - \vec{R}_j) \right\rangle \tag{19}$$

where N is the number of atoms and $\vec{R}_{ij} = \vec{R}_i - \vec{R}_j$. For systems interacting through a pair potential, thermodynamic quantities like temperature or pressure are accessible from the potential and the radial distribution function [26].

We denote the FT of $\rho(\vec{r})$ as $\rho(q)$, namely,

$$\rho(\vec{q}) = \sum_{j=1}^{N} e^{-i\vec{q} \cdot \vec{R}_j} \tag{20}$$

Note, however, that $\langle \rho(\vec{r}) \rangle = \rho$, which is not zero, and therefore, in the same spirit as discussed in equation 14, it is advantageous to consider the fluctuations around this average value, i.e.,

$$\delta\rho(\vec{r}) = \rho(\vec{r}) - \rho \quad , \quad \delta\rho(\vec{q}) = \rho(\vec{q}) - (2\pi)^3 \rho\delta(\vec{q}) \tag{21}$$

An experimentally accessible quantity which is closely related to $g(r)$ is the *static structure factor* defined by,

$$S(\vec{q}) = \frac{1}{N} \langle \delta\rho(\vec{q})\delta\rho(-\vec{q}) \rangle \tag{22}$$

$S(q)$ can be determined from NS and XRS experiments. It is connected to $g(r)$ through the FT:

$$
\begin{aligned}
S(\vec{q}) &= \frac{1}{N} \langle \delta\rho(\vec{q})\delta\rho(-\vec{q}) \rangle = \\
&= \frac{1}{N} \left\langle \left(\sum_j e^{-i\vec{q}\cdot\vec{R}_j} - (2\pi)^3 \rho\delta(\vec{q}) \right) \left(\sum_l e^{i\vec{q}\cdot\vec{R}_l} - (2\pi)^3 \rho\delta(\vec{q}) \right) \right\rangle = \\
&= 1 + \frac{1}{N} \left\langle \left(\sum_j e^{-i\vec{q}\cdot\vec{R}_j} - (2\pi)^3 \rho\delta(\vec{q}) \right) \left(\sum_{l\neq j} e^{i\vec{q}\cdot\vec{R}_l} - (2\pi)^3 \rho\delta(\vec{q}) \right) \right\rangle = \\
&= 1 + \frac{1}{N} \left\langle \int d\vec{r} e^{-i\vec{q}\cdot\vec{r}} \left(\sum_j \delta(\vec{r}-\vec{R}_j) - \rho \right) \int d\vec{s} e^{i\vec{q}\cdot\vec{s}} \left(\sum_{l\neq j} \delta(\vec{s}-\vec{R}_l) - \rho \right) \right\rangle = \\
&= 1 + \frac{1}{N} \int d\vec{r} \int d\vec{s} e^{-i\vec{q}\cdot(\vec{r}-\vec{s})} \left\langle \left(\sum_j \delta(\vec{r}-\vec{R}_j) - \rho \right) \left(\sum_{l\neq j} \delta(\vec{s}-\vec{R}_l) - \rho \right) \right\rangle = \\
&= 1 + \frac{1}{N} \int d\vec{r} \int d\vec{s} e^{-i\vec{q}\cdot(\vec{r}-\vec{s})} \left[\rho^2 g(\vec{r}-\vec{s}) - \rho^2 - \rho^2 + \rho^2 \right] = \\
&= 1 + \rho \int d\vec{t} e^{-i\vec{q}\cdot\vec{t}} \left[g(\vec{t}) - 1 \right]
\end{aligned}
\tag{23}
$$

The difference between using $\rho(\vec{q})$ or the correct $\delta\rho(\vec{q})$ in the calculation of $S(\vec{q})$ only affects the value at $q = 0$. This is important from a theoretical point of view, making $S(0)$ finite and moreover related to thermodynamic quantities as mentioned below. However, from a computational point of view from MD simulations, the value $q = 0$ is never attainable, and therefore it is safe to compute $S(q)$ as $\langle\rho(\vec{q})\rho(-\vec{q})\rangle/N$. For this reason, in the following we will not make distinctions bewteen the dynamic magnitudes and their corresponding fluctuations in the definitions of the correlation functions.

In isotropic systems, $S(\vec{q}) = S(q)$, and the previous integral turns out to be:

$$
S(q) = 1 + 4\pi\rho \int_0^\infty dr\, r^2 \left[g(r) - 1 \right] \frac{\sin qr}{qr}
\tag{24}
$$

Broadly speaking, the shapes of $S(q)$ and $g(r)$ in typical simple liquids are remarkably similar, although of course the physical meaning to be attributed to the various features is completely different in the wave vector domain. Thus, the first sharp peak of $S(q)$ reflects the existence of a dominant nearly regular arrangement of the particles in real space at value $q_{peak} \approx \frac{2\pi}{r_{max}}$. The sharp decrease of $g(r)$ at small distances is responsible for the subsequent maxima and minima of $S(q)$, which become more and more damped as q increases. Eventually, at large wave vectors, $S(q)$ probes the 'hard core' region where $g(r)$ is vanishingly small: here the contribution of the integral in equation 24 becomes negligible, and $S(q) \to 1$. In the opposite extreme, $S(q \to 0)$ reflects in an average sense the features of $g(r)$, including its asymptotic approach to unity at very large separations. As a consequence, $S(0)$ can be expected to be associated with some macroscopic property of the system. It can be shown [26],

$$
\lim_{q\to 0} S(q) = \rho k_B T \kappa_T
\tag{25}
$$

where κ_T is the isothermal compressibility. The very low values of $S(q \to 0)$ are typical for all liquids near melting, and reflect our very limited ability to compress such systems. This situation is to be compared with those taking place in an ideal gas (where $g(r) \equiv 1$ for all r, making $S(q) = 1$ at any q) and in a fluid near the liquid-gas critical point (where the onset of huge density fluctuations over macroscopic distances causes $S(0)$ to diverge).

Other functions used to investigate different static properties are the bond angle distribution function, and the electron-ion distribution function [26].

2.3.2 *Dynamic properties*

Single particle

The main dynamic quantity used to study the diffusion of the particles in the liquid is the *velocity autocorrelation function*, $Z(t)$, defined as,

$$Z(t) = \frac{1}{3} \langle \vec{v}_i(t) \cdot \vec{v}_i(0) \rangle \tag{26}$$

where $\vec{v}_i(t)$ is the velocity of the i-th particle. $Z(t)$ is a measure of the projection of the particle velocity at time t onto its initial value, averaged over all initial conditions.

The value of $Z(t)$ at $t = 0$ can be derived from the equipartition theorem,

$$Z(0) = \frac{k_B T}{m} \tag{27}$$

For times long compared with any microscopic relaxation times, the initial and final velocities are expected to be completely decorrelated, so that $Z(t \to \infty) = 0$. $Z(t)$ also has a slowly decaying part and the detailed behavior depends on both density and temperature. In a low density system, $Z(t)$ will decay slowly because the particles will collide with a low frequency. However, if the density is high, the autocorrelation can even take negative values, decaying in damped oscillations. This phenomenon is called *'cage effect'*, and represents the fact that the particles are surrounded by neighbours and their movement will consist in a number of collisions inside this cage.

There exists a general relationship between the self-diffusion coefficient, D, and the time integral of $Z(t)$. Consider a set of identical, tagged particles having positions around a point $\vec{r}(0)$. If the particles diffuse in time t to positions around $\vec{r}(t)$, the self-diffusion coefficient is given by a well-known relation due to Einstein,

$$D = \lim_{t \to \infty} \frac{1}{6t} \left\langle |\vec{r}(t) - \vec{r}(0)|^2 \right\rangle \tag{28}$$

This result is a direct consequence of Fick's law of diffusion. It is also a relation typical of a stochastic "random-walk" for which the mean-square displacement of the walker becomes a linear function of time after a sufficiently large number of random displacements have occurred. The connection between $\left\langle |\vec{r}(t) - \vec{r}(0)|^2 \right\rangle$, the mean square displacement, and $Z(t)$ is,

$$\left\langle |\vec{r}(t) - \vec{r}(0)|^2 \right\rangle = \int_0^t dt_1 \int_0^t dt_2 \langle \vec{v}(t_2) \cdot \vec{v}(t_1) \rangle =$$

$$= 3 \int_0^t dt_1 \int_0^t dt_2 Z(t_2 - t_1) = 6 \int_0^t dt_1 \int_0^{t-t_1} dt_2 Z(t_2 - t_1) = \tag{29}$$

$$= 6 \int_0^t d\tau \int_0^{t-\tau} dt_1 Z(\tau) = 6 \int_0^t d\tau (t - \tau) Z(\tau)$$

where the properties of symmetry with respect to time inversion and invariance under time translation have been used. It can be finally shown that,

$$D = \int_0^\infty Z(t) dt \tag{30}$$

This equation is an example of an important class of relations, often called "Green-Kubo formula", whereby a macroscopic, phenomenological transport coefficient is written as the time integral of a microscopic time-correlation function.

The FT of $Z(t)$ is called *frequency spectrum*, $Z(\omega)$. At low frequencies it is ruled by diffusive modes and provides information about the characteristic frequencies of the system, such as the main vibrational modes or possible couplings between the particles' velocities and the particle currents.

The typical time dependence of the mean square displacement at very short times displays a parabolic increase associated with free-particle behavior. After the initial parabolic behavior, the bulk of the results are consistent with the linear time dependence typical of the diffusive regime.

Collective dynamics

The collective dynamics is studied through the time correlation function associated with the dynamics of q-dependent density fluctuations defined by the *intermediate scattering function*, $F(\vec{q}, t)$:

$$F(\vec{q}, t) = \frac{1}{N} \langle \rho(\vec{q}, t)\rho(-\vec{q}, 0)\rangle = \frac{1}{N} \left\langle \sum_{j=1}^{N} \sum_{l=1}^{N} e^{-i\vec{q}\cdot(\vec{R}_j(t)-\vec{R}_l(0))} \right\rangle \tag{31}$$

This function describes the time dependency of the density fluctuations at different length scales. As with the static properties, if the system is homogeneous and isotropic, the vector dependency in $\vec{q}$ is reduced to the modulus, $F(q, t)$. The static structure factor is obtained as $F(q, 0) = S(q)$.

We may FT $F(q, t)$ back to the space domain to obtain the *van Hove correlation function*,

$$G(r, t) = \frac{1}{(2\pi)^3} \int d\vec{q}\, e^{i\vec{q}\cdot\vec{r}} F(q, t) = \frac{1}{N} \left\langle \sum_{j=1}^{N} \sum_{l=1}^{N} \delta(\vec{r} + \vec{R}_l(0) - \vec{R}_j(t)) \right\rangle \tag{32}$$

which is proportional to the probability of finding a particle at $(\vec{r}, t)$ given that at $t = 0$ there is a particle at the origin. It can be split into a 'self'-contribution with $j = l$ which accounts for the single-particle properties, and a 'distinct' part with $j \neq l$ responsible for collective properties. This separation also appears in the $F(q, t)$. $F_s(q, t)$ describes the evolution of the correlations where only one particle takes part.

Alternatively, from $F(q, t)$ we may proceed with a time FT into the frequency domain to obtain the *dynamic structure factor*, $S(q, \omega)$:

$$S(q, \omega) = \frac{1}{2\pi} \int_{-\infty}^{+\infty} dt F(q, t) e^{i\omega t} \tag{33}$$

As with the static structure factor, it can be measured directly through INS or XRS, being proportional to the differential cross section. In the case of INS, the double-differential cross section takes the form,

$$\frac{d^2\sigma}{d\Omega d\omega} = \frac{q_f}{q_i} \left[b_{coh}^2 S(\vec{q}, \omega) + b_{inc}^2 S(\vec{q}, \omega) \right] \tag{34}$$

where q_i and q_f are the incident and scattered wavevectors, and b_{coh} and b_{inc} are the coherent and incoherent scattering lengths of the nuclei conforming the system. The incoherent term appears when nuclei with spin different from zero are studied. In the case of inelastic X-ray scattering (IXS) which acts as a coherent probe only, the double-differential cross section takes the form,

$$\frac{d^2\sigma}{d\Omega d\omega} = \left(\frac{e^2}{m_e c^2} \right) \frac{q_f}{q_i} (\epsilon_i \epsilon_f)^{1/2} |f(q)|^2 S(q, \omega) \tag{35}$$

where ϵ_i and ϵ_f represent the polarization of the incident and scattered photons; and $f(q)$ is the atomic form factor [2]. Moreover, now the dynamic structure factor has a coherent part only.

One of the most interesting phenomena to study in liquid state dynamics is the existence of propagating modes in the system. These propagating modes represent collective fluctuations that travel in an analogous way as the phonon in a solid. A maximum in $S(q, \omega)$ at $\omega \neq 0$ is proof of the existence of these type of propagating modes

---

2 Note that $f(q \to 0) = Z$, i.e. the total number of electrons in the scattering atom.

in the liquid. However, these peaks are difficult to observe in experimental measurements, and their calculation through simulations can also be challenging. In fact, there is not yet a theory correctly describing the behavior of these modes outside the hydrodynamic regime ($q \rightarrow 0$). Therefore, is not possible to know beforehand if a system can support these modes or not and, if so, in which frequency range.

Another important dynamic variable is the particle current due to the overall motion of the particles, $\vec{J}(\vec{r}, t)$, previously defined in equation 18, and its FT,

$$\vec{J}(\vec{q}, t) = \sum_{j=1}^{N} \vec{v}_j(t) e^{-i\vec{q} \cdot \vec{R}_j(t)} \tag{36}$$

which is split into a longitudinal component, $\vec{J}_L(\vec{q}, t)$, and a transverse component, $\vec{J}_T(\vec{q}, t)$, to the wave vector $\vec{q}$. The *longitudinal and transverse current correlation functions* are defined as the autocorrelation functions of the respective components of the current,

$$C_L(q, t) = \frac{1}{N} \langle \vec{J}_L(\vec{q}, 0) \cdot \vec{J}_L(\vec{q}, t) \rangle \tag{37}$$

$$C_T(q, t) = \frac{1}{2N} \langle \vec{J}_T(\vec{q}, 0) \cdot \vec{J}_T(\vec{q}, t) \rangle \tag{38}$$

Their respective spectra in the frequency domain are defined as $C_L(q, \omega)$ and $C_T(q, \omega)$. The spectrum of the longitudinal current correlation function is directly related to the spectrum of the dynamic structure factor through the relation

$$q^2 C_L(q, \omega) = \omega^2 S(q, \omega) \tag{39}$$

From these relations it can be deduced that both correlation functions contain in essence the same information; however, it is interesting to analyze both.

The transverse current correlation function, $C_T(q, t)$, is not associated with any measurable quantity and can only be determined by means of computer simulations. It provides information on the shear modes and its shape evolves from a Gaussian, in both q and t, at the free-particle ($q \rightarrow \infty$) limit, towards a Gaussian in q and an exponential in t at the hydrodynamic limit ($q \rightarrow 0$), i.e.

$$C_T(q \rightarrow 0, t) = \frac{1}{\beta m} e^{-q^2 \eta |t|/m\rho} \tag{40}$$

where η is the shear viscosity coefficient, $\beta = (k_B T)^{-1}$ is the inverse of the temperature times the Boltzmann constant and m is the atomic mass. Whereas at both limits the corresponding $C_T(q, t)$ take positive values for all times, at intermediate q-values it may show a more complicated behavior, including well defined oscillations within a limited q-range. It is established that liquids, from the macroscopic point of view, cannot support shear waves as solids do. From the atomic scale, this means that transverse current fluctuations will vanish through diffusive processes. This situation is not so when deformations in the wave length and frequencies of the microscopic scale are considered. In this case, the system can sustain transverse modes. Their existence is revealed through side peaks in $C_T(q, \omega)$. From the calculated $C_T(q, t)$, the shear viscosity of the liquid, η, can be obtained.

Using Mori-Zwanzig's formalism, which will be introduced in the next chapter, a generalized shear viscosity coefficient, $\eta(q, z)$, can be defined in terms of $M_T(q, t)$ which is the first-order memory function of $C_T(q, t)$, namely

$$\tilde{C}_T(q, z) = \frac{1}{\beta m} \left[z + \tilde{M}(q, z) \right]^{-1} \equiv \frac{1}{\beta m} \left[z + \frac{q^2}{m\rho} \tilde{\eta}(q, z) \right]^{-1} \tag{41}$$

where $\tilde{C}_T(q, z)$ and $\tilde{M}(q, z)$ are the Laplace transforms of $C_T(q, t)$ and $M(q, t)$ respectively.

The area under the normalized $C_T(q, t)$ gives $\beta m \tilde{C}_T(q, z = 0)$; next the values $\tilde{\eta}(q, z = 0)$ are extrapolated to $q \rightarrow 0$ (hydrodynamic limit) which gives the usual shear viscosity coefficient, η.

2.4 EXTENSION TO BINARY SYSTEMS

2.4.1 *Structural properties*

In Chapter 8 of this thesis, it will be necessary to generalize the previously given expressions for the distribution and correlation functions. In general, the correlation functions will present double subscripts, each one related to each of the species in the alloy. In this way, it will describe the correlation among particles of the same type and between atoms of different types. For example, three partial distribution functions can be defined, $g_{ij}(r)$, describing the surrounding of particles of type j around one of type i. From these functions we can study the local structure of the alloy. From the knowledge of $g_{ij}(r)$, the distribution of nearest neighbours (NNs) can readily be obtained. If n_{ij} denote the number of j-type particles around an i-type particle within a sphere of radius R_{ij}, then

$$n_{ij} = 4\pi\rho \, x_j \int_0^{R_{ij}} r^2 g_{ij}(r) dr \,, \tag{42}$$

where x_j is the concentration of the j-type particles and R_{ij} can be identified with the position of the first minimum of the corresponding radial distribution function $G(r) = 4\pi r^2 g_{ij}(r)$ [28]. A way of quantifying the aforementioned ordering tendencies is provided by the Wagner [27] short range order (SRO) parameter for the first neighbour shell, α_1, which is defined as

$$\alpha_1 = 1 - \frac{n_{ij}}{x_j(x_i n_j + x_j n_i)} \qquad (j \neq i = 1, 2), \tag{43}$$

where x_j is the concentration of the j-type particles, $n_i = n_{ii} + n_{ij}$ ($i, j = 1, 2$) and n_{ij} is the number of j-type particles around an i-type which are located within a sphere of radius R_{ij}. A positive value of α_1 indicates that the liquid presents an homocoordinating tendency, i.e. particles of the same type tend to be surrounded by atoms of their same type. On the other hand, a negative value of α_1 indicates the contrary, i.e. a tendency towards heterocoordination. For a random distribution of atoms, $\alpha_1 = 0$.

Several types of static structure factors are used in the literature to study alloys.

Ashcroft-Langreth

The Ashcroft-Langreth (AL) partial static structure factors are the ones directly describing the different correlations between the particles [32].

$$S_{ij}(q) = \delta_{ij} + 4\pi\rho\sqrt{x_i x_j} \int_0^\infty dr r^2 \frac{\sin qr}{qr}[g_{ij}(r) - 1] \tag{44}$$

Bathia-Thornton

The Bhatia-Thornton (BT) partial structure factors [24, 31] are ideally suited for investigating chemical and topological ordering tendencies in a binary liquid alloy. These are the concentration-concentration, $S_{CC}(q)$, the number-number, $S_{NN}(q)$, and the number-concentration, $S_{NC}(q)$, partial structure factors, and they can be obtained from the above AL partial structure factors. Their long-wavelength limits provide microscopic information on the ordering tendencies of the liquid alloy, specially $S_{CC}(q \to 0)$.

NN: Number-number. Describes the global structure of the alloy without specifying the type of each particle. Mathematically it is the static correlation function of the number density in the Fourier space: $\rho(q) = \rho_1(q) + \rho_2(q)$.

$$S_{NN}(q) = x_1 S_{11}(q) + x_2 S_{22}(q) + 2(x_1 x_2)^{1/2} S_{12}(q) \tag{45}$$

CC: Concentration-concentration. Describes how the particles distribute and gather attending to their chemical species. The correlation function taking part here is the fluctuations' concentration: $\Delta x(q) = (V/N)[x_2\rho_1(q) - x_1\rho_2(q)]$,

$$S_{CC}(q) = x_1 x_2 [x_2 S_{11}(q) + x_1 S_{22}(q) - 2(x_1 x_2)^{1/2} S_{12}(q)] \tag{46}$$

As with equation 25, in the limit $q \to 0$ the static structure factors can be related to thermodynamic information. In particular, $S_{CC}(0)$ takes a value equal to $x_1 x_2$ if we have an ideal alloy, while deviations from this value indicate the tendency of the system: homocoordinating, if it tends to form pairs of same particles ($S_{CC}(q) > x_1 x_2$) or heterocoordination, if it tends to form pairs of different particles ($S_{CC}(q) < x_1 x_2$).

NC: Number-concentration. Describes the cross correlation between density fluctuations and density concentration,

$$S_{NC}(q) = x_1 x_2 \left[S_{11}(q) - S_{22}(q) + (x_2 - x_1) S_{12}(q)/(x_1 x_2)^{1/2} \right] \tag{47}$$

In an ideal alloy there is no such correlation and $S_{NC}(q) = 0$.

Total static structure factor

From the partial AL static structure factors $S_{ij}(q)$, the total neutron weighted static structure factor $S_T(q)$ is readily evaluated using the expression

$$\langle b^2 \rangle S_T^{(INS)}(q) = \sum_{i=1}^{2} \left(\langle b_i^2 \rangle - \langle b_i \rangle^2 \right) x_i + \sum_{i,j=1}^{2} (x_i x_j)^{1/2} \langle b_i \rangle \langle b_j \rangle S_{ij}(q) \tag{48}$$

where $\langle b_i \rangle$ is the coherent scattering length, $4\pi \langle b_i^2 \rangle$ is the total scattering cross-section and $\langle b^2 \rangle = \sum_{i=1}^{2} x_i \langle b_i^2 \rangle$ is the average cross-section per atom. In the case of IXS, the total static structure factor only presents the coherent term, namely,

$$S_T^{(IXS)}(q) = \sum_{i,j=1}^{2} (x_i x_j)^{1/2} \frac{f_i(q) f_j(q)}{\langle f^2(q) \rangle} S_{ij}(q) \tag{49}$$

where $f_i(q)$ are the atomic scattering form factors and $\langle f^2(q) \rangle = \sum_{i=1}^{2} x_i f_i^2(q)$.

As $S_T(q)$ is a weighted sum of the partial static structure factors, the experimental determination of the latter involves three independent measurements with different scattering lengths of the i and j species. If this is not possible, a common practice to derive them has been the application of the concentration method, which is based on the assumption that the partial pair distribution functions are independent of the alloy concentration.

The presented formulations to calculate the partial static structure factors contain the same information, given the relationships between them through linear combinations. However, each one is better suited to study different aspects of the alloy's properties.

2.4.2 *Dynamic properties*

In liquid systems, the information about several transport properties related to the mobility of the particles and the coupling between the velocities of distinct particles is provided by time correlation functions among the atomic velocities. These functions cannot be determined experimentally, and other methods, such as MD simulations, have to be used. We are mainly interested in the relative velocity correlation functions (VCFs),

$Z_{ij}(t)$, which are defined as the time correlation function of the relative velocity of the center of mass of species i with respect to the center of mass of species j [34, 35], i.e.,

$$Z_{ij}(t) = \frac{1}{3} x_i x_j N < [\mathbf{v}_i(t) - \mathbf{v}_j(t)] \cdot [\mathbf{v}_i(0) - \mathbf{v}_j(0)] > , \qquad (50)$$

where N is the total number of particles and $\mathbf{v}_i(t)$ is the mean molecular velocity of component i,

$$\mathbf{v}_i(t) = \frac{1}{N_i} \sum_{l(i)=1}^{N_i} \mathbf{v}_{l(i)}(t) , \qquad (51)$$

N_i being the total number of i-type particles and $\mathbf{v}_{l(i)}(t)$ the velocity of the i-type particle $l(i)$. The $Z_{ij}(t)$ can be separated into self, $Z_{ij}^0(t)$, and distinct, $Z_{ij}^d(t)$, contributions as

$$Z_{ij}(t) = (1 - \delta_{ij}) Z_{ij}^0(t) + x_i x_j Z_{ij}^d(t) , \qquad (52)$$

where δ_{ij} is Kronecker's delta, $Z_{ij}^0(t) = x_j Z_i^s(t) + x_i Z_j^s(t)$, $Z_i^s(t)$ being the well-known velocity autocorrelation function of a tagged i-type particle in the fluid, and $Z_{ij}^d(t)$ accounts for the contribution of the distinct velocity correlations. The time integrals of $Z_{ij}(t)$, $Z_{ij}^0(t)$, $Z_{ij}^d(t)$ and $Z_i^s(t)$, give the associated diffusion coefficients, D_{ij}, D_{ij}^0, D_{ij}^d and D_i^s, respectively, where D_i^s is the standard self-diffusion coefficient. For binary mixtures we may write

$$D_{12} = D_{12}^0 + x_1 x_2 \, D_{12}^d \; \equiv \; D_{12}^0 (1 + \gamma_{12}) , \qquad (53)$$

where $D_{12}^0 = x_2 D_1^s + x_1 D_2^s$ and γ_{12} is a measure of the deviation from an ideal mixture (when all species are identical, $\gamma_{12} = 0$). Within this formalism, the interdiffusion coefficient is written as

$$D_{int} = \theta \, D_{12} = \theta (1 + \gamma_{12}) D_{12}^0 , \qquad (54)$$

where $\theta = x_1 x_2 / S_{CC}(q \to 0)$. For a nearly ideal mixture, $\theta \approx 1$, $\gamma_{12} \approx 0$ and, therefore, $D_{int} \approx D_{12}^0$.

The collective dynamics of the density fluctuations in an alloy is usually described through the partial AL intermediate scattering functions $F_{ij}(\mathbf{q}, t) = \langle \rho_i(\mathbf{q}, t) \cdot \rho_j^*(\mathbf{q}, 0) \rangle$, where

$$\rho_j(\mathbf{q}, t) = \frac{1}{\sqrt{N_j}} \sum_{l(j)=1}^{N_j} \exp[-i\mathbf{q} \cdot \mathbf{R}_{l(j)}(t)] \qquad (55)$$

is the FT of the *i*-type component partial number density, N_j is the number of *j*-type particles, $\mathbf{R}_{l(j)}(t)$ is the position of the *j*-type particle l and $\langle .... \rangle$ denotes the ensemble average. The time FTs of the $F_{ij}(\mathbf{q}, t)$ into the frequency domain give the partial dynamic structure factors $S_{ij}(\mathbf{q}, \omega)$, which can be compared with the INS or IXS data.

Another important dynamical quantity is the *j*-type component particle current, defined as

$$\mathbf{J}_j(\mathbf{q}, t) = \frac{1}{\sqrt{N_j}} \sum_{l(j)=1}^{N_j} \mathbf{v}_{l(j)}(t) \, \exp[-i\mathbf{q} \cdot \mathbf{R}_{l(j)}(t)] , \qquad (56)$$

which is usually split into a longitudinal component $\mathbf{J}_j^L(\mathbf{q}, t)$, parallel to $\mathbf{q}$, and a transverse component $\mathbf{J}_j^T(\mathbf{q}, t)$, perpendicular to $\mathbf{q}$. The partial longitudinal and transverse current correlation functions, $C_{ij}^L(\mathbf{q}, t)$ and $C_{ij}^T(\mathbf{q}, t)$, are defined in terms of these as

$$C_{ij}^L(\mathbf{q}, t) = \langle \mathbf{J}_i^L(\mathbf{q}, t) \cdot \mathbf{J}_j^{L\,*}(\mathbf{q}, 0) \rangle \qquad (57)$$

and

$$C_{ij}^T(\mathbf{q}, t) = \frac{1}{2} \langle \mathbf{J}_i^T(\mathbf{q}, t) \cdot \mathbf{J}_j^{T\,*}(\mathbf{q}, 0) \rangle, \tag{58}$$

and their time FTs give the respective spectra, $C_{ij}^L(\mathbf{q}, \omega)$ and $C_{ij}^T(\mathbf{q}, \omega)$. For isotropic systems, all the previous correlation functions depend only on $q = |\mathbf{q}|$.

The first CMD simulations of transverse current correlations in binary systems were performed on molten salts [36], and showed that $C_{NN}^T(q, \omega)$ behaves similarly to $C^T(q, \omega)$ in one-component liquids, with a peak at intermediate q values. Subsequently, CMD studies have been performed on binary Lennard-Jones fluids [37], and both CMD and AIMD simulations for liquid Li-Mg, Li-Na, Li-Ba, K-Cs and Li-Pb alloys [38–41].

The alloy shear viscosity can be derived using the same method introduced in section 2.3.2 for the total transverse current correlation function $C_{tt}^T(q, t) = \langle J_t^T(q, t) J_t^{T\,*}(q, 0) \rangle$, where $J_t^T(q, t) = x_1^{1/2} m_1 J_1^T(q, t) + x_2^{1/2} m_2 J_2^T(q, t)$ is the total transverse current, m_1 and m_2 are the atomic masses and the $J_i^T(q, t)$ are defined as in Eq. (56). In the hydrodynamic limit [23],

$$C_{tt}^T(q \to 0, \ t) = \left(\frac{1}{\bar{m}\beta} \right) \exp\{ -q^2 \eta \, |t| \, / \bar{m}\rho \}, \tag{59}$$

where $\bar{m} = x_1 m_1 + x_2 m_2$ and η is the alloy shear viscosity.

2.5 FREE LIQUID SURFACES

The study of the structure of free liquid surfaces (FLSs) has attracted much theoretical and experimental work, with emphasis on the possible existence of liquid surface layers. In 1981 D'Evelyn and coworkers [42] predicted that the atomic density near the free surface of a metallic liquid would change in a non monotonic way, displaying a stratification in layers parallel to the interface. Moreover, those oscillations would show up as a Bragg-like peak in the X-ray (XR) reflectivity curve, $R(q_z)$. In this technique, x-rays impinge upon the liquid surface at a very small angle α and are scattered at the same angle within the reflection plane defined by the incident beam and the surface normal. The measured reflectivity has a peak located at a wave vector $q_z \approx 2\pi/\lambda$, where λ is the spacing between layers.

However, it took several years to obtain the first experimental proof of surface layering. In 1995 Magnussen and coworkers [43] reported the existence of surface layering in the free surface of liquid Hg (l-Hg) at room temperature. Since then, XR reflectivity measurements have been performed on other liquid-metal surfaces, such as Ga [44], In [45], potassium (K) [46], Sn [47], and Bi [48]; in all cases, the measured XR reflectivity curves displayed (or suggested, as in the case of l-K) the expected Bragg-like peak.

From a theoretical standpoint, the nature of the mechanisms behind the surface layering phenomenon has not been elucidated yet, although several hypotheses have been advanced. Zhao and coworkers [49] have pointed to the interconnection between the ionic and electronic densities and have noted that the rapid decay of the valence electronic density at the interface would generate a one-body potential whose gradient gives rise to a confining force that acts like a wall against which the ions are packed. Other explanations [50] have focused on the undercoordinated ions near the surface which would attempt to regain the coordination they had in the bulk liquid, resulting in an increased ionic density in the outermost liquid part and inducing the propagation of a density oscillation into the bulk.

More recently, it has been proposed [51] that surface layering is a rather universal phenomenon which in most cases is frustrated by solidification, and therefore it only appears in those systems whose melting temperature is very low in comparison to the critical temperature. This latter suggestion has received some confirmation from a recent XR reflectivity experiment [52] where surface layering was found in a molecular nonmetallic liquid with a

low melting point and a high critical point (as in a liquid metal), which suggests that the presence of an electron gas is not a basic condition in order to obtain an oscillating ionic density profile (DP). The oscillations in these types of systems are rather weak, showing values of the density maxima that are even smaller than the bulk density, in stark contrast to the strong oscillations found in liquid metals. Nevertheless, it was shown by Bomont *et al.* [53] that these strong oscillations can be obtained for liquids with a low melting temperature and a high critical temperature, provided that allowance is made for a change in the strength of the interactions (not in their form) across the liquid-vapor interface through a density dependence of this strength.

2.5.1 *Ionic density profile*

The experimental XR reflectivity data $R(q_z)$ have usually been analyzed by resorting to analytical models of the total electronic density profile (TEDP), which is the physical quantity probed by X-rays. These analytical models include several parameters which are fitted in order to reproduce the measured $R(q_z)$ curve. The distorted crystal (DC) model has been the preferred model and has provided a reasonable fitting for the reflectivities of liquid Hg, Ga, In, and K [43–46, 54].

However, some caution ought to be exercised when deriving an ionic DP from a measured $R(q_z)$, as it has been found that different DPs can lead to very similar $R(q_z)$ curves. In addition to a model for the ionic DP, it is also necessary to take into account how the thermally induced capillary waves in the surface affect the $R(q_z)$ data obtained in the measurement.

Another route to calculate an ionic (or electronic) DP is by resorting to computer simulations, which provide a detailed description of the ionic positions and therefore allow the direct evaluation of the ionic DP. The longitudinal ionic DP is computed from a histogram of the particle positions relative to the slab's center of mass, with the profiles from both halves of the slab being averaged. The wavelength, λ, of the ionic oscillations scales linearly with the radius of the Wigner-Seitz spheres, R_{WS}, while it shows no definite relationship with electronic parameters, like the radius per electron, r_s [55]. This suggests that the ionic oscillations are not a consequence of Friedel oscillations in the electronic density, but on the contrary they are due to atomic stacking against the surface.

Static properties

The planar FLS interfaces considered in this thesis are inhomogeneous systems along the z direction, but isotropic and homogeneous on the xy planes; consequently the two-body distribution functions, which provide information about the atomic structure, depend on the z coordinates of the two particles and on the transverse distance between them i.e., $g(\vec{r}_1, \vec{r}_2) = g(z_1, z_2, \mathbf{R}_{12})$ where $\mathbf{R}_{12} = \sqrt{(x_2 - x_1)^2 + (y_2 - y_1)^2}$.

2.5.2 *Reflectivity*

The XR reflectivity experiments on the FLS probe the total electronic density distribution. A particular source of complications due to the liquid nature of the samples is the presence of thermally induced capillary waves (CW) which blur the so-called intrinsic profile, $\rho_{int}(z)$, leading to an average profile $\rho_{av}(z)$, and deplete even more the measured reflectivity, $R_m(q_z)$. The effects of CW are removed from $R_m(q_z)$ through the use of the macroscopic CW theory, that boils down to a division of $R_m(q_z)$ by a Gaussian, Debye-Waller-like, factor that depends on a capillary roughness, σ_{CW}, leading to intrinsic reflectivity, $R_{int}(q_z)$. In most cases, this is further scaled by the Fresnel reflectivity, $R_F(q_z)$, that corresponds to a sharp flat surface and accounts for the overall decay of $R_{int}(q_z)$,

$$\frac{R_m(q_z)}{exp(-\sigma_c^2 q_z^2) R_F(q_z)} = |\Phi_{int}(q_z)|^2 \tag{60}$$

where $q_z = (4\pi/\zeta)\sin\alpha$ is the momentum transfer perpendicular to the interface, with ζ the wavelength of the incident X-rays. The resulting quantity, $|\Phi_{int}(q_z)|^2$, is called the surface structure factor which is directly related [44, 56] to the FT of the TEDP, $n_{e,int}^T(z)$, including both valence and core electrons,

$$\Phi_{int}(q_z) = \frac{1}{n_{e0}^T} \int_{-\infty}^{\infty} \left(\frac{\partial n_{e,int}^T(z)}{\partial z} \right) \exp(-iq_z z) \quad dz \tag{61}$$

where n_{e0}^T is the bulk mean total electron density. The exponential term in equation 60 accounts for the effect of surface roughness and is usually written as a sum of two contributions, namely,

$$\sigma_c^2 = \sigma_0^2 + \sigma_{CW}^2 \tag{62}$$

where σ_0 is and intrinsic surface roughness and σ_{CW} is quantified as,

$$\sigma_{CW}^2 = \frac{k_B T}{2\pi\gamma} \ln\left(\frac{q_{max}}{q_{min}} \right) \tag{63}$$

with γ is the surface tension, and q_{max} and q_{min} are respectively the largest and smallest wavevector contributions to the thermal excitation of the interface. A customary choice is $q_{max} = \pi/a$ with a being the ionic diameter, whereas q_{min} depends in general on the sample's size and the instrumental resolution.

Intrinsic density profile

The sample size in simulations is utterly smaller than in experiments and consequently the abundance of CW is much reduced, but it is not negligible. It is therefore important to take into account this difference for proper comparison with experimental data. In previous studies the procedure adopted has been the same macroscopic CW theory as used in experiments, except for the aforementioned size differences. However, a more direct access to the intrinsic profile and reflectivity is desirable, considering that the simulation samples are very far from being macroscopic.

One such method was proposed by Chacón and Tarazona (CT) [57]. The CT procedure to obtain the intrinsic DP (IDP) for a FLS relies on the computation, for each MD configuration, of a liquid-vapor separation surface, $z = \xi(x, y)$, so that the IDP is obtained from a histogram of the particles distances to this surface along the z-direction, i.e., according to their values of $z_{i;rel} = z_i - \xi(x_i, y_i)$, where i runs over all the particles of the sample.

3

MODELING THE LIQUID STATE

Chapter 2 dealt largely with the formal definition and general properties of time-correlation functions and with establishing the link between spontaneous time-dependent fluctuations and the response of a fluid to an external probe. The aim of the present chapter is to show how the decay of fluctuations can be described in terms of hydrodynamics and to obtain expressions for the macroscopic transport coefficients.

The microscopic structure of a liquid is revealed experimentally by the scattering of radiation of wavelength comparable with the interparticle spacing. When discussing the dynamics, it is necessary to consider simultaneously the scales of length and time. In keeping with traditional kinetic theory, it is conventional to compare wavelengths with the mean free path l and times with the mean collision time τ. The wavenumber-frequency plane may then be divided into three parts. The region in which $kl \ll 1$, $\omega\tau \ll 1$ corresponds to the *hydrodynamic regime*, where the behavior of the fluid is described by the phenomenological equations of macroscopic fluid mechanics. The range of intermediate wavenumbers and frequencies ($kl \simeq 1$, $\omega\tau \simeq 1$) forms the *intermediate dynamic regime*, where allowance must be made for the molecular structure of the fluid and where a treatment based on the microscopic equations of motion is required. Finally, the region where $kl \gg 1$, $\omega\tau \gg 1$, represents the *free-particle regime*; here the distances and times involved are so short that the particles are almost independent of each other.

3.1 THE HYDRODYNAMIC REGIME

In this section we will be concerned with the hydrodynamic regime, where the local properties of the fluid vary slowly on microscopic scales of length and time. The set of hydrodynamic variables consists of the densities of mass, momentum and energy. The hydrodynamic variables satisfy continuity equations, which express the conservation of matter, momentum and energy. In addition, the hydrodynamic variables obey certain constitutive relations between the fluxes (or currents) and the gradients of local variables, written in terms of phenomenological transport coefficients. Fick's law of diffusion and Fourier's law of heat transport are two of the more familiar examples of a constitutive relation.

3.1.1 *Single particle*

In the time scale characteristic of the hydrodynamic regime, a tagged particle will have suffered a given number of collisions with its neighbours and the microscopic density, $\rho_s(\vec{r}, t)$, will exhibit a diffusive behavior satisfying a continuity equation of the form,

$$\dot{\rho}_s(\vec{r}, t) + \nabla \cdot \vec{J}_s(\vec{r}, t) = 0 \tag{64}$$

and the corresponding constitutive relation is provided by Fick's law,

$$\vec{J}_s(\vec{r}, t) + D\nabla\rho_s(\vec{r}, t) = 0 \tag{65}$$

where $\vec{J}_s(\vec{r}, t)$ is the self current and D is the self-diffusion constant. Combining both,

$$\dot{\rho}_s(\vec{r}, t) - D\nabla^2\rho_s(\vec{r}, t) = 0 \tag{66}$$

or, in reciprocal space where it can be integrated to give,

$$\dot{\rho}_s(\vec{q}, t) + Dq^2\rho_s(\vec{q}, t) = 0 \implies \rho_s(\vec{q}, t) = \rho_s(\vec{q}, 0)e^{-Dq^2t} \tag{67}$$

If we multiply both sides by $\rho_s(-\vec{q}, 0)$ and average over initial conditions, we obtain the self intermediate scattering function for the hydrodynamic regime,

$$F_s(\vec{q}, t) = \frac{1}{N}\langle\rho_s(\vec{q}, t)\rho_s(-\vec{q}, t)\rangle = \frac{1}{N}\langle\rho_s(\vec{q}, 0)\rho_s(-\vec{q}, 0)\rangle e^{-Dq^2t} = e^{-Dq^2t} \tag{68}$$

From this result the van Hove self correlation function, $G_s(r, t)$, and the self dynamic structure factor, $S_s(q, \omega)$, are obtained

$$G_s(r, t) = (4\pi Dt)^{-3/2}exp\left(\frac{-r^2}{4D|t|}\right) \tag{69}$$

$$S_s(q, \omega) = \frac{1}{\pi}\frac{Dq^2}{\omega^2 + (Dq^2)^2} \tag{70}$$

Therefore, in the hydrodynamic regime $F_s(q, t)$ and $G_s(r, t)$ show a Gaussian behavior in q and r, respectively, with a diffusive component in time. Meanwhile, $S_s(q, \omega)$ is represented by a single Lorentzian curve centered at $\omega = 0$ with a half-width at half-height given by Dq^2.

3.1.2 *Collective dynamics*

The hydrodynamic picture of the liquid state is that of a continuum undergoing density fluctuations that displace it away from its equilibrium state. In this picture, the relaxation modes ruling the decay of these density fluctuations can be analyzed by means of the equations that govern the system at this scale (length scales much longer than interparticle distance, times scales much longer than the mean collision time), and by obtaining the corresponding correlation functions. In the case of a non-relativistic monatomic fluid the collective dynamics is studied through the conservation laws of mass, momentum and energy,

$$\dot{\rho}(\vec{r}, t) + \frac{1}{m}\nabla \cdot \vec{p}(\vec{r}, t) = 0 \tag{71}$$

$$\dot{\vec{p}}(\vec{r}, t) + \nabla \cdot \boldsymbol{\sigma}(\vec{r}, t) = 0 \tag{72}$$

$$\dot{Q}(\vec{r}, t) + \nabla \cdot \vec{J}^e(\vec{r}, t) = 0 \tag{73}$$

where $\vec{p}$ is the momentum density, $\boldsymbol{\sigma}(\vec{r}, t)$ is the stress tensor and $\vec{J}^e(\vec{r}, t)$ is the energy current defined through thermodynamic variables such as the local pressure, $P(\vec{r}, t)$ and temperature, $T(\vec{r}, t)$, and transport coefficients such as the thermal conductivity, ζ, the shear viscosity, η and the bulk viscosity, η_b.

We will not explicitly solve the equations, but just describe the general problem [1]. These equations are linearized under the assumption that the system is always close to equilibrium and the fluctuations are negligible beyond second order. Two independent variables are used to describe the equation of state, being ρ and T a standard choice. A set of differential equations in $(\vec{r}, t)$ is obtained for five fluctuating variables $\{\delta\rho, j^x, j^y, j^z, \delta T\}$, which turns into an algebraic set in $(\vec{q}, z)$ through the Fourier-Laplace transforms. It is important to separate $\vec{J}$ into the longitudinal and transverse components with respect to $\vec{q}$, which is usually chosen along the z-axis, so that j^z represents the longitudinal component and j^α, with $\alpha = \{x, y\}$, stands for the transverse components.

---

1 A thorough description of the hydrodynamic equations can be found in several books, i.e [26]

The system is arranged into a matrix form, $\mathbf{M}(\vec{q}) \cdot A(\vec{q}, z) = A(\vec{q}, 0)$, where $A(\vec{q}, z)$ and $A(\vec{q}, 0) = A(\vec{q})$ are,

$$A(\vec{q}, z) = \{\rho(\vec{q}, z), T(\vec{q}, z), j^z(\vec{q}, z), j^x(\vec{q}, z), j^y(\vec{q}, z)\} \tag{74}$$

$$A(\vec{q}) = \{\rho(\vec{q}), T(\vec{q}), j^z(\vec{q}), j^x(\vec{q}), j^y(\vec{q})\} \tag{75}$$

After the calculations previously mentioned, the *hydrodynamic matrix*, $\mathbf{M}(\vec{q})$, will have the following form,

$$\mathbf{M}(\vec{q}) = \begin{pmatrix} z & 0 & iq & 0 & 0 \\ 0 & z + aq^2 & \frac{iqT}{\rho^2 c_v}\left(\frac{\partial P}{\partial T}\right)_\rho & 0 & 0 \\ \frac{iq}{m}\left(\frac{\partial P}{\partial \rho}\right)_T & \frac{iq}{m}\left(\frac{\partial P}{\partial T}\right)_\rho & z + bq^2 & 0 & 0 \\ \hline 0 & 0 & 0 & z + \nu q^2 & 0 \\ 0 & 0 & 0 & 0 & z + \nu q^2 \end{pmatrix} \tag{76}$$

where P is the hydrostatic pressure, c_v is the specific heat at constant volume and,

$$a = \frac{\zeta}{\rho c_v} \quad , \quad b = \frac{4\eta/3 + \eta_b}{m\rho} \quad , \quad \nu = \frac{\eta}{m\rho} \tag{77}$$

The block-diagonal structure of the hydrodynamic matrix shows that the transverse current fluctuations are completely decoupled from the fluctuations in the other (longitudinal) variables. The determinant of the hydrodynamic matrix therefore factorizes into the product of purely longitudinal and purely transverse parts. Transverse modes have a double root, namely,

$$z = -\nu q^2 \tag{78}$$

The longitudinal part is a cubic equation in q, but because the hydrodynamic calculation is valid only in the long-wavelength limit, it suffices to calculate the complex frequencies to order q^2. Three longitudinal modes are obtained,

$$z = -D_T q^2 \tag{79}$$

$$z = -\Gamma q^2 \pm ic_s q \tag{80}$$

where D_T is the thermal diffusivity and Γ is the sound-attenuation coefficient,

$$D_T = \frac{\zeta}{\rho c_p} = \frac{a}{\gamma_0} \quad , \quad \Gamma = \frac{1}{2}\frac{a(\gamma_0 - 1)}{\gamma_0 + b} \tag{81}$$

with c_s the adiabatic sound velocity, c_p the specific heat at constant pressure and $\gamma_0 = \frac{c_p}{c_v}$. The purely real roots represent a diffusive process whose origin is the entropy fluctuations at constant pressure and it decays in time with a half life determined by D_T without propagating. The complex roots describe two acoustic modes whose origin is related to pressure fluctuations at constant entropy. These modes propagate with velocity c_s, and their half life is determined by the sound-attenuation coefficient, Γ.

Longitudinal collective modes

The longitudinal modes are those associated with fluctuations in density, temperature and the projection of the momentum along the direction of $\vec{q}$. The density can be expressed as,

$$\rho(q, t) = \rho(q, 0)\left[\left(\frac{\gamma_0 - 1}{\gamma_0}\right)e^{-D_T q^2 t} + \frac{1}{\gamma_0}e^{-\Gamma q^2 t}[\cos(c_s q t) + C\sin(c_s q t)]\right] \tag{82}$$

with $C = \left[3\Gamma - \eta/(\rho m)\right]/(c_s \gamma_0)$. From this expression, the dynamic structure factor, $S(q, \omega)$, containing all the information concerning the dynamics of density fluctuations is calculated. As already mentioned, $S(q, \omega)$ can be measured experimentally in scattering experiments. Finally, the following expression is obtained for the hydrodynamic $S(q, \omega)$,

$$
\begin{aligned}
S(q, \omega) = \frac{S(q)}{2\pi} & \left[\left(\frac{\gamma_0 - 1}{\gamma_0}\right) \frac{2D_T q^2}{\omega^2 + (D_T q^2)^2} + \right. \\
& \left. \left[+\frac{1}{\gamma_0}\left(\frac{\Gamma q^2}{(\omega + c_s q)^2 + (\Gamma q^2)^2} + \frac{\Gamma q^2}{(\omega - c_s q)^2 + (\Gamma q^2)^2}\right)\right]\right]
\end{aligned}
$$

(83)

The spectrum of density fluctuations therefore consists of three components: a Rayleigh line, centered at $\omega = 0$, and two Brillouin lines at $\omega = \pm c_s q$.

Transverse collective modes

The hydrodynamic behavior of the transverse current fluctuations in the time domain is governed by a first-order differential equation,, that is

$$
\frac{\partial}{\partial t} j^x(q, t) + \nu q^2 j^x(q, t) = 0
$$

(84)

Multiplying by $j^x(-q, 0)$ and taking the thermal average, we find that the transverse current autocorrelation function satisfies the equation,

$$
\dot{C}_T(q, t) + \nu q^2 C_T(q, t) = 0
$$

(85)

In the hydrodynamic limit, it takes the typical exponential decay of a diffusive process,

$$
C_T(q, t) = \frac{e^{-\nu q^2 t}}{m\beta}
$$

(86)

The corresponding power spectrum is of Lorentzian form,

$$
C_T(q, \omega) = \frac{1}{m\beta\pi} \frac{\nu q^2}{\omega^2 + (\nu q^2)^2}
$$

(87)

In conclusion, transverse modes are purely diffusive in the hydrodynamic regime, according to the traditional description of a liquid.

3.2 GENERALIZED HYDRODYNAMICS

In the previous section we have seen how the equations of hydrodynamics can be used to calculate the time correlation functions of conserved variables in the long wavelength and low frequency limit. The behavior of the correlation functions at short times is related to frequency sum rules that involve static distribution functions descriptive of the molecular structure of the fluid. It is precisely these sum rules that are violated by hydrodynamic expressions such as 83 and 87, because the resulting frequency moments beyond zeroth order all diverge. Similarly, an exponential decay, is incompatible with some general properties of time correlation functions previously discussed.

The failure of the hydrodynamic approach at short times (or high frequencies) does not occur abruptly, but instead proceeds progressively. It is linked to the presence of dissipative terms in the basic hydrodynamic equations; the latter, unlike the microscopic equations of motion, are not invariant under time reversal. For this reason, it was decided not to discard it directly but to maintain its basic ideas and generalize it by allowing the

transport coefficients and thermodynamic quantities to enter the equation as functions of time and space. The theories using the extension are considered inside what is called *generalized hydrodynamics*. In this section, we will describe some phenomenological generalizations of the hydrodynamic equations, based on the introduction of frequency and wavenumber-dependent transport coefficient, which have been used in attempts to bridge the gap between the hydrodynamic (small k, ω) and kinetic (large k, ω) regimes.

The ideas of generalized hydrodynamics can perhaps most easily be illustrated by considering the example of the transverse current correlations. In the hydrodynamic limit the correlation function decays exponentially with a relaxation time. However, molecular dynamics calculations [60, 61], which are the only source of "experimental" information on transverse current fluctuations in atomic liquids, show that within some intermediate wavenumber range the function $C_T(q, t)$ is not exponential and not even monotonically decaying; on the contrary, it displays an oscillatory behavior. The corresponding spectrum has a peak at non-zero frequency, suggestive of collective shear wave propagation. What this means physically is that at high frequencies the fluid has insufficient time to flow in response to an applied strain rate, but instead reacts elastically in the way that a solid would. The appearance of shear waves can be accounted for by the incorporation of viscoelastic effects into the hydrodynamic description of the transverse currents.

This generalization is based on making the response of the system sensitive in the temporal and spatial scales to the perturbations. This dependence is introduced through phenomenological ansatzs like the one described above, subject to limit conditions in (q, ω) and known sum rules but it lacks the theoretical fundaments to explain this new physics.

One of the most successful formalisms used is that of the projection operators introduced by R. Zwanzig and H. Mori [62], which from the basic mechano-statistical principles and with the spirit of Langevin equation which describes the Brownian movement, poses an equation of motion for the dynamic variables and, therefore, for the correlation functions,

$$\dot{A}(t) = -\int_0^t d\tau K(\tau) A(t - \tau) + F(t) \tag{88}$$

where the dot stands for the time derivative, $F(q)$ is the random force which originated the fluctuations and $K(t)$ is the memory function of the system, which describes the response of the system to these fluctuations.

A fundamental role in the development of this formalism is played by a projection operator which separates, for a second dynamic variable $B(t)$, the degrees of freedom parallel and perpendicular to $A(t)$[2]; the component orthogonal to $A(t)$ is associated with the variables of the system over which there is no control, and from which appears through different mechanisms, the random force $F(t)$ and the memory function $K(t)$. For the correlation function, the dynamic equation will be,

$$\dot{C}(t) = -\int_0^t d\tau K(\tau) C(t - \tau) \tag{89}$$

and its solution in Laplace space is,

$$\tilde{C}(z) = \frac{C(0)}{z + \tilde{K}(z)} \tag{90}$$

However, it does not solve the problem nor simplifies it since now the focus is on the memory function. Studying the mathematical structure of the problem, Mori proved [62] that the memory function $K(t)$ obeys also a Langevin equation with a self memory function, called $K_1(t)$, in such way that,

$$\dot{K}(t) = -\int_0^t d\tau K_1(\tau) K(t - \tau) \implies \tilde{K}(z) = \frac{K(0)}{z + \tilde{K}_1(z)} \tag{91}$$

---

2 Under this formalism, the dynamic variables of the system are considered vectors in a Hilbert space, under which a scalar product is defined, the thermodynamic average of the correlation function: $(A, B) \equiv \langle A * B \rangle$

$K_1(t)$ is the second order memory function of $C(t)$. This process can be iterated *ad infinitum*, generating memory functions of higher order, $K_2(t)$, $K_3(t)$,... The correlation function can be expressed as a continuous fraction,

$$\tilde{C}(z) = \cfrac{C(0)}{z + \cfrac{K(0)}{z + \cfrac{K_1(0)}{z + \cdots}}} \tag{92}$$

The values $K_i(0)$ can be obtained as combinations of the moments of the corresponding correlation function, which in the case of the density may be obtained to fourth order from basic information such as the temperature or the static structure. This representation can be employed to study the theoretical models used for the memory function of the intermediate scattering function proposed in the following section and used throughout this thesis.

3.2.1   *Models for the Intermediate Scattering Function*

A unified description of the various models applied to the interpretation of spectra of the density autocorrelation function in a classical fluid can be obtained in the framework of the memory function approach. Here we will only report a few basic formulas that are relevant for the understanding of the models. A fundamental result of the memory function theory is that the time evolution of the intermediate scattering function, $F(q, t)$, is described with the help of a memory function $N(q, t)$, leading to the integro-differential equation,

$$\ddot{F}(q,t) + \int_0^t dt' N(q, t - t') \dot{F}(q, t') + \langle \omega_Q^2 \rangle F(q, t) = 0 \tag{93}$$

where $\langle \omega_Q^2 \rangle$ is the second frequency moment of the normalized dynamic structure factor $S(q, \omega)/S(q)$ and takes the form,

$$\langle \omega_Q^2 \rangle = \frac{k_B T q^2}{m S(q)} \tag{94}$$

where k_B is the Boltzmann constant, T is the temperature and m is the mass of the particles. Going back to Eq. 93, $N(q, t)$ is the second-order memory function in a hierarchy of equations describing the time dependence of the density autocorrelation. Equation 93 can be derived by using an equation for $\dot{F}(q, t)$ in terms of a first-order memory function $M(q, t)$ [23, 63]

$$\dot{F}(q,t) + \int_0^t dt' M(q, t - t') F(q, t') = 0 \tag{95}$$

Equation 93 is solved via Laplace transformation with the initial conditions given by the relationship between the static structure factor, $S(q)$ and $F(q, t)$,

$$S(q) = \int_{-\infty}^{\infty} d\omega S(q, \omega) = F(q, 0) \tag{96}$$

and by $\dot{F}(q, 0) = 0$, yielding,

$$\frac{\tilde{F}(q, z)}{S(q)} = \left(z + \frac{\langle \omega_Q^2 \rangle}{z + \tilde{N}(q, t)} \right)^{-1} \tag{97}$$

where $\tilde{F}(q, z)$ and $\tilde{N}(q, z)$ are the Laplace transforms of $F(q, t)$ and $N(q, t)$.

In the framework of the memory function theory, attempts at grasping the main features of the microscopic dynamics of fluids are made by exploiting the known properties of the memory function and by modeling, through

reasonable guesses, the unknown time dependence of $N(q, t)$. All the models we will present here express $N(q, t)$ as a sum of terms with two basic types of time dependence: either a δ-function, which amounts to assuming no memory effects at all, or an exponential decay.

Generalized Hydrodynamic Model

The generalized hydrodynamic model is a generalization of the Rayleigh-Brillouin (RB) triplet, known to be an exact theoretical expression, although only valid asymptotically in the limit case $q \to 0$. Therefore, we will first introduce the RB triplet equations to, afterwards, generalize them. The hydrodynamic theory [23, 24, 64, 65] that leads to the expression of the RB spectrum is not formulated in terms of a memory function. However, to follow the same procedure in all cases, we can derive the RB line shape from an appropriate expression for $N(q, t)$ with the following form,

$$N(q, t) = 2\nu q^2 \delta(t) + (\gamma_0 - 1)\langle \omega_0^2 \rangle exp(-\gamma_0 D_T q^2 t) \tag{98}$$

where $\nu = [(4/3)\eta_s + \eta_b]/m\rho$ is the longitudinal kinematic viscosity, defined through the shear (η_s) and bulk (η_b) viscosities, γ_0 is the ratio of the constant pressure (c_p) to the constant volume (c_v) specific heat and $D_T = \zeta/\rho c_p$ is the thermal diffusivity with ζ the thermal conductivity. Inserting the Laplace transform of Eq. 98 into Eq. 97 gives,

$$\tilde{F}(q, z)/S(q) = \left(z + \frac{\langle \omega_0^2 \rangle}{z + \nu q^2 + \frac{(\gamma_0 - 1)\langle \omega_0^2 \rangle}{z + \gamma_0 D_T q^2}} \right)^{-1} \tag{99}$$

A detailed process of the solution of this equation can be found in [66]. Here we will only indicate the final result for the dynamic structure factor, which consists in a central (Rayleigh) Lorentzian line identified with a heat mode and two side (Brillouin) peaks identified with sound modes and frequencies ω_s and $-\omega_s$. The final expression for the intermediate scattering function is of the form,

$$F(q, t)/F(q, 0) = I_h e^{-z_h t} + I_s e^{-z_s t} \frac{\cos(\omega_s t - \varphi)}{\cos \varphi} \tag{100}$$

with $I_h, z_h, I_s, z_s, \omega_s$ and φ all dependent of the thermodynamic properties introduced in the expression of $N(q, t)$.

Based on the fact that the RB triplet is the exact behavior predicted by the linearized-hydrodynamics theory in the $q \to 0$ limit, it is a straightforward generalization to take it as a possible model in situations where its application with exact hydrodynamic coefficients cannot account properly for the spectral shape. The RB triplet then becomes a fit function referred to as the "generalized hydrodynamic model"[3]. In this case, the memory function is written as,

$$N(q, t) = B(q)\delta(t) + (\gamma(q) - 1)\langle \omega_Q^2 \rangle exp[-\Gamma_T(q)t] \tag{101}$$

with the four parameters being unknown functions of q to be determined, which at small q can be represented by series expansions with dominant, lowest-order, terms fixed by the exact RB theory. Therefore, for $q \to 0$ we have $\gamma(q) \sim \gamma_0$, $B(q) \sim 2\nu q^2$, $\Gamma_T(q) \sim \gamma_0 D_T q^2$, and $\langle \omega_Q^2 \rangle \sim \langle \omega_0^2 \rangle$.

The form of the intermediate scattering function is the same as Eq. 100. In this case, the different thermodynamic properties appearing in Eq. 101 can be expressed in terms of the different parameters appearing in Eq. 100 in the following way,

$$\Gamma_T(q) = z_h \left(1 - I_h \frac{(z_h - z_s)^2 + \omega_s^2}{z_s^2 + \omega_s^2} \right)^{-1}, \tag{102}$$

---

3 The term *generalized hydrodynamics* has often been used in the literature to refer to the insertion in the hydrodynamic equations of $q-$ and $\omega-$dependent thermodynamic and transport coefficients.

$$B(q) = 2(z_h + 2z_s - \Gamma_T(q)), \tag{103}$$

$$\langle \omega_Q^2 \rangle = \frac{z_h(z_s^2 + \omega_s^2)}{\Gamma_T(q)}, \tag{104}$$

$$\gamma(q) = \frac{2z_h z_s + z_s^2 + \omega_s^2 - (B(q)/2)\Gamma_T(q)}{\langle \omega_Q^2 \rangle} \tag{105}$$

Damped Harmonic Oscillator Model

In the context of the collective dynamics of liquids, the damped harmonic oscillator (DHO) model can be viewed as a simplified version of the hydrodynamic theory, corresponding to the special case of an RB triplet with $\gamma(q) = 1$. If the other parameters are given the same q dependence, the resulting spectrum is therefore only suitable for describing the very low q dynamics of a system with $\gamma(q) = 1$, a rather special case indeed. The DHO model is, in fact, typically used at larger q values, as a fit function with q-dependent free parameters. The corresponding memory function takes the form,

$$N(q, t) = 4\Gamma(q)\delta(t) \tag{106}$$

resulting in,

$$\frac{F(q, t)}{F(q, 0)} = e^{-z_s t} \frac{\cos(\omega_s t - \varphi)}{\cos \varphi} \tag{107}$$

with $\tan \varphi = z_s/\omega_s$. The dynamic structure factor only presents side peaks. The lack of a central peak makes it too rough a model in most cases. Thus, it is usual practice to let the DHO doublet play the role of describing the inelastic peaks due to the viscous relaxation, and to supplement the model with an extra central line, most often of Lorentzian shape, though this clearly violates the respect of sum rules.

Viscoelastic Model

The so-called viscoelastic model is a widely used representation of the dynamics of collective modes. The physical reasons behind the introduction of this model are clearly exposed in [23]. We only mention one distinctive property of the model, that marks its difference from those exposed in the previous sections, namely the fact that the memory function now has the correct, finite, zero-time value $N(q, 0) = \omega_L^2(q) - \langle \omega_Q^2 \rangle$, which implies the existence of a finite fourth moment of the dynamic structure factor. This result is simply the consequence of having removed the δ-function term by replacing it with an exponentially decaying term, so that

$$N(q, t) = \Delta_L^2(q)exp[-t/\tau(q)] + [\gamma(q) - 1]\langle \omega_Q^2 \rangle exp[-\Gamma_T(q)t] \tag{108}$$

where $\Delta_L^2(q) = \omega_L^2(q) - \gamma(q)\langle \omega_Q^2 \rangle$, $\tau(q)$ denotes the new time constant and $\omega_L^2(q)$ is defined as $\langle \omega_Q^4 \rangle = \omega_L^2(q)\langle \omega_Q^2 \rangle$ with $\langle \omega_Q^4 \rangle$ the fourth frequency moment of the normalized dynamic structure factor. All the parameters entering Eq. 108 are to be fitted to the data, and are unknown functions of q except for the $q \to 0$ behavior, which, as for the generalized hydrodynamic model, is known to be $\gamma(q) \sim \gamma_0$, $\Gamma_T(q) \sim \gamma_0 D_T q^2$, and $\langle \omega_Q^2 \rangle \sim \langle \omega_0^2 \rangle$, and moreover, $\omega_L^2(q) \sim c_L^2 q^2$.

As for the low-q behavior of $\tau(q)$, an important feature of the viscoelastic model is that $1/\tau(q)$ does not vanish for $q \to 0$ [23], but tends to a limit value $1/\tau_0$. Inserting the Laplace transform of 108 into 97 gives,

$$\frac{\tilde{F}(q, z)}{S(q)} = \left(z + \frac{\langle \omega_Q^2 \rangle}{z + \frac{\Delta_L^2(q)}{z + 1/\tau(q)} + \frac{[\gamma(q) - 1]\langle \omega_Q^2 \rangle}{z + \Gamma_T(q)}} \right)^{-1} \tag{109}$$

Solving the equation gives an expression for $F(q,t)$ of the following form,

$$\frac{F(q,t)}{F(q,0)} = I_h e^{-z_h t} + I_2 e^{-z_2 t} + I_s e^{-z_s t}\frac{\cos(\omega_s t - \phi)}{\cos\phi} \qquad (110)$$

where φ (Eq. 107) and ϕ have a different dependence of the other model parameters. More details can be found in Ref. [66].

The frequency spectrum of 110 presents a four-line structure, which, compared to the generalized hydrodynamic model, has an additional central Lorentzian.

Before proceeding to the next section, it is important to note one aspect regarding the names used in the literature for the different models previously described. The names here introduced correspond to the ones used in Ref. [66]. However, in a previous paper of Copley and Lovesey [67], the term "'viscoelastic model" is used to describe a memory function with a single exponential. Moreover, the name *generalized hydrodynamic* was meant to join the long wavelength region (hydrodynamic) to the larger q region, where they were using the viscoelastic model, in a smooth way by using two exponential functions in $N(q,t)$. In addition, the two exponential model of $N(q,t)$ can be named in two different ways, depending on the relative values of the decay rate of both exponentials. This question was first studied by Scopigno *et al.* in Ref. [68] in their study of the dynamic structure of liquid Li. Their conclusion was that for non conducting liquids thermal relaxation (brought about by the exchange of energy between atoms) is slow and viscoelastic relaxation is faster. However, for liquid metals the thermal conductivity is very high due to the electronic contribution, and therefore thermal relaxation is the faster process, contrary to the case of insulating liquids. The existence of two possibilities, i.e. thermal=slow or thermal=fast, is what led to naming the same model in two different ways. We call the first possibility *generalized hydrodynamics* (because thermal is the slow term as in hydrodynamics), and the second possibility *generalized viscoelastic* (because thermal is not the slow channel, contrary to hydrodynamics).

In the work performed in Chapter 6, our intention in the analysis is to determine which of the two possibilities describe better the situation by studying the behaviour of the amplitudes of the exponentials.

3.3 MODE COUPLING THEORY

When studying the behavior of the correlation function or the memory functions of a given dynamic variable, it is often found that they show several rates of decay. Only the slowest of them survives for long times, and the main idea behind mode-coupling (MC) theories is that this long-lasting term comes from the coupling of the variable studied with other slowly decaying ones (modes).

The development of MC theories started in the 70's and they have been derived to study the correlation function of several functions, such as the particle velocity (velocity autocorrelation function) [69], the single particle density (self intermediate scattering function) [70], the particle density (intermediate scattering function) [71], and the transverse current (transverse current correlation function) [69]. The slowly decaying modes appearing in the different theories include the single particle density, the density, the time derivative of the density, the longitudinal current and the transverse current.

A very successful application of MC ideas has been the study of structural arrest in undercooled liquids, which signals a variant of glass formation (see, for a review, Ref.[72]). Basically one looks for the possibility that $F(q_p, t)$ develops a solution that does not decay to zero for long times. MC theories have also been applied to dense gases, high temperature liquids or hard-sphere models, where, for instance, they explain the appearance of an algebraic decay in the velocity autocorrelation function.

Their application to liquids near their melting temperature is however somewhat more scarce (for a recent review see Ref.[73]). In order to study this type of systems, the original MC theories were modified during the 80's in order to consider not only the long-time behavior but also the short-time one [26, 74–76]. This part is mostly caused by binary atomic collisions, but it can also include couplings with fast decaying modes.

Basically a heuristic treatment of this part is performed, rewriting the MC part in a way that it vanishes rapidly (as t^4) for short times, and modeling the fast part by a Gaussian-like function that incorporates the full value and initial decay of the memory function being considered. Such modifications were spurred by the observations of Levesque and Verlet about the memory function of $Z(t)$ obtained by MD simulations for LJ systems [77]. These modified theories have been applied at different levels of approximation and self-consistency by several groups to study the dynamic properties of LJ systems, liquid alkalies, liquid Pb and liquid Sn and liquid germanium (Ge) [74, 76, 78–84].

We have applied the MC formalism to study the longitudinal dynamics, where the fast/slow decomposition is performed at the level of $N(q, t)$, and the transverse dynamics, where the decomposition is performed at the level of the first memory function of the transverse current correlation function, $M_T(q, t)$, namely,

$$N(q, t) = N^f(q, t) + N^{MC}(q, t), \tag{111}$$

$$M_T(q, t) = M_T^f(q, t) + M_T^{MC}(q, t). \tag{112}$$

where 'f' indicates the fast component and 'MC' the mode coupling component.

In the mode-coupling components we include only the particle density as a slow mode, so that these terms appear as integrals over wavevectors of functions that involve the intermediate scattering functions. The full expressions for the fast and MC components are given in Appendix A, and more details can be found in Ref. [23].

3.3.1 *Velocity autocorrelation function*

There are several theories that try to quantify the influence of slowly decaying collective variables on the behavior of $Z(t)$. For instance, Wahnström and Sjögren [76] put forward a MC-theory in the same spirit at that mentioned above for collective currents, namely, the memory function of $Z(t)$ is split into a fast term and a MC term given in terms of an integral over wavevectors. A different approach was followed by Gaskell and Miller [85] who considered a "velocity field" of the fluid, and analyzed how this is influenced by longitudinal and transverse currents using mode-coupling ideas. This led to an integral formula for $Z(t)$ (not its memory function), that incorporates longitudinal and transverse current correlation functions:

$$Z_{GM}(t) = \frac{1}{24\pi^3} \int d\vec{q} \, f(q) F_s(q, t) \left[C_L(q, t) + 2C_T(q, t) \right]. \tag{113}$$

Here $f(q)$ is the FT of a normalized function that describes the localization of a typical particle, usually taken as the Wigner-Seitz sphere. In this case the expression is $f(q) = (3/\rho) j_1(aq)/(aq)$, where $(4/3)\pi a^3 = 1/\rho$, and $j_1(x)$ is the spherical Bessel function of the first order.

Separating the sum in the integral into its two parts, each defines naturally the longitudinal, $Z_{GM}^L(t)$, and transverse, $Z_{GM}^T(t)$, contributions to the VACF, coming from the couplings of the single particle velocity with each of the polarizations of the collective current.

4

COMPUTATIONAL METHOD

The study of the structural and dynamical properties of disordered systems such as liquids is substantially helped by the results of MD simulations in which the arrangement and velocities of the atoms/ions, consistent with a given thermodynamical state and an assumed interatomic force law, are followed in time. Unlike crystalline systems in which periodicity and the harmonic approximation constitute a good basis for studying the motion of the atoms/ions, liquids are disordered at the atomic level and the motion of the atoms/ions is complex. Inevitably, measured quantities for these systems involve an average over configurations and these can be obtained by resorting to MD simulations, which provide information about the microscopic atomic arrangement and the way it evolves in time.

Except for the lightest atoms, the motion of the ions in MD is governed by Newtonian mechanics [10]. A sample set of ions representing a liquid are placed in a cell and periodic boundary conditions are applied. The system is allowed to evolve in time at chosen thermodynamic conditions under the action of the forces acting on the ions. After sufficient time has elapsed for equilibrium to be established the positions and velocities of the ions are recorded at each time and used to compute average quantities of interest. Individual atomic configurations can be studied to trace the origin of particular features. The representation of the liquid by the simulation is limited by the number of atoms in the sample, which should be as large as possible to reduce the effects of the periodic boundary conditions, and by the time over which configurations are available for the calculation of dynamical quantities, which should be as long as possible. The size of the sample cell and the simulation time place lower limits respectively on the wave vectors and frequencies of phenomena relevant to the liquid.

Early MD simulations were entirely classical using model potentials such as hard sphere or LJ potentials. These CMD studies gave useful insights into generic liquid and cluster behavior. However, a simulation with the objective of investigating a particular system, requires forces appropriate to the system. The valence electrons play a crucial role in the behavior of metallic systems, forming a glue that holds together the ions against the Coulomb repulsion of the ionic charges. The embedded atom model (EAM) of Daw and Baskes [58] incorporates the electron density in the interaction energy following the work of Stott and Zaremba [59] and has been used successfully for metallic systems. However, the interaction is empirical and results can depend substantially on the way the parameters are chosen. In principle, the solution to Schrödinger equation for the electrons provides the energy of the system and from this the forces on the ions, but there are many electrons to be considered and these are coupled one to another by their Coulomb repulsion as well as to the ions. The complexity posed by the electron-electron interactions can be handled by the Density Functional Theory (DFT), which introduces the electron density distribution as a fundamental variable for the system, and shows how to replace the interacting many-body system of electrons by an auxiliary system of non-interacting particles moving in an external field, a much simpler system amenable to solution. DFT is the basis of present-day simulations.

4.1 DENSITY FUNCTIONAL THEORY

Two papers published over 50 years ago by Hohenberg, Kohn, and Sham (HKS) [1, 2] laid the foundation for modern density-functional theory. The two Hohenberg Kohn (HK) theorems [1] first legitimized the ground-state (GS) electron density $n_0(\vec{r})$ as the basic variable of the GS quantum chemistry and the Kohn-Sham (KS) method [2] then offered a specific numerical implementation for this theory.

The first HK theorem [1] guarantees that, for an N-electron quantum system, its total GS electronic energy is a functional of $n_0(\vec{r})$,

$$E[\Psi_0] \equiv E[n_0] \tag{114}$$

where Ψ_0 is the GS electronic wave function. The second HK theorem[1] ensures that the GS energy complies with the variational principle,

$$E[n_0] \leqslant E[n'] \tag{115}$$

where n' is any electronic density different from the GS electronic density.

DFT shows that the electronic energy can be written as a functional of the electron density, $n(\vec{r})$, as follows,

$$E[n(\vec{r})] = T_s[n] + E_{ext}[n] + E_H[n] + E_{xc}[n] \tag{116}$$

where $T_s[n]$ is the kinetic energy of a non-interacting system of density $n(\vec{r})$, $E_{ext}[n]$ is due to the interaction of the electrons with the ions, $E_H[n]$ is the classical electrostatic Hartree energy given by[1],

$$E_H[n] = \frac{1}{2} \int \int d\vec{r} d\vec{s} \frac{n(\vec{r})n(\vec{s})}{|\vec{r} - \vec{s}|} \tag{117}$$

and $E_{xc}[n]$ is the exchange-correlation energy, for which well tested approximations are available.

The exchange-correlation energy has been the subject of a great deal of research [87] because the only obstacles to an exact treatment of the electronic energy using the KS-AIMD method described in the next section lie in this term. Approximate forms of $E_{xc}[n]$ are of two types. The first are the local density approximations (LDA) in which the electron gas is treated locally at $\vec{r}$ as though it were a uniform electron gas of mean density $n(\vec{r})$, and uses the results of many-body calculations of the uniform electron gas. Two popular LDA approximations [88, 89] are parametrizations of the results of Monte Carlo treatments of the interacting electron gas of Ceperley [90] and Ceperley and Alder [91]. More sophisticated approximations involve density gradients as well as the density at $\vec{r}$ and are known as generalized gradient approximations (GGA); one in common use is due to Perdew *et al.* [92]. However, the simple LDA has usually been sufficient in orvital-free (OF) calculations because the errors associated with the approximate kinetic energy functional are expected to be much greater than those associated with $E_{xc}[n]$.

4.1.1 *Kohn-Sham approach*

The most common application of DFT in simulations uses the approach of Kohn and Sham (KS) [2] who introduced the electron kinetic energy functional, $T_s[n]$, for an auxiliary system of independent particles with the same density $n(\vec{r})$ as the physical electron system of interest. This step isolates all effects of the electron-electron interaction in a single term, the exchange-correlation energy functional, $E_{xc}[n]$, for which approximations have been developed. KS then showed how to evaluate $T_s[n]$ exactly in terms of the single particle orbitals, $\phi_i(\vec{r})$ for the auxiliary system which are self-consistent solutions of the Schrödinger equation with an effective external potential, v_{eff}, for which a prescription is given. The orbitals satisfy the single particle equations,

$$\left(-\frac{1}{2}\nabla^2 + v_{eff}[n, \vec{r}] \right) \phi_i = \epsilon_i \phi_i \quad , \quad i = 1, 2, \dots \tag{118}$$

which must be solved self-consistently because the effective potential v_{eff} depends explicitly on the density, which is obtained from the occupied orbitals,

$$n(\vec{r}) = \sum_{occ} |\phi_i(\vec{r})|^2 \tag{119}$$

---

1 Atomic units are used throughout, unless stated otherwise, with $\hbar = e = m_e = 1$

The ground state kinetic energy, T_s, can be obtained exactly in terms of these orbitals,

$$T_s = \int d\vec{r} \sum_{occ} \phi_i(\vec{r}) * (-\frac{1}{2}\nabla^2 \phi_i(\vec{r})) \tag{120}$$

which leaves $E_{xc}[n]$ as the only small source of error in equation 116 for the electronic energy of the ground state. In addition, highly accurate and transferable nonlocal pseudopotentials may be used for describing the electron-ion interaction.

In practice the KS equations are not solved directly, a time consuming process, instead the ground state electronic energy is found by minimizing iteratively the energy functional with respect to the orbitals while ensuring that the orbitals are mutually orthogonal [93]. Orthogonalization is itself time consuming requiring order N^3 operations. Storing the order N orbitals and manipulating them place computational limits on the number of atoms that can be simulated and the length of the MD run. The most that can be done at present are about a few hundreds of atoms, which is a small sample to investigate dynamical effects in disordered systems, like liquid metals.

4.1.2 *Orbital Free approach*

The OF approach [94–96] follows the KS development of DFT but retains the electron density as the fundamental variable. Because the KS orbitals are no longer needed, memory requirements scale linearly with system size as opposed to quadratically for the KS approach. There are also enormous savings in computational time because there is only the electronic density distribution to manipulate rather than the whole set of orbitals, provided the $T_s[n]$ is simple to evaluate. Costly orthogonalization of the orbitals and Brillouin zone sampling are no longer required. The savings in computational time and memory of the OF scheme allow for the simulation of much larger systems for longer simulation times than would otherwise be possible. However, an explicit form for $T_s[n]$ is required, and since only approximate forms for $T_s[n]$ are known, errors are made in the kinetic energy which can be serious because the kinetic energy is of the same order of magnitude as the total energy.

If an explicit density functional is adopted for $T_s[n]$, the ground state electronic energy can be obtained by minimizing $E[n]$ in equation 116 with respect to the density subject to the constraint $\int d\vec{r}n(\vec{r}) = N_e$ which maintains the number of electrons as N_e. The choice of $T_s[n]$ will be discussed later. Minimization could proceed by expanding $n(\vec{r})$ in a set of plane waves having the periodicity of the superlattice, as follows,

$$n(\vec{r}) = \sum_{\vec{G}} n_{\vec{G}} e^{-i\vec{G}\cdot\vec{r}} \tag{121}$$

$$\vec{G} = \frac{2\pi}{L}(n_1, n_2, n_3) \tag{122}$$

where L is the side of the supercell assumed for simplicity to be a cube, and minimizing $E[n]$ with respect to the $n_{\vec{G}}$. The number of electrons can easily be held constant by keeping $n_{\vec{G}=0} = N_e/V$. However, it is necessary physically to maintain $n(\vec{r}) \geqslant 0$[2] and this constraint might impose a close monitoring of the calculations.

Instead of using $n(\vec{r})$ as the system variable, we have had success using a single effective orbital $\psi(\vec{r})$ where $n(\vec{r}) = |\psi(\vec{r})|^2$. If $\psi(\vec{r})$ is initially real it remains real throughout the iterations and $n(\vec{r})$ is guaranteed to be non-negative. Representing $\psi(\vec{r})$ in the plane waves,

$$\psi(\vec{r}) = \sum_{\vec{G}} c_{\vec{G}} e^{-i\vec{G}\cdot\vec{r}} \tag{123}$$

---

2 If this is breached, the iterative minimization becomes unstable.

minimization can be performed with respect to the Fourier coefficients, $c_{\vec{G}}$. The plane wave expansion is truncated at a maximum wave vector G_c corresponding to an energy cutoff $E_c = G_c^2/2$. Plane waves are a good basis set for the systems we have treated; they span the whole space, they are independent of the ion positions, and the completeness is controlled by the single parameter E_c which can be varied to test convergence. In contrast, constraining the number of electrons during minimization is harder to accomplish with $\psi(\vec{r})$ than when working directly with $n(\vec{r})$.

4.1.3 Kinetic Energy Density Functionals

The use of an explicit electron kinetic energy functional, $T_s[n]$, is the main feature distinguishing the OF from the full KS scheme. The theorems of Hohenberg and Kohn show that such a functional exists but little is known about the form of the functional, and compared to the electronic exchange-correlation energy functional, $E_{xc}[n]$, not much work on $T_s[n]$ has been done; nevertheless the prospect of an accurate OF-AIMD scheme has stimulated interest and several approximate functionals have been proposed. Approximate forms have been based on the known forms of $T_s[n]$ in a few limiting cases.

The Thomas-Fermi Model

In the limit of a uniform noninteracting electron gas the kinetic energy is given by the Thomas-Fermi (TF) functional [97–101]

$$T_{TF} = a_0 \int d\vec{r} \quad n(\vec{r})^{5/3} \tag{124}$$

where $a_0 = 3(3\pi^2)^{2/3}/10$, and this functional is appropriate for systems in which the electron density, $n(\vec{r})$ is slowly varying. Indeed, the TF functional is also the leading term in an expansion of $T_s[n]$ in density gradients. The gradient expansion was first developed by Kirzhnits [102] who reported the second and fourth order corrections to the TF result. An error in the fourth order term was noted and corrected by Hodges [103] whose method is easy to follow. Subsequently, the sixth order term has been obtained by Murphy [104]. The calculation of these gradient corrections becomes increasingly complicated with the order and although corrections higher than the sixth can undoubtedly be calculated, the effort may not be worthwhile. The functional may be written,

$$T_s[n] = \int d\vec{r} \quad t_s(\vec{r}) \tag{125}$$

in terms of a kinetic energy density, and gradient corrections up to fourth order are,

$$t_s^{(0)} = a_0 n^{5/3} \tag{126}$$

$$t_s^{(2)} = \frac{|\nabla n|^2}{72n} \tag{127}$$

$$t_s^{(4)} = \frac{n^{1/3}}{540(3\pi^2)^{2/3}} \left[\left(\frac{\nabla^2 n}{n}\right)^2 - \frac{9}{8}\left(\frac{\nabla^2 n}{n}\right)\left(\frac{\nabla n}{n}\right)^2 + \frac{1}{3}\left(\frac{\nabla n}{n}\right)^4 \right] \tag{128}$$

A few points regarding the gradient expansion are worth noting. The fourth order correction, $t_s^{(4)}$, involves $|\nabla n|^2$ and $\nabla^2 n$ which are readily calculated, but not the fourth derivative. It is also positive everywhere. For an exponentially decaying density such as one would find in the outer region of an atom or molecule, or outside the surface of a solid or a liquid, $t_s^{(6)}$ and higher order terms diverge exponentially. These results are for a three dimensional system, but curiously, for two dimensions all density gradient corrections of the Kirzhnits type to the TF functional vanish [105, 106]. This is not to say that TF is exact in two dimensions but rather that there are technical problems with the expansion.

The von Weizsäcker Functional

The von Weizsäcker functional [107],

$$T_{vW} = \frac{1}{8} \int d\vec{r} \ \frac{|\nabla n|^2}{n} \tag{129}$$

is exact for a one electron system for which $\psi(\vec{r}) = \sqrt{n(\vec{r})}$ (or for two if the state is doubly occupied for spin) and is therefore correct in the outer regions of a localized system. It has the same form as the leading, second order, correction in the density gradient expansion although larger by a factor nine. In addition, T_{vW} is widely recognized to be correct in the limit of a rapidly varying density and this is supported by some results of linear response (LR) theory, which we now comment.

A weakly perturbed uniform electron gas provides another limiting case for the kinetic energy functional [108]. If the gas has a uniform density $\bar{n}$ and the LR of the system to the perturbing potential leads to a change in density $\delta\bar{n}(\vec{r})$, then perturbation theory to second order in the potential gives for the kinetic energy,

$$T_{LR} = V\bar{n}^{5/3} + \frac{1}{2} \sum_{\vec{q} \neq 0} \delta\tilde{n}_{\vec{q}} [\chi(q, \bar{n})]^{-1} \delta\tilde{n}_{-\vec{q}} \tag{130}$$

where,

$$\delta\tilde{n}_{\vec{q}} = \int d\vec{r} \ \delta n(\vec{r}) exp(i\vec{q} \cdot \vec{r}) \tag{131}$$

and $\chi(\vec{q})$ is the so-called Lindhard function given by,

$$\chi(\vec{q}) = -\frac{\bar{k}_F}{2\pi^2} \left(1 + \frac{1-x^2}{2x} ln \left| \frac{1+x}{1-x} \right| \right), \qquad x = q/2\bar{k}_F \tag{132}$$

where $\bar{k}_F$ is the Fermi wavevector corresponding to the electron density $\bar{n}$.

The second order gradient correction $\int d\vec{r} \ t_s^{(2)}(\vec{r})$ (Eq. 127), and T_{vW} (Eq. 129) have the same form but differ by a factor of nine. Jones and Young [109] analyzed the LR result for the kinetic energy and showed that the factor $1/72$ is correct when the dominant Fourier components of the perturbing potential are at small wave vectors $\vec{q}$, that is when the potential is slowly varying. However, when the dominant Fourier components are at large $\vec{q}$ and the potential is rapidly varying, the von Weizsäcker term with its factor of $1/8$ is correct.

4.1.4 *Approximate functionals*

Several approximate kinetic energy functionals have been proposed which give the TF, von Weizsäcker and the LR results in the appropriate limiting conditions. The first of these was due to Wang and Teter [110] who also investigated the possibility of including quadratic response. With Perrot's work as the basis [111], Madden and coworkers [112, 113] have developed functionals which also correctly recover the TF, von Weizsäcker and LR limits [112] and they included the quadratic response [113] too. OF-AIMD simulations of simple metal systems using such functional, have yielded promising results. Later, Carter and coworkers [114] investigated these functionals, and proposed a linear combination of functionals as a suitable form for T_s.

The evaluation of these functionals requires only order N operations and OF-AIMD simulations based on them are very efficient. Unfortunately, they have two undesirable features. They are not positive definite, so that minimization of the energy functional can lead to an unphysical negative kinetic energy. Secondly, the functionals that incorporate the weakly perturbed electron gas through the linear or higher order response functions must specify a reference uniform electron gas density, $\bar{n}$. In the case of systems such as bulk liquid simple metals in which there are small variations in the electron density, the mean electron density of the system is an appropriate

choice for $\bar{n}$. However, the choice of a uniform reference system is problematic when there are more substantial variations in the electron density such as may appear in some simple metals and alloys, for example when the components of an alloy have a large size and/or valence difference, and especially for the surface of a solid or a liquid where the electron density drops through the interface from the bulk value to zero in the vacuum.

Approximate functionals of the GGA form have been proposed which include some features of electron gas LR but avoid the need for a uniform reference density. The first of these due to DePristo and Kress [115, 116] incorporated the correct small $\vec{q}$ and large $\vec{q}$ forms of the LR function and fitted parameters in a Padé approximant to the total kinetic energy of all-electron Hartree-Fock rare gas atoms. Wang *et al.* [117] investigated GGA's more appropriate for smoother pseudodensities. Parameters were fit to give $\delta T_s / \delta n(\vec{r}) = -V(\vec{r}) + \mu$ for a model pseudoatom. The gradient expansion through fourth order was found to give good electronic kinetic energies and it was suggested that an interpolation between the gradient expansion including fourth order for slowly varying density and T_{vW} when densities are rapidly varying might be a useful kinetic energy functional. Perdew and Constantin [118] developed a functional that met these requirements and tested it for a variety of systems by evaluating it for an exact density and comparing the results with the corresponding kinetic energy. Their functional was reported to be a strong improvement over the gradient expansion.

However, to be useful in OF-AIMD simulations not only $T_s[n]$ but also $\delta T_s / \delta n(\vec{r})$ must be accurate so that the variational principle can be used to obtain the ground state density $n_0(\vec{r})$ and hence $T_s = T_s[n_0]$; the functional is untested in this regard. A functional of this type is attractive because it does not require a uniform reference density and might be more widely applicable than those which incorporate uniform electron gas response functions [110–113] and are limited to systems in which the variations in electron density around the mean value are small. However, it cannot give any Fermi surface effects that would be expected for metallic systems, such as Friedel oscillations. Even so, tests should be performed for impurities in a gas and for the jellium surface to determine if some truncated or damped oscillatory behavior in the density is present.

Chacón, Alvarellos and Tarazona [119] have developed a different type of kinetic energy functional, which employs an "average density" and recovers the TF, von Weizsäcker and LR limits. The functional has been investigated and generalized by García-González *et al.* [120–122]. These functionals have the merit of incorporating Fermi surface effects through the uniform gas response but do not require a fixed reference density, and they can be chosen to be positive definite, an essential requirement if they are to be used variationally. However, they are somewhat complicated to apply and more time consuming to evaluate because they require an additional level of computation in order to determine the averaged density. Consequently, they scale as N^2 which diminishes the advantage of the OF-AIMD approach over the full KS-AIMD method.

In most of the applications of the OF-AIMD method described in this thesis, the simplified version of González *et al.* [96, 123] of the averaged density approach of Chacón, Alvarellos and Tarazona [119] and García-González *et al.* [120–122] has been used, with the kinetic energy given by,

$$T_s = T_{vW}[n] + T_\beta[n] \tag{133}$$

$$T_\beta[n] = \frac{3}{10} \int d\vec{r} \quad n(\vec{r})^{5/3-2\beta} \quad \tilde{k}(\vec{r})^2 \tag{134}$$

$$\tilde{k}(\vec{r}) = (3\bar{k}_F)^3 \int d\vec{s} \quad k(\vec{s}) \quad w_\beta(2\bar{k}_F|\vec{r}-\vec{s}|) \tag{135}$$

$$k(\vec{r}) = (3\pi^2)^{1/3} n(\vec{r})^\beta \tag{136}$$

where $\bar{k}_F$ is the Fermi wavevector corresponding to a reference mean electron density $\bar{n}$, and $w_\beta(x)$ is a rigid weighting function, determined by requiring the correct recovery of the LR limit at the reference mean density and the TF limit. The advantage of the simplification is that $\tilde{k}(\vec{r})$ appears as a convolution which for a plane

wave basis can be performed rapidly by the usual fast Fourier transform techniques. This renders the functional order N in scaling. The functional is a generalization of one with $\beta = 1/3$, used earlier in a study of expanded liquid Cs [124].

The details of the functional are given in González *et al.* [96, 123] and are reproduced in Appendix B. Its main characteristics are as follows: (i) β is a real positive number whose maximum value still leading to a mathematically well behaved weight function is ≈ 0.6, (ii) the functional recovers the uniform and LR limits, and is positive definite (iii) when $\bar{k}_F \to 0$ because the mean electron density vanishes, i.e. for a finite system, the von Weizsäcker term is recovered if $\beta = 4/9$, whereas for other values of β, the limit is $T_{vW} + CT_{TF}$, (iv) for values of $\beta > 0.5$ it is expected that $\mu(\vec{r})\psi(\vec{r})$, which is the driving force for the dynamic minimization of the energy, remains finite even for very small electron densities $n(\vec{r})$. For systems in which there will be regions where the density will decay exponentially such as clusters or a liquid/vapor interface the von Weizsäcker term should appear as limit of the functional and a value of β as close as possible to $4/9$ is called for. Unless otherwise stated, the simulations described in this thesis used $\beta = 0.51$, which in the limit $\bar{n} \to 0$ gives $C = 0.046$ and guarantees, at least for the systems considered, that $\mu(\vec{r})\psi(\vec{r})$ remains finite and not too large everywhere so that the energy minimization can be achieved.

4.2 PSEUDOPOTENTIALS

Ab-initio simulations using the KS-AIMD approach invariably employ nonlocal pseudopotentials obtained by fitting to properties of the free atom [125, 126]. The non-locality is a consequence of the pseudopotential acting on the pseudoatom stripped of the valence electrons -the pseudoion- having different potentials acting on different angular momentum components of the valence electron orbitals.

$$V_{ion} = v_{local}(\vec{r}) + \sum_{l,m}^{l_{max}} |l,m > \delta v_l(r) < l,m| \tag{137}$$

where l_{max} is usually one or two. The nonlocal part of the potential is time consuming to evaluate with a plane wave basis and in *ab initio* simulations a procedure due to Kleinman and Bylander [127] is invariably used which leads to a factorization of the matrix elements and considerable time saving.

The fitting procedure of the so-called "norm-conserving" pseudopotentials guarantees that the pseudoion scatters electrons in the same way as the true ion not only at the valence energy levels but also over an energy range about them. These pseudopotentials work well for many elements, but for some i.e. oxygen and the 3d transition elements, the ion core is small, and extensive and therefore costly plane wave basis sets are necessary. For these and other cases Vanderbilt's ultrasoft pseudopotential [128] is often used. Vanderbilt enlarged the ion core leading to a softer pseudopotential, but at the cost of sacrificing the norm conservation which required some adjustment to the charge density.

Since the OF scheme is free of orbitals the ion-electron interaction energy has the form,

$$E_{e-ion} = \int d\vec{r} \quad V(\vec{r}) \quad n(\vec{r}) \tag{138}$$

where $n(\vec{r})$ is the electron pseudodensity,

$$V(\vec{r}) = \sum_i v_i(\vec{r} - \vec{R}_i) \tag{139}$$

and $v_i(\vec{r})$ is the electron-ion interaction for ion i. This form apparently excludes the possibility of using nonlocal pseudopotentials like Eq. 137 in OF-AIMD simulations and a local pseudopotential must be selected. But, this question is worth of further study.

4.2.1 *Local pseudopotentials*

There are two types of local pseudopotentials. Most are empirical and often have some simple analytic form; a few are from first principles. Early OF calculations [94, 112, 113, 124, 130] used empirical local pseudopotentials. However, great care must be taken in using empirical potentials outside the set of data used in their fitting and the degree of confidence to be placed in the results is unknown. Ideally, a local pseudopotential would be used for the electron-ion interaction which is fitted to give the suitably pseudized free atom electron density and designed to be transferable from the atom in free space to the atom in other electronic environments of interest. Wang and Stott obtained first principles local pseudopotentials for group IV elements based on the free atoms [129]. The electron density of the free pseudoatom used to construct the nonlocal pseudopotential in, for instance, the Bachelet-Hamman-Schluter [125] or the Troullier-Martins [126] schemes can of course be constructed from the nonlocal potential, but DFT tells us that there is a unique local pseudopotential that yields the same density. The potentials constructed in this way may be regarded as the local equivalents of the nonlocal pseudopotentials. Wang and Stott found such local potentials for C, Si and Ge and used them in full KS calculations of dimers and crystalline solids. Fairly good results were obtained for bond lengths and lattice constants while the results for energies compared less well with the results obtained using the original nonlocal potentials.

In the absence of a transferable local pseudopotential based on the free atom, an alternative is to calculate the pseudopotential for a reference system in which the environment of the atom is similar to that of the physical systems of interest. Watson *et al.* [131] used a bulk crystal as a reference system. KS calculations were performed for a popular nonlocal pseudopotential and the Fourier components of the electron density were obtained. The Fourier components of the local KS effective potential which produced this density using the OF functional were found and "unscreened" to yield the local ion pseudopotential. Some interpolation was necessary in order to obtain the potential at all q-values, not just those at the reciprocal lattice vectors of the reference crystal. Application of these peudopotentials using the OF scheme gave good agreement for a variety of crystalline properties, with the results of full KS calculations performed with the original nonlocal pseudopotential for Na, Li and Al.

Neutral Pseudoatom Method

Many applications of the OF-AIMD method to liquid metal systems presented in this thesis use a first principles local pseudopotential similarly constructed from the electron density obtained from a full KS calculation treatment of a liquid-like reference system [96]. The reference system has the atom at the centre of a spherical cavity in the positive background of a uniform electron gas having a density equal to the mean valence electron density of the system of interest. The radius of the cavity is such that the positive charge removed to make the hole is equal to the valence charge of the atom, and a so-called neutral pseudoatom [132, 133] is formed. This reference system represents the situation of an atom in a liquid metal when its surroundings are smeared out to form a uniform gas. The first step in the construction is an all-electron KS density functional calculation to obtain the displaced valence electron density, $n_{disp}(r)$, i.e. the change in the electron density induced by the atom and the cavity. Next, $n_{disp}(r)$ is pseudized by removing the contribution from core electrons and eliminating the core-orthogonality oscillations to give $n_{ps}(r)$. Finally, an effective local ion pseudopotential is found using the OF density functional which, when inserted into the uniform electron gas along with the cavity, reproduces the $n_{ps}(r)$, that is the pseudized displaced electron density. The development proceeds as follows. The minimization of the energy functional gives the Euler-Lagrange equation for the pseudopotential in the jellium-vacancy system,

$$\mu_s(r) + V_{ext}(r) + V_H(r) + V_{xc}(r) - \mu = 0 \tag{140}$$

where each of the terms is the derivative of the corresponding term in Eq. 116, namely,

$$\mu_s(r) = \mu_{vW}(r) + \mu_\beta(r) \tag{141}$$

with the expressions for the von-Weizsäcker term and the β-term given in Appendix B,

$$V_{ext}(r) = v_{ps}(r) + v_{cav}(r) + v_{jell}(r) \tag{142}$$

$$V_H(r) = \int d\vec{s}\, n(s)/|\vec{r} - \vec{s}| \tag{143}$$

with $n(r) = \bar{n} + n_{ps}(r)$. Given $n(r)$, $v_{ps}(r)$ can be obtained from Eq. 140, and the constant μ is an energy origin set to give a pseudopotential that decays to zero at large distances.

4.3 MOLECULAR DYNAMICS

MD consists in solving the equations of motion for the particles that conform the system along a given time. To start a MD simulation, initial positions and velocities have to be assigned to all the particles in the system. The particle positions should be chosen compatibly with the structure that is going to be simulated.

The total energy of a system of N classical ions carrying charge Z at positions $\vec{R}_l$ in a volume V, and interacting with $N_e = NZ$ valence electrons, may be written within the Born-Oppenheimer approximation as,

$$E(\vec{R}_l) = T_{ion} + V_{ion-ion} + E_e(\vec{R}_l) \tag{144}$$

where the first two terms are the ion kinetic energy and the direct Coulomb interaction energy, and E_e is the ground state energy of the electrons in the presence of the ions. The ground state energy for N_e electrons can be obtained by treating the coefficients $c_{\vec{G}}$ in Eq. 123 as dynamical variables and conducting a simulated anneal as first introduced by Car and Parrinello [14]. A fictitious kinetic energy, $\sum |\dot{c}_{\vec{G}}|^2/2M_c$ is introduced and the equation of motion for the $c_{\vec{G}}$ is,

$$M_c \ddot{c}_{\vec{G}} = -2 \int d\vec{r}\, \mu(\vec{r}) \psi(\vec{r}) e^{i\vec{G}\cdot\vec{r}} + 2\bar{\mu} V c_{\vec{G}} \tag{145}$$

where $\mu(\vec{r}) = \delta E/\delta n(\vec{r})$ and $\bar{\mu}$ the chemical potential for which the system contains the required number of particles N_e. These equations are solved numerically using the Verlet leapfrog algorithm [7, 93] with an electronic timestep Δt_c. The velocities $\dot{c}_{\vec{G}}$ are reduced at every timestep or so and the system cools until static equilibrium[3] is reached to within preset tolerances. However, the chemical potential $\bar{\mu}$ is not known in advance but replacing $\bar{\mu}$ in equation 145 by its stationary value $\int d\vec{r}\mu(\vec{r})n(\vec{r})/\int d\vec{r}n(\vec{r})$ at each timestep, and renormalizing the density so that $\int d\vec{r}n(\vec{r}) = N_e$, gives good convergence to the ground state.

The forces on an ion are,

$$\vec{F}_i = \sum_j Z^2 \vec{R}_{ij}/R_{ij}^3 - \frac{\partial E_e}{\partial \vec{R}_i} \tag{146}$$

where $\vec{R}_{ij} = \vec{R}_i - \vec{R}_j$ and the Hellman-Feynman theorem [86] has been used. The simulation then proceeds by solving Newton's equations for the ions numerically using, for example, the Verlet algorithm and a suitable time step.

In almost all the atomic systems, the ion dynamics can be described satisfactorily through Newton's equations, and most MD algorithms work with this hypothesis in mind. To quantify the adequacy of this approximation, we compare the associated de Broglie thermal wavelength,

$$\Lambda = \sqrt{\frac{\beta\hbar^2}{2\pi m}} \tag{147}$$

---

3 The electronic ground state

with the typical interatomic wavelength $\sim 3\text{Å}$. This approximation is good in most case scenarios, failing only when dealing with the lightest atoms or liquids at very low temperature, where quantum effects are important.

Most MD algorithms use finite differences methods [24]: with the dynamic information of the system known at time t, all the quantities can be evaluated at time $t + \delta t$. The iteration of this process for a big enough number of timesteps generates the trajectories and provides all the necessary information to study the relevant properties of the system. The method for generating new coordinates is intrinsically inexact because it truncates the expansion of $\vec{r}(t)$ in powers of δt. Therefore, an adequate choice of δt, even though the detail depends on the algorithm used, must be significantly smaller than a characteristic time of the system and sufficiently small so that truncation errors have minor importance.

The first part of the simulation is carried out considering the system in the isokinetic ensemble (N, V, E_c) with the goal of thermalizing the system at the desired temperature. The rest of the simulation is performed in the microcanonical ensemble (NVE). The equations of motion to solve in each case are different. In the NVE ensemble one has only to treat with Newton's equations,

$$\frac{d\vec{r}}{dt} = \vec{v} \qquad \frac{d\vec{v}}{dt} = \frac{\vec{F}}{m} \tag{148}$$

Initially, the kinetic energy corresponding to the desired temperature is calculated and distributed among all the particles following a Maxwell-Boltzmann distribution. After each timestep, the kinetic energies obtained after solving Newton's equations are rescaled so as to obtain the desired kinetic energy. After a given number of time steps (usually a few thousand), the total energy ends up oscillating around a mean value. At this point, a configuration of the system is chosen (along with positions and velocities), which is the same as fixing the total energy, and a MD simulation in the microcanonical ensemble (NVE) can be started.

4.3.1   *Verlet, integration of the equations of motion.*

The Verlet algorithm, along with its evolutions and modifications, is one of the most used algorithms to integrate the equations of motion. The original idea comes from the addition of the two expansions,

$$\vec{r}(t + \delta t) = \vec{r}(t) + \vec{v}(t)\delta t + \vec{a}(t)\delta t^2/2$$
$$\vec{r}(t - \delta t) = \vec{r}(t) - \vec{v}(t)\delta t + \vec{a}(t)\delta t^2/2 \tag{149}$$

so that $\vec{r}(t + \delta t)$ can be obtained in terms of $\vec{r}(t)$, $\vec{r}(t - \delta t)$ and $\vec{a}(t)$. Moreover, to calculate the kinetic energy, the velocities of the particles must be known. By substracting eqns. 149, we obtain (to order $O(\delta^2)$),

$$\vec{v}(t) = \frac{\vec{r}(t + \delta t) - \vec{r}(t - \delta t)}{2\delta t} \tag{150}$$

The biggest weakness of the method comes from the velocities; apart from the low accuracy (δt^2) it happens that at time t, only the evolution of $\vec{v}(t - \delta t)$ is available; this means that, at storage and data treatment, the algorithm is non-optimal. The two most known improvements to the Verlet algorithm are the leap frog and the velocity versions, both guided towards this direction. In all the simulations performed in this thesis we have used the leap frog version of the Verlet algorithm.

5
ACCURATE LOCAL PSEUDOPOTENTIALS

In this chapter we describe the methods for the improvement in the construction of local pseudopotentials to be used within orbital free studies, and show some applications of the methods.

In the first section the idea of force-matching is introduced, and applied to the study of liquid alkaline-earth metals. In the second section a more general procedure is presented that allows the construction of optimized pseudopotentials of global applicability, including solids, liquids and interfaces. Some results are also shown for several systems.

5.1 FORCE-MATCHING FOR LOCAL PSEUDOPOTENTIALS: LIQUID ALKALINE EARTHS

Liquid alkali metals, because of their particular electronic structure, are considered as the model of simple metallic liquids. This key position among liquid metals has promoted a large number of studies from the experimental, theoretical and computational points of view.

On the other hand, their neighbours in the periodic table, alkaline-earth metals, have received much less attention in general and in the liquid phase in particular the information available in the literature is very scarce. However, the study of some solid state properties of these systems, especially their phase diagram as a function of pressure, has received recent impulse, being investigated both experimentally and theoretically and several interesting phenomena have been discovered.

The scarcity of experimental information about the liquid alkaline-earth metals has lead to an also very restricted dedication to their study from a theoretical point of view. To achieve some more knowledge about the structural and dynamic properties of alkaline-earth metals, we have studied liquid Be, Ca and Ba at thermodynamic conditions near their respective melting points (Be at 0.12 GPa, Ca and Ba at ambient pressure). The OF-AIMD method requires the use of a local pseudopotential, which we have constructed following a force-matching method.

5.1.1 *Computation details*

We have performed OF-AIMD simulations for all the three systems studied, using the average kinetic energy density functional introduced in Chapter 4. A key ingredient of every OF-AIMD study is the local pseudopotential. The construction of the local pseudopotentials for our systems has two steps. In the first step we construct a local pseudopotential using the NPA method (Chapter 4) that, within the chosen OF scheme, reproduces the same pseudized valence electron density that the one obtained by all-electron KS calculations for a model system that contains an atom located in the center of a spherical cavity dug in a homogeneous electron gas. However this model is not completely realistic due to the discrete nature of the surrounding atoms. A more realistic model would take into account explicitly the presence of such atoms around the central one. An all electron calculation of this type is not feasible at present, but on the contrary a pseudopotential KS-AIMD simulation of the liquid system to be studied (so that only valence electrons are taken into account) using standard non-local pseudopotentials is nowadays within the reach of many computing facilities. To improve the liquid representation with OF-AIMD and the LPS to be as close to the KS-AIMD representation with an NLPS, we modify the initial LPS through a force-matching (FM) process. After the local pseudopotentials were constructed, we proceeded to perform OF-AIMD simulation runs for samples of 2000 particles, during 20 000 equilibrium timesteps of 0.002 ps

for Be and 0.003 ps for Ca and Ba. The cutoff energies for the local pseudopotentials were 30, 18 and 18 Ryd for Be, Ca and Ba respectively.

5.1.2 *Results and discussion*

The method developed to refine the construction of local pseudopotentials for use within OF-DFT strategies has been applied to the study of l-Be, l-Ca and l-Ba with successful results.

Concerning the static structure, we have found a rather common behavior in most of the aspects studied. All the systems present an asymmetric second peak akin to that exhibited by liquid transition metals which has been linked to an abundance of five-fold symmetry local structures. Their single-particle dynamics is quasi-universal if the time is scaled properly in terms of the Einstein frequencies. Concerning collective dynamic properties, we have observed a large degree of positive dispersion for all the systems, which increases with atomic size. The comparison with experimental data, whenever they are available, is rather satisfactory, concerning static structural properties, transport coefficients like the shear viscosity and dynamic properties as the sound velocity. However, some peculiarities appear like a large violation of the Stokes-Einstein equation in l-Be or l-Ba having the largest positive dispersion found so far. The following paper reports on this part of our work.

Orbital free *ab initio* simulations of liquid alkaline earth metals: from pseudopotential construction to structural and dynamic properties

Beatriz G del Rio and Luis E González

Departamento de Física Teórica, Universidad de Valladolid, C/ Real De Burgos, S/N 47011 Valladolid, Spain

E-mail: beatriz@metodos.fam.cie.uva.es and luisen@metodos.fam.cie.uva.es

Abstract

We have performed a comprehensive study of the properties of liquid Be, Ca and Ba, through the use of orbital free *ab initio* simulations. To this end we have developed a force-matching method to construct the necessary local pseudopotentials from standard *ab initio* calculations. The structural magnitudes are analyzed, including the average and local structures and the dynamic properties are studied. We find several common features, like an asymmetric second peak in the structure factor, a large amount of local structures with five-fold symmetry, a quasi-universal behaviour of the single-particle dynamic properties and a large degree of positive dispersion in the propagation of collective density fluctuations, whose damping is dictated by slow thermal relaxations and fast viscoelastic ones. Some peculiarities in the dynamic properties are however observed, like a very high sound velocity and a large violation of the Stokes–Einstein relation for Be, or an extremely high positive dispersion and a large slope in the dispersion relation of shear waves at the onset of the wavevector region where they are supported for Ba.

Keywords: liquid alkaline earth metals, *ab initio* molecular dynamics, local peudopotentials, single particle and collective dynamic properties

(Some figures may appear in colour only in the online journal)

1. Introduction

Liquid alkali metals, due to their particular electronic structure, are considered as the epitome of simple metallic liquids, at least as far as their properties near the triple point are concerned. This key position among liquid metals has promoted a large number of studies from the experimental, theoretical and computational points of view. When liquid alkali metals are either expanded near the liquid–vapor coexistence line or compressed near the solid–liquid coexistence line, new features appear (like electron localization, peculiar melting lines with decreasing melting temperature upon pressurization, possible liquid liquid coexistence, etc) that still make these systems very attractive for study.

Their immediate neighbors in the periodic table, i.e. the alkaline-earth metals, have received much less attention in general and in the liquid phase in particular the information available in the literature is very scarce. The study of some solid state properties of these systems, especially their phase diagram as a function of pressure, has however received recent impulse, being investigated both experimentally and theoretically and several interesting phenomena have been discovered.

For instance, Be is known to crystalize in the hcp structure at ambient pressure and low temperatures. Some old measurements [1] suggested that upon heating a transformation into a bcc structure takes place almost immediately before melting, so that there was a small pocket in

the P-T phase diagram at low pressures and high temperatures hosting a bcc structure. The existence of this region has been intensely debated, as most calculations deduced that the bcc structure is dynamically unstable [2] and recent experiments have indeed found hcp to be the stable phase all the way below the melting line for pressures from ambient pressure up to 205 GPa [3]. At larger pressures it is expected that Be transforms into bcc, but no experimental proof exists yet. Solid Be has also peculiar properties that make it interesting for aerospace, defense and nuclear industries, as its low mass density, high strength and high thermal conductivity. It also has some fundamental unique characteristics such as the exceptionally low axial ratio of the hcp structure (around 1.57), much lower than the ideal value and a particularly high sound velocity, around 13 000 m s^{-1} at ambient pressure and low temperature. Be melts at a rather high temperature, 1562 K (that increases with pressure up to around 4000 K at 200 GPa), which along with other inconvenient properties of the system (like its reactivity and especially its toxicity) makes Be one of the few one-component metals for which the liquid structure factor, $S(q)$, has not been measured yet. In fact, very few measurements have been performed for liquid Be and there are not even reliable data for properties as basic as the ionic mass density of the melt. We are only aware of one experiment [4] which addressed the measurement of the adiabatic sound velocity, c_s, (and indirectly the density) for the solid and the liquid phases at 0.12 GPa. It turned out that the sound velocity in the liquid is still very high, around 8500 m s^{-1}.

The phase diagram of Mg displays a stable hcp structure from which the system melts at low pressures and a bcc phase for larger pressures and temperatures. However, a new dhcp structure has been recently observed at pressures around 10–20 GPa below the melting curve [5], whose range of stability is presently uncertain. Mg is exceptional among the alkaline earths because several studies of the properties of the molten system near the melting point at ambient pressure have been carried out rather recently, including a measurement of $S(q)$ through x-ray diffraction (XD) and neutron diffraction (ND) [6], with much better resolution and intensity than older measurements of Waseda [7] and a study of the dynamical properties of the system through inelastic x-ray scattering (IXS) [8]. Also theoretical investigations, using orbital free *ab initio* molecular dynamics simulations (OF-AIMD), have been performed recently producing results in good agreement with the new experimental data [9]. One particular interesting feature observed in the new $S(q)$ is the presence of a shoulder at the high-q side of its second peak. This feature could not be observed in the older data and is suggestive of abundant icosahedron-like units in the liquid. The OF-AIMD study has indeed found such predominance, which had only been observed previously in metals and alloys made up of transition elements.

In the heavier alkaline-earth metals, the presence of a d electronic band above the Fermi energy and its increasing occupation upon pressurization plays an important role in the appearance of further phases at high pressures. Both Ca and Sr have the fcc structure as the minimum energy one at ambient pressure and zero temperature, but upon increasing temperature and/or pressure they transform into a bcc structure, from where they melt. Upon further compression Ca transforms at room temperature into a simple cubic (sc) structure at around 30 GPa and into other complex structures at higher pressures; up to now 7 phases have been discovered, the latest one above 210 GPa (see [10] and references therein). Sr displays a large variety of solid phases starting around 25 GPa, with some of them being quite complex, including a host structure and inconmensurate chains of guest atoms lying on the channels of the host [11], similar to a previously observed phase of Ba [12]. The melting curves of Ca and Sr start with positive slope but become rather flat in the region where they melt from bcc and, in the case of Ca also in the region of melting from the sc structure, after an initial increase of the melting temperature for pressures near the bcc-sc transition. The melting line of Sr, however, shows a negative slope in a small pressure range, leading to a local maximum and a local minimum in the melting temperature [13].

In the case of Ba, the ambient pressure ground state is bcc, which upon compression undergoes a series of transformations into hcp, host-guest and again hcp and its melting line also exhibits a negative slope in a pressure region of a similar extent as Sr, but located at much lower pressures [13, 14]. The bcc phase of solid Ba at room temperature shows a unique dynamic feature, as the frequency of the transverse mode along the ΓH line is larger than that of the longitudinal mode (and therefore the velocity of shear waves is larger than the sound velocity) [15]. This 'anomaly' has been theoretically studied [16] and attributed to the influence of the d electronic band in the dynamic properties.

At present, the only experimental information available for liquid Ca, Sr and Ba is that provided by the old experiments of Waseda, namely, the structure factor and the density near the triple points [7]. Some unpublished preliminary data for the dynamic structure factors of liquid Ba, based on inelastic neutron scattering (INS) experiments and liquid Ca (IXS and INS experiments), were obtained recently [17] and have been kindly made available to us.

The scarcity of experimental information about the liquid alkaline-earth metals has lead to an also very restricted dedication to their study from a theoretical point of view. In this respect we are only aware of theoretical calculations by Gonzalez *et al* [18], classical molecular dynamics (CMD) simulations by Alemany *et al* [19] and by Wax *et al* [20] and *ab initio* calculations for Mg by deWijs *et al* (Kohn–Sham calculations) [21] and Sengül *et al* (OF-AIMD calculations) [9]. However, the observation in liquid Mg of a structured second peak of $S(q)$ and the abundance of icosahedron-like structures naturally leads to the question of their possible existence in the other liquid alkaline-earth metals. Moreover, it is also interesting to study the dynamic properties of the molten metals and discern if the peculiarities appearing in the solid phases still persist in the liquid. Finally it is important to analyze the physical mechanisms that are responsible for the behaviour of the dynamic properties of these liquids. Such analysis is usually performed by resorting to models for the intermediate scattering functions

(as the generalized hydrodynamic theory [22], or the theory of generalized collective modes (GCM) [23][1]) or to models of their second order memory function, wich is defined through the Mori–Zwanzig formalism [24] (mode coupling theories [25–28], generalized viscoelastic theories [27, 29]). The parameters appearing in the theories have direct physical significance in terms of thermophysical magnitudes in the longwavelegth limit and their wavevector dependence determines the mechanisms involved in the propagation of waves, their damping and the presence of relaxing (non propagating) modes that also contribute to the shape of the dynamic structure factors.

In this paper we report results of such a study, performed within the OF-AIMD scheme, which, through the use of density functional theory (DFT) [30], shows much better accuracy than previous theoretical studies [18–20] that used interatomic pair potentials based on the application of second order perturbation theory to a homogeneous electron gas and therefore entailed more approximations in the study of the electronic subsystem. We have studied liquid Be, Ca and Ba at thermodynamic conditions near their respective melting points (Be at 0.12 GPa, Ca and Ba at ambient pressure). The OF-AIMD method requires the use of a local pseudopotential, which we have constructed following a force-matching method. This is described, together with other technical details, in section 2. Section 3 presents an analysis of the results obtained for the static structural properties, the common neighbour analysis (CNA) of local structures and the dynamic properties and we end up with some conclusions in the last section.

2. Technical details

Most *ab initio* studies of condensed matter are performed using pseudopotential DFT, in which only the valence electrons are explicitly taken into account in the description of the electronic density and the interactions between valence electrons and nucleus plus core electrons (ionic cores) are described through the use of pseudopotentials. The separation between valence and core electrons is somewhat arbitrary and in some cases not clear a priori. In the case of Be there is no such problem, since the core 1s level is well separated in energy and in distance from the valence 2s level. In Ba, on the other hand, the 5p orbitals and the 6s orbitals are not far from each other and in some previous studies (especially under pressure) the 5p electrons are taken as semicore states [31] (meaning they are treated as valence electrons). The same situation occurs in the case of Ca (3p and 4s orbitals respectively).

The Kohn–Sham (KS) scheme [32] of DFT enables the calculation of the electronic density in terms of one-electron orbitals corresponding to a system of non-interacting particles and moreover allows the exact calculation of the non-interacting kinetic energy in terms of the orbitals. The explicit appearance of orbitals also allows the use of different pseudopotentials for different angular momentum of the orbitals, i.e. non-local pseudopotentials. Orbital free schemes

intend the calculation of the electronic density and non-interacting kinetic energy without resorting to one-electron orbitals. This approach has three important consequences: first, there are large savings in required memory, since only the electron density is required and computing time, especially because no orthogonalization constraints between orbitals are needed; second, the non-interacting kinetic energy cannot be obtained exactly anymore, instead it has to be approximated; and third, it is not possible to use non-local pseudopotentials (there are no orbitals with different angular momentum), so a local pseudopotential (only dependent on the position of the electron relative to the ion) has to be used.

In this work we have used a non-interacting kinetic energy functional with explicit dependence on the density, which recovers the exact form in several limits (one- or two-electron systems, uniform systems and uniform systems weakly perturbed) and posseses adequate mathematical properties (like non-negativity). It is fully described in [33].

The construction of the local pseudopotentials for our systems has two steps. In the first step we construct a local pseudopotential that, within the chosen OF scheme, reproduces the same pseudized valence electron density that the one obtained by all-electron KS calculations for a model system that contains an atom located in the center of a spherical cavity dug in a homogeneous electron gas. This has been the method of choice for pseudopotential construction in several previous studies of liquid metals within the OF-AIMD approach and it is called the neutral pseudoatom method (NPA) [33]. The reference model (atom in cavity in a jellium) aims to mimic the environment that an atom actually finds in a liquid metal. However this model is not completely realistic due to the discrete nature of the surrounding atoms. A more realistic model would take into account explicitly the presence of such atoms around the central one. An all electron calculation of this type is not feasible at present, but on the contrary a pseudopotential KS-AIMD simulation of the liquid system to be studied (so that only valence electrons are taken into account) using standard non-local pseudopotentials is nowadays within the reach of many computing facilities. The simulation sample has to be small enough and the simulation time short enough so as to perform the simulation in a reasonable run time. Specifically, in the present study we have used samples that contain 120 atoms and are simulated for 300 timesteps. The properties obtained during these runs are used as benchmarks in the development of the local pseudopotentials to be used in the OF-AIMD runs, as explained below.

It should be mentioned that in some cases the OF-AIMD results obtained with NPA pseudopotentials reproduce the KS-AIMD ones extremely well. Such is the case of liquid Mg, where ionic and electronic properties obtained within the OF scheme [9] and KS scheme [21] are practically coincident and also agree very well with experimental data, including both static [6] and dynamic [8] properties.

In some other cases, like those considered in this work, the OF versus KS comparison is still good but leaves some room for improvement. Particularly important in this respect are the forces acting on the atoms, since obviously they determine the

---

[1] For a recent review, see Bryk (2001).
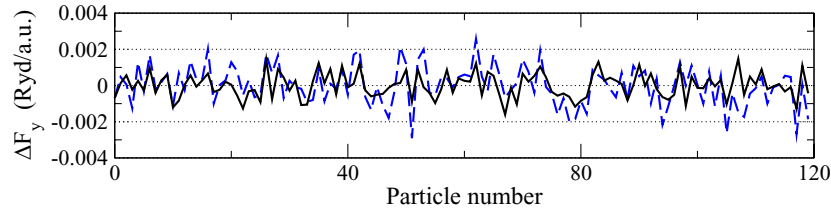
Figure 1. Differences between the y-components of the forces on Ca atoms as obtained from KS and OF calculations before (dashed) and after (solid) pseudopotential optimization, for an atomic configuration sampled from the KS-AIMD simulation.
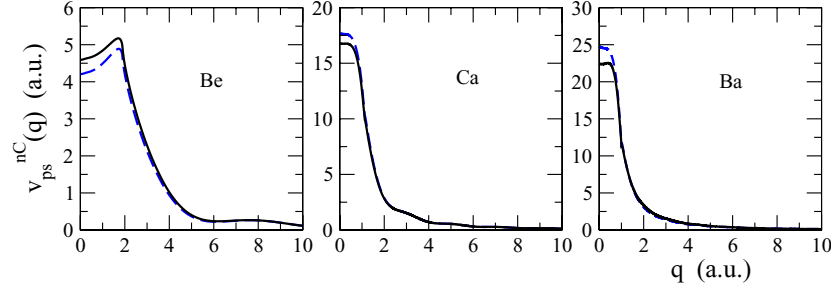
Figure 2. Local pseudopotentials before (dashed) and after (solid) optimization through force matching.

dynamic evolution of the system and consequently its static and dynamic structural and transport properties. Therefore, after initial equilibration of the KS simulations, when the atomic configurations are typical of the liquid sample, we collect the forces that act on each of the atoms. In the second step of the construction of local pseudopotentials we take several atomic configurations from the KS-AIMD run and compute with the OF-AIMD formalism and the NPA pseudopotential the forces acting on the atoms. As commented above, the OF forces are usually quite similar to the KS ones. However the comparison can be improved by modifying the NPA pseudopotential in two important regions of reciprocal space: near $q = 0$ and near $q = 2k_F$, where k_F is the Fermi momentum corresponding to the mean electron density of the system. In both regions we add to the NPA pseudopotential a gaussian function, whose amplitudes and widths are taken as parameters to be fitted so as to minimize the difference between KS forces and OF forces. The optimized local pseudopotentials differ slightly for different atomic configurations (all of them typical of the liquid structure) and therefore we perform an average over a few configurations in order to obtain the final local pseudopotential. Figure 1 shows the comparison between KS forces and OF ones for one atomic configuration corresponding to liquid Ca obtained through the NPA method (first step) and after optimization (second step). The overall discrepancy between the two sets of forces, as measured by the quantity ϵ, defined as

$$\epsilon = \frac{1}{3N_{at}} \sum_{i=1}^{N_{at}} \left| \boldsymbol{F}_i^{OF} - \boldsymbol{F}_i^{KS} \right|^2 \qquad (1)$$

amounts to $\epsilon = 1.31 \times 10^{-4}, 1.22 \times 10^{-6}, 3.68 \times 10^{-6}$ Ryd^2/(au^2) for Be, Ca and Ba respectively before optimization and $\epsilon = 1.25 \times 10^{-4}, 4.73 \times 10^{-7}, 1.87 \times 10^{-6}$ respectively after optimization. The improvement is notable in Ca and Ba, but not so much in Be. It should be noted that

the modules of the forces are also much larger for Be than for Ca and Ba. Figure 2 shows the non-coulombic part of the pseudopotentials of Be, Ca and Ba in reciprocal space before and after the force-matching optimization.

Two final checks for the local pseudopotentials thus constructed were performed. In the first one we made an OF-AIMD simulation for the same systems (120 atoms) as the KS ones, but lasting somewhat longer time (2000 timesteps) in order to compare some physical properties, for instance, the pair correlation function, obtained from both methods. The results of such comparison are shown in figure 3. In the second check we tested the changes brought about by the optimization procedure, by comparing the results for the structure factor as obtained from the NPA pseudopotential and from the optimized one. Both are shown, along with experimental data, in figure 4 where the improvement is manifest.

For the KS-AIMD simulations we used the local density approximation for exchange and correlation (PBE generalized gradient approximation in the case of Ba), including non linear core corrections, with a norm-conserving pseudopotential for Be (2 valence electrons) and ultrasoft pseupotentials for Ca and Ba, including in both of them the p electrons as semicore (8 valence electrons). The separable pseudopotentials were generated using the atomic code included in the Quantum-Espresso package, from an atomic configuration $1s^2 2s^2$ for Be, $[Ar]4s^{1.8}3d^{0.2}$ for Ca and $[Xe]6s^2$ for Ba. The local part of the pseudopotential was the p-component in Be, the all-electron potential (coulombic from 3.90 atomic units onwards) in Ca and the s-component in Ba. The energy dependence of the logarithmic derivatives, computed at distances around half the average distance between near neighbors in the liquid, was checked against the all-electron ones up to $l = 3$, producing an excellent agreement and good transferability to different electronic configurations was also achieved. The absence of ghost states was also established for the three systems. Table 1
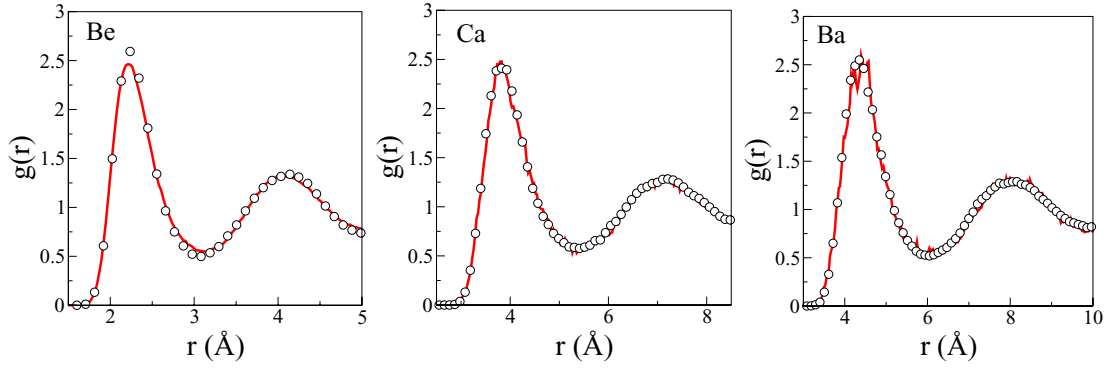
Figure 3. Pair correlation functions, obtained from KS-AIMD (line) and OF-AIMD with optimized local pseudopotential (circles).

lists the pseudization radii for the orbitals (the same value for all the angular momenta), for which we used the RRKJ scheme [34] and for the core density, for which we used the Louie *et al* scheme [35]. It also shows the number of projectors for each angular momentum and the corresponding energies and the cutoff energy used in the simulations.

The samples used in the KS-AIMD simulations contained the 120 particles in a cubic simulation box that reproduces for each system the experimental number density at thermodynamic conditions near melting that are listed in table 2.

In the construction of the local pseudopotentials we considered only two valence electrons for the three systems, together with nonlinear core corrections for exchange and correlation. We have found that this choice produces an accurate reproduction of the forces obtained in the KS-AIMD calculations. After the local pseudopotentials were constructed, we proceeded to perform OF-AIMD simulation runs for samples of 2000 particles at the same thermodynamic conditions as shown in table 2, during 20 000 equilibrium timesteps of 2×10^{-3} ps for Be and 3×10^{-3} ps for Ca and Ba. The cutoff energies for the local pseudopotentials were 30, 18 and 18 Ryd for Be, Ca and Ba respectively; these were confirmed to produce converged forces on the atoms. The equilibrium configurations generated were used to perform the averages needed for the calculation of the properties of the system, including the static structure, dynamic properties and transport coefficients, as discussed in the next section for each system.

3. Results

For the three systems considered we have studied the static structure, as described by the pair correlation function $g(r)$ and the static structure factor, $S(q)$, both of which are directly accessible from the ionic coordinates along the simulation. We have also analyzed the local structure around pairs of near neighbors, (separated by distances smaller than the minimum of $g(r)$), through a common neighbor analysis (CNA). As for the dynamic properties, we have studied single particle and collective magnitudes. The former type includes the velocity autocorrelation function, $Z(t)$ and mean squared displacement, $\delta r^2(t)$, which yield the diffusion coefficient, D. The collective
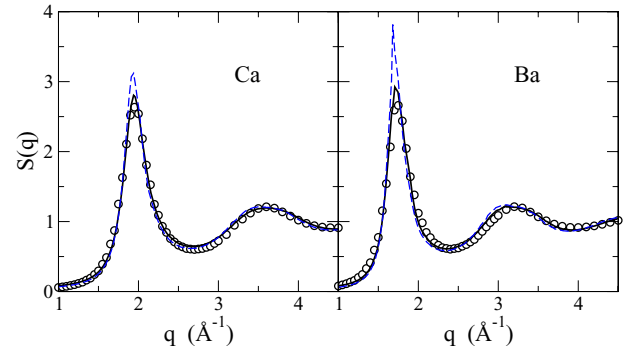
Figure 4. Structure as obtained from OF-AIMD with the NPA pseudopotential (dashed line) and with the optimized one (full line) compared with experimental data [7].

properties we have studied are the intermediate scattering functions, $F(q, t)$ and their Fourier Transforms, the dynamic structure factors, $S(q, \omega)$ and the longitudinal and transverse current correlation functions and their spectra, $C_L(q, \omega)$ and $C_T(q, \omega)$. The latter also enables the calculation of the shear viscosity, η, of the systems. We have finally made an analysis of the physical mechanisms responsible for the behavior of the collective dynamical magnitudes, through the calculation of the second order memory function, $N(q, t)$, of the intermediate scattering functions and its behavior as function of the wavevector.

3.1. Static structure

Figure 5 shows the structure factors obtained from the OF-AIMD simulations together with the XD data of Waseda for Ca and Ba. The agreement is quite satisfactory regarding positions and amplitudes of the peaks. The main peak is somewhat higher than the XD one, whereas previous simulations through CMD (not shown in the figure) produced clearly higher main peaks. The right panel of figure 5 shows an enlarged view of the second peak of $S(q)$ as obtained from the simulations, in terms of the reduced wavevector, q/q_p, where q_p is the position of the main peak of $S(q)$ (3.48, 1.95 and 1.72 Å^{-1} for Be, Ca and Ba respectively). A split structure can be seen in all cases, with a maximum at $q_2/q_p \approx 1.75$, 1.85 and 1.80 for Be, Ca and Ba and a shoulder at a higher $q_2'/q_p \approx$

Table 1. Parameters defining the pseudopotentials used in the KS-AIMD simulations. Radii are given in atomic units and energies in Ryd. The projector energies include the all-electron eigenvalues and additional energies, which are given in parenthesis.

Element	r_{ps}	r_{core}	E_{proj}^s		E_{proj}^p		E_{proj}^d		E_{proj}^f		E_{cut}
Be	1.50	0.98	−0.412	(−0.342)	−0.155	—	—	—	—	—	20
Ca	2.90	0.95	−0.273	(−0.10)	−2.008	(−0.10)	−0.126	—	—	—	13
Ba	4.00	2.00	−0.237	—	−1.377	(−0.08)	−0.148	(0.10)	(−0.05)	(0.05)	18

Table 2. Thermodynamic states studied for liquid Be, Ca and Ba.

System	T (K)	ρ (Å^{-3})
Be	1600	0.09781
Ca	1150	0.02058
Ba	1053	0.01460
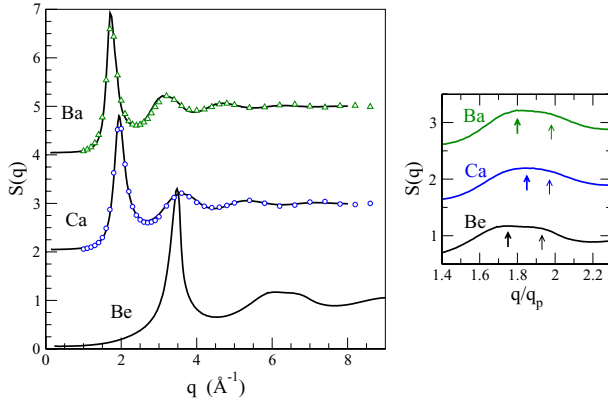
Figure 5. Structure factors, $S(q)$, for Be, Ca and Ba. Full lines are OF-AIMD results and symbols are experimental XD data from Waseda. The right panel shows an expanded view of the second peaks of $S(q)$.

Figure 6. Pair correlation functions, $g(r)$, for Be, Ca and Ba. Full lines are OF-AIMD results and symbols are experimental XD data from Waseda.

1.93, 1.97 and 1.98, respectively. This type of structure had been previously reported for liquid transition metals (at 1.74 and 1.95 in the case of Ni) and also recently for liquid Mg (at 1.79 and 1.97) and it has been linked to a relative abundance of five-fold symmetry structures existent in the liquid. In the next section we analyze in detail this type of structures.

A quadratic extrapolation of the structure factor towards $q = 0$ allows the determination of the isothermal compressibility of the systems, through the well known relation $S(0) = \rho k_B T \chi_T$, where k_B is Boltzmann constant. This approach leads to OF-AIMD values of $\chi_T = 0.248 \pm 0.001$, 1.26 ± 0.13 and $1.98 \pm 0.18 \times 10^{-10}\,\mathrm{N^{-1}m^2}$. There is no experimental result for Be to compare with, while the measurements for Ca and Ba at melting are 1.10 and 1.744, respectively [37].

The pair correlation functions of liquid Be, Ca and Ba are shown in figure 6, where a good agreement is observed with experimental data from Waseda. The coordination number, or number of nearest neighbors, can be obtained by integrating the radial distribution function (RDF), $G(r) = 4\pi\rho r^2 g(r)$, up to its first minimum (or up to the first minimum of $g(r)$) which defines the first coordination shell. A less arbitrary method relies on the calculation of the partial RDFs corresponding to the first, second, third, ... , nth, neighbor of an atom. The

bordeline between two coordination shells is located at the partial RDF of minimum peak height and maximum width at half-height. For Be integration up to the minimum of $g(r)$ leads to a coordination number of 11.6, while the other two methods yield a coordination number of 11. For Ca and Ba, integration up to the minimum of $G(r)$ produces a coordination number around 12, whereas the other two methods lead to 13 nearest neighbors.

3.2. Common neighbor analysis

The pair correlation function describes the *average* distribution of atoms around one taken as the origin. The *local* structure can be better understood in terms of some magnitudes that describe how the nearest neighbors are located around a given atom, or, more conveniently, a given pair of atoms. Honeycutt and Andersen introduced the CNA [36] to study this local structure. The different local arrangements are characterized by 4 indexes $ijkm$, where i denotes the coordination shell to which the chosen pair belongs (1 for the first coordination shell, 2 for the second one, etc), j denotes the number of atoms that are near neighbors of both atoms of the root pair, k counts how many near neighbor links exist between this j atoms and finally m describes different possible topologies of structures with the same values of j and k (if this is possible). It turned out that different crystalline structures are characterized by an appearance of well defined distributions of local structures (clusters) with characteristic sets of indexes. For instance the bcc structure (considering as near neighbors those separated up to the side of the cube, i.e. 14 atoms), is

Table 3. Relative abundance of CNA clusters in a perfect centered icosahedron (icos), in several ideal crystalline structures, in hot bcc (h-bcc) and fcc (h-fcc) solids and in liquid Be, Ca and Ba as obtained in the present work. The column for Mg is a reanalysis of previous simulations [9] by finding the inherent structures prior to the calculation.

Pairs	h-bcc	bcc	icos	hcp	fcc	h-fcc	Be	Ca	Ba	Mg
1661	0.33	0.57	0.00	0.00	0.00	0.02	0.01	0.08	0.11	0.03
1441	0.25	0.43	0.00	0.00	0.00	0.02	0.01	0.06	0.08	0.02
1421	0.00	0.00	0.00	0.50	1.00	0.21	0.04	0.03	0.02	0.06
1422	0.00	0.00	0.00	0.50	0.00	0.15	0.07	0.06	0.04	0.11
1311	0.00	0.00	0.00	0.00	0.00	0.14	0.11	0.02	0.02	0.06
1321	0.00	0.00	0.00	0.00	0.00	0.00	0.09	0.02	0.02	0.03
1431	0.04	0.00	0.00	0.00	0.00	0.16	0.28	0.19	0.17	0.23
1541	0.08	0.00	0.00	0.00	0.00	0.14	0.14	0.21	0.19	0.21
1651	0.05	0.00	0.00	0.00	0.00	0.00	0.00	0.01	0.01	0.00
1551	0.07	0.00	1.00	0.00	0.00	0.02	0.18	0.30	0.31	0.20

characterized by a 43% (6/14) abundance of 1441 clusters and a 57% (8/14) abundance of 1661 clusters. The characteristic abundances of other common crystalline phases, as fcc or hcp, are shown in table 3. Other regular structures, even if not typical of crystalline solids, also have well defined abundances of characteristic clusters, for instance in a perfect centered icosahedral structure there is a 100% abundance (12/12) of 1551 clusters. Deformed icosahedra give rise to other possible clusters, such as 1541, 1431 and 1321. In a hot solid the atoms vibrate and during this vibration the local clusters distort. This distortion is sometimes quite important and a direct calculation of the abundance of different clusters in the hot solid may lead to a misleading results. Table 3 shows that some structures, as bcc, are not very prone to local distortion, since around 60 percent retain the characteristic 1661 and 1441 clusters in a proportion similar to the ideal one. On the other hand the hot fcc solid changes drastically with respect to the ideal structure: the 1421 and 1422 clusters seem to indicate a 35% of hcp clusters, while the rest seem mostly distorted icosahedra, also in a 30% ratio and 1311 clusters (and other types not shown). Therefore it is very important, in order to characterize the underlying local structure of a system, to remove the thermal disorder present in the system, by searching the so called 'inherent structure'. This is the one to which the atoms relax when thermal energy is supressed and corresponds to the local energy minimum closest to the atomic configuration being considered. For the hot fcc solid, this procedure turn all the clusters back into 1421, as corresponds to a perfect fcc crystal. In a liquid any type of cluster is possible and the relative abundances indicate the amount of local underlying characteristic structures. We have therefore selected several atomic configurations for each system, performed the energy minimization towards the corresponding inherent structure and calculated the relative abundance of the different types of clusters. The results are shown in table 3. We also include in the table the data for liquid Mg, which had been previously analyzed without recoursing to the inherent structure [9].

In all cases we see that the majority local structures have five-fold symmetry, either ideal or distorted (69%, 72% and 69% in Be, Ca and Ba respectively). The abundances of these types of clusters is similar to that found in liquid transition metals as Zr (60%) or Ni (80%). Such type of structures is incompatible with long range order and therefore somehow

can act as a nucleation barrier that enables undercooling the liquids below their thermodynamic melting temperatures. We are not aware of any experimental investigation about this undercooling ability so far. The liquids also show some memory of the phase from which they melt, i.e. hcp in the case of Be and bcc in Ca and Ba; on the average about 16% of the local structures reflect the underlying solid phase. Note that the new results for Mg, upon considering the inherent structure, are not dramatically different from the previously reported ones [9] and that they are well in line with the data obtained for the other liquid alkaline-earth metals studied here. Finally one can note the relatively large abundance of 1311 clusters in the particular case of liquid Be. This type of local structure is not easily ascribed to a particular crystal phase and suggests truly disordered structures.

3.3. Dynamic structure and transport properties

3.3.1. Velocity autocorrelation function and diffusion coefficient.
The normalized velocity autocorrelation function, $Z(t) = \langle v(t) \cdot v(0) \rangle / \langle v(0) \cdot v(0) \rangle$ measures quantitatively how much memory a particle has of its original velocity after a time interval t has elapsed. In dense liquids it usually has a highly damped oscillatory behavior, showing a first negative minimum followed by oscillations with very small amplitude. The first negative minimum, which indicates backscattering where the velocity has a component in the opposite direction to its initial one, is due to the so called cage effect produced by the bouncing of the particle against the cage formed by its nearest neighbors. The initial decay rate of $Z(t) \sim 1 - \omega_E^2 t^2 / 2 + \cdots$ is dictated by the Einstein frequency, ω_E, which can be directly evaluated in the simulations from the particles velocities and accelerations. The values obtained for liquid Be, Ca and Ba are 78.2, 19.3 and 9.53 ps^{-1}, which reflect the intrinsic rates of dynamic evolution of the systems and are linked not only to the atomic masses but also to the densities, the interatomic interactions and the structure.

In figure 7 we have plotted the normalized velocity autocorrelation function with respect to $\omega_E t$ and the results show an almost universal behavior: the backscattering minima occur for the same scaled time and their depth is quite similar (in fact it is a little deeper for Ba and shallower for Be). The power spectrum, $Z(\omega)$, is the Fourier Transform of $Z(t)$ and it usually shows a maximum at the frequency of the oscillations
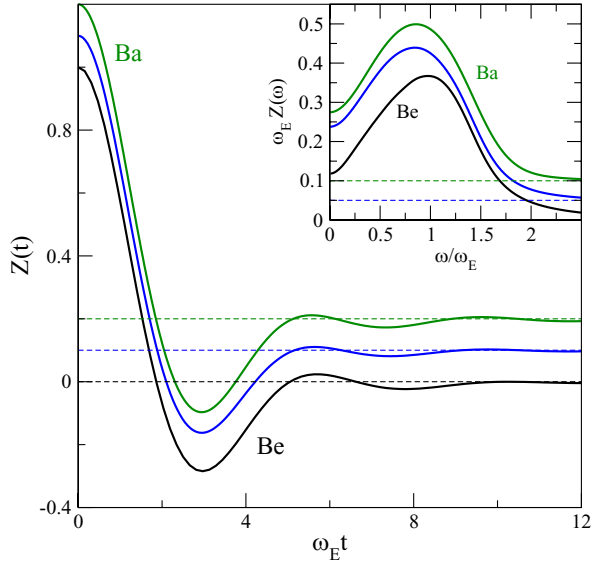
Figure 7. Normalized velocity autocorrelation functions of liquid Be, Ca and Ba, with time scaled by the Einstein frequencies. The inset shows the scaled power spectrum in terms of the scaled frequency. The data for Ca and Ba are displaced upwards for clarity.

Table 4. Transport coefficients obtained from the present study (OFAIMD), from experimental measurements [41] (exp) and from previous classical molecular dynamics studies [20] (CMD) (results in parenthesis are from Alemany *et al* [19]). Results obtained using the Stokes–Einstein (SE) relation are also included. Diffusion coefficients are given in Å^2/ps and shear viscosities in GPa ps.

	Be	Ca	Ba
D^{OFAIMD}	0.99	0.73	0.34
D^{CMD}	1.04	1.01 (0.61)	0.33 (0.23)
$\eta_{\text{SE}}^{\text{OFAIMD}}$	1.62	0.91	1.58
η^{OFAIMD}	2.78 ± 0.15	1.12 ± 0.02	1.67 ± 0.02
η^{exp}	—	1.20	1.74

of $Z(t)$, broadened due to their damping. In terms of ω/ω_E the power spectra of liquid Be, Ca and Ba (figure 7) show again an almost universal behavior, with a broad maximum at $\omega \approx 0.86\,\omega_E$ (a little displaced towards larger frequency for Be).

The diffusion coefficient can be obtained from the time integral of the velocity autocorrelation function and also from the slope of the mean squared displacement of an atom in the liquid for long times. Both routes lead to essentially equal values of D for the three systems considered, namely, 0.99, 0.73 and 0.34 Å^2 ps^{-1} for Be, Ca and Ba, respectively (see table 4, where shear viscosities are also reported). Unfortunately there are no experimental values to compare with. Previous CMD calculations by Alemany *et al* [19] produced values for Ca and Ba rather smaller than our present results. Wax *et al* 's CMD [20], on the other hand, led to a value for Ca rather higher than ours, whereas the data for Be and Ba showed good agreement with the present ones.

3.3.2. Intermediate scattering functions and dynamic structure factors. The intermediate scattering functions, $F(q, t)$,

provide information about the time evolution of collective excitations (propagation and damping) and are directly accessible from the MD simulations through the wavevectors allowed by the periodic boundary conditions associated to the simulation box and the time evolution of the ionic positions. They are defined by the relation

$$F(q, t) = \frac{1}{N} \langle \rho(\boldsymbol{q}, t + t_0)\rho(-\boldsymbol{q}, t_0) \rangle , \qquad (2)$$

where $\rho(\boldsymbol{q}, t)$ is the q-Fourier component of the collective microscopic density,

$$\rho(\boldsymbol{q}, t) = \sum_{\ell=1}^{N} \exp[-i\boldsymbol{q} \cdot \boldsymbol{R}_\ell(t)] . \qquad (3)$$

In (2) the average is taken over initial times t_0 and wavevectors with the same module.

The Fourier Transforms into the frequency domain yield the dynamic structure factors, $S(q, \omega)$. These are directly related to the intensity measured in an inelastic x-ray scattering (IXS) experiment and to the coherent component of the intensity measured in inelastic neutron scattering (INS). We are only aware of some preliminary measurements of $S(q, \omega)$ through INS and IXS for Ca and Ba, so we will compare our results with these data where appropriate.

Figure 8 shows the normalized intermediate scattering functions of Be, Ca and Ba for several q-values. The lowest wavevector corresponds to the minimum value consistent with the periodic boundary conditions, namely, $q_{\min} = 2\pi/L$, where L is the side of the simulation box.

The $F(q, t)$ show damped oscillations superimposed on a monotonic decay up to $q \approx 2.55\,\text{Å}^{-1} \approx 0.7q_p$ in Be, up to $q \approx 1.56\,\text{Å}^{-1} \approx 0.8q_p$ in Ca and up to $q \approx 1.45\,\text{Å}^{-1} \approx 0.85q_p$ in Ba. The damping increases with increasing q and for $q = q_{\min}$ the oscillations are most marked, leading in fact to negative values for Ca and less so for Ba. The functions corresponding to $q \approx q_p$ display a very slow decay, which is characteristic of these wavevectors due to the strong structural correlations present and is known as 'de-Gennes narrowing' ($F(q, t)$ in fact widens, so $S(q, \omega)$ narrows).

The dynamic structure factors, as obtained from the time Fourier Transform of the $F(q, t)$ are shown in figure 9 in a region of wavevectors in which side-peaks are visible. These reflect the existence of propagating collective excitations and the q-range where this happens spans from $q = q_{\min}$ up to $q \approx 0.4q_p$ in Be, up to $q \approx 0.7q_p$ in Ca and up to $q \approx 0.8q_p$ in Ba. The frequencies where these maxima appear define the dispersion relation $\omega_m(q)$. In the limit of small wavevectors $\omega_m(q)$ should vary linearly with q and the slope corresponds to the adiabatic sound velocity, c_s. We postpone the discussion to the next section in order to consider jointly the dispersion of the maxima in $S(q, \omega)$ with that of the peaks in the spectrum of the longitudinal current correlation functions. For the moment we just mention that the quasi-universal behavior exhibited by the single-particle dynamic properties is not observed in the collective dynamics.
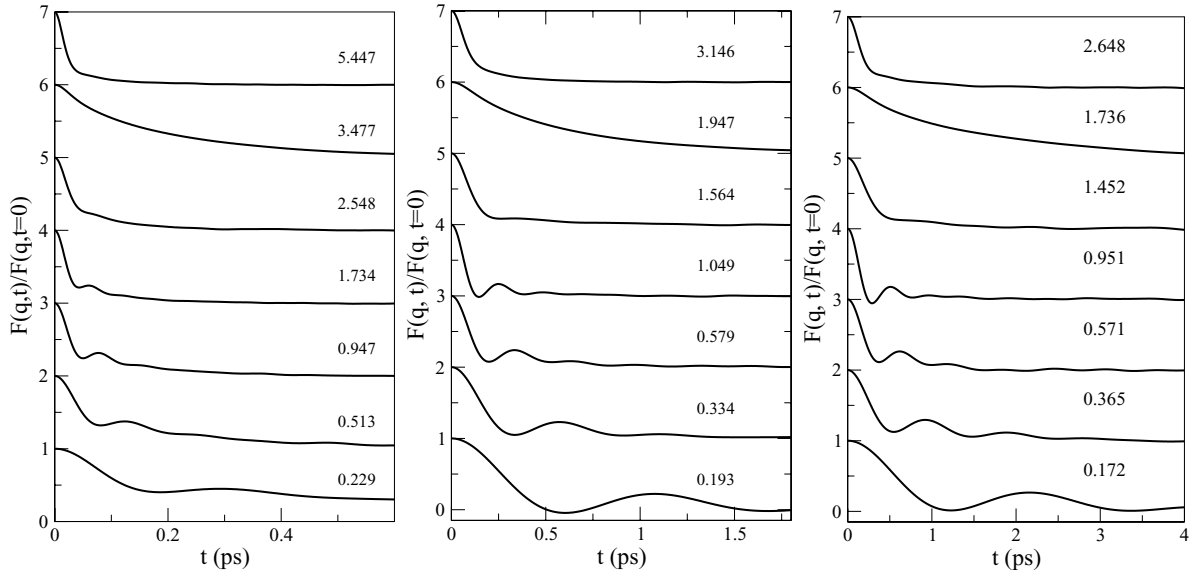
Figure 8. $F(q, t)$ for selected wavevectors (shown above each curve in Å^{-1}) in liquid Be (left), Ca (center) and Ba (right).
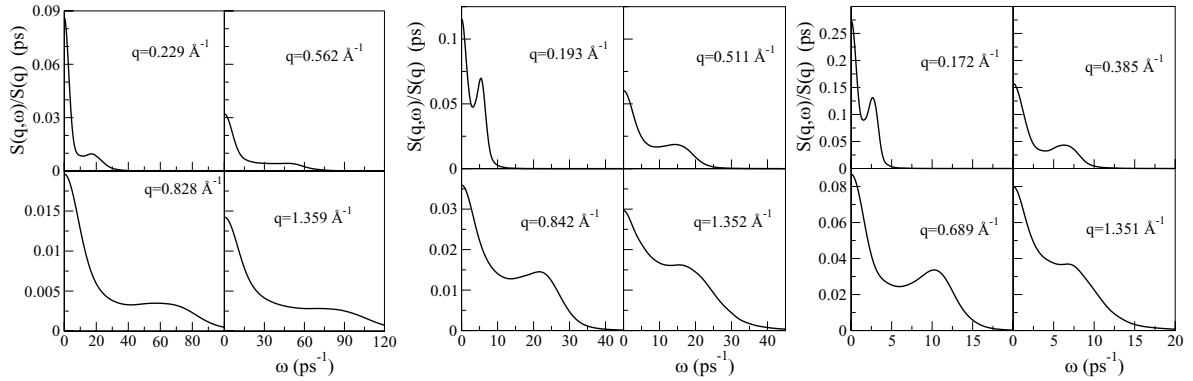
Figure 9. $S(q, \omega)$ for selected wavevectors in liquid Be (left), Ca (center) and Ba (right).

3.3.3. Longitudinal current correlation functions, dispersion relations, sound velocity and positive dispersion. The microscopic current is defined from the velocities of the particles and their positions, namely,

$$J(q, t) = \sum_{\ell=1}^{N} V_\ell(t) \exp[-i q \cdot R_\ell(t)]. \qquad (4)$$

This can be decomposed into a longitudinal, parallel to q, component, $J_L(q, t) = (J(q, t) \cdot u_q) u_q$, where $u_q = q/q$ is the unit vector in the direction of q and a transverse, perpendicular to q, component, $J_T(q, t) = J(q, t) - J_L(q, t)$.

The autocorrelation function of the longitudinal current is then calculated as

$$C_L(q, t) = \frac{1}{N} \langle J_L(q, t + t_0) J_L(-q, t_0) \rangle, \qquad (5)$$

where averages are again taken over wavevectors with the same module and over time origins. Fourier transforming into the frequency domain leads to the longitudinal spectra, $C_L(q, \omega)$.

The relation between the time derivative of the microscopic density and the longitudinal current implies that

$C_L(q, \omega) = (\omega^2/q^2) S(q, \omega)$. As a consequence $C_L(q, \omega)$ shows side peaks for any wavevector, whose frequency we denote as $\omega_L(q)$. These peak positions define another dispersion relation, which in general does not coincide with that obtained from $\omega_m(q)$, except in the limit $q \rightarrow 0$, where both vary linearly with a slope given by c_s.

It should be noted that in many cases where IXS or INS experiments are performed the data analysis is made through a fitting to a model. In particular, the most widely used model to describe the inelastic part of the data is the damped harmonic oscillator (DHO) model. This model yields a characteristic frequency and width of the side peak. In fact, it turns out that the frequency thus obtained corresponds to the maxima of the longitudinal spectra, so the proper comparison in this case is with $\omega_L(q)$.

The experimental (IXS and INS) and theoretical (CMD and AIMD) studies performed so far for a wide variety of liquid metals (and other liquids too) have revealed a quite common behavior of $\omega_L(q)$ for q increasing above the hydrodynamic region. It has been named positive dispersion and is best described in terms of the phase velocity $c_L(q) = \omega_L(q)/q$.
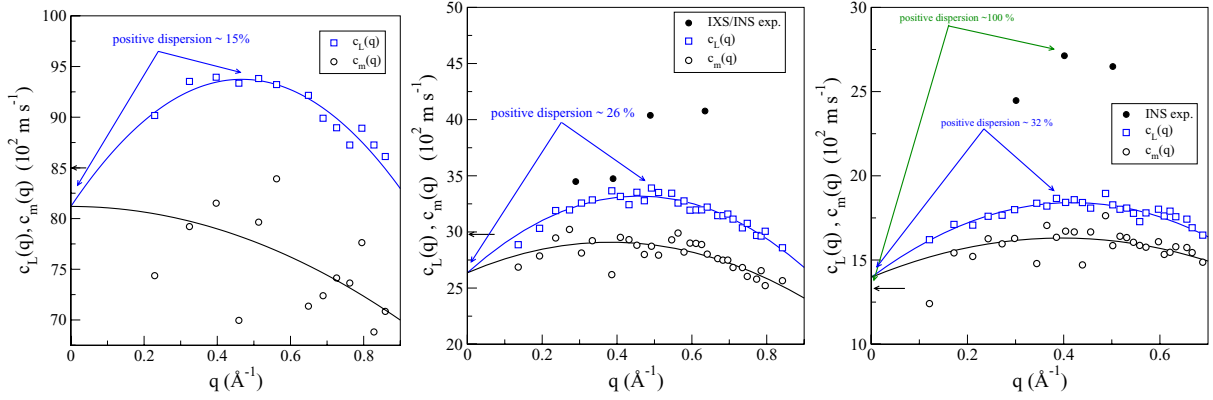
Figure 10. Phase velocities obtained from the dispersions of the longitudinal spectra, $c_L(q)$ and the dynamic structure factor, $c_m(q)$, in liquid Be (left), Ca (center) and Ba (right). The lines are fits to the points made as explained in the text. The experimental data are taken from [17].

Table 5. Sound velocity (c_s), velocity of transverse waves (c_T), starting wavevector of the range where transverse waves are supported (q_T in the linear fit, or q_{Tv} in the viscoelastic model) and final wavevector of this region (q_m). Experimental data are taken from Boivineau [4] for Be and from Blairs [37] for Ca and Ba. Velocities are given in m s^{-1} and wavevectors in Å^{-1}.

	Be	Ca	Ba
c_s	8120 ± 200	2636 ± 200	1397 ± 150
c_s^{exp}	8500 ± 500	2978	1331
c_T	5971 ± 350	2583 ± 100	1591 ± 50
q_T	0.14	0.17	0.15
q_{Tv}	0.25	0.22	0.20
q_m	7.20	4.35	4.02

The positive dispersion signals an increase in $c_L(q)$ above c_s at finite wavevectors, leading to an apparent sound velocity higher than the hydrodynamic one. The q-value at which positive dispersion is maximum and the magnitude of this maximum value vary from one system to another, the highest one observed so far near the melting point corresponds to liquid Hg, where an almost 50% increase in the apparent sound velocity has been observed in INS (in IXS and AIMD the increase reported was rather smaller, around 20%).

The OF-AIMD simulations show, for the three alkaline-earth metals considered, the existence of positive dispersion, as evinced in figure 10, where we have plotted $c_L(q)$. The phase velocity $c_m(q) = \omega_m(q)/q$ is also displayed in the figure and is consistently smaller than $c_L(q)$. In order to quantify the amount of positive dispersion an estimate of c_s is needed. We have obtained it by first fitting $c_L(q)$ by a second degree polynomial in the region where positive dispersion is evident and from this c_s is obtained. Second, $c_m(q)$ is fitted with the same functional form, but imposing the value of $c_m(q = 0) = c_s$ as determined previously. If such a fit is indeed possible then we can guarantee the consistency between all the results. This common fit has been indeed possible and the sound velocities obtained are shown in table 5 where they are also compared with experimental data. The agreement in the case of Be and Ba is within the error bars whereas in Ca we underestimate somewhat the experiment, although no uncertainties in the experimental data for Ca and Ba were reported and there is

a small mismatch in the temperatures (experiments are at 1123 and 1003 K for Ca and Ba respectively) [37].

The amount of positive dispersion clearly increases with increasing atomic size of the atoms and reaches quite high values, especially in the case of Ba, larger than those found in any previous studies near melting. For Be the positive dispersion is around 15%, with the apparent velocity reaching ca 9400 m s^{-1} at $q \approx 0.47$ Å^{-1}. In the case of liquid Ca our results show a maximum positive dispersion around 26% at $q \approx 0.45$ Å^{-1}, for which c_L is around 3320 m s^{-1}. Notably the preliminary IXS and INS results of Sani *et al* [17] give quite similar apparent velocities up to 0.4 Å^{-1}; however for larger q the experimental data still increase (contrary to our results), in a way inconsistent with data for other systems and with known theoretical approaches. In the case of Ba the positive dispersion at $q \approx 0.4$ Å^{-1} reaches around 32%, an exceptionally high value for liquid metals near melting and the corresponding phase velocity is around 1840 m s^{-1}. The INS data for Ba do show a very large positive dispersion [17], reaching 100% at wavevectors similar to ours, but we consider this value as unrealistically large.

The possible phyiscal origin of the positive dispersion has been discussed by Bryk *et al* in connection with measurements for supercritical Ar [38]. The GCM approach predicted, in the asymptotic long-wavelength region, a change in the initially linear dispersion which is proportional to q^3 with a coefficient that could be positive or negative (producing positive or negative dispersion in this region). Within the so-called viscoelatic-GCM it was shown that the origin of the correction is the coupling of the hydrodynamic sound mode with a structural relaxation mode and the sign of the correction depends upon the values of the isothermal and elastic sound velocities. Further terms in the correction to linear dispersion were obtained within a GCM approach that includes thermal fluctuations, which in the case of Ar turned to be negative and included the effects of an additional non-hydrodynamic thermal relaxation mode. This new term is however expected to be small in metals and in particular in Ba due to the value of γ_0 close to 1, where γ_0 is the ratio between the specific heats at constant pressure and at constant volume. It was also mentioned that for higher values of q the coupling to other

non-hydrodynamic modes (either relaxing or propagating, for instance, heat waves) could possibly be deemed responsible for further bending up of the dispersion relation outside the long-wavelength region, as was indeed observed even when the small-q term was negative.

We have performed a viscoelastic-GCM analysis of our results. Of course this cannot capture all the details of the dynamics, since thermal effects are always present, but within AIMD calculations it is not clear how to pursue a thermoviscoelastic-GCM study, because it is not possible to assign a portion of the total energy to each particle. However, we expect to obtain the correct trends and be able to analyze the origin of the positive dispersion. The viscoelastic GCM approach comes down to diagonalizing a 3×3 matrix

$$T(q) = \begin{pmatrix} 0 & -\mathrm{i}\sqrt{M_0} & 0 \\ -\mathrm{i}\sqrt{M_0} & 0 & -\sqrt{N_0} \\ 0 & \sqrt{N_0} & \dfrac{M_0 + N_0}{M_0 \tau} \end{pmatrix} \quad (6)$$

where $\tau = \tau(q) = \int_0^\infty \mathrm{d}t\, F(q,t)/S(q)$ and $M_0 = M(q,0)$ and $N_0 = N(q,0)$ are the initial values of the first and second order memory functions of $F(q,t)$. Their values are related to the frequency moments of $S(q,\omega)$ and can be directly obtained from the simulations. In particular $M_0 = k_B T q^2/(m S(q))$.

Within this approach, solved perturbatively in the long wavelength region, the expression for the frequency of the propagating modes was found to be [38]

$$\omega(q) = c_0 q \sqrt{1 + \frac{2\beta_{ve}}{c_0} q^2} \approx c_0 q + \beta_{ve} q^3 + \cdots, \quad (7)$$

where

$$\beta_{ve} = \frac{D_L^2}{8c_0}\left(\frac{5 - (c_\infty/c_0)^2}{(c_\infty/c_0)^2 - 1}\right). \quad (8)$$

In these expressions c_0 is the isothermal sound velocity, c_∞ is the elastic (or high frequency) sound velocity and D_L is the kinematic longitudinal viscosity. All of them are obtained from the magnitudes appearing in the matrix $T(q)$ in the limit $q \to 0$, namely,

$$\begin{aligned} M_0 &\to c_0^2 q^2 \\ M_0 + N_0 &\to c_\infty^2 q^2 \\ \tau(q) &\to \tau(0) = D_L/c_0^2 \end{aligned} \quad (9)$$

Within this approach the values obtained for Be, Ca and Ba, normalized to the corresponding isothermal velocities are $\beta_{ve}/c_0 = -0.7, 11.0$ and $11.9\,\text{Å}^2$ respectively. This hints to an increasing positive dispersion from Be to Ba. However, the results do not seem satisfactory, since for Be a negative dispersion appears in the long-wavelength region. The bending up for larger q could be attributed to coupling to other modes, as suggested by Bryk *et al* [38]. We propose alternatively to extend (7) to larger q by substituting the long-wavelength magnitudes by the corresponding q-dependent ones, namely

$$\begin{aligned} c_0 &\to \sqrt{M_0}/q \\ (c_\infty/c_0)^2 &\to \frac{M_0 + N_0}{M_0} \\ D_L &\to \tau(q) M_0/q^2 \end{aligned} \quad (10)$$

In this way, the frequency of the propagating mode turns

$$\omega(q) = \sqrt{M_0}\sqrt{1 + \frac{\tau^2 M_0 (4M_0 - N_0)}{4N_0}}. \quad (11)$$

This expresion leads to several changes in the initially linear dispersion relation. First, the increase in the structure factor appearing in the denominator of M_0 bends down the dispersion. Second, the effects of coupling with other modes appear as the correction term inside the square root and this term is a product of two quantities. The first one, $f_1(q) = \tau(q)^2 M(q,0)/4$, in general decreases mildly from the long-wavelength region towards larger q, with further increase in the region of the main peak of $S(q)$. On the contrary the second factor $f_2(q) = (4M(q,0) - N(q,0))/N(q,0)$ can start at positive (Ca, Ba) or negative (Be) values, but always increases and then decreases, showing a maximum at a certain q-vector. This leads to a maximum in the dispersion relation which, as shown in figure 11 is in qualitative agreement with the simulation result, as we observe an increase in the magnitude of the maximum going from Be to Ba.

We conclude that, at least on a qualitative level, there is no need to invoke further modes that come into play to explain the bending up of $\omega(q)$ after an initially negative dispersion. The most important factor in the evolution with q of the dispersion relation is the term $(4M_0 - N_0)/N_0$ which not only turns negative into positive in Be, but also explains the appearance of a maximum positive dispersion at a certain q in all the systems.

Of course, the agreement is not quantitative for several reasons: first, the lack of thermal variables in the GCM model we have used, which implies the appearance of the isothermal sound velocity instead of the adiabatic one and the absence of kinetic thermal modes that also couple with the hydrodynamic sound mode which give an extra contribution to the modification of the dispersion relation. But we must also mention that the results reported from the simulation are in fact the positions of the maxima of $C_L(q,\omega)$ and these in general are not exactly the same as the frequencies of the propagating modes.

3.3.4. Transverse current correlation functions and shear viscosity. The autocorrelation function of the transverse currents is obtained from the definition

$$C_T(q,t) = \frac{1}{2N}\langle \boldsymbol{J}_T(\boldsymbol{q}, t + t_0) \cdot \boldsymbol{J}_T(-\boldsymbol{q}, t_0)\rangle, \quad (12)$$

and the corresponding spectrum, $C_T(q,\omega)$, as its Fourier Transform. These functions are not accessible experimentally, but they are interesting since they give information about the ability of the system to sustain shear waves. In the hydrodynamic limit this is not possible and $C_T(q,t)$ decays exponentially in time, with a coefficient related to the shear viscosity. In the region of large wavevectors, where the lengthscale is much smaller than the interatomic distances, all the collective magnitudes reduce to the single-particle analogs and in particular $C_T(q,t)$ becomes gaussian in time, again decaying monotonically. However, for intermediate wavevectors, $q_T \leqslant q \leqslant q_m$, the function $C_T(q,t)$ may show
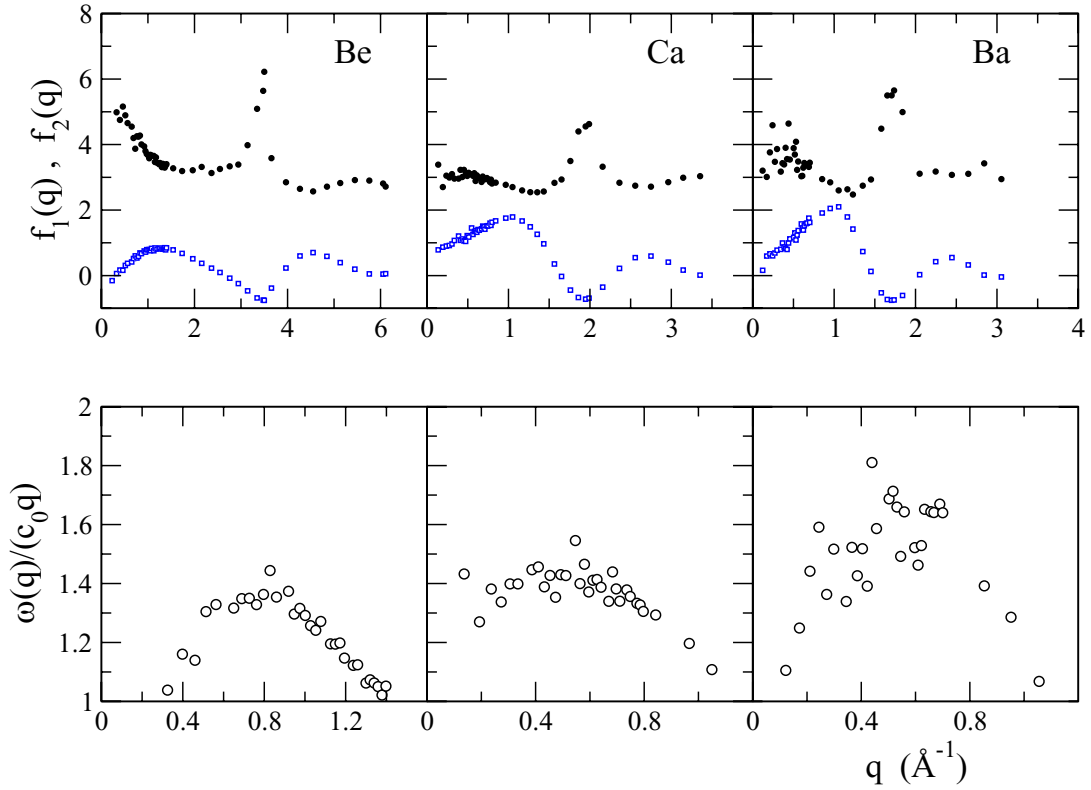
Figure 11. Factors appearing in the viscoelastic GCM dispersion expression; full circles: $f_1(q)$, open squares: $f_2(q)$ (upper panel) and positive dispersion results (lower panel).

some (damped) oscillatory behavior and $C_T(q, \omega)$ may display side peaks, indicative of propagating transverse waves, akin to those appearing in solids. This is indeed the case for the three systems considered in this work, as shown in figures 12–14. The smallest q displayed in each figure is the first one, among those allowed by the periodic boundary conditions and the simulation box, for which side peaks appear in $C_T(q, \omega)$ and we denote the frequencies of these peaks as $\omega_T(q)$. Obviously these q values are therefore larger than the corresponding q_T. We have fitted the dispersion relation for the shear waves in the region where these start appearing, by a linear relation $\omega_T(q) = c_T(q - q_T)$, so as to obtain the value of the effective velocity c_T. The results of the fit, together with the transverse dispersion relation are plotted in figure 15, where we have also included $\omega_L(q)$, $\omega_m(q)$ and the linear dispersion with slope given by c_s as obtained previously.

Such a linear behavior of $\omega_T(q)$ is not backed by theoretical models. For instance, the viscoelastic model for transverse currents [27, 39] leads to a dispersion relation that starts as $\omega_T^v(q) \approx \sqrt{\alpha(q^2 - q_{Tv}^2)}$. This model corresponds to a transverse current correlation function with an exponential memory function, that leads to an expresion for $C_T(q, t)$, as

$$C_T^v(q, t) = C_0 e^{-at}(\cos(t\sqrt{b - a^2}) + a\frac{\sin(t\sqrt{b - a^2})}{\sqrt{b - a^2}}),$$

(13)

where a and b are constants to be fitted and C_0 can either be fitted or taken from the known initial value of the correlation functions.

An expression in terms of two real exponentials is also possible, which should apply for small q, but within the range covered by the present simulations the oscillatory solution describes well the data. In figure 15 we have also included the results obtained from this model. Note that we have plotted the frequencies of the peaks of $C_T(q, \omega)$, which correspond to $\sqrt{b - 2a^2}$, not the frequencies of the transverse modes, i.e. $\sqrt{b - a^2}$ (see discussion in [39]). The viscoelastic dispersion is non-analytic at q_{Tv}; but nevertheless, it is clear that it behaves quasi-linearly in a certain q range above q_{Tv}; it is only when approaching this cutoff q that the viscoelastic dispersion bends down departing from the linear variation.

The range of wavevectors for which shear waves are supported is shown in table 5 and, taking the viscoelastic cutoff q_{Tv} as the lower end of the range, goes from $0.07q_p$ to $2.00q_p$ in Be, from $0.11q_p$ to $2.53q_p$ in Ca and from $0.12q_p$ to $2.34q_p$ in Ba. For larger q values $C_T(q, t)$ evolves smoothly towards a gaussian function. The effective velocity of transverse waves, as obtained from the previous fit near q_T is also shown on table 5. Note that the velocity of transverse waves is smaller than the sound velocity in the case of Be, both are similar in liquid Ca and in Ba the transverse velocity is slightly higher than the longitudinal one. This last aspect is somehow reminiscent of the similar behavior in solid bcc Ba.

The shear viscosity can be obtained from the calculated transverse current correlation functions by considering the area under $C_T(q, t)$ in the limit $q \to 0$. The details of the procedure can be found in [40]. Following this route we have obtained
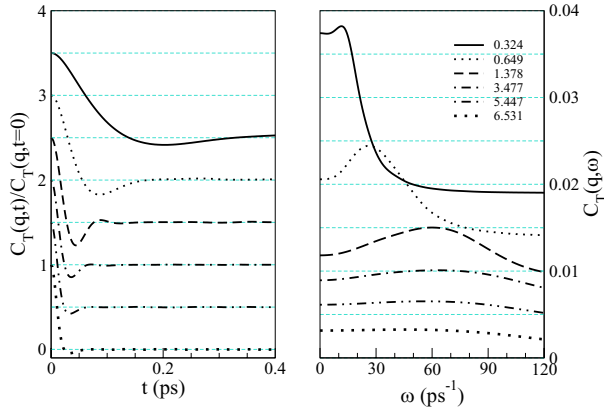
Figure 12. $C_T(q, t)$ and $C_T(q, \omega)$ for selected wavevectors (shown in Å^{-1}) in liquid Be.
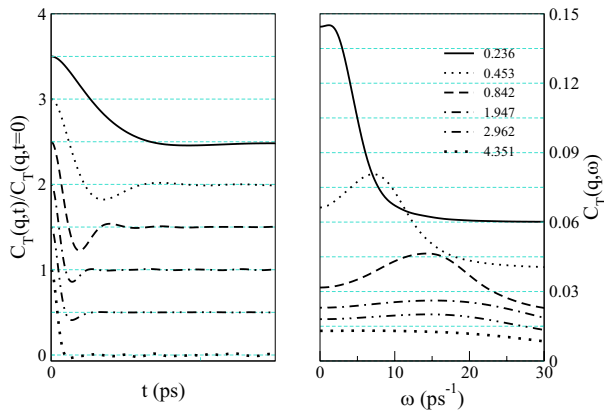
Figure 13. $C_T(q, t)$ and $C_T(q, \omega)$ for selected wavevectors (shown in Å^{-1}) in liquid Ca.
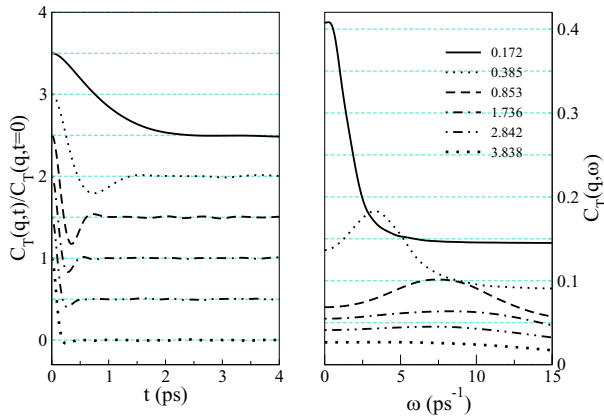
Figure 14. $C_T(q, t)$ and $C_T(q, \omega)$ for selected wavevectors (shown in Å^{-1}) in liquid Ba.

the shear viscosity coefficients displayed in table 4, where we observe a good agreement with experiment in the cases of Ca and Ba (no experimental data exist for Be).

Within the context of the Brownian motion of a macroscopic particle of diameter σ in a liquid of shear viscosity η at a temperature T, the Stokes–Einstein relation links the difusion coefficient of the particle, D and the shear viscosity
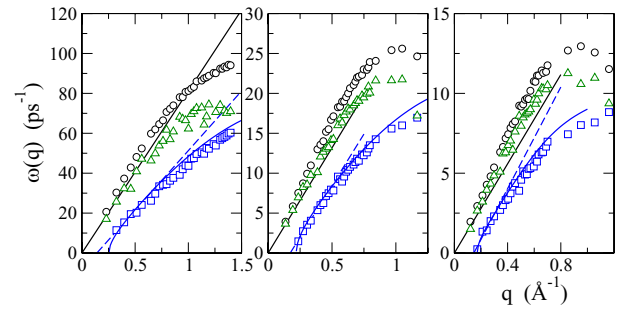
Figure 15. Dispersion relations for liquid Be (left), Ca (center) and Ba (right). Circles denote $\omega_L(q)$, up triangles are $\omega_m(q)$ and squares $\omega_T(q)$. The straight lines are the linear fits to the data as described in the text. The curved lines correspond to the dispersion of shear waves as obtained from the viscoelastic model.

of the liquid η: $\eta D = k_B T / (2\pi\sigma)$. This relation has often been applied to obtain an estimation of D or η of a given liquid identifying one of the atoms as the particle under Brownian motion, assuming in this case that the atomic diameter is given by the position of the maximum of $g(r)$. From the diffusion coefficients and pair correlation functions determined above, we have evaluated the shear viscosity predicted by the Stokes–Einstein relation. The results are also shown in table 4 and reveal a large underestimation of η in the case of Be, with better results for Ca and especially for Ba, where the Stokes–Einstein expression produces a good estimate. The Stokes–Einstein relation is well known to break down in undercooled liquids near the glass transition, but this is not the case in the studied thermodynamic state of Be. Certainly Be is the smallest atom and this could be the reason for the large error obtained through the use of this approximate expression, but nevertheless a more detailed study of the influence of atomic size on the validity of the Stokes–Einstein relation would be in order.

3.4. Damping mechanisms for collective excitations

The analysis of the physical mechanisms that govern the propagation and dissipation of a perturbation of the liquid that couples to the collective microscopic density are usually analyzed in by resorting to the second order memory function of the intermediate scattering function. These were introduced through the Mori–Zwanzig formalism, but are most easily described in Laplace space. The first, second, $\cdots$, order memory functions of $F(q, t)$ can be obtained from the relations

$$\tilde{F}(q, z) = \frac{F(q, t = 0)}{z + \tilde{M}(q, z)},$$
$$\tilde{M}(q, z) = \frac{M(q, t = 0)}{z + \tilde{N}(q, z)}, \cdots \qquad (14)$$

The initial values $F(q, 0) = S(q)$ are obtainable from the atomic positions in the simulations and the initial values of the n-th order memory function are also computable in terms of the atomic positions and their derivatives up to order n.

The hydrodynamic model plays a central role in the theoretical studies of the dynamics of liquids. It applies in the long wavelegth regime, for $q \rightarrow 0$ and states that collective
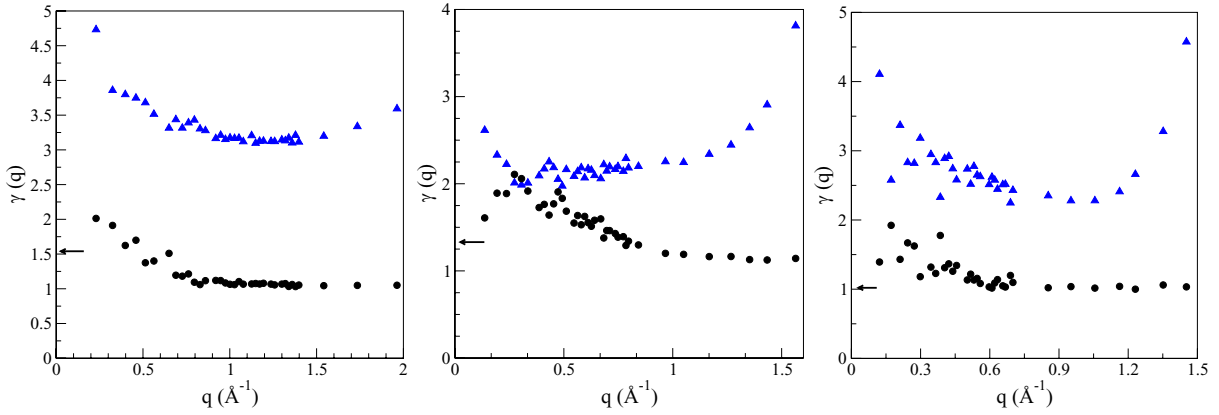
Figure 16. $\gamma(q)$ as obtained from the GVM (triangles) and the GHM (circles) in liquid Be (left), Ca (center) and Ba (right). The arrows indicate the experimental values of γ_0.

density fluctuations propagate as pressure waves, damped through longitudinal viscous processes and dissipate entropy, through thermal relaxations; the former are responsible for the side peaks in the dynamic structure factor, while the latter are resposible for the quasielastic central peak. These two mechanisms appear in $N(q, t)$ as a sum of two contributions, namely, an instantaneously decaying (Dirac-δ like) viscous term and an exponentially decaying term whose decay rate is related to the thermal diffusivity.

Aiming to extend the model outside the hydrodynamic regime, the generalized hydrodynamic model (GHM) introduces q dependent thermophysical quantities, which in the limit $q \to 0$ recover their hydrodynamic values, but also replaces the instantaneus viscous decay by a fast viscoelastic exponentially decaying function that takes into account the possible elastic response of the liquid to a perturbation of shorter wavelengths. So we can define the GHM as describing $N(q, t)$ as a sum of a fast-decaying exponential corresponding to viscoelastic processes and a slowly-decaying exponential corresponding to thermal processes.

This approach was successful to describe the dynamics of dense gases, but was questioned in the case of liquid metals, where the thermal diffusivity is very high due to the electronic contribution to this magnitude, so that it may happen that the fast processes are in fact thermal in nature, while the slow processes would be the viscoelastic ones [42]. This has been in fact a debated point, as it was suggested that it is only the ionic contribution to thermal diffusivity that should be taken into account and this is two orders of magnitude smaller [43]. In any case this model is analytically identical to the generalized hydrodynamic one, but the physical interpretation is certainly different. We refer to this as a generalized viscoelastic model (GVM). Incidentally, a purely viscoelastic model amounts to the neglect of the thermal term, so that $N(q, t)$ has a single exponential term of viscoelastic origin.

Therefore both in the GHM and in the GVM we have

$$N(q, t) = a_s \mathrm{e}^{-t/\tau_s} + a_f \mathrm{e}^{-t/\tau_f} , \qquad (15)$$

but in the GHM we identify the slow (s) term with thermal processes and the fast (f) one with viscoelastic processes,

so that

$$a_s^{\mathrm{GHM}} = (\gamma(q) - 1)M(q, 0), \quad \tau_s^{\mathrm{GHM}} = (\gamma(q)D_T(q))^{-1} ,$$

$$a_f^{\mathrm{GHM}} = N(q, 0) - (\gamma(q) - 1)M(q, 0), \quad \tau_f^{\mathrm{GHM}} = \tau_v(q) ,$$

whereas in the GVM the opposite identification is made, namely,

$$a_s^{\mathrm{GVM}} = N(q, 0) - (\gamma(q) - 1)M(q, 0), \quad \tau_s^{\mathrm{GVM}} = \tau_v(q) ,$$

$$a_f^{\mathrm{GVM}} = (\gamma(q) - 1)M(q, 0), \quad \tau_f^{\mathrm{GVM}} = (\gamma(q)D_T(q))^{-1} .$$

In the hydrodynamic region the q-dependent magnitudes introduced in these equations should reduce to the expressions given by the hydrodynamic model, namely, $\gamma(q) \to \gamma_0 = C_p/C_v$, the ratio of specific heats at constant pressure and at constant volume and $D_T(q) \to D_T q^2$, where D_T is the thermal diffusivity.

The second order memory functions that we have computed from the simulated OF-AIMD $F(q, t)$ have been found to be best described by the sum of two exponential functions in the cases of Be and Ba. The fast term in the $N(q, t)$ of liquid Ca could not be modeled properly using an exponential function, so we used a gaussian function instead. For this reason we will focus our analysis on the behavior of the slow term, in particular its variation with q. Note that within the GHM, we can obtain

$$\gamma^{\mathrm{GHM}}(q) = 1 + \frac{a_s}{M(q, 0)} , \qquad (16)$$

whereas in the case of the GVM

$$\gamma^{\mathrm{GVM}}(q) = \frac{N(q, 0) + M(q, 0) - a_s}{M(q, 0)} \qquad (17)$$

In figure 16 we show the q variation of $\gamma^{\mathrm{GHM}}(q)$ and $\gamma^{\mathrm{GVM}}(q)$ as obtained from each of the models. We expect that the more accurate model will produce a $\gamma(q)$ that goes smoothly to the experimental value of γ_0 as q decreases (1.54 for Be, 1.33 for Ca and 1.02 for Ba) [37]. Moreover, some direct calculations of $\gamma(q)$ have been performed through CMD for liquid metals whose interactions were modeled through pair potentials (Li, Pb and Bi) or embedded-atom potentials (Fe), by studying

the correlation functions of energy fluctuations [44]. These studies have produced $\gamma(q)$ that decreases from γ_0 at $q = 0$ to values close to one for $q \approx q_p/2$ and increases for larger q. From the results shown in figure 16 we conclude that the GHM leads to more consistent results both for the variation with q and especially for the limit $q \to 0$. Therefore we conclude that the slow term in $N(q, t)$ corresponds to thermal relaxation, whereas the fast one is the viscoelastic term. This interpretation is common to all the alkaline earths considered here and moreover a similar analysis of the previous results for liquid Mg leads to the same conclusion. This type of behavior has also been recently found in liquid Bi, which is in any case a bad metal. However these results suggest that a more detailed studied is needed concerning whether or not the electronic contribution to thermophysical properties has to be taken into account for the study of the ionic dynamics.

4. Conclusions

We have developed a method to refine the construction of local pseudopotentials for use within OF-DFT strategies, by applying a force-matching criterion to configurations obtained in KS calculations. The method has proved to be quite successful in reproducing KS-calculated magnitudes.

Concerning the alkaline-earth liquid metals studied, we have found a rather common behavior in most of the aspects studied. All the systems present an asymmetric second peak akin to that exhibited by liquid transition metals. They all show a large abundance of five-fold symmetry local structures, although they also have around 15–20% of local structures reminiscent of the phase from which they melt. Their single-particle dynamics is quasi-universal if the time is scaled properly in terms of the Einstein frequencies. Concerning collective dynamic properties, we have observed a large degree of positive dispersion for all the systems, which increases with atomic size, attaining rather high values, more than 30%, in liquid Ba. All the systems support shear waves in a similar q-range relative to the main peak of $S(q)$. Finally, in all the systems the collective excitations are damped through slow thermal relaxations and fast viscoelastic ones.

The comparison with experimental data, whenever they are available, is rather satisfactory, concerning static structural properties, transport coefficients like the shear viscosity and dynamic properties as the sound velocity (slightly underestimated in the case of Ca).

Nevertheless some peculiarities of the different systems must be mentioned. Liquid Be has an exceptionally high sound velocity, well accounted for by the present simulations and this is the only experimental result available. In liquid Be we also observe a large violation of the Stokes–Einstein relation between diffusion and shear viscosity, which deserves future analysis. In Ca we find that the fast component of the second order memory function is not well described by an exponential function. This may be related to the fact that the analytical form of an exponential is intrinsically wrong at short times, where the dynamic functions vary quadratically with time; this again deserves further studies in order to use functions that satisfy this requirement at short times but turn

into exponential functions for longer times. Finally, in liquid Ba, the amount of positive dispersion is the largest one found so far by MD simulations for a liquid metal near its triple point. We analyzed this behavior approximately in the light of the viscoelastic GCM approach and found that it can be related to the behavior of a factor that involves the frequency moments, which shows a maximum of incrasing amplitude when going from Be to Ba. We note that this factor involves only static magnitudes and coming from a viscoelastic approach, indicates that the most important reason for the behavior of the dispersion relation is the coupling of the sound mode with structural relaxation. We also found that, even though the dispersion of the frequencies of shear waves is non-analytic at the onset of their appearance, it becomes quasi-linear later and an effective velocity of transverse waves can be defined. For liquid Ba, this velocity was found to be rather large, in fact larger than the sound velocity, which is probably reminiscent of the similar behavior in solid bcc Ba.

Acknowledgments

References

[1] Martin A J and Moore A 1959 *J. Less-Common Met.* **1** 85
[2] Robert G, Legrand P and Bernard S 2010 *Phys. Rev.* B **82** 104118
Luo F, Cai L-C, Chen X-R, Jiang F-Q and Alfè D 2012 *J. Appl. Phys.* **111** 053503
[3] Lazicki A, Dewaele A, Loubeyre P and Mezouar M 2012 *Phys. Rev.* B **86** 174118
[4] Boivineau M, Arles L, Vermeulen J M and Thevenin Th 1993 *Int. J. Thermophys.* **14** 427
[5] Errandonea D, Meng Y, Häusermann D and Uchida T 2003 *J. Phys.: Condens. Matter* **15** 1277
[6] Tahara S, Fujii H, Yokota Y, Kawakita Y, Kohara S and Takeda S 2006 *Physica* B **385/386** 219
[7] Waseda Y 1980 *The Structure of Non-Crystalline Materials* (New York: McGraw-Hill)
[8] Kawakita Y, Hosokawa S, Enosaki T, Ohshima K, Takeda S, Pilgrim W C, Tsutsui S, Tanaka Y and Baron A Q R 2003 *J. Phys. Soc. Japan* **72** 1603
[9] Sengül S, González D J and González L E 2009 *J. Phys.: Condens. Matter* **21** 115106
[10] Fujihisa H, Nakamoto Y, Sakata M, Shimizu K, Matsuoka T, Ohishi Y, Yamawaki H, Takeya S and Gotoh Y 2013 *Phys. Rev. Lett.* **110** 235501
[11] McMahon M I, Bovornratanaraks T, Allan D R, Belmonte S A and Nelmes R J 2000 *Phys. Rev.* B **61** 3135
[12] Nelmes R J, Allan D R, McMahon M I and Belmonte S A 1999 *Phys. Rev. Lett.* **83** 4081
[13] Errandonea D, Boehler R and Ross M 2001 *Phys. Rev.* B **65** 012108
[14] Yoneda A and Endo A 1980 *J. Appl. Phys.* **51** 3216
Winzenick M and Holzapfel W B 1997 *Phys. Rev.* B **55** 101

[15] Mizuki J, Chen Y, Ho K-M and Stassis C 1985 *Phys. Rev. B* **32** 666

[16] Chen Y, Ho K M, Harmon B N and Stassis C 1986 *Phys. Rev. B* **33** 3684

[17] Sani L, Bove L E, Scopigno T, Petrillo C and Sacchetti F 2010 *XIV Liquid and Amorphous Metals conf. (Rome, 11–16 July 2010)*

[18] González L E, Meyer A, Íñiguez M P, González D J and Silbert M 1993 *Phys. Rev. E* **47** 4120

[19] Alemany M M G, Casas J, Rey C, González L E and Gallego L J 1997 *Phys. Rev. E* **56** 6818

[20] Wax J F, Albaki R and Bretonnet J L 2000 *Phys. Rev. B* **62** 14818

[21] de Wijs G A, Pastore G, Selloni A and van der Lugt W 1995 *Phys. Rev. Lett.* **75** 4480

[22] Hansen J P and McDonald I R 1986 *Theory of Simple Liquids* (London: Academic)

[23] Mryglod I M, Omelyan I P and Tokarchuk M V 1995 *Mol. Phys.* **84** 235
Bryk T 2011 *Eur. Phys. J. Spec. Top.* **196** 65

[24] Zwanzig R 1960 *J. Chem. Phys.* **33** 1338
Zwanzig R 1961 *Phys. Rev.* **124** 983
Mori H 1965 *Prog. Theor. Phys.* **33** 423
Mori H 1965 *Prog. Theor. Phys.* **34** 399

[25] Götze W and Lücke M 1975 *Phys. Rev. A* **11** 2173
Ernst M H and Dorfman J R 1975 *J. Stat. Phys.* **12** 311
de Schepper I M and Ernst M H 1979 *Physica* A **98** 189

[26] Sjögren L and Sjölander A 1979 *J. Phys. C: Solid State Phys.* **12** 4369
Sjögren L 1980 *J. Phys. C: Solid State Phys.* **13** 705
Sjögren L 1980 *Phys. Rev. A* **22** 2866
Sjögren L 1980 *Phys. Rev. A* **22** 2883

[27] Balucani U and Zoppi M 1994 *Dynamics of the Liquid State* (Oxford: Clarendon)

[28] Casas J, González D J and González L E 1999 *Phys. Rev. B* **60** 10094
Casas J, González D J, González L E, Alemany M M G and Gallego L J 2000 *Phys. Rev. B* **62** 12095

[29] Lovesey S W 1971 *J. Phys. C: Solid State Phys.* **4** 3057
Levesque D, Verlet J and Kurkijarvi J 1973 *Phys. Rev. A* **7** 1690
Scopigno T, Balucani U, Ruocco G and Sette F 2000 *J. Phys.: Condens. Matter* **12** 8009

[30] Hohenberg P and Kohn W 1964 *Phys. Rev.* **136** B864

[31] Chen Y, Ho K M and Harmon B N 1988 *Phys. Rev. B* **37** 283

[32] Kohn W and Sham L J 1965 *Phys. Rev.* **140** A1133

[33] González D J, González L E, López J M and Stott M J 2002 *Phys. Rev. B* **65** 184201

[34] Rappe A M, Rabe K M, Kaxiras E and Joannopoulos J D 1990 *Phys. Rev. B* **41** 1227

[35] Louie S G, Froyen S and Cohen M L 1982 *Phys. Rev. B* **26** 1738

[36] Honeycutt J D and Andersen H C 1987 *J. Phys. Chem.* **91** 4950

[37] Blairs S 2007 *Int. Mater. Rev.* **52** 321

[38] Bryk T, Mryglod I, Scopigno T, Ruocco G, Gorelli F and Santoro M 2010 *J. Chem. Phys.* **133** 024502

[39] Murillo M S 2000 *Phys. Rev. Lett.* **85** 2514

[40] Palmer B J 1994 *Phys. Rev. E* **49** 359
Balucani U, Brodholt J P, Jedlovszky P and Vallauri R 2000 *Phys. Rev. E* **62** 2971
Puscasu R M, Todd B D, Daivis P J and Hansen J S 2010 *J. Phys.: Condens. Matter* **22** 195105

[41] Shimoji M and Itami T 1986 *Atomic Transport in Liquid Metals* (Switzerland: Trans Tech Publications)

[42] Scopigno T, Ruocco G and Sette F 2005 *Rev. Mod. Phys.* **77** 881

[43] Singh S and Tankeshwar K 2004 *Phys. Rev. E* **70** 013202

[44] Canales M, González L E and Padró J A 1994 *Phys. Rev. E* **50** 3656
Bryk T and Mryglod I 2000 *J. Phys.: Condens. Matter* **12** 3543
Bryk T and Mryglod I 2001 *J. Phys.: Condens. Matter* **13** 1343
Bryk T and Mryglod I 2001 *Phys. Rev. E* **63** 051202
Bryk T and Belonoshko A B 2012 *Phys. Rev. B* **86** 024202

5.2 GLOBALLY OPTIMIZED LOCAL PSEUDOPOTENTIALS

Orbital-free density functional theory (OFDFT) has been increasingly employed in the study of solid and liquid materials. Local pseudopotentials (LPSs) representing the elec-tron-ion interactions play an important role in ensuring accuracy of the simulations, while keeping computational costs manageable. As a collaboration with Prof. Carter's group at Princeton University we have developed a global optimization strategy for LPSs that enables OFDFT to reproduce solid and liquid properties obtained from Kohn-Sham density functional theory (KSDFT). We show that our global fitting or refitting of LPSs yields superior reproduction of fitted properties and also retains or improves predictions of independent test properties. Our optimization strategy can fit arbitrary properties from both solid and liquid phases, so the resulting globally optimized local pseudopotentials (goLPSs) can be used in solid and/or liquid phase simulations depending on the fitting process. We show three test cases proving that we can 1) improve solid properties compared to our previous bulk local pseudopotential (BLPS) generation scheme; 2) refine predicted liquid and solid properties by adding force matching (FM) data; and 3) generate a from-scratch, accurate goLPS from the local channel of a non-local pseudopotential (NLPS). The proposed scheme therefore serves as a full and improved LPS construction protocol.

5.2.1 *Introduction*

In recent years, orbital-free density functional theory (OFDFT) [1, 95] has attracted increasing interest due to its huge advantage in numerical simplicity and efficiency. OFDFT can be made to scale quasi-linearly with system size with a small prefactor, thus enabling otherwise unfeasible large-scale first-principles simulations with higher-scaling orbital-based approaches such as conventional Kohn-Sham density functional theory (KSDFT) [2]. For example, researchers simulated the plastic deformation of aluminum (Al) nanowires [134]; studied complex magnesium (Mg)-Al intermetallic compounds [135], free liquid metal surfaces [55, 136], and metal grain boundaries [137]; and have reported OFDFT benchmark calculations for over one million metal atoms [138, 139]. Some orbital-based linear-scaling methods have been developed typically using localized orbitals but are limited to materials with band-gaps [140–142], whereas OFDFT thus far primarily occupies the complementary application space of metallic systems.

OFDFT and KSDFT differ in two fundamental aspects. First, OFDFT approximates the kinetic energy of electrons using a KEDF [95], while KSDFT adopts KS orbitals to exactly evaluate the non-interacting electron kinetic energy. OFDFT uses the electron density as its sole variable without a need for orbitals. This enormous simplification significantly increases the number of atoms that may be treated as no expensive matrix diagonalization and orbital orthonormalization are required. Much research thus centers around accurately reproducing the KS kinetic energy with a KEDF [95, 110, 113, 114, 119, 143–147]. Second, although NLPSs [126] or projector-augmented-wave (PAW) potentials [148, 149] are typically used in periodic KSDFT to accurately describe electron-ion interactions, pure OFDFT must utilize LPSs since no orbitals are available to use with the orbital-based, non-local projectors present in NLPS schemes. A LPS therefore must be carefully constructed and tested. Its goal is similar to that of KEDF construction: to match an electronic density obtained with the LPS to a NLPS KSDFT benchmark for one or more bulk solid [150, 151] or liquid [96, 152] references. This procedure ensures good agreement for typical solid observables such as the bulk modulus, cell volume, and energy per atom, or good static and dynamic properties for the liquid observables. However, until now there has been no construction procedure that guarantees a correct representation of both phases.

In this thesis, we present a systematic way to obtain LPSs designed to reproduce a variety of properties in both liquid and solid phases, thereby achieving transferability between phases. Moreover, since this new method does not require a good initial guess for the LPS, we can replace the previous bulk-derived local pseudopotential (BLPS) construction scheme entirely by using the local channel of a NLPS as the initial guess for our procedure.

We introduce the LPS theory and implementation of the algorithm in section 5.2.2. The advantages of using globally optimized LPSs (goLPSs) are discussed in section 5.2.3. We parametrize the goLPSs against different reference data sets, showing their capability to both directly improve the agreement with reference data as well as be

transferable enough so that it is superior for other, non-fitted properties. We demonstrate this approach for three separate elements each with different valencies: gallium (Ga), lithium (Li), and calcium (Ca). For Ga, we improve upon an earlier BLPS [144] for solid-state properties by optimizing against α-Ga and β-Ga solid properties. We also test its transferability by comparing bulk properties for other solid phase structures: I-43d [220] (Ga-II) and I4/mmm [139] (Ga-III). For Li, we improve both solid and liquid properties by adding FM [153] to KSDFT-PAW atomic forces from liquid phase configurations into the fit. For Ca, we construct the LPS directly from the local channel of the NLPS. We also optimize the LPS against body-centered-cubic (bcc) and face-centered-cubic (fcc) solid phase properties and benchmark quality against simple cubic (sc) and cubic diamond (cd) properties to test transferability. We draw conclusions in section 5.2.4.

5.2.2   *Theory and Algorithms*

LPSs and their use in OFDFT

There are two major differences between OFDFT and KSDFT: 1) the use of a KEDF to evaluate the kinetic energy directly from the electronic density compared to the sum of the expectation values of KS orbitals, and 2) the use of a LPS for the core electrons compared to the typically employed NLPSs or PAW potentials in KSDFT. The overall accuracy of OFDFT compared to KSDFT thus only depends on the accuracy of the KEDF and the pseudopotential (PP) used. In this contribution, we do not discuss the KEDF aspect in detail, as our focus here is on improving LPSs. We simply assume that the employed KEDF can provide a reliable mapping of the electron density to the kinetic energy and its potential (density functional derivative) for the liquid and solid systems studied here. We refer to the literature for a more in-depth discussion of the design and application of KEDFs [95, 110, 113, 114, 119, 143–147].

   Several protocols have been devised to generate good LPSs for use in OFDFT simulations, some of which include: atomic LPSs (ALPSs), based on a KS valence electron density for an atom [150] that suffer a lack of transferability and sufficient accuracy when applied to crystals; BLPSs [131, 150, 151, 159], most commonly used for solid-state applications, although they have been successfully applied to liquid Li [159–161]; and the NPA [96, 152, 162–165] method most commonly used in liquid metals studies [55, 96, 136, 152, 166, 167]. However, all current methods are inaccurate when trying to represent phases different from the one used for their construction. BLPSs take into account discrete environments of atoms in different solid structures. This is due to the method following their construction that uses as a reference only one or two atoms in defined crystalline positions. The NPA method takes one atom as a reference model and aims to mimic the environment that such an atom actually finds in a liquid, again including a discrete environment for the atom. One such attempt to solve this problem in liquids was carried out by introduction of the FM method [153]. FM can produce more accurate LPSs for the liquid state, but it unfortunately fails for solids. An ideal scheme for transferable LPS construction therefore should account for the presence of surrounding atoms either implicitly (via various physical properties) or explicitly (via direct calculation of forces) in both the solid and liquid states.

BLPSs and force matching

The method used to construct a BLPS is based on previous work by Zhou *et al.* [150], where a converged KSDFT-NLPS valence electron density is used as input to invert the KSDFT equations utilizing the exact non-interacting kinetic energy operator. A local KS effective potential thus is derived, thereby reproducing this valence electron density, as formally guaranteed by the first Hohenberg-Kohn theorem [1]. Subsequently, this potential is unscreened by removing the Hartree electron repulsion and XC potentials to obtain the ionic external potential. The valence electron density is generated in a bulk crystalline environment [131, 150, 151, 168], so the bulk crystal's structure factor is needed to further convert the total ionic external potential into an atom-centered ionic potential, which is the BLPS of that atom. Zhou *et al.* demonstrated for silicon (Si) that the Si BLPS is more transferable than the Si LPS built from the valence electron density of simply a Si atom. Two free-fitting parameters are tuned in the BLPS construction procedure: 1) the value of the non-Coulombic part of the BLPS in reciprocal space at q=0, namely, $v_{nc}^{BLPS}(q = 0)$; and 2) r_c as the point beyond which the Coulombic tail is enforced onto

the BLPS in real space, namely, $v^{BLPS}(r)$. However, deficiencies remained, such as incorrect energy ordering between β-tin and bct5 Si and between bcc and fcc Si, as well as the necessity to use a very large plane-wave kinetic energy cutoff [150, 151].

To address these problems, two adjustments were introduced by Huang and Carter [151], both of which improve on how the tails of the BLPS are handled in real and reciprocal space. These improvements include 1) the introduction of a cutoff function multiplying $v^{BLPS}(q)$ to reduce the oscillating tail in real space; and 2) a systematic means to determine r_c . The two free parameters, $v_{nc}^{BLPS}(q=0)$ and r_c, are fitted by hand while comparing the resulting bulk moduli, equilibrium volumes, and relative energies to those obtained using a NLPS with a KSDFT method. Apart from being a cumbersome way to obtain a LPS, our preliminary findings using such BLPSs in the study of liquids reveal poor transferability for non-alkaline elements, predicting too-high melting points and too-low diffusion coefficients compared to experiment.

A possible solution to this problem could be using the FM method [153], where a KSDFT molecular dynamics (KSDFT-MD) simulation of the liquid is performed on a small sample over a short simulation time. The properties obtained during these runs are used as a training set in developing the LPS. In particular, the forces on the atoms are used because they determine the dynamic evolution of the system and consequently its static and dynamic structural and transport properties. We therefore collect the forces acting on each of the atoms after initial equilibration of the KSDFT-MD simulations, when the atomic configurations are typical of a liquid sample. In the second step of the FM-LPS construction, we take several atomic configurations from the KSDFT-MD run and compute the forces acting on the atoms with OFDFT and a LPS. The OFDFT forces are usually quite similar to the KSDFT ones. However, the match can be improved by modifying the LPS through the addition of Gaussians, where the amplitudes, widths, and positions are taken as parameters to be fitted so as to minimize the difference between OFDFT and KSDFT forces. This modification is performed on the non-Coulombic part of the LPS in reciprocal space:

$$v_{nc}^{new}(q) = v_{nc}^{old}(q) + \sum_{i=1}^{N} a_i \quad e^{-b_i(q-c_i)^2} \tag{151}$$

where v_{nc}^{new} stands for the modified LPS; v_{nc}^{old} is the initial LPS; and a_i, b_i and c_i are the respective amplitudes, widths, and positions of each Gaussian added to v_{nc}^{old}. Again, this process is manual and cumbersome, requiring expert knowledge and iterative improvement of the FM-LPS construction until an arbitrary, subjective target is met. We can arrive at a good liquid representation by solely performing a FM method on the BLPS, but we find that representability of solid phases is sacrificed along the way.

Global optimization and evolutionary algorithms

Prior application of FM to improve PPs has shown that optimizing the location, width, and magnitude of Gaussian functions manipulating an initial guess is sufficient to significantly improve the agreement of LPS-based OFDFT simulations with NLPS-based KSDFT ones for liquid properties. A multitude of possible solutions will arise for any non-trivial number of Gaussian functions. Even without a formal proof of non-deterministic polynomial-time hardness (NP-hardness), global optimization techniques such as evolutionary algorithms (EAs) or genetic algorithms (GAs) have proven their worth for such optimization problems [169, 170]. We hence propose to use EAs as implemented in the ogolem framework [171–173] to optimize the Gaussian variables globally and arrive at a goLPS.

A short introduction to EAs as implemented in a pool-based incarnation in the ogolem framework will be given here; for more detailed explanations, we refer to the literature [174–176]. It has been candidly argued before that the standard language used to describe this class of heuristic global optimization strategies is needlessly and sometimes misleadingly biological in nature [177, 178]. We agree with this assertion and will keep the biological language to a minimum in the following.

To apply EAs, the optimization problem first needs to be encoded as a solution string, the genome. A candidate solution is defined by its solution string and fitness value, a number of which form a solution pool. Two known

solutions will be taken from the pool and undergo a series of operations to generate new solution candidates. First, part of the genome is exchanged to mix existing solution knowledge. New solution knowledge is then added with a certain probability by randomly changing small parts of the genome. Only the latter operation allows for truly unknown parts of the search space to be explored. The resulting new pair of candidates can be completed by either evaluating an objective function (the fitness function) or optimizing their genome with respect to said fitness function by means of local exploration.

It is commonly accepted that hybrid, local-global optimization techniques, i.e., those coupling global search space exploration with local minimum exploitation, are vastly superior in convergence behavior to pure global optimization algorithms [179]. However, local exploitation typically relies on gradient information that can be tedious to obtain. We have positive experience with and therefore have long advocated the use of trust region methods, such as Powell's Bound Optimization BY Quadratic Approximation (BOBYQA) [180]. We employ these methods in an altered version of the Apache Commons implementation [181].

Next, the candidate solution with the better (by definition, lower) fitness will be attempted to be added to the pool. The solution will be accepted only if it is a sufficiently unique new one (determined by a diversity criterion) and its fitness value is better than the worst candidate in the pool. This entire cycle is repeated numerous times until the solution pool is deemed converged. To apply these global optimization techniques to the problem of LPS creation, we need to first encode the problem as a genome and then define a fitness function as a metric of LPS quality, which will be discussed next.

Property-based LPS optimization

Encoding the optimization problem as a genome is relatively straightforward: similar to the FM approach, we define the location, width, and magnitude of the Gaussian manipulators for a given initial guess LPS as the real-numbered genome. The fitness function definition is also straightforward in formulation:

$$F_{cand} = \sum_i^{N_p} w_i \cdot \Delta(P_{i,ref} - P_{i,cand})^{e_i} \tag{152}$$

where the fitness of a given candidate LPS is defined as the sum of weighted differences Δ between a reference value for a property and its value with the candidate LPS . The importance of different reference properties for the fit is included with a weight and an exponent per term. Terms typically should be weighted so that the value and scaling of their differences are of similar numerical magnitude. If terms are found to compete, weighting them to prefer one over the other is not advisable as such competition indicates a lack of transferability for the underlying KEDF and thus OFDFT method.

Note that it would be theoretically feasible and arguably more generic to obtain the goLPS at the KSDFT level, i.e., one would evaluate the candidate properties on the KSDFT/LPS level, compare them to reference values from a KSDFT/NLPS or KSDFT/PAW simulation, and then minimize the difference. Such an approach would remove the KEDF dependency from the fitting, eliminating the risk of KEDF-specific fitting artifacts. However, our fitting will be based on the OFDFT level of theory with a selected KEDF, given the vastly higher computational footprint of a KSDFT calculation for any system compared to the equivalent OFDFT one. Candidate properties will be obtained from OFDFT computations and compared to KSDFT reference property values that are obtained with either a NLPS or PAW potential. The KEDF therefore must be chosen appropriately to minimize fitting artifacts originating from an unphysical description of the system. At no point should there be compensation for a bad KEDF description with an unphysical LPS. On the contrary, we argue that our fitting scheme and subsequent benchmarks will clearly reveal bad KEDF approximations. We currently limit our optimization to one element at a time to decouple the optimization problems. However, no principal restriction exists to forbid the optimization of multiple LPSs at the same time.

After a sufficient number of property evaluations with OFDFT, local optimizations of the Gaussian variables, and cycles through the EA we obtain a pool of low-fitness candidate solutions for the global minimum. Each

of these candidates represents a possible set of Gaussian manipulations of the initial LPS, providing maximal agreement of the properties obtained with OFDFT compared to KSDFT for a given KEDF.

We hence trade a deterministic fitting scheme (BLPSs) for a heuristic one (goLPS), offering substantial benefits. First and foremost, the goLPS scheme permits (re)shaping a given LPS to improve the quality of an OFDFT prediction of one or more given properties. It is systematic insofar as the quality and applicability of the resulting goLPS depends only on the property space covered by the references, assuming a properly converged fit. As long as the KEDF is capable of appropriately describing the physics of interest, fitting against solid properties will improve the agreement of OFDFT with the reference KSDFT for solid properties. Likewise, fitting against liquid properties will improve the agreement for those as well. Fitting against both properties will allow the LPS to properly describe liquid and solid states and, ideally, solid-liquid phase transitions.

Our proposed fitting scheme offers another indirect benefit in that it scales very well with available computational resources. While previous standard fitting schemes will simply speed up when provided with more computational resources, our scheme will actually improve the quality of the solution. Longer runs will ensure that the globally optimal solution will be found reliably, while the addition of more complicated properties into the fit will extend the applicability of the goLPS. In a world of ever-increasing computational resources, we consider this feature to be extremely beneficial. The implementation has been carried out within the ogolem framework and is freely available under the BSD 4-clause license via https://www.ogolem.org.

Three questions remain, which we will answer in the following: 1) What level of agreement within the KSDFT reference data can be achieved through the automatic global optimization of Gaussian-based manipulations of an initial LPS? 2) How transferable are such goLPSs to situations for which they have not been optimized? And 3) how large of a modification is possible and still beneficial, and how relevant is an initial guess for the quality of the resulting goLPS?

5.2.3 *Globally Optimized LPSs*

Here, we provide three examples to showcase all of the important advantages of our goLPS algorithm. First, the initial BLPS of Ga was optimized for the solid phases α-Ga and β-Ga [144]. We evaluated its quality and transferability by comparing bulk properties computed with KSDFT/NLPS, initial BLPS, and final goLPS for the Ga-II and Ga-III phases. Second, the BLPS of Li was optimized to improve the reproduction of atomic forces in liquid phase configurations. We maintained some properties of the bcc and fcc phases, as well as tested sc and cd properties and other atomic forces from snapshots of the liquid phase MD as benchmarks. Lastly, our previous BLPS construction scheme [150, 151] for Ca could not yield a reasonable pseudopotential due to great dispersion in the final data obtained for the atom-centered LPS in reciprocal space. We therefore use the method introduced here to obtain a LPS for Ca, starting directly from the local channel of an existing NLPS and fitting to KSDFT/PAW solid properties of both fcc and bcc structures. This process thereby will show that the scheme proposed can be employed as an independent, improved LPS construction algorithm. We also tested the transferability of the final goLPS for Ca by evaluating solid phase properties of sc and cd structures.

Computational details

Reference solid and liquid properties for each element are obtained with periodic KSDFT calculations with NLPSs ("KSDFT/NLPS"). These calculations are performed using the ABINIT plane-wave DFT code [182, 183]. We also used the Vienna ab initio simulation package (VASP) [184] to perform KSDFT/PAW calculations for Li and Ca. The PAW method [148, 149] is employed with the standard PAW projectors that treat the one and two valence electrons respectively of each Li and Ca atom self-consistently in the presence of all-electron, frozen-core atomic densities. Periodic OFDFT calculations are conducted with the FORTRAN90-based code, PROFESS (Princeton Orbital-Free Electronic Structure Software), developed by the Carter group [185]. In all calculations (KSDFT- and OFDFT), we employ the Perdew-Burke-Ernzerhof (PBE) functional for electron XC [92].

Calculations with the ABINIT code are done using Troullier-Martins (TM) NLPSs [126], generated with the FHI98PP code [186]. We use the default core cutoff radii in the FHI98PP code for Ga, Li, and Ca. For the cases of Ga and Li, we started our fitting from an already-constructed BLPS. The Ga BLPS construction details can be found in Ref. [144], and the Li BLPS construction details can be found in Appendix C. We use Fermi-Dirac smearing with a width of 0.1 eV to smooth out the Fermi surface for all systems. All k-point meshes in the Brillouin zone are generated using the Monkhorst-Pack method [187].

In all OFDFT calculations, the Wang-Govind-Carter99 (WGC99) KEDF [114] is used with the parameters $\gamma = 2.7$, $\alpha = (5 + \sqrt{5})/6$ and $\beta = (5 - \sqrt{5})/6$. To make the evaluation of the WGC99 KEDF linear scaling, we compute it approximately by Taylor-expanding the WGC99 KEDF kernel around the relevant average bulk electron density to second order.

Improving solid properties: Gallium

We initially test our goLPS method's ability to improve solid structure representation for Ga. We first evaluated properties of α-Ga, β-Ga, Ga-II, and Ga-III crystals with KSDFT/NLPS. For geometry relaxations and energy calculations of α- and β-Ga, we used primitive cells consisting of four and two atoms, respectively, and conventional cells consisting of 12 and two atoms for Ga-II and Ga-III, respectively. The Monkhorst-Pack k-point grids employed for these primitive cells were, correspondingly, 20 x 20 x 20, 20 x 20 x 36, 10 x 10 x 10, and 20 x 20 x 12. A 1200-eV kinetic-energy cutoff for the plane-wave basis set was used. The selected plane-wave kinetic energy cutoff and *k*-point meshes ensure that the accuracy of the total energy is converged to within 1.0 meV/atom. In the case of the α-Ga, β-Ga, and Ga-III solid phases, we relaxed cell vectors and ion positions at the KSDFT/NLPS, OFDFT/BLPS, and OFDFT/goLPS levels to obtain minimum-energy structures. Convergence thresholds for the stress tensor elements and forces on ions were 5×10^{-7} hartree bohr^{-3} and 5×10^{-5} hartree bohr^{-1}, respectively. Once the equilibrium cell vectors were determined, the ratio of cell vectors was fixed and the cell volume was changed to calculate the bulk modulus, equilibrium volume, and the equilibrium energy of each phase.

The quality of the (B)LPSs will be judged by calculating properties related to the potential energy surface for various phases. This was done by performing a least-squares-fit of the results to Murnaghan's equation of state [188]:

$$E_{tot}(V) = \frac{B_0 V}{B_0'} \left(\frac{(V0/V)^{B_0'}}{B_0' - 1} + 1 \right) + \text{const.} \tag{153}$$

where B_0 and B_0' are the bulk modulus and its pressure derivative at the equilibrium volume V_0, respectively.

Table 1 displays the properties for the crystalline phases evaluated with KSDFT using NLPS and OFDFT using the initial BLPS and the goLPS. We will evaluate the quality of the fit (in α-Ga and β-Ga) and its transferability (for II-Ga and III-Ga) for each property studied. Although all equilibrium volumes are slightly smaller with goLPS, worse than the already mostly too-small OFDFT/BLPS volumes, the OFDFT/goLPS volumes are all now consistently smaller than the KSDFT/NLPS references. We observe a significant improvement for the bulk moduli of α-Ga and β-Ga using OFDFT/goLPS versus OFDFT/BLPS, evidence that the fitting procedure is working well. Bulk moduli of the other two phases are slightly worse, indicative of the compromises these fits pose. Use of goLPS over the initial BLPS in OFDFT recovers the KSDFT/NLPS phase energy orderings, since the magnitudes of the energy differences are worse than using the initial BLPS in OFDFT. Two-thirds of the ratios between cell vectors, c/a, become smaller with goLPS and therefore are slightly worse (by 0.003 and 0.01) than the BLPS values. Cell vector angles γ are fine with both LPSs. Recall that the parametrization and terms in the objective function employed in the goLPS fitting procedure ultimately defines which properties are more important than others. Hence, quality in some properties will be sacrificed to improve others when perfect agreement of all properties is impossible. Changing the parametrization of the objective function will change that equilibrium.

Improving liquid properties: Lithium

For Li, the goal is to obtain a LPS which correctly represents both solid and liquid phases. We start by constructing the BLPS as discussed in Refs. [150, 151] and detailed in Appendix C. We select the fcc, bcc, sc, and cd structures

TABLE 1: Ga bulk crystal properties calculated with the three different methods (KSDFT/NLPS, OFDFT/BLPS, and OFDFT/goLPS): equilibrium volume (V_0), bulk modulus (B_0), equilibrium total energy relative to α-Ga ($\Delta E_{min} = E_{min} - E_{min}^{\alpha-Ga}$) for other bulk phases, lattice vector angle γ, and the ratio between two cell lattice vectors c/a. Underlined solid phases were used as reference data in the goLPS construction.

	α-Ga	β-Ga	Ga-II	Ga-III
V_0 (Å^3/atom)				
KSDFT / NLPS	20.972	19.852	19.597	19.788
OFDFT / BLPS	21.154	18.847	18.679	18.298
OFDFT / goLPS	20.376	18.752	18.372	18.055
B_0 (GPa)				
KSDFT / NLPS	45.6	45.1	46.3	47.7
OFDFT / BLPS	29.8	49.0	52.2	49.8
OFDFT / goLPS	39.2	44.7	52.4	43.2
ΔE_{min} (eV/atom)				
KSDFT / NLPS	0.000	0.013	0.017	0.019
OFDFT / BLPS	0.000	0.004	0.018	-0.004
OFDFT / goLPS	0.000	0.091	0.104	0.109
γ				
KSDFT / NLPS	119	146	90	90
OFDFT / BLPS	121	146	90	90
OFDFT / goLPS	120	146	90	90
c/a				
KSDFT / NLPS	1.019	0.627	N/A	1.739
OFDFT / BLPS	1.015	0.606	N/A	1.416
OFDFT / goLPS	1.016	0.596	N/A	1.413

to use a wide range of bulk densities as input. These four structures span a range of coordination numbers from 12 for fcc down to four for cd, with sc and bcc exhibiting intermediate coordination numbers of six and eight, respectively. By including densities over this range of coordination, we anticipate that our BLPS should work well in both close-packed and more open condensed matter environments.

One way to evaluate a given LPS in the liquid phase would be to study several static and dynamic properties. However, it would be prohibitively expensive to evaluate these properties during optimization of a large number of possible LPSs. We prefer to compare forces acting on the atoms, because they ultimately determine the system's static and dynamic properties and are straightforward to evaluate. However, KSDFT/NLPS does not describe the liquid state correctly *(vide infra)*. By contrast, KSDFT/PAW correctly reproduces both liquid and solid structure properties. We therefore used a 90-atom sample simulated with KSDFT-MD/PAW in the NVT ensemble as the benchmark for the liquid state. This number of atoms guarantees a correct representation of the liquid, as with other studied cases [189–191]. Two thermodynamic states (TSs) were studied: the first (TS_1) is characterized by a temperature T=523 K and experimental atomic number density [192] $\rho = 0.0438$ Å^{-3}, whereas the second (TS_2) is characterized by T=500 K and $\rho = 0.1097$ Å^{-3}. An MD time step of 1 fs was used. After 300 steps and reaching thermal equilibrium, both TSs were propagated further for 5 ps. The pressures in the NVT MD simulations were 0.3 ± 0.1 GPa for TS_1 (in agreement with the zero pressure corresponding to the experimental atomic number density used) and 38.6 ± 0.5 GPa for TS_2. We randomly chose atomic configuration number 3000 from both TSs as references in the liquid phase for particle configurations and forces to fit to for the goLPS creation.

Figure 5.1 displays the forces in the Cartesian x-direction computed with KSDFT/PAW and OFDFT/BLPS. As mentioned previously, the quantitative agreement between both sets of forces is not optimal and can be improved by optimizing the BLPS. We thus globally optimize the BLPS by using as reference data the solid-phase properties of fcc and bcc Li obtained with KSDFT/PAW. For the liquid phase, we minimize the overall discrepancy ϵ between the two sets of forces (OFDFT/goLPS, F^{OF} and KSDFT/NLPS, F^{KS}) to become:

$$\epsilon = \sqrt{\frac{1}{3N_{at}} \sum_{i=1}^{N_{at}} |F_i^{OF} - F_i^{KS}|^2} \tag{154}$$
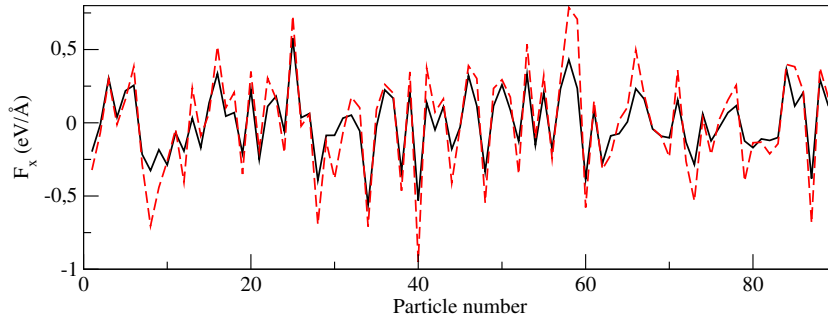
FIGURE 5.1: x-components of the forces on Li atoms obtained from KSDFT-MD/PAW (black continuous curve) and OFDFT-MD/BLPS (red dashed curve) calculations for one of the atomic reference configurations (♯ 3000 from TS_1) sampled from the KSDFT-MD simulation of liquid Li.

Properties of crystalline phases predicted by KSDFT, using NLPS and PAW formalisms, and by OFDFT, using the initial BLPS and final goLPS, are given in Table 2. First, we compare the quality of LPS fits, followed by tests of transferability. OFDFT/goLPS results are compared to their KSDFT/PAW fitting reference, whereas OFDFT/BLPS results are compared to their KSDFT/NLPS fitting reference. The KSDFT bcc bulk modulus and equilibrium volume, along with the KSDFT fcc equilibrium volume, are better reproduced by OFDFT/goLPS than by OFDFT/BLPS; the OFDFT/goLPS fcc bulk modulus is slightly worse than the OFDFT/BLPS when compared to

Table 2: Li bulk crystal properties calculated with the four different methods (KSDFT/NLPS, OFDFT/BLPS, KSDFT/PAW and OFDFT/goLPS): equilibrium volume (V_0), bulk modulus (B_0), equilibrium total energy relative to bcc-Li ($\Delta E_{min} = E_{min} - E_{min}^{bcc-Li}$) for other bulk phases. Underlined solid phases were used as reference data in the goLPS construction.

	bcc	fcc	sc	cd
V_0 (Å^3/atom)				
KSDFT / NLPS	20.205	20.163	20.375	25.792
OFDFT / BLPS	21.111	21.051	22.141	25.237
KSDFT / PAW	20.355	20.301	20.462	25.778
OFDFT / goLPS	20.074	19.949	21.296	25.157
B_0 (GPa)				
KSDFT / NLPS	12.1	13.8	13.1	6.4
OFDFT / BLPS	14.1	14.7	14.3	10.5
KSDFT / PAW	13.9	13.9	12.3	4.9
OFDFT / goLPS	14.0	15.3	13.9	8.5
ΔE_{min} (eV/atom)				
KSDFT / NLPS	0.000	-0.002	0.121	0.517
OFDFT / BLPS	0.000	-0.003	0.133	0.498
KSDFT / PAW	0.000	-0.003	0.118	0.514
OFDFT / goLPS	0.000	-0.004	0.125	0.402

their respective benchmarks. Relative energies are of similar quality for both types of LPSs. Next, we consider sc and cd static structural properties as benchmarks to test transferability of the final goLPS. KSDFT sc equilibrium volume and relative energy and cd bulk modulus are better reproduced by OFDFT/goLPS, whereas the other KSDFT sc and cd properties are better reproduced by OFDFT/BLPS. Overall, the goLPS exhibits reasonable transferability for solid properties.

Table 3 displays the force difference metric ϵ obtained with the initial BLPS and final goLPS for the two reference structures (# 3000 from TS_1 and TS_2). The discrepancy is almost halved in TS_1, at zero pressure. The higher pressure of TS_2 appears to be more challenging for OFDFT as the discrepancy is reduced less than the zero-pressure case. Nevertheless, both results indicate the success of the goLPS procedure when including FM.

Table 3: Differences between forces (Eq. 154) for the liquid Li configurations used as references, calculated with KSDFT/PAW and OFDFT along with the BLPS and goLPS.

	Force Difference (eV/Å)	
Method	TS_1	TS_2
OFDFT / BLPS	0.1502	0.2578
OFDFT / goLPS	0.0855	0.2248

TABLE 4: Differences between forces (Eq. 154) for the liquid Li configurations used to test transferability, calculated with KSDFT/PAW and OFDFT along with the BLPS and goLPS.

	Force Difference (eV/Å)					
Method	TS_1			TS_2		
	♯ 2000	♯ 4000	♯ 5000	♯ 2000	♯ 4000	♯ 5000
OFDFT / BLPS	0.1465	0.1433	0.1470	0.2824	0.2682	0.2578
OFDFT / goLPS	0.0850	0.0865	0.0857	0.2519	0.2393	0.2248

We also tested transferability to assess whether the new PP provides an improved description of the liquid phase. We did this by comparing the difference in forces calculated with the initial BLPS and final goLPS for six other configurations, i.e., three from each TS, of the liquid not used as references in the fitting. Table 4 shows the obtained values. We again observe a marked improvement in the forces with OFDFT/goLPS when comparing with KSDFT/PAW, and this improvement is maintained throughout the configurations sampled.

Figure 5.2 compares the forces in the Cartesian x-direction from the same configuration as in Figure 5.1, computed with both KSDFT/PAW and OFDFT/goLPS. The agreement is greatly improved for all atoms. Moreover, the agreement is improved for configurations other than those used as references. In Figure 5.3, we have evaluated the forces in the Cartesian x-direction for a configuration randomly picked from TS_1 and not used as a reference in the fitting.
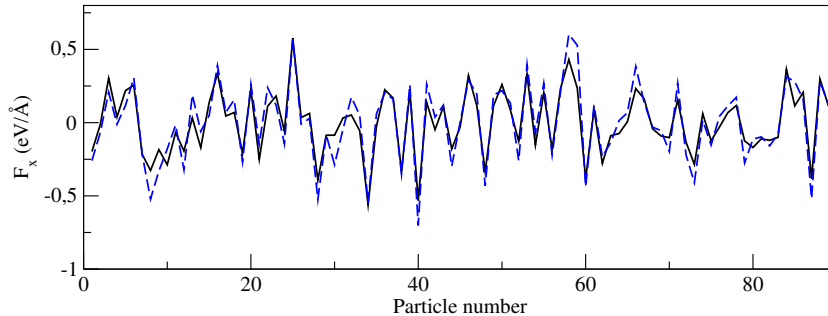
FIGURE 5.2: x-components of the forces on Li atoms obtained from KSDFT-MD/PAW (black continuous curve) and OFDFT-MD/goLPS (blue dashed curve) calculations for one of the reference atomic configurations (♯ 3000 from TS_1) sampled from the KSDFT-MD simulation of liquid Li.

A final benchmark of the constructed goLPS was performed. We evaluated static and dynamic properties of liquid Li at two different TSs using the initial BLPS and final goLPS, comparing them to KSDFT-MD/PAW benchmarks. Both TSs consisted of 90 atoms at two experimental atomic number densities [192] of $\rho = 0.0444$ Å^{-3} at T=463 K and $\rho = 0.0438$ Å^{-3} at T=523 K. The TSs were propagated for 20 ps with an MD time step of 1 fs. We used the same number of particles, density, and time step as with the KSDFT-MD simulation, except for using 20,000 time steps instead of 5000; better sampling is enabled with OFDFT-MD due to its speed. To check transferability, we also performed a KSDFT-MD/PAW calculation at the TS of $\mathsf{rho} = 0.0444$ Å^{-3} at T=463 K with 90 atoms. We restricted the total time of the simulation to 5 ps with an MD time step of 1 fs. We also included KSDFT-MD/NLPS results obtained from a calculation with 100 particles at the TS of $\rho = 0.0438$ Å^{-3} at T= 523 K for 800 time steps with an MD time step of 1 fs.
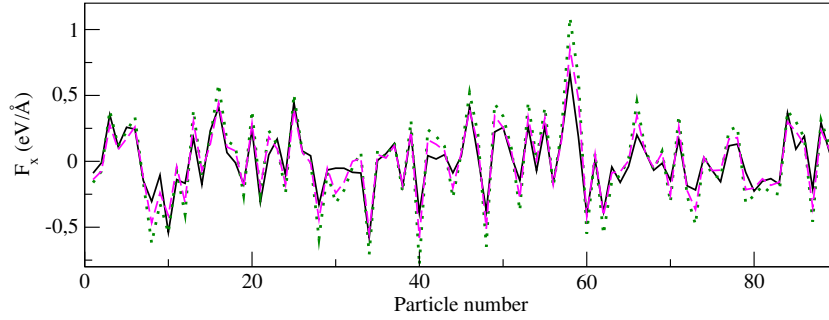
FIGURE 5.3: x-components of the forces on Li atoms obtained from KSDFT-MD/PAW (black continuous curve), OFDFT-MD/BLPS (green dotted curve), and OFDFT-MD/goLPS (pink dashed curve) calculations for a non-reference atomic configuration randomly sampled from the KSDFT-MD simulation of liquid Li at TS_1.

Figures 5.4 and 5.5 show a comparison of the pair distribution, $g(r)$, and the static structure factor, $S(q)$, respectively, at both temperatures with results from KSDFT-MD/NLPS, KSDFT-MD/PAW, OFDFT-MD/BLPS, OFDFT-MD/goLPS, and experimental X-ray diffraction (XRD) [192] and neutron diffraction (ND) [193].
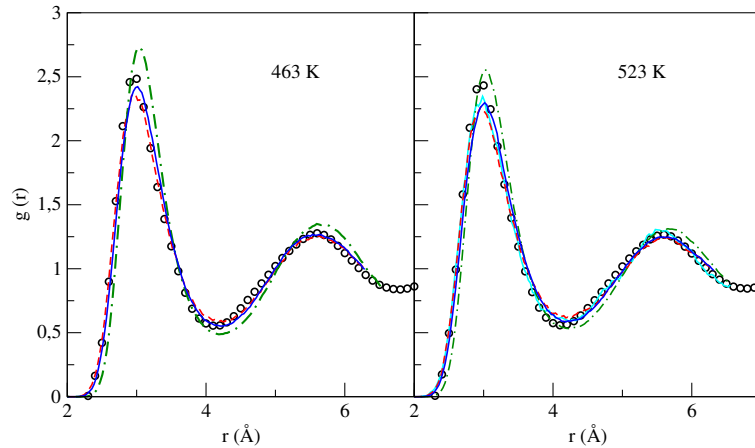
FIGURE 5.4: Liquid Li pair correlation functions obtained from KSDFT-MD/NLPS (light blue continuous curve), KSDFT-MD/PAW (red dashed curve), OFDFT-MD/BLPS (green dash-dotted curve), and OFDFT-MD/goLPS (dark blue continuous curve). Circles: XRD data [192].

The goLPS improves upon the BLPS OFDFT-MD predictions of $g(r)$ at both temperatures when compared to KSDFT-MD and experimental XRD data. Specifically, the onset and position of the first peak and the overall shape, position, and height of the second peak are recovered better with the goLPS. The first peak's height and the depth of the first minimum at T=523 K are slightly worse with the goLPS when compared to experiment, but are better when compared to the KSDFT-MD/PAW data used as references in the fitting.

The poor representation of the liquid by KSDFT-MD/NLPS is clearly evident in $S(q)$ at T=523 K and justifies our previous decision to use KSDFT/PAW data as the reference for fitting the goLPS. The main peak's height and the second peak position at 523 K is better reproduced with OFDFT-MD/goLPS than with the BLPS, when compared to the KSDFT-MD reference results. At T=463 K, we observe striking improvement: in the OFDFT-MD/BLPS results, which exhibit very marked peaks, indicative of solidification. OFDFT-MD/goLPS results do not show this feature and compare very well with ND data. Comparison with XRD data is also satisfactory, although the height of the main peak is slightly overestimated by both KSDFT-MD/PAW and OFDFT-MD/goLPS. However, recall that ND experiments sample the ion distribution in the sample, while XRD data sample the
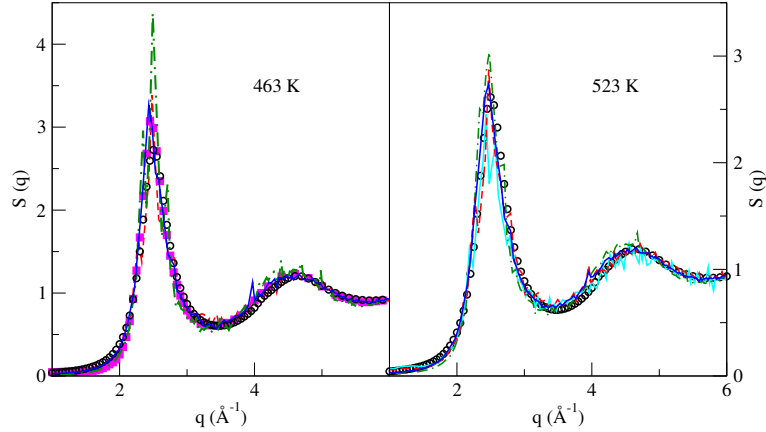
FIGURE 5.5: Liquid Li static structure factor obtained from KSDFT-MD/NLPS (light blue continuous curve), KSDFT-MD/PAW (red dashed curve), OFDFT-MD/BLPS (green dash-dotted curve), and OFDFT-MD/goLPS (dark blue continuous curve). Circles: XRD data [192]. Pink filled squares: ND data at 470 K [193].

TABLE 5: Self-diffusion coefficients of liquid Li in the thermodynamic states studied.

Temp. [K]	D_{PAW} [Å² p s⁻¹]	D_{BLPS} [Å² p s⁻¹]	D_{goLPS} [Å² p s⁻¹]	D_{exp} [Å² p s⁻¹]
463	0.63 ± 0.03	0.31 ± 0.01	0.66 ± 0.02	0.69 ± 0.09[a]
				0.64 ± 0.04[b]
				0.67 ± 0.06[c]
523	1.04 ± 0.04	0.65 ± 0.03	0.96 ± 0.01	0.95 ± 0.12[a]
				0.90 ± 0.06[b]
				0.93 ± 0.93[c]

[a]Reference [194], [b]Reference [195], [c]Reference [196, 197]

electron distribution. Normally, differences between these two experimental techniques are minor, except in cases where the number of electrons in the ion is similar to the number of valence electrons. This is the case of Li, where we have only two electrons in the core of each ion and one valence electron. The more correct comparison therefore is between the MD and the ND data in this particular case.

We also evaluated dynamic behavior of liquid Li, as evidenced by the self-diffusion coefficient, D, computed as the integral of the normalized velocity autocorrelation function, $Z(t)$, as detailed in Chapter 2. Table 5 displays the results. At both temperatures, we obtain much better diffusion coefficients with goLPS than with the initial BLPS when compared to experiment and KSDFT-MD/PAW. The KSDFT-MD/PAW results have a slightly larger uncertainty due to the smaller number of configurations available in the shorter trajectory that we could afford to run.

All of these results support the initial assumption that BLPSs will, in general, work well in solid phases but less well in liquid phases due to the nature of their construction. Modifications targeted to match additional liquid reference data improve the description of the liquid state.

Direct goLPS creation from NLPS local channel: Calcium

The goLPS fitting method presented here always requires an initial guess for the LPS. Here, we analyze the importance of the quality of the initial LPS and whether or not we must start from an existing BLPS. For example,

TABLE 6: Ca bulk crystal properties calculated with the three different methods (KSDFT/PAW, OFDFT/LPS, and OFDFT/goLPS): equilibrium volume (V_0), bulk modulus (B_0), equilibrium total energy relative to fcc-Ca ($\Delta E_{min} = E_{min} - E_{min}^{fcc-Ca}$) for other bulk phases. Underlined solid phases were used as reference data in the goLPS construction.

	fcc	bcc	sc	cd
V_0 (Å^3/atom)				
KSDFT / PAW	42.278	42.216	43.540	80.314
OFDFT / LPS	49.533	49.045	58.174	88.408
OFDFT / goLPS	42.755	43.425	51.900	79.251
B_0 (GPa)				
KSDFT / PAW	17.3	16.1	10.9	4.1
OFDFT / LPS	17.3	17.4	11.2	5.5
OFDFT / goLPS	17.2	16.1	14.3	6.3
ΔE_{min} (eV/atom)				
KSDFT / PAW	0.000	0.017	0.393	1.044
OFDFT / LPS	0.000	0.005	0.470	0.998
OFDFT / goLPS	0.000	0.015	0.440	0.949

the BLPS construction process for Ca is severely complicated by difficulties in obtaining a reasonable atom-centered LPS in reciprocal space using the data of the different solid phases. Due to this problem, we decided to test the goLPS scheme using the local channel of an existing TM-NLPS for Ca [198] as the initial guess. In this example, benchmark properties were evaluated at the PAW-DFT level for fcc, bcc, sc, and cd Ca crystals, using primitive cells for geometry relaxations and energy calculations consisting of one atom for fcc, bcc, and sc and two atoms for cd. The Monkhorst-Pack k-points grids employed for these primitive cells are 24x24x24 for bcc, fcc, and sc and 15x15x15 for cd. A 900-eV kinetic-energy cutoff for the plane-wave basis set was used. The selected plane-wave kinetic energy cutoff and k-point meshes ensure that the total energy is converged to within 1.0 meV/atom.

Crystalline properties evaluated are again the bulk modulus, equilibrium volume per atom, and energy per atom. We employed the fcc and bcc structural properties calculated with KSDFT/PAW as references for the fitting of the solid-phase properties, because this method gave more accurate results for the Ca case than the KS-DFT/NLPS method. We thus evaluate structural properties of sc and cd Ca as benchmarks to assess the transferability obtained with the final goLPS. Table 6 compares the static structural properties studied using KSDFT/PAW and OFDFT with the final goLPS. We have also included the results obtained with OFDFT and the LPS, the local channel of the NLPS, to show the quality of the initial guess for the LPS.

As can be seen in Table 6, although relative energies and bulk moduli predicted by OFDFT and the initial guess for the LPS are quite reasonable, the equilibrium volumes per atom for all crystals studied are far off from the KSDFT/PAW predictions. These discrepancies are greatly reduced with the final goLPS, especially for fcc, bcc, and cd crystals. The sc properties, although improved over those obtained with the local channel of the NLPS, still show some differences when evaluated with OFDFT/goLPS. This might be solved by including sc properties as benchmarks in the fitting, but could also point to the well-known accuracy limitations of the WGC99 KEDF for such open structures as sc. Finally, the OFDFT/goLPS relative energies are of similarly good quality, while the bulk moduli deteriorate slightly (except for bcc) compared to the initial guess LPS results. Overall, the starkly improved volumes with little sacrifice of accuracy in moduli and energies points to the high quality of the goLPS.

5.2.4   *Conclusions*

We have developed a systematic, automated way to create LPSs applicable to solids, liquids, or both. We have demonstrated improvements over derived BLPSs compared to KSDFT/NLPS results for both solid and liquid phases, as well as for both reference and benchmark data. The optimization strategy employed is powerful enough to make use of initial guesses of very different qualities, including simply the local channel of an already existing NLPS. This characteristic facilitates the creation of possible goLPSs for more complex elements with multiple p-valence electrons or even transition metals, where previous LPS creation methods proved challenging or impossible. An immediate next step will be to extend our library of goLPSs to allow for more accurate OFDFT studies of other main group elements for which KEDFs are reliable.

6

BULK LIQUID METALS

In this chapter we show the results of the study of the static and dynamic structure of several transition metals. These are interesting materials from a physical and technological point of view, but they are in general challenging to study, both experimentally and theoretically. An important source of complication from the experimental point of view is the high melting temperature. For many liquid transition metals there is no experimental information about dynamic properties, and even the static structure has proved to be difficult to determine (see the case of liquid Ti). From the theoretical viewpoint the main complication for first principles studies is the large number of electrons per atom that are required to be considered explicitly because of the importance of the d-band on the properties of the systems. Orbital-free schemes, on the other hand, have had so far limited success for systems with d-electrons due to the requirement of using local pseudopotentials and also to the approximations inherent to the expressions used for the kinetic energy density functional.

The KS AIMD studies presented here are therefore interesting both in order to provide information complementary to that experimentally observed (if this exists) and also to provide benchmark data for the future development of KEDFs and local pseudopotentials adequate for d-electron systems, which would enable greater statistical accuracy in their theoretical study through orbital-free approaches.

This chapter includes three sections. In the first one we report a study of liquid Ni, for which experimental information does exist. However we show the existence of some peculiarities, unobserved so far in liquids at normal pressure, in the transverse dynamic properties. The second section shows results for liquid Ti, whose static and dynamic properties are analyzed in detail. Finally the last section is concerned with the study of liquid Pd and Pt, for wich very scarce experimental information exists.

6.1 AB INITIO STUDY OF SEVERAL STATIC AND DYNAMIC PROPERTIES OF BULK LIQUID NI NEAR MELTING.

Transition metals such as iron and nickel have an important role in geophysical science because of their presence in many planetary cores, including the Earth's core. Iron is the dominant constituent of the Earth's solid inner core and liquid outer core, which has prompted a substantial amount of studies on a variety of properties of solid and liquid iron under the extreme temperature/pressure conditions of the Earth's core. Nickel is also another (minor) component of the core and its presence (along with other light elements, e.g. sulfur, silicon) should be taken into account in order to achieve an accurate understanding of the different phenomena occurring in the core.

Recently AIMD studies of liquid iron at thermodynamic conditions near its triple point [249] as well as at several high pressure/temperature states [191], have been performed in the group. Now, we apply the same simulation technique to liquid Ni as a preliminary step towards the study of those Fe-Ni alloys of geophysical interest.

We have evaluated several static and dynamic properties of l-Ni near its triple point by *ab-initio* molecular dynamics (AIMD) simulations.

6.1.1   *Computational details.*

We adopted the local density approximation, as parametrized by Perdew and Zunger,[89, 91] including non-linear core corrections. The ion-electron interaction has been described by means of an ultrasoft pseudopotential,[128] which was generated from a scalar-relativistic calculation of the atomic electron configuration $[Ar]3d^9 4s^1$.

   The thermodynamic state was characterized by a number density, $\rho_i = 0.0792$ Å^{-3} and temperature $T = 1773$ K. We used 120 atoms (i.e. 120 x ($9d+1s$, p) = 1200 valence electrons) in a cubic supercell. The system was thermalized during 10 ps of simulation time and therefrom microcanonial KS-AIMD simulations were performed over 21000 time steps, which amounted to 115.5 ps of simulation time. We have used a plane-wave representation with an energy cutoff of 25.0 Ryd and the single Γ point was used in sampling the Brillouin zone. Finally, we note that the 21000 equilibrium configurations were employed for the evaluation of the static and dynamic properties of bulk l-Ni.

6.1.2   *Results and discussion.*

Several static properties have been evaluated ($g(r)$, $S(q)$, common neighbour analysis (CNA), etc) with very good agreement with experimental data. Moreover, the CNA analysis has confirmed the connection of the asymmetry in the second peak of $S(q)$ to an icosahedral short-range order. The evaluation of the dynamic properties provides good agreement with different dynamic properties (adiabatic sound velocity, shear viscosity) to experimental results. In addition, a close analysis of $S(q, \omega)$ reveals the existence of the same type of transverse-like excitation modes found by Hosokawa *et al.* in their IXS data [246]. The following paper reports on this part of our work.

Ab initio study of several static and dynamic properties of bulk liquid Ni near melting

B. G. del Rio, L. E. González and D. J. González
Departamento de Física Teórica, Universidad de Valladolid, 47011 Valladolid, Spain

Several static and dynamic properties of bulk liquid Ni at a thermodynamic state near its triple point have been evaluated by *ab initio* molecular dynamics simulations. The calculated static structure shows very good agreement with the available experimental data, including an asymmetric second peak in the static structure factor, which underlines a marked local icosahedral short-range order in the liquid. The dynamical structure reveals propagating density fluctuations, and the calculated dynamic structure factors, $S(q, \omega)$, show a good agreement with the inelastic x-ray scattering measurements. The obtained dispersion relation closely follows that obtained from the inelastic x-ray scattering measurements; moreover we analyze the possible reasons behind its discrepancy with respect to the dispersion relation derived from the inelastic neutron scattering data. The dynamical processes behind the $S(q, \omega)$ have been analyzed by using a model with two decay channels (a fast and a slow) associated with the relaxations of the collective excitations. We have found that the transverse current spectral functions exhibit some features which, so far, had previously been shown by high pressure liquid metals only. Furthermore, the calculated $S(q, \omega)$ show, within some q-range, the appearance of transverse-like excitation modes, similar to those recently found in other liquid metals. Finally, results are also reported for several transport coefficients. *Published by AIP Publishing.* [http://dx.doi.org/10.1063/1.4973803]

I. INTRODUCTION

Transition metals such as iron and nickel play a very relevant role in geophysical science because of their presence in many planetary cores, including the Earth's core. Iron is the dominant constituent of the Earth's solid inner core and liquid outer core, which has stimulated a substantial amount of studies on a variety of properties of solid and liquid iron under the extreme temperature/pressure conditions of the Earth's core. Nickel is also another (minor) component of the core, and its presence (along with other light elements, e.g., sulfur and silicon) should be taken into account in order to achieve an accurate understanding of the different phenomena occurring in the core.

Recently, we have performed simulation studies on a range of static and dynamic properties of liquid iron at thermodynamic conditions near its triple point[1] as well as at several high pressure/temperature states.[2] Now, we apply the same simulation technique to liquid Ni as a preliminary step towards the study of those Fe–Ni alloys of geophysical interest.

The static structure factor of l-Ni near its triple point has been measured by X-ray diffraction (XD)[3,4] and neutron diffraction (ND)[5,6] techniques. It displays a symmetric main peak followed by a second maximum with a weak shoulder on its right-hand side. This peculiar feature in the second maximum has been found in other transition metals (Fe, Ti, Zr)[6,7] and has been related to icosahedral (either ideal or distorted) short-range order which is enhanced upon undercooling.[8,9]

The first experimental study on the microscopic dynamics of l-Ni was carried out by Johnson *et al.*[10] who performed inelastic neutron scattering (INS) measurements of l-Ni at

T = 1870 K. Two different isotopic concentrations, one with natural abundance ratio and the other a wholly incoherent mixture, were chosen in order to study separately the coherent and incoherent scattering contributions. Subsequently, the Vineyard approximation[11] was used in order to relate both contributions. The dynamic, $S(q, \omega)$ and self-dynamic, $S_s(q, \omega)$ structure factors were reported for $2.2 \leq q \leq 4.4$ Å^{-1} and $0 \leq \omega \leq 121.5$ ps^{-1}. For some q-values, the corresponding $S(q, \omega)$ showed small side peaks which, it was suggested, could be indicative of collective excitations in l-Ni; however they refrained from ascertaining its existence, and it was concluded that further studies were needed. Several years later, Bermejo *et al.*[12] performed INS measurements of l-Ni at the lower temperature T = 1763 K. The scattered intensity was determined within the range $0.8 \leq q \leq 3.5$ Å^{-1}, and the results were analyzed by modeling the total dynamic structure factor in terms of two Lorentzian functions for the quasielastic contributions plus a damped harmonic oscillator (DHO) model for the inelastic contribution. Propagating collective excitations were detected and its associated dispersion relation yielded a sound velocity well below the expected adiabatic value,[13–15] $\approx$4058 m/s, reaching for the smallest q, a value around 3000 m/s. This could be interpreted as signaling an isothermal regime above the q-region where the adiabatic behavior dominates, namely, above the hydrodynamic region.

Chathoth *et al.*[16] have performed quasielastic neutron scattering (QNS) measurements of the self-dynamic structure factor of l-Ni at several temperatures within the range 1514 K $\leq T \leq$ 1940 K. Its main objective was the experimental determination of the self-diffusion coefficient and this was achieved by fitting the measured $S_s(q, \omega)$ to a Lorentzian

function whose half-width at half-maximum was used to determine the associated self-diffusion coefficient.

More recently, in an attempt to verify the existence of an isothermal regime for dynamics, Cazzato *et al.*[17] have performed inelastic X-ray scattering (IXS) measurements of l-Ni at $T = 1767$ K. This technique allows the direct measurement of the dynamic structure factor, $S(q, \omega)$, which was determined within a range $0.2 \leq q \leq 0.8$ Å^{-1}, and the results were analyzed in terms of a Lorentzian function plus the DHO model. They did not observe any indication of isothermal behavior. On the contrary the results produced dispersion in good agreement with the adiabatic speed of sound.

Prompted by the above experimental data, we have performed a study on several static and dynamic properties of l-Ni near its triple point. It has been carried out by an *ab initio* molecular dynamics (AIMD) simulation method which is nowadays a standard technique for the study of a wide range of condensed matter systems. Most AIMD methods are based on density functional theory (DFT)[18] which, starting with a collection of atoms/ions at specified positions, allows to compute the ground state electronic energy and, via the Hellmann-Feynman (HF) theorem, the forces acting on the atoms/ions. Therefore, in the AIMD simulations the atomic/ionic positions evolve according to classical mechanics while the electronic subsystem follows adiabatically. Although the AIMD methods require significant computational resources and impose important constrains concerning the simulation times and size of the systems under study, these drawbacks are compensated by the accurateness of the results yielded.

Molecular dynamics (MD) simulations, both classical (CMD) and *ab initio*, have already been performed on l-Ni for a wide range of thermodynamic states, although most studies have focused on those thermodynamic states around the triple point and have evaluated structural static properties.

Around twenty years ago, Alemany *et al.*[19] performed a CMD simulation study of several static and dynamic properties of l-Ni at $T = 1775$ and 1875 K. They used an interatomic potential constructed within the framework of the embedded atom model (EAM)[20] which provided a good description of the static structure. Moreover, their calculated dynamic structure factors showed a fair agreement with the INS data of Johnson *et al.*[10] A similar combination of CMD simulations with EAM-based interatomic potentials was used by Cherne *et al.*[21] to calculate the melting point, static structure factor, self-diffusion and shear viscosity of l-Ni.

Some years later, Ruiz-Martin *et al.*[22] carried out a CMD simulation study of l-Ni at $T = 1800$ K by using an interatomic pair potential constructed within the EAM scheme.[23] This simulation used a large number of particles (4000 particles) which allowed analyzing the dynamic structure factors up to very small q-values.

The first AIMD calculation of l-Ni near the melting point was reported by Jakse *et al.*[24,25] for $T = 1850$ K. They used the VASP code[26] combined with the projector augmented wave all-electron description of the electron-ion interaction. The study focused on some single particle and collective dynamical properties, and they also obtained estimates for the self-diffusion and shear viscosity coefficients. Recently, Rozas *et al.*[27] have studied a range of thermophysical properties

of liquid Ni (melting temperature, enthalpy, self-diffusion, shear viscosity, and thermal diffusivity) by means of CMD simulations and EAM-based interatomic potentials. They also reported AIMD results for the static structure factor and mean square displacement of l-Ni near melting.

In this paper, we report an AIMD simulation study of the dynamic (and static) properties of l-Ni at a thermodynamic state near its triple point. Besides its intrinsic interest, we have chosen this specific thermodynamic state because of the availability of the experimental inelastic scattering data, both IXS and INS. The layout of the paper is as follows: In Section II we briefly sketch the theory underlying the present AIMD simulations and describe some technical details as well as some of the terms appearing in the Kohn-Sham energy functional. In Section III we present and discuss the obtained structural and dynamical results which are compared with other previous studies as well as with the available experimental data. Finally some conclusions are drawn.

II. COMPUTATIONAL METHOD

The total potential energy of a system composed of N ions with valence Z, enclosed in a volume Ω, and interacting with $N_e = NZ$ valence electrons can be written, within the Born-Oppenheimer (BO) approximation, as the sum of the direct ion-ion Coulombic interaction energy, $E_{i-i}[\{\vec{R}_l\}]$, plus the ground state energy of the electronic system subjected to the external potential created by the ions, $V_{ext}(\{\vec{R}_l\})$,

$$E(\{\vec{R}_l\}) = E_{i-i}[\vec{R}_l] + E_g[\rho_g(\vec{r}), V_{ext}(\{\vec{R}_l\})], \quad (1)$$

where $\rho_g(r)$ is the ground state electronic density and $\vec{R}_l$ are the ionic positions. According to DFT, the ground state electronic density minimizes an energy functional

$$E[\rho(\vec{r})] = T_s[\rho] + E_{ext}[\rho] + E_H[\rho] + E_{xc}[\rho], \quad (2)$$

where $T_s[\rho]$ is the electronic kinetic energy of a non-interacting system with density $\rho(\vec{r})$, $E_{ext}[\rho]$ is the electron-ion interaction energy, $E_H[\rho]$ is the classical electrostatic Hartree energy, and $E_{xc}[\rho]$ is the electronic exchange-correlation energy for which we will adopt the local density approximation, as parametrized by Perdew and Zunger,[28] including non-linear core corrections. The ion-electron interaction has been described by means of an ultrasoft pseudopotential,[29] which was generated from a scalar-relativistic calculation of the atomic electron configuration [Ar]3d^{9}4s^1.

We performed AIMD calculations for l-Ni at a thermodynamic state characterized by a number density, $\rho_i = 0.0792$ Å^{-3} and temperature $T = 1773$ K. We used 120 atoms (i.e., 120 $\times (9d + 1s, p) = 1200$ valence electrons) in a cubic supercell. The system was thermalized during 10 ps of simulation time and therefrom microcanonical KS-AIMD simulations were performed over 21 000 time steps, which amounted to 115.5 ps of simulation time, with the ionic dynamics being generated using the Verlet algorithm with HF forces, as implemented in the Quantum-Espresso package.[30] We have used a plane-wave representation with an energy cutoff of 25.0 Ry, and the single Γ point was used in sampling the Brillouin zone. Finally, we note that the 21 000 equilibrium configurations were employed for the evaluation of the static and dynamic properties of bulk

l-Ni. This same simulation method has already provided an accurate description of several static and dynamic properties of bulk l-Sn, l-Hg, and l-Cd.[31,32]

III. RESULTS

A. Static properties

The AIMD simulations provide a direct evaluation of both the pair distribution function, $g(r)$, and the static structure factor, $S(q)$. Figure 1 shows the obtained AIMD result for $g(r)$ which is compared with the corresponding XD[3,4] and ND[6] data.

The coordination number (CN) has been evaluated by integrating the radial distribution function, $4\pi\rho_i r^2 g(r)$, up to the position of its first minimum, which for the calculated AIMD $g(r)$ is located at $R_{min} = 3.29$ Å, leading to a value CN ≈ 12.0 atoms. Had we chosen $R_{min} = 3.40$ Å, which is the position for the first minimum in $g(r)$, then CN ≈ 12.6 atoms. Notwithstanding the procedure used to evaluate the CN, the obtained values are typical of the simple liquid metals at thermodynamic conditions near their respective triple point.[33]

Figure 2 shows the AIMD result for $S(q)$, which is compared with the XD[3,4] and ND[5,6] data. The experimental $S(q)$'s have a symmetric main peak located at a position $q_p \approx 3.10$ Å^{-1} and its height takes values between $S(q_p) \approx 2.30$[6] and $S(q_p) \approx 2.75$.[5] Also, the ND data of Schenk et al.[6] show a weak shoulder in the second maximum of the $S(q)$ at $q \approx 6.0$ Å^{-1}. Moreover, the ND data[6] for undercooled l-Ni show that this shoulder becomes more noticeable with decreasing temperature.

The AIMD result for $S(q)$ stands in good agreement with the experimental data, i.e., its main peak's position is at $q_p \approx 3.10$ Å^{-1} and its height is $S(q_p) \approx 2.75$, whereas the subsequent oscillations are in phase with the experimental data; moreover, it displays an asymmetric second peak which qualitatively follows the ND data.[6] We note that our value of $S(q_p) \approx 2.75$ is similar to other calculations, i.e., the AIMD results of Jakse et al.[24,25] and Rozas et al.[27] yielded $S(q_p) \approx 2.60$ and ≈ 2.66, respectively, whereas the CMD study of Alemany et al.[19] gave ≈ 2.90. Recalling that the XD[3,4] data and the ND data of Johnson et al.[5] are $S(q_p) \approx 2.45$ and ≈ 2.75,
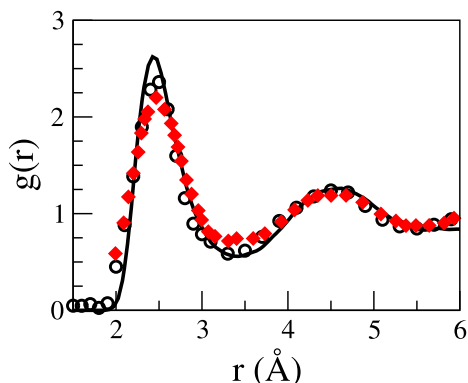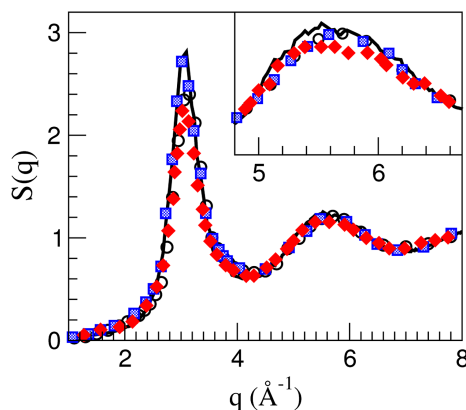
FIG. 2. Static structure factor, $S(q)$, of liquid Ni at $T = 1773$ K. Continuous line: Present AIMD calculations. Open circles: Experimental XD data from Waseda.[3,4] Hatched squares and full diamonds: Experimental ND data from Johnson et al.[5] at $T = 1875$ K and Schenk et al.[6] at $T = 1765$ K, respectively. The inset shows a detailed comparison for the second maximum.

respectively, we believe that the value of $S(q_p) \approx 2.30$ corresponding to the ND data of Schenk et al.[6] may some what underestimate the amplitude of the main peak.

Interestingly, an asymmetric shape of the second peak of $S(q)$ has been experimentally observed in several liquid transition metals, and it has been related to an important presence of icosahedral (ICOS) local order. A first indication of this type of short range order is given by the positions of the maximum of the second peak of $S(q)$, q_2, and its shoulder, q_2', as compared to the position of the main peak. The corresponding values for l-Ni in this study are $q_2/q_p = 1.77$ and $q_2'/q_p \approx 1.95$, which are similar to those found for l-Fe (1.79 and 1.91) or l-Ti and l-Zr (1.76 and 1.92, respectively) and not far from those corresponding to an ideal icosahedral environment in a curved space[34] of 1.71 and 2.04.

We have also estimated the isothermal compressibility, κ_T, of l-Ni by resorting to the relation $S(q \to 0) = \rho_i k_B T \kappa_T$ where k_B is Boltzmann's constant. To this end, the calculated $S(q)$ has been extrapolated to $q \to 0$ by using a least squares fit $S(q) = s_0 + s_2 q^2$ of the q-values for $q \leq 1.2$ Å^{-1}. We obtained a value $S(q \to 0) = 0.018 \pm 0.002$, which yields a result $\kappa_T = 0.95 \pm 0.10$ (in units of 10^{11} m^2 N^{-1}), which is close to the corresponding experimental data $\kappa_T \approx 1.04 \pm 0.02$.[14]

A more detailed, three dimensional, description of the local order in l-Ni can be achieved by resorting to the common neighbor analysis[35] (CNA) method. Now, each pair of atoms is characterized by four indices, with the first index being 1 if the distance between the atoms is smaller than 3.40 Å, which corresponds to the first minimum of $g(r)$, the second index stands for the number of common first neighbors, and the third index is the number of bonds that connect those shared first neighbors. Finally, the fourth index is used to distinguish among configurations with the same first three indices but with a different topology. The CNA method allows discriminating FCC, HCP, BCC, and ICOS packings as well as more complex polytetrahedral environments. For example, FCC and HCP crystalline order are composed of 142×-type pairs, BCC is typified by 144× and 166× pairs whereas ICOS is characterized by 155× pairs, and the distorted ICOS is described by the 154× and 143× pairs.

FIG. 1. Pair distribution function, $g(r)$, of l-Ni at $T = 1773$ K. Continuous line: Present AIMD calculations. Circles and diamonds: XD data from Waseda[3,4] and ND data of Schenk et al.[6] at $T = 1765$ K, respectively.

TABLE I. Common neighbor analysis of the AIMD configurations of l-Ni at 1773 K compared with several local structures.

Pairs	1551	1541	1431	1321	1421	1422	1301	1441	1661
l-Ni	0.25	0.24	0.21	0.02	0.06	0.08	0.03	0.04	0.06
ICOS	1.0	0.0	0.0	0.0	0.0	0.0	0.0	0.0	0.0
HCP	0.0	0.0	0.0	0.0	0.50	0.50	0.0	0.0	0.0
FCC	0.0	0.0	0.0	0.0	1.0	0.0	0.0	0.0	0.0
BCC	0.0	0.0	0.0	0.0	0.0	0.0	0.0	0.57	0.43

For several configurations generated in the present AIMD simulation, we have first removed the thermal noise for each one so as to obtain the closest local minimum energy configuration, i.e., the inherent structure, and then performed a CNA calculation. The average over configurations of these results are summarized in Table I. First, notice that the fivefold symmetry dominates in l-Ni, as the sum of perfect and defective icosahedral structures amounts to ≈70% of the pairs, with the number of perfect ones being more than one third of the total. We also find an ≈10% appearance of local BCC-type pairs and there is less than 6% appearance of local FCC environments which, oddly enough, is the phase in which l-Ni crystallizes. These results are very similar to those already obtained in the AIMD simulations of Jakse and Pasturel;[24] moreover, their calculation for undercooled l-Ni showed an increase in the percentage of 1551 pairs.

We do not expect a significant size dependence of these data since we are probing the local structure, which typically involves at most eight atoms, and whose size is much smaller than the simulation box.

B. Dynamic properties

We have calculated several dynamic properties, both single-particle (self-intermediate scattering functions, self-dynamic structure factors, velocity autocorrelation function, and mean square displacement) and collective ones (intermediate scattering functions, dynamic structure factors, and longitudinal and transverse currents). The evaluation of the time correlation functions has been performed by taking time origins every five time steps. Several correlation functions have a dependence on the wavevector $\vec{q}$ which, for an isotropic system, reduces to a dependence on $q \equiv |\vec{q}|$ only.

1. Single particle dynamics

The most comprehensive information on the single-particle properties is provided by the self-intermediate scattering function, $F_s(q,t)$, which probes the single-particle dynamics over different length scales, ranging from the hydrodynamic to the free-particle limit. This magnitude has been evaluated as

$$F_s(q,t) = \frac{1}{N} \left\langle \sum_{j=1}^{N} e^{-i\vec{q}\vec{R}_j(t+t_0)} e^{i\vec{q}\vec{R}_j(t_0)} \right\rangle \quad (3)$$

and Fig. 3 depicts, for some q-values, the calculated AIMD results for the $F_s(q,t)$, where we observe the usual monotonic decay with time. A good agreement is observed between our results and the corresponding QNS data of Chathoth et al.[16]
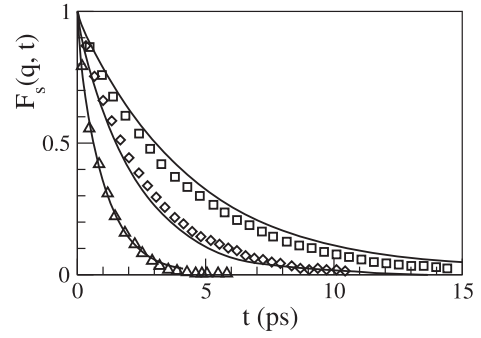
FIG. 3. Self-intermediate scattering function, $F_s(q,t)$, of l-Ni for several q-values. Symbols: Experimental data of Chathoth et al.[16] for $T = 1795$ K and (from top to bottom) $q = 0.8$, 1.0, and 1.6 Å^{-1}. Full lines: Calculated AIMD results for $T = 1773$ K and $q = 0.77$, 1.09, and 1.64 Å^{-1}, respectively.

The time Fourier Transform (FT) of the $F_s(q,t)$ gives its frequency spectrum, $S_s(q,\omega)$, known as the self-dynamic structure factor, which has experimental importance due to its connection with the incoherent part of the INS cross section. The AIMD calculated $S_s(q,\omega)$ exhibit a monotonic decay with frequency, starting from a peak value at $\omega = 0$. In Fig. 4 we have compared, for the same constant ω-values, our calculated $S_s(q,\omega)$ with the INS data of Johnson et al.[10] for l-Ni at $T = 1870$ K. Given the temperature difference, it is expected that the AIMD calculations yield slightly smaller values than the experimental data; indeed this is the main trend observed in Fig. 4 excepting those results for $\omega = 0$ and $q \leq 3.5$ Å^{-1}. Nevertheless, it must be recalled that the accurate experimental determination of the spectral features around $\omega = 0$ is a delicate task and the discrepancies between AIMD calculations and experimental data should not be automatically ascribed to the calculations. In fact, the data reported by Johnson et al.[10] were obtained after applying a deconvolution process to their original raw data, and the deconvolution correction is the largest[19] in the region around $\omega = 0$.

Closely related to $F_s(q,t)$ is the velocity autocorrelation function (VACF) of a tagged ion in the fluid, $Z(t)$, which can be obtained as the $q \rightarrow 0$ limit of the first-order memory function of $F_s(q,t)$. However, in the present simulations the
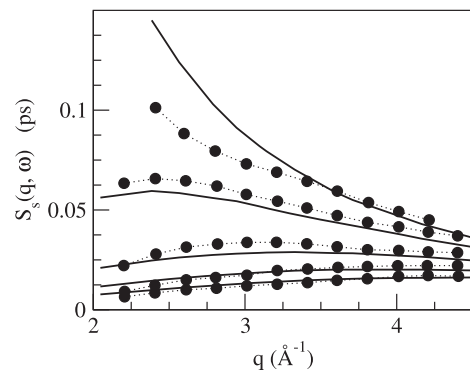
FIG. 4. Self-dynamic structure factor, $S_s(q,\omega)$, of l-Ni for several ω-values (from top to bottom $\omega = 0$, 2.28, 4.56, 6.84, and 9.12 ps^{-1}). Symbols: INS data of Johnson et al.[10] at $T = 1870$ K. Full lines: Calculated AIMD results for $T = 1773$ K.

(normalized) $Z(t)$ has been obtained from its definition

$$Z(t) = \langle \vec{v}_1(t) \cdot \vec{v}_1(0) \rangle / \langle v_1^2 \rangle \qquad (4)$$

with $\vec{v}_1(t)$ being the velocity of a tagged ion in the fluid at time t and $\langle \ldots \rangle$ stands for the ensemble average.

Figure 5 shows the AIMD calculated $Z(t)$ which displays the typical backscattering behavior with a marked first minimum which is followed by rather weak oscillations. This first minimum is related to the so-called cage effect by which a given particle rebounds against the cage formed by its nearest neighbors. Interestingly, the first maximum still remains below zero. An estimate of the frequency at which a given particle vibrates within its near neighbor's cage[36] can be derived by the short time expansion $Z(t) = 1 - \omega_E^2 t^2/2 \ldots$, where ω_E is the so-called Einstein frequency of the system. A short time fitting of the $Z(t)$ curve in Fig. 5 gives $\omega_E \approx 34.8$ ps^{-1}. The inset in Figure 5 represents the associated power spectrum, $Z(\omega)$, which shows a maximum located at ≈ 25 ps^{-1} and a shoulder at ≈ 40 ps^{-1}; parenthetically we note that ω_E stands between the two peaks (in fact, the peak and the shoulder) of $Z(\omega)$, which is a characteristic feature of the simple liquid metals.[33]

The self-diffusion coefficient, D, can be found by either the time integral of $Z(t)$ or from the slope of the mean square displacement $\delta R^2(t) \equiv \langle |\vec{R}_1(t) - \vec{R}_1(0)|^2 \rangle$ of a tagged ion in the fluid. In this AIMD study, both routes have yielded the same value, namely, $D_{\text{AIMD}} = 0.375 \pm 0.008$ Å^2/ps at $T = 1773$ K, which compares rather well with the QNS data of $D_{\text{Exp}} = 0.380 \pm 0.006$ Å^2/ps at $T = 1795$ K of Chathoth et al.[16] Incidentally, the QNS technique has also been used by Meyer and co-workers[37] to determine the self-diffusion coefficient of l-Ni within a temperature range from 200 K above to about 200 K below the melting point in the metastable regime of an undercooled melt. On the other hand, by using experimental data of other thermodynamic magnitudes, Iida et al.[38] have suggested a value $D_{\text{exp}} \approx 0.41$ Å^2/ps for l-Ni at $T = 1773$ K.

For the sake of comparison, we mention that several authors have also evaluated the self-diffusion coefficient of l-Ni near melting. For example, the CMD calculation of Alemany et al.[19] gave $D = 0.354 \pm 0.005$ Å^2/ps at $T = 1775$ K whereas a similar CMD calculation by Jakse et al.[39] yielded $D = 0.385 \pm 0.003$ Å^2/ps at $T = 1795$ K.
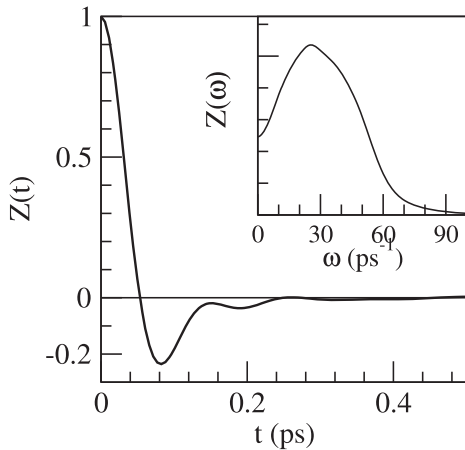
FIG. 5. Normalized AIMD calculated velocity autocorrelation function of liquid Ni at 1773 K (full line). The inset represents its power spectrum $Z(\omega)$.

2. Collective dynamics

The intermediate scattering function, $F(q, t)$, contains information on the collective dynamics of density fluctuations and it is defined as

$$F(q,t) = \frac{1}{N} \left\langle \left(\sum_{j=1}^{N} e^{-i\vec{q}\vec{R}_j(t+t_0)} \right) \left(\sum_{l=1}^{N} e^{i\vec{q}\vec{R}_l(t_0)} \right) \right\rangle. \qquad (5)$$

Its frequency spectrum is the dynamic structure factor, $S(q, \omega)$, which can be directly measured by either inelastic neutron scattering (INS) or inelastic X-ray (IXS) experiments.

Another important magnitude, also connected to the density fluctuations, is the current due to the overall motion of the particles, defined as

$$\vec{j}(q,t) = \sum_{j=1}^{N} \vec{v}_j(t) \exp[i\vec{q} \cdot \vec{R}_j(t)], \qquad (6)$$

which is usually split into a longitudinal component $\vec{j}_L(q,t)$, parallel to $\vec{q}$, and a transverse component $\vec{j}_T(q,t)$, perpendicular to $\vec{q}$ (see Refs. 33 and 36). The longitudinal and transverse current correlation functions are obtained as

$$C_l(q,t) = \frac{1}{N} \langle j_L(q,t) j_L^*(q,0) \rangle \qquad (7)$$

and

$$C_t(q,t) = \frac{1}{2N} \langle \vec{j}_T(q,t) \cdot \vec{j}_T^*(q,0) \rangle. \qquad (8)$$

The corresponding time FT gives the associated spectra $C_l(q,\omega)$ and $C_t(q,\omega)$, with $C_l(q,\omega) = \omega^2 S(q,\omega)/q^2$. These dynamical magnitudes have been calculated from the configurations generated in the present AIMD simulations. Moreover, in order to analyze the microscopic mechanisms ruling the collective dynamics, we have resorted to the generalized Langevin formalism which allows a more detailed theoretical analysis of the $F(q, t)$. In this way, starting from the calculated AIMD results for the $F(q, t)$, we have evaluated its first- and second-order memory functions, $M(q, t)$ and $N(q, t)$, respectively;[40] therefrom the $N(q, t)$ has been fitted to an analytical model which contains two exponentially decaying functions (a slow one and a fast one) i.e.,

$$N(q,t) = A_s(q)e^{-t/\tau_s(q)} + A_f(q)e^{-t/\tau_f(q)}, \qquad (9)$$

where $\tau_s(q)$ and $\tau_f(q)$ represent slow and fast relaxation times. Physically, one relaxation channel is considered of thermal origin and the other one is related to the viscoelastic behavior of the liquid. This modeling of the $N(q, t)$ allows two possible physical interpretations for its components. One choice (generalized hydrodynamic model) would be to identify the thermal relaxation with the slow channel whereas the viscoelastic relaxation is described by the fast one. The other choice (generalized viscoelastic model), which implies making the reverse identifications, has been suggested by Scopigno et al.[41] as a result of their analysis of experimental IXS data for liquid Li. More details about this modeling scheme are given in the Appendix.

Figure 6 depicts, for several q-values, the calculated AIMD results for $F(q, t)$. We observe an oscillatory behavior up to $q \approx (4/5)q_p$, with the amplitude of the oscillations
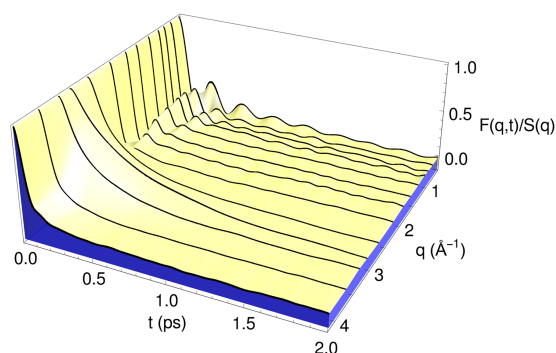
FIG. 6. Normalized AIMD intermediate scattering functions, $F(q, t)$, at several q-values, for liquid Ni at $T = 1773$ K.

becoming weaker for increasing q-values; moreover, this oscillatory shape is superposed on a weak diffusive component. At $q \approx q_p$, the $F(q, t)$ exhibit a slow decay, known as de Gennes narrowing, which is induced by the strong spatial correlations at around those q-values. Indeed, this is a typical trend exhibited by the simple liquid metals near their respective triple point.[42,44–47]

From the obtained AIMD results for $F(q, t)$, we have calculated their respective second order memory functions, $N(q, t)$, and in Figure 7 we have plotted, for some q-values, the obtained $N(q, t)$ along with its two components, namely, its fast and slow decay channels. At the smaller $q = 0.55$ Å^{-1}, both channels compete in the short time range below ≈ 60 fs although for smaller times the fast channel has a contribution more than twice that of the slow one. With increasing q-values, the contribution of the fast channel at short times becomes more prevalent although its time span remains practically constant whereas that of the slow channel increases.

Next, we analyze the physical origin of both relaxation channels in order to find out whether the obtained $N(q, t)$ are consistent with a generalized hydrodynamic model (fast viscoelastic channel and a slow thermal one), or a generalized viscoelastic model, where the fast term is the thermal one. Therefore, we have evaluated the generalized heat capacity ratio, $\gamma(q)$, which in the $q \rightarrow 0$ limit leads to the thermophysical value γ_0, i.e., the ratio between specific heats at constant pressure and at constant volume (see the Appendix). The values of $\gamma(q)$ are dependent on the model used. If the thermal relaxation proceeds along the slow channel, then $A_s(q) = (\gamma(q) - 1)M_0(q)$ and $\tau_s(q) = (\gamma(q)D_T(q))^{-1}$; however, if the viscoelastic relaxation occurs along the slow channel, then
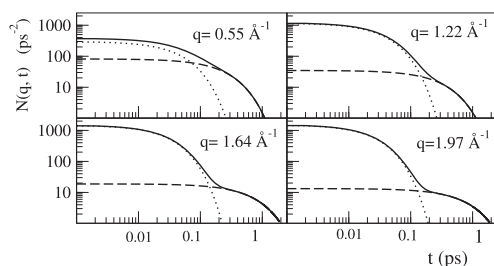
$A_s(q) = \omega_L^2(q) - \gamma(q)M_0(q)$. Thus, by using the $A_s(q)$ values obtained in the evaluation of the $N(q, t)$, we have calculated the functions $\gamma_{th}(q)$ and $\gamma_v(q)$ which correspond, respectively, to the thermal and the viscoelastic relaxations along the slow channel; these results are plotted in Figure 8.

Oddly enough, two different results are quoted as a experimental macroscopic value[12] $\gamma(q \rightarrow 0) \equiv \gamma_0$, namely, 1.34[14] and 1.88.[12,48] Nevertheless, whatever value is identified as γ_0, it is observed that the $\gamma_v(q)$ takes greater values (at least from the smallest attainable q-value ≈ 0.55 Å^{-1} onwards) and it quickly increases with q. On the other hand, the $\gamma_{th}(q)$ remains always smaller than γ_0 and, starting from $q \approx 0.55$ Å^{-1} it decreases with increasing q and tends to one at $q \approx q_p/2$. The trend exhibited by the $\gamma_{th}(q)$ is very similar to that obtained by Ruiz-Martin *et al.*[22] in a memory function type analysis of their CMD simulation results for l-Ni. Moreover, a qualitatively similar trend has also been obtained in theoretical calculations of $\gamma(q)$ for liquid Li, Bi, Pb, Hg, and Cd.[32,49] Finally, we recall that this very same trend is also exhibited by the experimental data of Hosokawa *et al.*[50] for the $\gamma(q)$ of l-Fe near melting.

The above results suggest that the slow channel is the one by which the thermal relaxation takes place and that the generalized hydrodynamic model is the appropriate one for describing the microscopic dynamics of l-Ni near the triple point.

Now, we report the results for the $S(q, \omega)$, which have been obtained by numerical Fourier transformation of the AIMD $F(q, t)$. The general trend exhibited by the calculated $S(q, \omega)$ is as follows: they show side-peaks, indicative of collective density excitations, up to $q \approx (3/5)q_p$; therefrom the side-peaks evolve into shoulders lasting until $q \approx (4/5)q_p$ and for greater q-values, the corresponding $S(q, \omega)$ show a monotonic decreasing behavior.

Figure 9 provides a comparison of the AIMD results with the IXS data of Cazzato *et al.*[17] Previously, the AIMD calculated $S(q, \omega)$ have been convoluted with the experimental resolution function and the detailed balance factor[33] has also been included. It is observed that the AIMD results show a qualitative good agreement with their respective IXS

FIG. 7. Memory function $N(q, t)$ for several q values (full line) along with its two exponential components. The dashed line represents the slow component and the dotted line stands for the fast component.
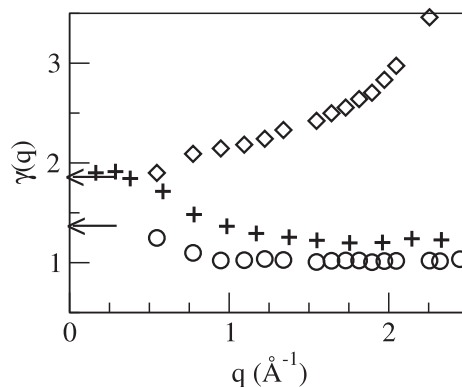
FIG. 8. Generalized specific heat ratio, $\gamma(q)$, as obtained from the generalized hydrodynamic model (circles) and the generalized viscoelastic model (lozenges). The crosses are the CMD-based results of Ruiz-Martin *et al.*[22] The arrows show the two published experimental hydrodynamic values $\gamma_0 \approx 1.34$[14] and 1.88.[12,48]
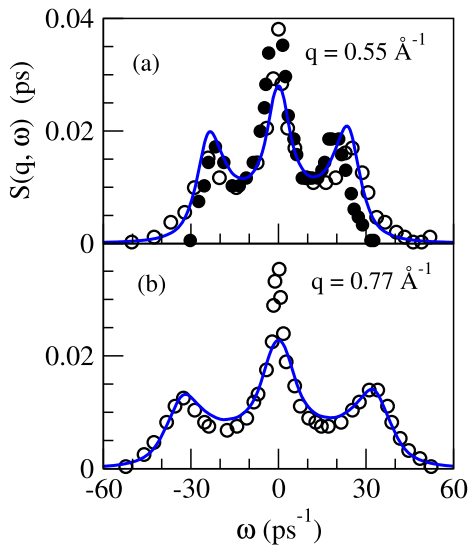
FIG. 9. Dynamic structure factors, $S(q,\omega)$, of liquid Ni. (a) Full and open circles: Experimental IXS data for $q = 0.50$ and 0.60 Å^{-1}, respectively, at $T = 1767$ K (Ref. 17). Line: AIMD results for $q = 0.547$ after convolution with the experimental resolution function and including the detailed balance condition. (b) Same as before but for experimental data are for $q = 0.80$ and the AIMD results correspond to 0.774 Å^{-1}.

ones, especially concerning the position and amplitude of the side-peaks. In Figure 10 we perform additional comparisons between the present AIMD results and the INS data of Johnson *et al.*[10] Now, the $S(q,\omega)$ is plotted as a function of q for fixed
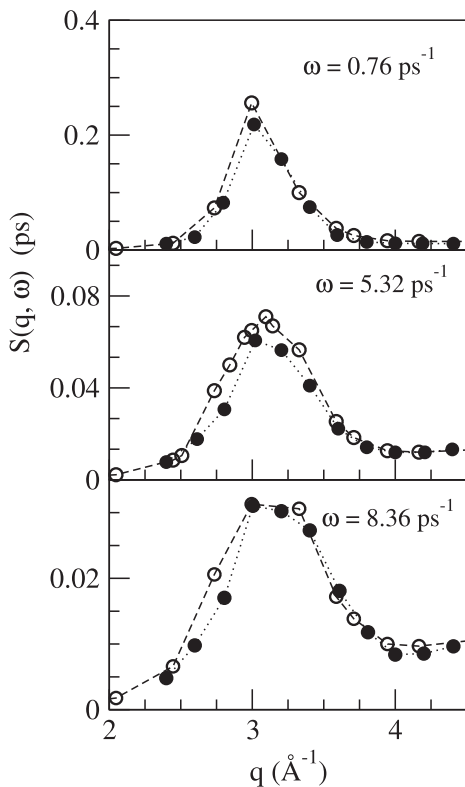
FIG. 10. Comparison of the AIMD results for $S(q,\omega)$ for l-Ni at $T = 1773$ K (open circles) for several ω values with the experimental data (full circles) of Johnson *et al.*[10] at $T = 1870$ K. The lines joining points are drawn for visual aid.

ω-values. Again, we observe a good agreement between the AIMD calculated $S(q,\omega)$ and the corresponding experimental data.

Our AIMD calculated $C_l(q,\omega)$ show one peak for each q-value and from the frequencies of those peaks, the longitudinal dispersion relation, $\omega_l(q)$, has been obtained and is plotted in Fig. 11, where we have also depicted the INS and IXS experimental dispersion relations of Bermejo *et al.*[12] and Cazzato *et al.*,[17] respectively. The IXS experimental dispersion relation was extracted by fitting the experimental scattered intensity to an expression composed of a Lorentzian (accounting for the quasielastic part) plus the DHO model (for the inelastic part). A similar procedure was followed to obtain the INS experimental dispersion relation, although an additional Lorentzian function was included to account for the incoherent part. Identifying the DHO frequency to that of the inelastic peaks, the experimental dispersion relation was finally obtained.

A first noticeable feature in Fig. 11 is the discrepancy between both experimental dispersion relations in that small q-region where they overlap. This difference has been explained[17] in terms of some kinematic limitations in the INS experiment which prevented, for the smaller q-values, a reliable estimate of the DHO model parameters.

On the other hand, we notice that in this small q-region ($q \leq 1.2$ Å^{-1}), there is a very good agreement between the IXS experimental dispersion relation and the present AIMD one. In the low-q region, the slope of the $\omega_l(q)$ curve gives a q-dependent adiabatic sound velocity which in the limit $q \to 0$ reduces to the bulk adiabatic sound velocity, c_s. We have used the AIMD results for $\omega_l(q)$, within the range $q \leq 1.0$ Å^{-1}, to evaluate its slope at $q \to 0$ and we obtained a qualitative estimate $c_{s,\text{AIMD}} \approx 4250 \pm 150$ m/s. For comparison, we recall that the experimental hydrodynamic value is $c_{s,\text{exp}} \approx 4040 \pm 150$ m/s.[13–15]

Parenthetically, we note that by resorting to the expression[36] $c_s = [\gamma k_B T/(mS(q \to 0))]^{1/2}$, where m is the atomic mass and using our calculated values for c_s and $S(q \to 0)$, we obtain an estimate $\gamma_0 \approx 1.30$ which is much closer to the experimental value reported by Blairs.[14]
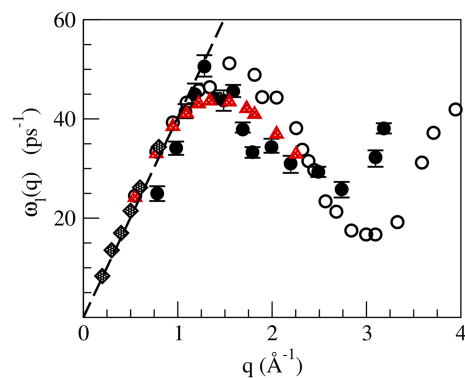
FIG. 11. Dispersion relation for l-Ni at $T = 1773$ K. Open circles: AIMD results from the positions of the maxima in the spectra of the longitudinal current, $C_l(q,\omega)$. Full circles with error bars: INS data from Bermejo *et al.* (Ref. 12). Diamonds: IXS data from Cazzato *et al.* (Ref. 17). Triangles: Dispersion relation obtained by fitting the AIMD total (neutron weighted) dynamic structure factor to a model of two Lorentzians plus the DHO model. Broken line: Linear dispersion with the hydrodynamic sound velocity, $c_s = 4030$ m/s.

For larger q's, we observe a significant difference between the INS experimental dispersion relation and the present AIMD results. Indeed, as our results are very similar to those obtained by using either CMD[19,22] or AIMD[25] simulations, we have decided to check the accuracy of the scheme followed by Bermejo *et al.*[12] to obtain the INS experimental dispersion relation. Therefore, for several q-values, we have used our AIMD results for the dynamic, $S(q, \omega)$ and self-dynamic, $S_s(q, \omega)$, structure factors which, after weighting with the corresponding coherent and incoherent neutron cross sections of Ni, were added so as to obtain the total dynamic structure factor. Subsequently, this AIMD total dynamic structure factor was modeled according the above mentioned scheme of Bermejo *et al.*[12] and therefrom, the excitation frequencies of the DHO model were evaluated in order to derive the corresponding dispersion relation. The thus obtained dispersion relation is depicted in Figure 11. We notice that this procedure recovers the correct dispersion relation as obtained directly from the AIMD currents for $q \leq 1.2$ Å^{-1}; however, it fails to reproduce the original $\omega_l(q)$ in the q region between 1.2 Å^{-1} and 2.2 Å^{-1}. In fact, it yields systematically smaller frequency values which are much closer to the INS experimental dispersion relation. It must be noted that using one Lorentzian plus one DHO to fit the coherent part gives results in good agreement with $\omega_l(q)$ in the whole q range considered. Therefore we can conclude that the problem in finding the correct frequency of the DHO in this region of q's appears because of the frequency dependence of the incoherent term added.

In our opinion, the above results may explain the discrepancies between the INS experimental dispersion relation, on the one hand, and the theoretical dispersion relations obtained by different authors, including the present AIMD results.

The transverse current correlation function, $C_t(q, t)$, is not directly measurable and provides information on the shear modes. Its spectrum, $C_t(q, \omega)$, when plotted as a function of ω, may display peaks, within some q-range, which are related to propagating shear waves. In Figs. 12 and 13 we depict, for some q's, the AIMD results for both $C_t(q, t)$ and $C_t(q, \omega)$. The calculated $C_t(q, \omega)$ already shows a peak for the smallest attainable q, i.e., $q_{\min} = 0.18 \, q_p$ and the peaks appear up to $q \leq 3.0 \, q_p$; this behavior is comparable to that of the simple liquid metals.[33] Moreover, we have found that for a small q-range, the $C_t(q, \omega)$ shows two peaks.

From the position of the peaks in the $C_t(q, \omega)$, a dispersion relation for the transverse modes has been obtained and this is
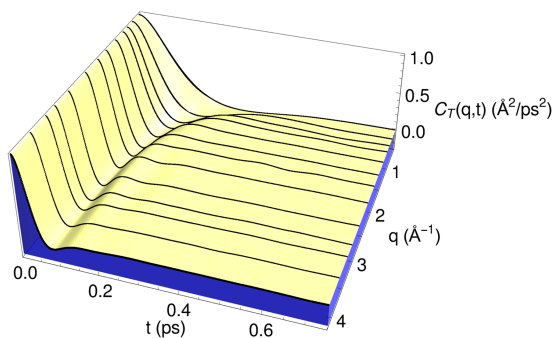
FIG. 13. Same as before, but for $C_t(q, \omega)$.

plotted in Fig. 14. We observe two branches, a high-frequency branch, $\omega_t^H(q)$, with a limited extent around q_p, and a low-frequency branch, $\omega_t^L(q)$, whose shape is typical of simple liquid metals near melting. The low-frequency branch starts at a value q_T (which is smaller than the $q_{\min}$ of the simulation), smoothly increases up to $\approx (3/5)q_p$, and therefrom it exhibits a quasi-flat behavior. Although the behavior of $\omega_t^L(q)$ at the onset of shear wave propagation is predicted to be non-analytic,[33] it is possible to define a "transverse sound velocity" in terms of the slope of $\omega_t^L(q)$ near q_T, where the dispersion is quasi-linear, i.e., it is well described by the formula $\omega_t^L(q) = c_t(q - q_{T,\text{lin}})$ where c_t is the transverse velocity of sound, and $q_{T,\text{lin}} < q_T$ is a parameter in the previous formula. We obtain (using the smallest four q-values allowed in the simulation) the estimates $q_{T,\text{lin}} \approx 0.24$ Å^{-1} and $c_T \approx 2300$ m/s. A fit to the non-analytic formula[33] $\omega_t^L = \alpha\sqrt{q^2 - q_T^2}$ leads to $q_T \approx 0.40$ Å^{-1}.

The appearance of a high frequency branch is quite unusual in monoatomic liquids. To our knowledge, it has only been found in studies performed for high pressure l-Li, l-Fe, and l-Na,[2,51,52] and it could be been explained in relation to the coupling of shear waves with other propagating modes.

From the AIMD results for the $C_t(q, t)$, we have also calculated[42,43] the associated shear viscosity coefficient η, and we obtained a value $\eta_{\text{AIMD}} = 4.10 \pm 0.20$ GPa ps. For comparison, we note that the experimental value for l-Ni at melting ($T = 1728$ K) is $\eta = 4.70$ GPa ps,[15] but its extrapolation to $T = 1773$ K gives $\eta_{\exp} \approx 4.37$ GPa ps.

Within the context of the Brownian motion of a macroscopic particle with a diameter d in a liquid of viscosity

FIG. 12. Transverse current correlation function, $C_t(q, t)$, at several q-values for l-Ni at $T = 1773$ K.
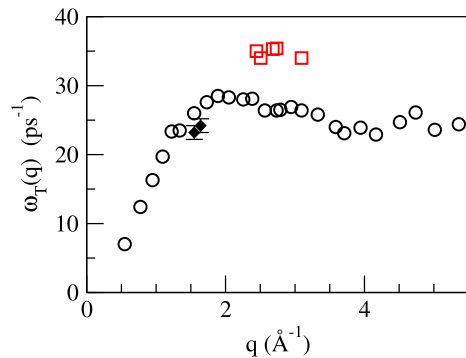
FIG. 14. Transverse dispersion relation for liquid Ni at $T = 1773$ K. Open circles and squares: AIMD results from the positions of the peaks in the spectra $C_t(q, \omega)$. The lozenges with error bars (full circles with error bars) are the positions of the transverse-like inelastic modes in the calculated (experimental) dynamic structure factors, $S(q, \omega)$.
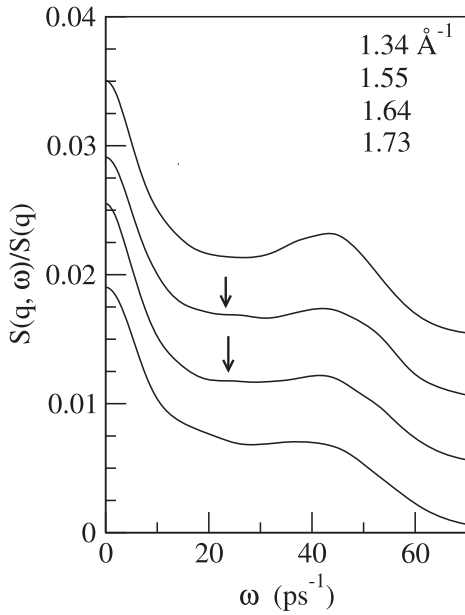
FIG. 15. AIMD calculated dynamic structure factors $S(q, \omega)/S(q)$ for (top to bottom) $q = 1.34$, 1.55, 1.64, and 1.73 Å^{-1}. The vertical scales are offset for clarity. The arrows point to the locations of the transverse-like excitations at $q = 1.55$ and 1.64 Å^{-1}.

η, the Stokes-Einstein-Sutherland relation $\eta D = k_B T/2\pi d$, establishes a connection between η and the self-diffusion coefficient D. Although not intended for atoms, this relation has been used to estimate η (or D) by identifying d with the position of the main peak of $g(r)$. The present calculations give $d = 2.43$ Å, and combined with our obtained value $D_{\text{AIMD}} = 0.375 \pm 0.02$ Å^2/ps yields an estimate $\eta = 4.27 \pm 0.3$ GPa ps which is very close to previous AIMD value.

Recently, it has been suggested[53] that transverse-like low-energy excitations may show up as shoulders located in the region between the quasielastic peak and the longitudinal inelastic peak of the dynamic structure factors. These excitations could be observed within a small q-range around $q_p/2$, because for smaller q-values they are either overcome by the quasielastic peak or quick decrease in intensity. These transverse-like excitations were first detected in the IXS spectra of l-Ga[53] at 313 K; subsequently they have also been observed in l-Cu, l-Sn, l-Na, and l-Fe.[54–56] Therefore, we have analysed the present AIMD results for $S(q, \omega)$ and they are plotted in Fig. 15. Notice that within the range 1.35 Å^{-1} ≤ q ≤ 1.70 Å^{-1}, weak shoulders are observed in the region between the quasielastic and the inelastic peaks. On the other hand, no shoulders or similar features are visible in the $S(q, \omega)$ corresponding to q's outside the above range. Additionally, as shown in Fig. 14, the energies associated with these shoulders practically agree with the peak positions of the transverse current spectra.

IV. CONCLUSIONS

We have reported an *ab initio* simulation study on the dynamical properties of l-Ni at a thermodynamic state near its triple point. This study has been spurred by the availability of INS and IXS measurements.

Several static properties have also been evaluated. Thus, results have been reported for the pair distribution function, $g(r)$, and the static structure factor, $S(q)$; both magnitudes show a very good agreement with the available experimental data.[3,5,6] The $S(q)$ shows an asymmetric shape in its the second peak, which has been connected to the appearance of icosahedral short-range order; this has been confirmed by a more detailed CNA study of the liquid structure.

The calculated intermediate scattering functions, $F(q, t)$, have been used to analyze the decay channels associated with the relaxations of the collective excitations. Specifically, the associated second-order memory function was evaluated and then fitted to two exponentially decaying functions aiming to describe a fast and a slow relaxation process. An analysis of the physical origin of both relaxation processes has concluded that a generalized hydrodynamic model is adequate for describing the microscopic dynamics of l-Ni near the triple point.

The AIMD dynamic structure factors, $S(q, \omega)$, show side-peaks which are indicative of collective density excitations and they fairly agree with the IXS data. Moreover, the calculated dispersion relation closely follows the experimental IXS data. An analysis of the modeling scheme followed to obtain the INS dispersion relation has uncovered some shortcomings which could explain its marked disparity with the dispersion relation obtained in the present study and in other simulations, both CMD and AIMD.

Furthermore, closer analysis of the AIMD $S(q, \omega)$ has revealed the same type of transverse-like excitation modes as found by Hosokawa *et al.*[54] in their IXS data.

The AIMD transverse current correlation functions, $C_t(q, t)$, exhibit clear oscillations around zero, and the associated spectra, $C_t(q, \omega)$, have inelastic peaks which reflect the presence of shear waves in l-Ni. The transverse dispersion relation shows, besides the typical low-frequency branch, a short, high-frequency one, which has not been previously found in any other monoatomic liquid metal near melting. The calculated self-diffusion and shear viscosity transport coefficients show a good agreement with experiment data.

ACKNOWLEDGMENTS

APPENDIX: MODEL FOR *N(q, t)*

We begin with the hierarchy of memory functions of $F(q, t)$ and this is most conveniently achieved through the use of the Laplace Transform technique, $\tilde{f}(z) = \int_0^\infty f(t) \exp[-zt]\, dt$. In this way, the first, $M(q, t)$, and second order, $N(q, t)$, memory functions of $F(q, t)$ are defined as

$$\tilde{F}(q, z) = \frac{F_0(q)}{z + \tilde{M}(q, z)}, \qquad \tilde{M}(q, z) = \frac{M_0(q)}{z + \tilde{N}(q, z)}, \quad (A1)$$

where $F_0(q)$ and $M_0(q)$ are the initial ($t = 0$) values of $F(q, t)$ and $M(q, t)$, respectively, and their values are $F_0(q) = S(q)$ and $M_0(q) = -\ddot{F}(q, 0)/F_0(q) = k_B T q^2/(mS(q))$, the dot denoting time derivative, with k_B the Boltzmann constant and m the

atomic mass. Moreover, since $F(q,t)$ is a real even function of time, its second derivative can be related to the second frequency moment of the $S(q,\omega)$, so that $M_0(q) = \langle\omega^2(q)\rangle/S(q) = \int_{-\infty}^{\infty} \omega^2 S(q,\omega)/S(q)\,d\omega$.

The second order memory function, $N(q,t)$, accounts for all the relaxation processes in the collective dynamics and it is a basic magnitude in most theoretical models for $F(q,t)$. Usually, the $N(q,t)$ has been written as a sum of a rapidly decaying term, which aims to describe the interactions of a particle with its nearest neighbors, plus a slowly decaying term to account for the cooperative motion of large number of particles. A convenient mathematical description is provided by writing the $N(q,t)$ as a sum of two exponentially decaying functions (a slow and a fast one), namely,

$$N(q,t) = A_s(q)e^{-t/\tau_s(q)} + A_f(q)e^{-t/\tau_f(q)}$$

$$\tilde{N}(q,z) = \frac{A_s(q)}{z + \tau_s(q)^{-1}} + \frac{A_f(q)}{z + \tau_f(q)^{-1}}. \tag{A2}$$

This model[57] conventionally ascribes to one of the exponentials the physical origin of a thermal decay channel, with amplitude $(\gamma(q)-1)M_0(q)$ and relaxation time $(\gamma(q)D_T(q))^{-1}$ whereas the other exponential accounts for a viscoelastic decay channel, with amplitude $\omega_L^2(q) - \gamma(q)M_0(q)$ and relaxation time $\tau_v(q)$. The values of the amplitudes are such that $N(q, t=0)$ recovers its correct value in terms of the second and fourth derivatives of $F(q,t)$ at $t=0$ or alternatively in terms of the second and fourth frequency moments of $S(q,\omega)$, where in particular $\omega_L^2(q) = \langle\omega^4(q)\rangle/\langle\omega^2(q)\rangle$. The other q-dependent magnitudes, namely, $\gamma(q)$ and $D_T(q)$, are generalizations of the thermophysical parameters $\gamma_0 = C_P/C_V$ (the ratio between specific heats at constant pressure and at constant volume) and the thermal diffusivity D_T.

[1] M. Marqués, L. E. González, and D. J. González, Phys. Rev. B **92**, 134203 (2015).
[2] M. Marqués, L. E. González, and D. J. González, J. Phys.: Condens. Matter **28**, 075101 (2016).
[3] Y. Waseda and M. Ohtani, Phys. Status Solidi B **62**, 535 (1974).
[4] Y. Waseda, *The Structure of Non-Crystalline Materials* (McGraw-Hill, New York, 1980).
[5] M. W. Johnson, N. H. March, B. McCoy, S. K. Mitra, D. I. Page, and R. C. Perrin, Philos. Mag. **33**, 203 (1976).
[6] T. Schenk, D. Holland-Moritz, V. Simonet, R. Bellisent, and D. M. Herlach, Phys. Rev. Lett. **89**, 075507 (2002).
[7] G. W. Lee, A. K. Gangopadhyay, R. W. Hyers, T. J. Rathz, J. R. Rogers, D. S. Robinson, A. I. Goldman, and K. F. Kelton, Phys. Rev. B **77**, 184102 (2008); N. Jakse and A. Pasturel, Sci. Rep. **6**, 20689 (2016).
[8] T. H. Kim and K. F. Kelton, J. Chem. Phys. **126**, 054513 (2007).
[9] N. Jakse and A. Pasturel, Phys. Rev. Lett. **91**, 195501 (2003); N. Jakse, O. Le Bacq, and A. Pasturel, J. Non-Cryst. Solids **353**, 3684 (2007).
[10] M. W. Johnson, B. McCoy, N. H. March, and D. I. Page, Phys. Chem. Liq. **6**, 243 (1977).
[11] G. H. Vineyard, Phys. Rev. **110**, 999 (1958).
[12] F. J. Bermejo, M. L. Saboungi, D. L. Price, M. Alvarez, B. Roessli, C. Cabrillo, and A. Ivanov, Phys. Rev. Lett. **85**, 106 (2000).
[13] S. Blairs, Phys. Chem. Liq. **45**, 399 (2007).
[14] S. Blairs, Int. Mater. Rev. **52**, 321 (2007).
[15] T. Iida and R. I. L. Guthrie, *The Thermophysical Properties of Metallic Liquids* (Oxford University Press, 2015).
[16] S. Mavila Chathoth, A. Meyer, M. M. Koza, and F. Juranyi, Appl. Phys. Lett. **85**, 4881 (2004).
[17] S. Cazzato, T. Scopigno, S. Hosokawa, M. Inui, W. C. Pilgrim, and G. Ruocco, J. Chem. Phys. **128**, 234502 (2008).
[18] P. Hohenberg and W. Kohn, Phys. Rev. **136**, B864 (1964); W. Kohn and L. J. Sham, *ibid.* **140**, A1133 (1965).
[19] M. M. G. Alemany, C. Rey, and L. J. Gallego, Phys. Rev. B **58**, 685 (1998); M. M. G. Alemany, O. Dieguez, C. Rey, and L. J. Gallego, *ibid.* **60**, 9208 (1999).
[20] A. F. Voter and S. P. Chen, in *Characterization of Defects in Materials*, MRS Symposia Proceedings No. 82, edited by R. W. Siegel, J. R. Weertman, and R. Sinclair (Materials Research Society, Pittsburg, 1987), p. 175.
[21] F. J. Cherne, M. I. Baskes, and P. A. Deymier, Phys. Rev. B **65**, 024209 (2001).
[22] M. D. Ruiz-Martin, M. Jimenez-Ruiz, M. Plazanet, F. J. Bermejo, R. Fernandez-Perea, and C. Cabrillo, Phys. Rev. B **75**, 224202 (2007); J. Non-Cryst. Solids **353**, 3113 (2007).
[23] E. Ogando Arregui, M. Caro, and A. Caro, Phys. Rev. B **66**, 054201 (2002).
[24] N. Jakse and A. Pasturel, J. Chem. Phys. **120**, 6124 (2004).
[25] N. Jakse, J. F. Wax, and A. Pasturel, J. Chem. Phys. **126**, 234508 (2007).
[26] G. Kresse and J. Furthmuller, Phys. Rev. B **54**, 11169 (1996).
[27] R. E. Rozas, A. D. Demirag, P. G. Toledo, and J. Horbach, J. Chem. Phys. **145**, 064515 (2016).
[28] D. M. Ceperly and B. J. Alder, Phys. Rev. Lett. **45**, 566 (1980); J. P. Perdew and A. Zunger, Phys. Rev. B **23**, 5048 (1981).
[29] D. Vanderbilt, Phys. Rev. B **41**, 7892 (1990).
[30] P. Gianozzi *et al.*, J. Phys.: Condens. Matter **21**, 395502 (2009).
[31] L. Calderín, D. J. González, L. E. González, and J. M. López, J. Chem. Phys. **129**, 194506 (2008).
[32] L. Calderín, L. E. González, and D. J. González, J. Chem. Phys. **130**, 194505 (2009); J. Phys.: Condens. Matter **23**, 375105 (2011); **25**, 065102 (2013); M. M. G. Alemany, R. C. Longo, L. J. Gallego, D. J. González, L. E. González, M. L. Tiago, and J. R. Chelikowsky, Phys. Rev. B **76**, 214203 (2007).
[33] U. Balucani and M. Zoppi, *Dynamics of the Liquid State* (Clarendon, Oxford, 1994).
[34] S. Sachdev and D. R. Nelson, Phys. Rev. Lett. **53**, 1947 (1984).
[35] J. D. Honeycutt and H. C. Andersen, J. Phys. Chem. **91**, 4950 (1987).
[36] J. P. Hansen and I. R. McDonald, *Theory of Simple Liquids* (Academic Press, London, 1986); J. P. Boon and S. Yip, *Molecular Hydrodynamics* (Dover, New York, 1991).
[37] A. Meyer, S. Stuber, D. Holland-Moritz, O. Heinen, and T. Unruh, Phys. Rev. B **77**, 092201 (2008).
[38] T. Iida, R. I. L. Guthrie, and N. Tripathi, Metall. Mater. Trans. B **37**, 559 (2006).
[39] N. Jakse and A. Pasturel, J. Chem. Phys. **123**, 244512 (2005).
[40] J. Souto, M. M. G. Alemany, L. J. Gallego, L. E. Gonzalez, and D. J. Gonzalez, Phys. Rev. B **81**, 134201 (2010).
[41] T. Scopigno, U. Balucani, G. Ruocco, and F. Sette, J. Phys.: Condens. Matter **12**, 8009 (2000).
[42] D. J. González, L. E. González, J. M. López, and M. J. Stott, Phys. Rev. B **65**, 184201 (2002); J. Chem. Phys. **115**, 2373 (2001).
[43] B. J. Palmer, Phys. Rev. E **49**, 359 (1994); U. Balucani, J. P. Brodholt, P. Jedlovszky, and R. Vallauri, *ibid.* **62**, 2971 (2000).
[44] A. Torcini, U. Balucani, P. H. K. de Jong, and P. Verkerk, Phys. Rev. E **51**, 3126 (1995); M. M. G. Alemany, L. J. Gallego, and D. J. González, Phys. Rev. B **70**, 134206 (2004).
[45] F. Shimojo, K. Hoshino, and M. Watabe, J. Phys. Soc. Jpn. **63**, 141 (1994); S. Sengul, L. E. González, and D. J. González, J. Phys.: Condens. Matter **21**, 115106 (2009).
[46] S. Kambayashi and G. Kahl, Phys. Rev. A **46**, 3255 (1992); J. Phys.: Condens. Matter **6**, 10897 (1994).
[47] L. E. González, D. J. González, and M. Canales, Z. Phys. B: Condens. Matter **100**, 601 (1996); J. Casas, D. J. González, and L. E. González, Phys. Rev. B **60**, 10094 (1999); J. Casas, D. J. González, L. E. González, M. M. G. Alemany, and L. J. Gallego, *ibid.* **62**, 12095 (2000).
[48] T. Scopigno, G. Ruocco, and F. Sette, Rev. Mod. Phys. **77**, 881 (2005).
[49] M. Canales, L. E. González, and J. A. Padró, Phys. Rev. E **50**, 3656 (1994); T. Bryk and I. Mryglod, J. Phys.: Condens. Matter **12**, 3543 (2000); **13**, 1343 (2001); Phys. Rev. E **63**, 051202 (2001).
[50] S. Hosokawa, M. Inui, K. Matsuda, D. Ishikawa, and A. Q. R. Baron, Phys. Rev. B **77**, 174203 (2008).
[51] T. Bryk, G. Ruocco, T. Scopigno, and A. P. Seitsonen, J. Chem. Phys. **143**, 104502 (2015).
[52] M. Marqués, D. J. González, and L. E. González, Phys. Rev. B **94**, 024204 (2016).

[53] S. Hosokawa, M. Inui, Y. Kajihara, K. Matsuda, T. Ichitsubo, W.-C. Pilgrim, H. Sinn, L. E. González, D. J. González, S. Tsutsui, and A. Q. R. Baron, Phys. Rev. Lett. **102**, 105502 (2009); Eur. Phys. J. Spec. Top. **196**, 85 (2011).

[54] S. Hosokawa, S. Munejiri, M. Inui, Y. Kajihara, W.-C. Pilgrim, A. Q. R. Baron, F. Shimojo, and K. Hoshino, AIP Conf. Proc. **1518**, 695 (2013).

[55] S. Hosokawa, S. Munejiri, M. Inui, Y. Kajihara, W.-C. Pilgrim, Y. Ohmasa, T. Sutsui, A. Q. R. Baron, F. Shimojo, and K. Hoshino, J. Phys.: Condens. Matter **25**, 112101 (2013).

[56] V. M. Giordano and G. Monaco, Proc. Natl. Acad. Sci. U. S. A. **107**, 21985 (2010).

[57] U. Bafile, E. Guarini, and F. Barocchi, Phys. Rev. E **73**, 061203 (2006).

6.2 FIRST PRINCIPLES STUDY OF BULK LIQUID TI NEAR MELTING.

Several static and dynamic properties of bulk liquid Ti at a thermodynamic state near its triple point have been evaluated by *ab-initio* molecular dynamics simulations. The calculated static structure shows very good agreement with the available experimental data, including a marked shoulder on the second peak in the structure factor, which underlines a notable local icosahedral short-range order in the liquid. The dynamical structure reveals propagating density fluctuations whose dispersion relation and damping closely follows the data obtained from the inelastic x-ray scattering measurements. The dynamical processes behind the $S(q, \omega)$ have been analyzed in terms of a model with two decay channels (a fast and a slow) associated to the relaxations of the collective excitations. Finally, results are also reported for several transport coefficients.

6.2.1 *Introduction.*

Titanium is the fourth most abundant of structural metals (after Al, Fe and Mg) and the ninth most abundant element on Earth. It has great technological interest because its high strength to weight ratio, low density, high corrosion resistance and biocompatibility. In fact, it is the key component of strong, lightweight structural alloys used in aerospace, military, automotive and biomedical application. At ambient conditions, titanium has a hexagonal close-packed structure (α phase) and on temperature increase above 1155 K, it undergoes a phase transition to a body centered cubic structure (β phase) which persists up to the melting temperature T= 1941 K. Moreover, on temperature increase at ambient pressure, the α phase transforms into a hexagonal structure, known as the ω phase.

Those important technological features of titanium can be further improved by controlling its crystallographic phases by resorting to alloying and/or high pressure work. However, a theoretical approach towards achieving this goal, would imply an accurate knowledge of the phase diagram of pure titanium. Therefore, it is no wonder that a substantial amount of work has been performed in order to generate the phase diagram of titanium [199–205].

Recently, the melting curve of titanium up to 120 GPa and $\approx$ 3500 K, has been studied by both experiment and AIMD simulations [204]. The electronic structure of the above mentioned phases have been studied by different authors [206, 207]. Balkony *et al.* have used the linear muffin-tin orbital method of band structure calculation whereas Jafari *et al.* [207] used DFT combined with the linearized-augmented-plane-wave method and the generalized gradient approximation for the electronic exchange and correlation energy. Recently, Stutzumann *et al.* [204] have studied the melting curve of Ti up to 120 GPa and $\approx$ 3500 K, using both laser heated diamond anvil cells and AIMD simulations.

However, when compared with the solid phases, the liquid part of the phase diagram has attracted much less attention and substantialy fewer works, both theoretical and experimental, have been devoted to its study. The static structure factor, $S(q)$, is an important quantity whose determination allows to extract information concerning the structural short-range order in a liquid system. For liquid Ti (l-Ti) near melting, its $S(q)$ was first measured in 1975 by an XS experiment performed by Waseda and Tamaki (WT) [208]. Their obtained $S(q)$ showed a main peak of amplitude $S(q_p) \approx 2.38$ located at $q_p \approx 2.46$ Å^{-1}, followed by symmetric oscillations of decreasing amplitude.

It took nearly 30 years until additional measurements of the $S(q)$ of l-Ti were carried out. In 2004, Lee *et al.* [209] performed another XS experiment for l-Ti at T= 1973 K and their obtained $S(q)$ showed a main peak of similar amplitude as Waseda's result but its position was located somewhat to the right, namely at $q_p \approx 2.65$ Å^{-1}. Moreover, the second peak displayed a marked shoulder on the high q side, whose intensity was even greater than that of the second peak. It is worth noting that shoulders on the high-q side of the second peak of $S(q)$ have already been found in other transition metals (Fe, Ni, Zr) [210, 211]; moreover, they are enhanced upon undercooling [212, 213]. Three years later, Holland-Moritz *et al.* [214] performed NS measurements of Ti in the liquid and undercooled states. Their data for l-Ti at T= 1965 K yielded an $S(q)$ located at the same position as Lee *et al.*'s but its second peak was fairly symmetrical with no trace of shoulders whatsoever. Notwithstanding

the discrepancies concerning the second peak, however these two latter measurements showed that Waseda and Tamaki's result for S(q) had underestimated its main peak's position by ≈ 0.20 Å^{-1}.

The first experimental investigation into the microscopic dynamics of l-Ti was carried out by Said *et al.* [215] who performed inelastic X-ray scattering (IXS) measurements of l-Ti at T = 2020 K. The scattered intensity was determined within the range $0.52 \leqslant q \leqslant 3.0$ Å^{-1} and the results were analyzed by modeling the total dynamic structure factor in terms of a generalized hydrodynamic model, namely, a Lorentzian function for the quasielastic contribution plus a DHO model for the inelastic contribution. Propagating collective excitations were detected up to q slightly greater than q_p and the related dispersion relation yielded an adiabatic velocity of sound $\approx$ 4520 ± 50 m/s. Horbach *et al.* [216] have performed quasielastic neutron scattering (QNS) measurements of the self-dynamic structure factor of l-Ti at several temperatures within the range 1953 K $\leqslant$ T $\leqslant$ 2110 K. A main objective of this experiment was the determination of the self-diffusion coefficient and this was achieved by fitting the measured self-intermediate scattering function, $F_s(q, t)$, to an exponential decay function from which the associatted self-diffusion coefficient was determined.

Stimulated by the above experimental data, we have performed a study on several static and dynamic properties of l-Ti at thermodynamic conditions near its triple point. It has been carried out by an AIMD simulation method based on DFT [1, 2].

Several theoretical studies have already focused on bulk l-Ti, by using either semiempirical or more fundamental methods. Among the early semiempirical works, we highlight Ref.[217] which basically used the hard spheres (HS) model with a packing fraction chosen so as that the calculated S(q) stood in the best possible agreement with the experimental one of WT. Haustleitner *et al.* [218] have studied the static structure of several liquid transition metals, including l-Ti, by means of an effective interionic pair potential [219] whereas the corresponding liquid static structure was derived by means of both CMD simulations and liquid state theories. A similar approach was also followed by Bhuiyan *et al.* [220] as they used effective interionic pair potentials, derived within the pseudopotential perturbation theory, combined with the variational modified hypernetted chain (VMHNC) theory of liquids [221] to analyze the static structure of liquid titanium and vanadium. Subsequently, they improved the construction of the effective interionic pair potentials by using the embedded atom model [222] which were combined with the VMHNC theory to compute the static structure factors, Helmholtz free energies, internal energies, and entropies of the 3d, 4d, and 5d liquid transition metals [223].

Interestingly, all the above mentioned theoretical calculations obtained S(q) whose main peak was closer to the recent results of Lee *et al.* [209] and Holland-Moritz *et al.* [214]. However, at that time they could only compare with Waseda and Tamaki's result and the clear discrepancy somehow hindered the effort to extend the theoretical investigations to other static and/or dynamic properties.

In this thesis, we report an AIMD simulation study of the dynamic (and static) properties of l-Ti at a thermodynamic state near its triple point. To our knowledge, this is the first AIMD investigation on the static and dynamic properties of bulk l-Ti. Besides its intrinsic interest, we have chosen this specific thermodynamic state because of the recent availability of IXS measurements. The layout of the study is as follows: in section 6.2.2 we briefly sketch the theory underlying the present AIMD simulations and describe some technical details as well as some of the terms appearing in the Kohn-Sham energy functional. In section 6.2.3 we present and discuss the obtained structural and dynamical results which are compared with other previous studies as well as with the available experimental data. Finally some conclusions are drawn.

6.2.2 *Computational details.*

We performed AIMD calculations for l-Ti at a thermodynamic state [225] characterized by a number density, $\rho_i = 0.0522$ Å^{-3} and temperature T = 2000 K. The electronic exchange-correlation energy adopted is the local generalized gradient approximation of Perdew and Wang [224], including non-linear core corrections. The ion-electron interaction has been described by means of an ultrasoft pseudopotential [128], which was generated from a scalar-relativistic calculation of the atomic electron configuration [Ne]$3s^2$ $3p^6$ $3d^2 4s^2$.

We used 100 atoms (i.e. 100 x (2d+10s, p) = 1200 valence electrons) in a cubic supercell. The system was thermalized during 10 ps of simulation time and therefrom microcanonical AIMD simulations were performed over 30700 time steps which, by using an ionic time step of 0.0045 ps, amounted to 138.15 ps of simulation time. The ionic dynamics was generated by using the Verlet algorithm [226] with HF forces as implemented in the Quantum-Espresso package [227]. We have used a plane-wave representation with an energy cutoff of 25.0 Ryd and the single Γ point was employed for sampling the Brillouin zone. Finally, we remark that the 30700 equilibrium configurations were employed for the evaluation of the static and dynamic properties of bulk l-Ti. This same simulation method has already provided an accurate description of several static and dynamic properties of bulk l-Sn, l-Hg, l-Cd, l-Ag and l-Ni.[189, 190, 228–231]

6.2.3 *Results.*

Static properties.

The AIMD simulations provide a direct evaluation of both the pair distribution function, $g(r)$, and the static structure factor, $S(q)$. Figure 6.1 shows the obtained AIMD result for $g(r)$ which is compared with the corresponding XS data of Waseda [192, 208] and the NS diffraction data of Holand-Moritz *et al.* [214].

The coordination number (CN) has been evaluated by integrating the radial distribution function, $4\pi\rho_i r^2 g(r)$, up to the position of its first minimum, which for our calculated AIMD $g(r)$ is located at $R_{min} = 3.92$ Å, leading to a value CN ≈ 13.3 atoms. Had we chosen $R_{min} = 4.0$ Å, which is the position for the first minimum in $g(r)$, then CN ≈ 14.0 atoms. Notwithstanding the procedure used to evaluate CN, the obtained values are typical of simple liquid metals at thermodynamic conditions near their respective triple point [23].

The bond angle distribution function $g_3(\theta)$ gives information about the distribution of bond angles defined by atoms up to a distance which we have taken as the first minimum in $g(r)$. The calculated $g_3(\theta)$, shown in the inset of Figure 6.2, exhibits two distinct peaks at 55° and 108°. This feature, along with the previous values of CN, are close to those of a system with local icosahedral structure, which is something common in the simple liquid metals near melting [23].

Figure 6.2 shows the AIMD result for $S(q)$, which is compared with the XS [192, 208, 209] and NS [214] diffraction data. First, we mention that Waseda and Tamaki's XS data are clearly different from the more recent XS [209] and NS [214] data which, moreover, are very similar to the present AIMD simulations. Therefore, we will focus our discussion on these more recent experimental data. The experimental $S(q)$'s have a symmetric main peak located at a position $q_p \approx 2.65$ Å^{-1} and its height takes values between $S(q_p) \approx 2.35$ and ≈ 2.68 according to the XS [209] and NS [214] data respectively. Interestingly, the XS data of Lee *et al.* [209] yieded an $S(q)$ with a second oscillation located at $q \approx 4.9$ Å^{-1} along with an even more intense shoulder at $q \approx 5.1$ Å^{-1}. Oddly enough, this feature does not show up in the NS data [214] as its measured $S(q)$ shows a symmetric second peak located at $q \approx 4.9$ Å^{-1}.

The present AIMD simulations yield an $S(q)$ in overall good agreement with the experimental data, i.e. its main peak's position is at $q_p \approx 2.63$ Å^{-1} and its height is $S(q_p) \approx 2.82$, whereas the subsequent oscillations are almost in phase with the experimental data. Moreover, our calculated second maximum, which is located at $q \approx 4.7$ Å^{-1}, has also a small shoulder located at the same position as in the XS data of Lee *et al.* [209]. An asymmetric shape of the second peak of $S(q)$ has been experimentally observed in several liquid transition metals and it has been related to an important presence of icosahedral (ICOS) local order. A first indication of this type of short range order is given by the positions of the maximum of the second peak of $S(q)$, q_2, and its shoulder, q'_2, as compared to the position of the main peak. The present AIMD results for l-Ti are $q_2/q_p = 1.79$ and $q'_2/q_p \approx 1.94$, which compare well with those of Lee *et al.* [209], namely 1.85 and 1.92 respectively. Besides, these ratios are analogous to those found in other liquid transition metals such as l-Fe (1.79 and 1.91), l-Ni (1.77 and 1.95) and l-Zr (1.76 and 1.92). By the way, we remind that the respective values for an ideal icosahedral cluster are 1.71 and 2.04 [232].
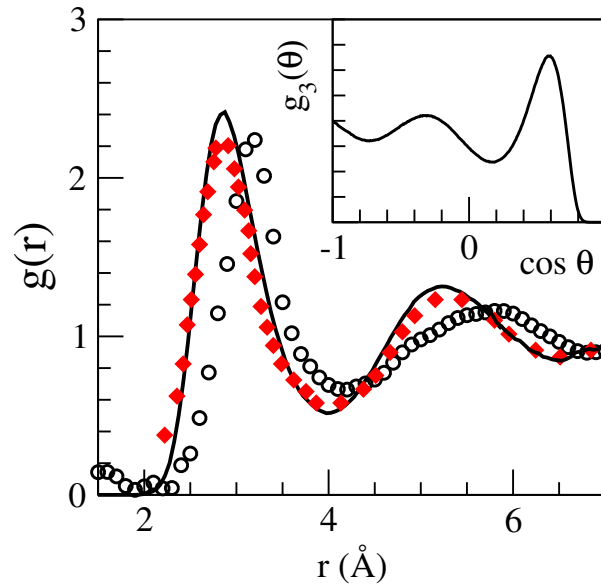
FIGURE 6.1: Pair distribution function, $g(r)$, of l-Ti. Continuous line: present AIMD calculations at T=2000 K. Open circles: XS diffraction data from Waseda [192, 208] at T=1973 K. Full diamonds: NS diffraction data from Holand-Moritz *et al.* [214] at T= 1965 K. The inset shows the computed bond angle distribution, $g_3(\theta)$.
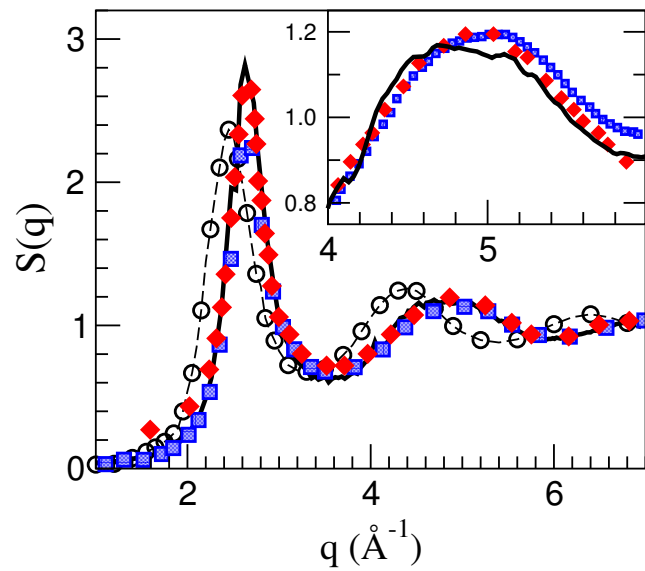
FIGURE 6.2: Static structure factor, $S(q)$, of liquid Ti at T=2000 K. Continuous line: present AIMD calculations. Open circles and blue squares: experimental XS diffraction data from Waseda [192, 208] and Lee *et al.* [209] at T=1973 K. Red diamonds: experimental NS diffraction data from Holand-Moritz *et al.* [214] at T= 1965 K. The inset shows a detailed comparison for the second maximum.

TABLE 7: Common neighbour analysis of the AIMD configurations of l-Ti at 2000 K compared with several local structures.

Pairs	1551	1541	1431	1321	1421	1422	1301	1441	1661
l-Ti	0.42	0.13	0.09	0.0	0.0	0.01	0.0	0.12	0.20
ICOS	1.0	0.0	0.0	0.0	0.0	0.0	0.0	0.0	0.0
HCP	0.0	0.0	0.0	0.0	0.50	0.50	0.0	0.0	0.0
FCC	0.0	0.0	0.0	0.0	1.0	0.0	0.0	0.0	0.0
BCC	0.0	0.0	0.0	0.0	0.0	0.0	0.0	0.43	0.57

We have estimated the isothermal compressibility, κ_T, of l-Ti by resorting to the relation $S(q \rightarrow 0) = \rho_i k_B T \kappa_T$, where k_B is Boltzmann's constant. To this end, the calculated $S(q)$ has been extrapolated to $q \rightarrow 0$ by using a least squares fit $S(q) = s_0 + s_2 q^2$ for $q \leqslant 1.2$ Å^{-1}. We obtained a value $S(q \rightarrow 0) = 0.018 \pm 0.001$, which yields a result $\kappa_T = 1.28 \pm 0.10$ (in units of 10^{11} m^2 N^{-1}). We are not aware of any experimental data for this property but for comparison we mention that Blairs [233] has suggested a value $\kappa_T \approx 1.67 \pm 0.02$ which was obtained by resorting to an empirical formula relating isothermal compressibility, surface tension and surface thickness in liquid metals.

A more detailed, three dimensional, description of the local order in l-Ti can be achieved by refering to the common neighbour analysis [234] (CNA) method already described in bulk liquid Ni's study. Using a few configurations generated in the present AIMD simulation, we have first removed the thermal noise by finding the corresponding inherent structures, and then we have performed a CNA calculation. The results are summarized in Table 7.

First, notice that the fivefold symmetry dominates in l-Ti, as the sum of perfect ($\approx 42\%$) and distorted ($\approx 22\%$) ICOS structures amounts to $\approx 64\%$ of the pairs. The analysis performed by Holland-Moritz *et al.* [214] concluded that a good description of their NS measurements was attained by assuming that perfect ICOS clusters prevail in l-Ti, Furthermore, the agreement was improved if they assumed the existence of larger polytetrahedral clusters (such as dodecahedra).

It should be noted that 1551 clusters (usually named perfect icosahedral ones) show indeed the same number and type of bonds as the pentagonal bipyramid associated to an ideal icosahedron. However, the particular location of the five common neighbours of the root pair could be distorted as compared to the icoshaedral pentagon. In particular, they may not lie on a single plane, the pentagon may not be regular, or the position of the closest plane to the five atoms may be shifted with respect to that of the icosahedron, so that the bond between the root pair and that from one atom to a common neighbour may form an angle different from the icosahedral one. This latter distortion was particularly contemplated by Lee *et al.* [209], who related it to the strength of the shoulder in the second peak of $S(q)$. In particular for a distortion larger than around 5 degrees, their model turned the shoulder in fact higher than the peak, in correspondence with their measured $S(q)$. We have analyzed the 1551 structures obtained in our simulations, and found that the bond angles are actually distorted by around 7 degrees from the icosahedral one, whereas the pentagons are fairly planar and regular. However we cannot directly related such distortion to the relative strengths of the components of the second peak due to the large statistical noise associated to the limited number of configurations for which we have performed the CNA analysis.

Finally we mention the existence of a significant $\approx 32\%$ appearance of local BCC-type pairs which happens to be the phase in which l-Ti crystallizes.

Dynamic properties

We have calculated several dynamic properties, both single-particle (self- intermediate scattering functions, self-dynamic structure factors, velocity autocorrelation function and mean square displacement) and collective ones

(intermediate scattering functions, dynamic structure factors, longitudinal and transverse currents). The evaluation of the time correlation functions has been performed by taking time origins every five time steps.

Single particle dynamics

The obtained AIMD results for the $F_s(q,t)$ show, for all q values, the typical monotonic decreasing behavior with time. This is shown in Fig. 6.3 where we provide a comparison, for some q-values, between our calculations and the QNS data of Horbach *et al.* [216] for l-Ti at T=1953 K.
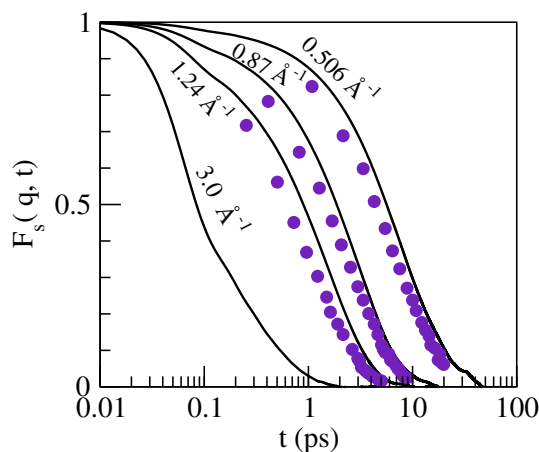
FIGURE 6.3: Self-intermediate scattering function, $F_s(q,t)$, of l-Ti for several q-values. Full circles: Experimental data of Horbach *et al.* [216] for T=1953 K and (from right to left) $q = 0.50$, 0.90 and 1.30 Å^{-1}. Full lines: Calculated AIMD results for T = 0.506, 0.87, 1.24 and 3.0 Å^{-1} respectively.

Closely related to $F_s(q,t)$ is the velocity autocorrelation function (VACF) of a tagged ion in the fluid, $Z(t)$.
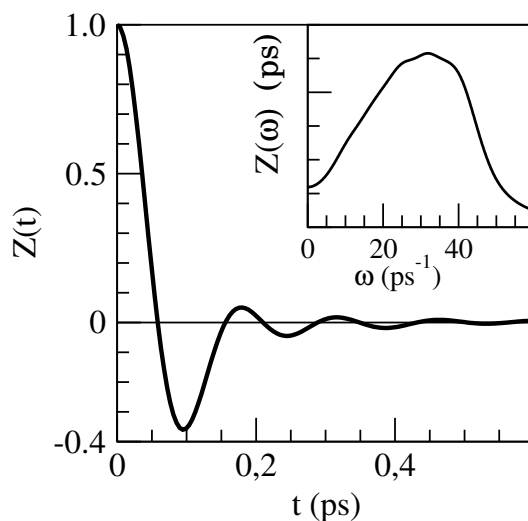
FIGURE 6.4: Normalized AIMD calculated velocity autocorrelation function of liquid Ti at 2000 K (full line). The inset represents its power spectrum $Z(\omega)$.

Our AIMD result for $Z(t)$ is plotted in Figure 6.4 where we observe the typical backscattering behavior along with a marked first minimum which is followed by oscillations of decreasing amplitude. A short time fitting of

the $Z(t)$ curve in Fig. 6.4 gives a value for the Einstein frequency of $\omega_E \approx 29.5$ ps^{-1}. The inset in Figure 6.4 represents the associated power spectrum, $Z(\omega)$, which shows a weak shoulder located at ≈ 26 ps^{-1} and a peak at ≈ 33 ps^{-1}; parenthetically we note that ω_E stands between the shoulder and the peak of $Z(\omega)$, which is a characteristic feature of the simple liquid metals [23].

The self-diffusion coefficient, D, can be found by either the time integral of $Z(t)$ or from the slope of the mean square displacement $\delta R^2(t) \equiv \langle |\vec{R}_1(t) - \vec{R}_1(0)|^2 \rangle$ of a tagged ion in the fluid. In this AIMD study, both routes have yielded the same value, namely $D_{AIMD} = 0.49 \pm 0.01$ Å^2/ps at T = 2000 K, which compares well with the QNS data of $D_{exp} \approx 0.53 \pm 0.02$ Å^2/ps for l-Ti at T = 2000 K of Horbach *et al.* [216]. Indeed, by means of the QNS technique they determined the self-diffusion coefficient of l-Ti within a temperature range up to ≈ 170 K above the melting point.

Collective dynamics.
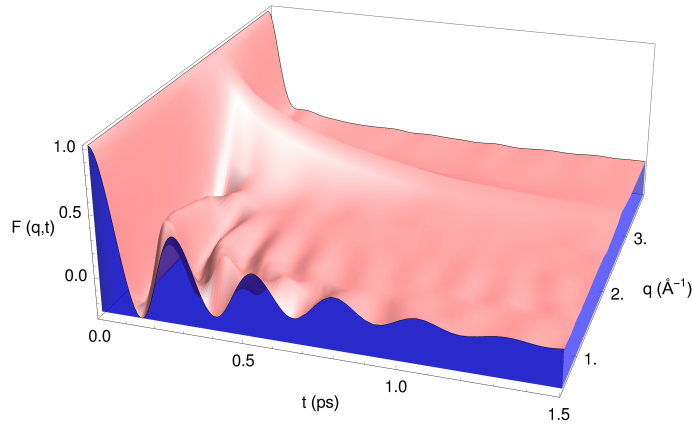
FIGURE 6.5: Normalized intermediate scattering functions, $F(q,t)$, at several q-values (in Å^{-1} units), for liquid Ti at T = 2000 K. Dotted lines: present AIMD results. Full lines: fittings of the AIMD results to the analytical model indicated in the text.

Figure 6.5 depicts, for a range of q-values, the AIMD results for $F(q,t)$ which show an oscillatory behaviour up to $q \approx (4/5)\ q_p$, with the amplitude of the oscillations becoming weaker for increasing q-values. At $q \approx q_p$, the $F(q,t)$ exhibits a slow decay responsible of the known "de Gennes narrowing" of the corresponding spectrum.

Resorting to the generalized Langevin formalism provides some insight into the microscopic mechanisms ruling the collective dynamics. To this end, we have used the calculated AIMD results for the $F(q,t)$ in order to evaluate its associated first- and second-order memory functions, $M(q,t)$ and $N(q,t)$ respectively; then, the obtained $N(q,t)$ have been fitted to an analytical model used in the previous study of bulk liquid Ni,

$$N(q,t) = A_s(q)e^{-t/\tau_s(q)} + A_f(q)e^{-t/\tau_f(q)} \tag{155}$$

where $\tau_s(q)$ and $\tau_f(q)$ represent slow and fast relaxation times.

We have calculated the second order memory functions, $N(q,t)$, and in Figure 6.6 we have plotted, for some q-values, the obtained $N(q,t)$ along with its two components, namely, its fast and slow decay channels. At the smaller q =0.506 Å^{-1}, both channels contribute in the time range below ≈ 10 fs although for smaller times the fast channel has a contribution which is around twenty times greater than that of the slow one. With increasing q-values, the contribution of the fast channel at short times becomes more dominant although its time span decreases whereas that of the slow channel hardly changes.
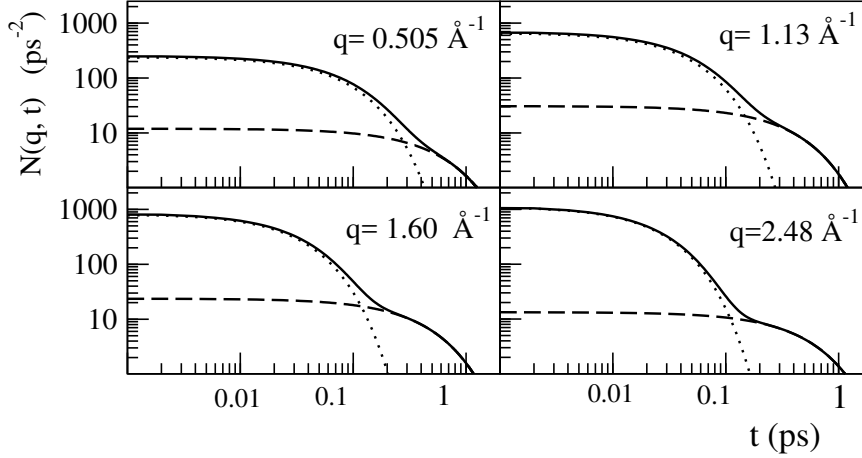
FIGURE 6.6: Memory function $N(q, t)$ for several q values (full line) along with its two exponential components. The dashed line represents the slow component and the dotted line stands for the fast component.

We have analyzed the physical origin of both relaxation channels in order to find out whether the obtained $N(q, t)$ are consistent with a generalized hydrodynamic model (fast viscoelastic channel and a slow thermal one), or a generalized viscoelastic model, where the fast term is the thermal one, following the notation previously explained in Chapter 3. Therefore, we have evaluated the generalized heat capacity ratio, $\gamma(q)$, which in the $q \to 0$ limit leads to the thermophysical value γ_0, i.e. the ratio between specific heats at constant presure and at constant volume (see Appendix D).

It is observed that, starting from the smallest attainable q value, $q_{min} = 0.506\,\text{Å}^{-1}$, where $\gamma_v(q_{min}) \approx 1.65$, then it shows a monotonous increasing behaviour. On the other hand, the $\gamma_{th}(q)$ starts from a value $\gamma_{th}(q_{min}) \approx 1.0$ and practically remains constant until near q_p where it increases up to a value $\gamma_{th}(q_p) \approx 1.25$, therefrom it smoothly decreases towards values ≈ 1.0. Although there are no experimental data for $\gamma(q)$ in l-Ti, we can reach some conclusions by comparing with the trends exhibited by the $\gamma(q)$ in other liquid metals near melting. According to those studies [189, 190, 229, 239], the $\gamma(q)$ shows a continuous decrease from the initial value $\gamma(q = 0) \equiv \gamma_0$ towards values around 1.0 at $q_p/2$ and then there is a smooth increase with a maximum at $\approx q_p$. We also recall that this same trend is also exhibited by the "experimental" data of Hosokawa *et al.* [240] for the $\gamma(q)$ of l-Fe near melting. Consequently, we conclude that the previous results suggest that the slow channel is the one associated to the thermal relaxation and that the generalized hydrodynamic model is the appropriate one for describing the microscopic dynamics of l-Ti near its triple point.

The model of Eq. (155) leads to an associated $F(q, t)$ with an analytical expression comprising four exponential terms (two real and two with complex conjugate amplitudes and exponents), i.e.

$$
\begin{aligned}
\frac{F(q,t)}{S(q)} = \quad & A_1(q)\,\exp(-a_1(q)t) + A_2(q)\,\exp(-a_2(q)t) + \\
& \exp(-b(q)t)\,[\,B(q)\,\cos(\omega_s(q)t) + C(q)\,\sin(\omega_s(q)t)]
\end{aligned}
\tag{156}
$$

Out of the eight q-dependent parameters ($A_1(q), A_2(q), B(q), C(q), a_1(q), a_2(q), b(q), \omega_s(q)$), only four are left as independent when the correct short time behavior (initial value equal to one, zero initial values for the first and third derivatives and initial value of the second derivative equal to the second frequency moment) is imposed. The time FT of Eq. (156) gives the associated $S(q, \omega)$ whose analytical expression comprises a sum of two central Lorentzians plus a pair of asymmetric Lorentzians inelastic peaks.
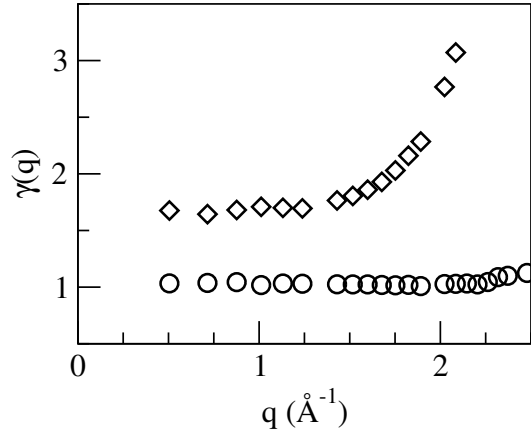
FIGURE 6.7: Generalized specific heat ratio, $\gamma(q)$, as obtained from the generalized hydrodynamic model (circles) and the generalized viscoelastic model (lozenges).

We have verified that the model of Eq. (156) provides an excellent fitting for the present AIMD results for $F(q,t)$. The associated $S(q,\omega)$ has been computed by both direct numerical FT calculation and by using the analytical expression derived from Eq. (156). Both routes yielded very similar $S(q,\omega)$'s and the only noticeable difference was the contact value, $\omega=0$.

In figure 6.8 we have plotted, for a range of q-values, the AIMD results for $S(q,\omega)$ which were obtained by numerical FT of the corresponding $F(q,t)$. The general trend exhibited by the $S(q,\omega)$ is as follows: they show side-peaks, indicative of collective density excitations, up to $q \approx (4/5)q_p$ and for greater q-values the corresponding $S(q,\omega)$ show a monotonic decreasing behavior.
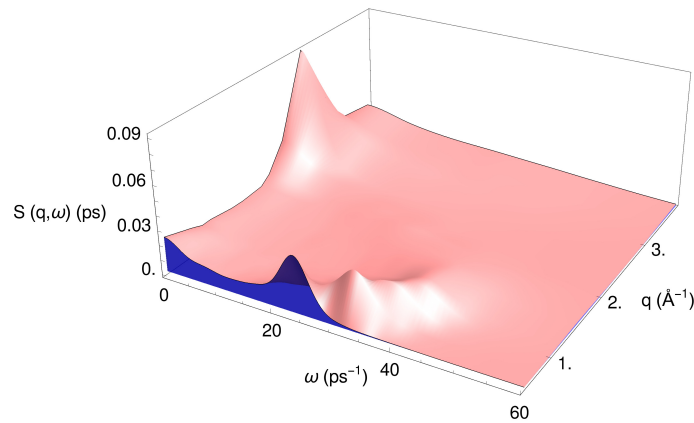
FIGURE 6.8: Dynamic structure factors, $S(q,\omega)$, of liquid Ti at T=2000 K and several q values.

From the positions of the side-peaks, $\omega_m(q)$, the corresponding dispersion relation of the density fluctuations has been derived and it is plotted in Figure 6.9. The slope of the $\omega_m(q)$ curve at $q \to 0$ yields the adiabatic sound velocity, c_s; however the small size of the simulation box implies that the smallest attainable q value, q_{min}, is not small enough to afford a precise quantitative estimate of c_s. Nevertheless a qualitative guess may be extracted

as $c_{s,AIMD}(q_{min}) = \omega_m(q_{min})/q_{min} \approx 4640 \pm 100$ m/s which compares well with the experimental hydrodynamic value $c_{s,exp} \approx 4407 \pm 108$ m/s [241].

Figure 6.9 also includes the dispersion relation for the longitudinal modes, $\omega_L(q)$, which has been obtained from the AIMD results for the spectra $C_L(q,\omega)$. For each q-value, the associated $C_L(q,\omega)$ shows just one peak and from the frequencies of these peaks the dispersion $\omega_L(q)$ has been derived. We have also depicted in Figure 6.9 the IXS "experimental" dispersion relation of of Said *et al.* [215] which was extracted by fitting the experimental scattered intensity to an analytical expression of the generalized hydrodynamic model composed of a lorentzian (accounting for the quasielastic part) plus the DHO model (for the inelastic part). Next, by identifying the DHO frequency to that of the inelastic peaks, the "experimental" dispersion relation was obtained. Moreover, from low-q linear behaviour of their obtained IXS "experimental" dispersion Said *et al.* [215] obtained an estimate $c_{s,IXS} \approx 4520 \pm 50$ m/s which is in reasonable agreement with the experimental hydrodynamic value.

Another important quantity derived by Said *et al.* [215] from the above mentioned fitting procedure, was the half-width at half-maximum (HWHM) of the inelastic peaks which provides information on the lifetimes of the collective density excitations. Their obtained "experimental" values of the HWHH are plotted Figure 6.9 where we observe an almost linear behavior up to $q \approx q_p/2$, suggesting that the hydrodynamic limit (quadratic law) is restricted to very low q values. Figure 6.9 also includes the corresponding AIMD results for the HWHM of the inelastic peaks which closely follow the experimental data. We notice that its calculation requires to single out the contribution from the propagating excitations to the $S(q,\omega)$; for this purpose, we have fitted the AIMD $F(q,t)$ to Eq. (156) and the obtained values for the parameter $b(q)$ were identified with the HWHM.

Another result derived by Said *et al.* [215] was the HWHM of the central, quasielastic, peak and in Figure 6.10 we have depicted their "experimental" data which are compared with the results obtained in the present AIMD simulations. There is a good qualitative agreement with both curves attaining their minimum value at the position of the main peak of the $S(q)$; in fact, this type of behaviour has already been observed in other liquid metals [63].
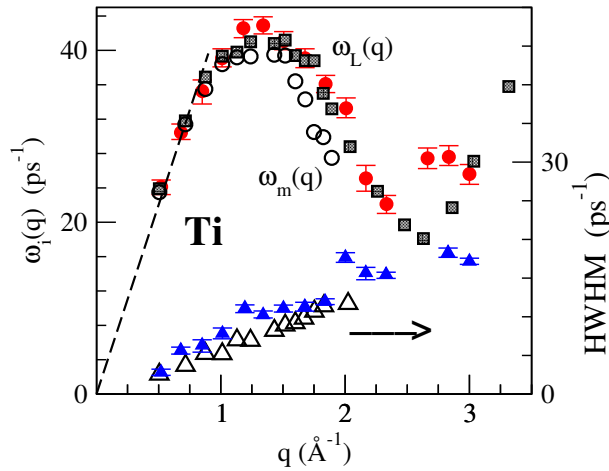
FIGURE 6.9: Dispersion relation for l-Ti at T = 2000 K. Open circles and grey squares: AIMD results from the positions of the inelastic peaks in the $S(q,\omega)$ and from the maxima in the spectra of the longitudinal current, $C_L(q,\omega)$, respectively. Full circles with error bars: IXS experimental data at T= 2020 K, from Said *et al.* (Ref. [215]). The open triangles represent the AIMD results for the HWHM of the inelastic peaks of $S(q,\omega)$ whereas the full triangles with error bars stand for the corresponding IXS experimental data (Ref. [215]). Broken line: linear dispersion with the hydrodynamic sound velocity, c_s = 4407 m/s. (Ref. [241]).

We note that by resorting to the expression [24] $c_s = [\gamma_0 k_B T/m S(q \to 0)]^{1/2}$, where m is the atomic mass and using our AIMD values for c_s (4640 m/s) and $S(q \to 0)$ (0.018), we obtain an estimate $\gamma_0 \approx 1.12$, which is in qualitative agreement with the low-q behaviour of $\gamma(q)$ as evinced by Figure 6.7.
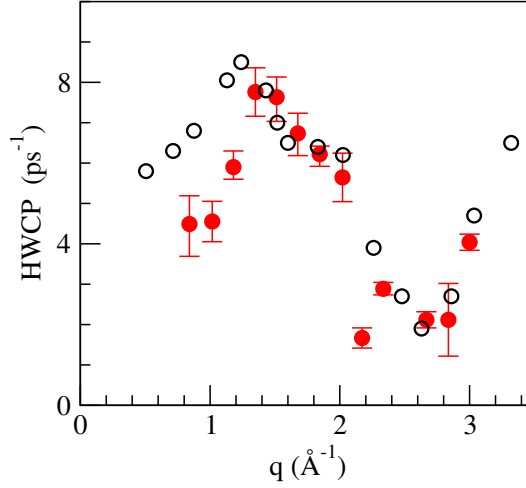
FIGURE 6.10: The HWHM of the central quasielastic peak of the $S(q,\omega)$. Open circles: AIMD results from the positions of the obtained $S(q,\omega)$. Full circles with error bars: IXS experimental data at T= 2020 K, from Said *et al.* (Ref. [215]).

In Figures 6.11-6.12 we have depicted, for some q range, the obtained AIMD results for both the transverse current correlation function, $C_T(q,t)$, and its spectrum, $C_T(q,\omega)$. The calculated $C_T(q,\omega)$ already show a peak for the smallest attainable q ($q_{min} = 0.506$ Å^{-1}), and with increasing q-values the peaks become broader and less marked, lasting up to $q \leqslant 3.0$ q_p. This is a trend similar to what has already been found in several simple liquid metals [23].
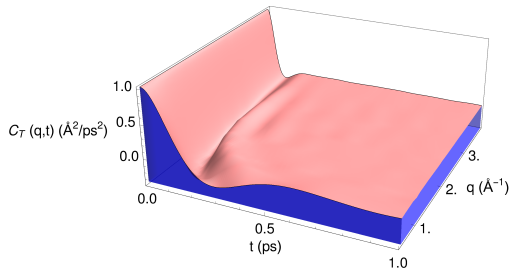
FIGURE 6.11: Transverse current correlation function, $C_T(q,t)$, at several q-values for l-Ti at $T = 2000$ K.
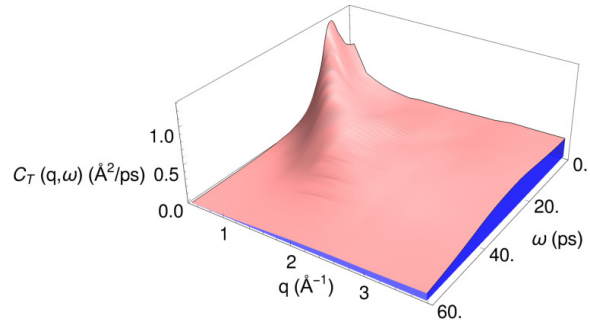
FIGURE 6.12: Same as before, but for $C_T(q,\omega)$.

From the position of the peaks in the $C_T(q,\omega)$, a dispersion relation for the transverse modes has been obtained and this is plotted in Fig. 6.13. We observe one branch, $\omega_t(q)$, whose shape is comparable to that shown by the simple liquid metals near melting. It sets in at a value $q_T > 0$ (which is smaller than the q_{min} of the simulation), smoothly increases up to $\approx(4/5)q_p$ where it reaches a maximum and therefrom smoothly decreases. Although the behavior of $\omega_T(q)$ at the onset of shear wave propagation is predicted to be non-analytic [23], it is possible to define a "transverse sound velocity" in terms of the slope of $\omega_T(q)$ near q_T, where the dispersion is quasi-linear, i.e., it is well described by the formula $\omega_t(q) = c_t(q - q_{T,lin})$ where c_T is the transverse velocity of sound, and $q_{T,lin} < q_T$ is a parameter in the previous formula. We obtain (using q-values up to ≈ 1.13 Å^{-1}) the estimates $q_{T,lin} \approx 0.11 \pm 0.01$ Å^{-1} and $c_T \approx 2450 \pm 100$ m/s. A fit to the non-analytic formula [23] $\omega_t = \alpha\sqrt{q^2 - q_T^2}$ leads to $q_T \approx 0.25 \pm 0.02$ Å^{-1}.

From the AIMD results for the $C_T(q,t)$, we have also calculated [96, 123, 242] the associated shear viscosity coefficient η, and we obtained a value $\eta_{AIMD} = 2.85 \pm 0.15$ GPa ps. To our knowledge, there are two (rather dissimilar) experimental data to compare with. Agaev *et al.* [243] measured the shear viscosity of l-Ti at melting (T = 1943 K) by using the capillary technique and they obtained $\eta_{exp} \approx 2.2$ GPa ps. On the other hand, Paradis *et al.* [244] used the oscillation drop technique in a levitated sample to measure the shear viscosity of l-Ti in the temperature range 1750 K $\leqslant$ T $\leqslant$ 2050 K; for the melting temperature (T=1943 K) they obtained $\eta_{exp} \approx 4.42$ GPa ps which is twice the value reported by Agaev *et al.*. In any case, we notice that the AIMD result stands between the two previous experimental data.

Within the context of the Brownian motion of a macroscopic particle with a diameter d in a liquid of viscosity η, the Stokes-Einstein-Sutherland (SES) relation $\eta D = k_B T/2\pi d$, establishes a connection between η and the self-diffusion coefficient D. Although not intended for atoms, this relation has been used to estimate η (or D) by identifying d with the position of the main peak of $g(r)$. The present calculations give d = 2.87 Å, and combined with our obtained value $D_{AIMD} = 0.49 \pm 0.01$ Å^2/ps yields an estimate $\eta = 3.15 \pm 0.10$ GPa ps which is slightly greater, by $\approx$10%, than the calculated AIMD value. We recall that similar deviations have been found in the application of the SES relation to a variety of liquid metals near melting.
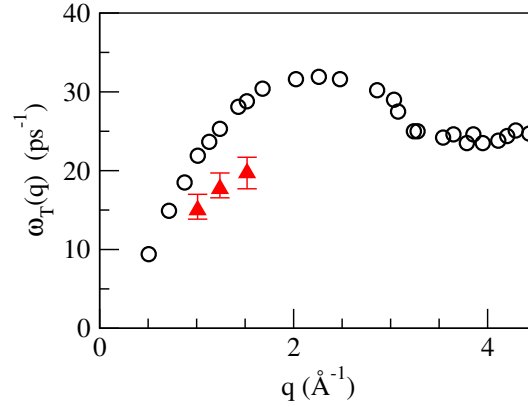
FIGURE 6.13: Transverse dispersion relation for liquid Ti at T = 2000 K. Open circles: AIMD results from the positions of the peaks in the spectra $C_T(q,\omega)$. The lozenges with error bars (full circles with error bars) are the positions of the transverse-like inelastic modes in the calculated (experimental) dynamic structure factors, $S(q,\omega)$, shown in next Fig. 6.14

Recently, it has been suggested [245] that transverse-like low-energy excitations might be observed as weak shoulders located in the region between the quasielastic and the longitudinal inelastic peaks of the dynamic structure factors. These excitations are usually visible within a small q-range around $q_p/2$, because for smaller/greater q-values they are overcome by the quasielastic/inelastic peaks. These transverse-like excitations were first detected in the IXS spectra of l-Ga [245] at 313 K; subsequently they have also been observed in l-Cu, l-Sn, l-Na, l-Fe and l-Ni [231, 246–248].

We have analysed the AIMD results for $S(q,\omega)$ and found that within the range 1.00 Å^{-1} $\leqslant$ q $\leqslant$ 1.45 Å^{-1}, some weak shoulders show up in the ω-region located between the quasielastic and the inelastic peaks. This is shown in Fig. 6.14 where it is also noticed that outside the above q-range, those weak shoulders are no longer visible in the $S(q,\omega)$. Furthermore, as shown in Fig. 6.13, the energies associated to these shoulders are close to those corresponding to the peaks in the transverse current spectra.

Electronic properties: Density of states

We have also calculated the single-particle partial and total electronic density of states, $n(E)$. This has been obtained from the self-consistently determined eigenvalues, and it was averaged over six ionic configurations well separated in time ($\approx$ 18.0 ps) and sampling over six q-points.
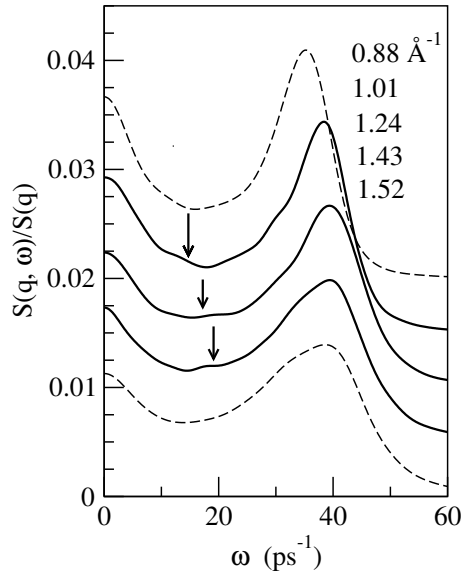
FIGURE 6.14: AIMD calculated dynamic structure factors $S(q,w)/S(q)$ for (top to bottom) q= 0.88, 1.01, 1.24, 1.43 and 1.53 Å^{-1}. The vertical scales are offset for clarity. The arrows point to the locations of the transverse-like excitations

Fig. 6.15 shows the obtained results for the single-particle partial and total $n(E)$ associated to the outer four valence electrons. The electronic states are dominated by the 3d states, with a very small contribution from the s and p states. For comparison we have also plotted the $n(E)$ corresponding to the solid β phase [206, 207] of Ti, where it is observed that the contribution from the 3d states is even greater than in the liquid phase.

For both phases, the corresponding $n(E)$ clearly point to a metallic character. In l-Ti the Fermi level E_F lies very near the maximum of $n(E)$ curve whereas for the solid β-Ti, it is also located near the maximum. Notice that the value $n(E_F)$ decreases with melting, going from a value ≈ 2.16 for β-Ti to ≈ 1.80 for l-Ti. On the other hand, the bottom of the valence band lies at practically the same value, i.e. $E − E_F ≈ -6.0$ eV.
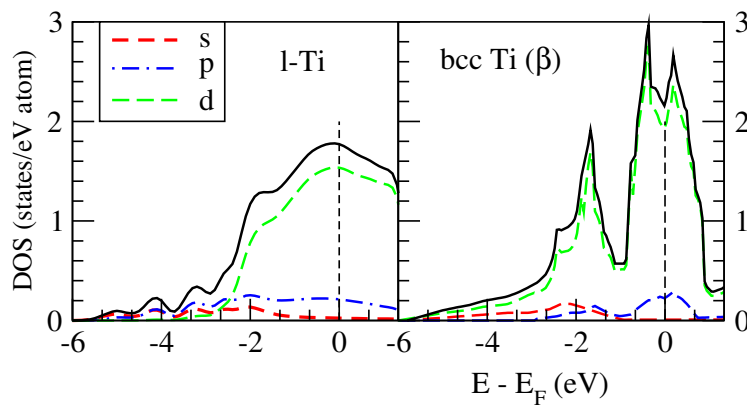
FIGURE 6.15: Total electronic density of states (black line) for bcc Ti (β) and l-Ti at 2000 K. The angular momentun decomposition of the DOS in s (red dashed line), p (blue dash-dotted line), d (green dashed line).

6.2.4 *Conclusions*

An *ab initio* simulation method has been used to calculate several static and dynamic properties of bulk l-Ti at a thermodynamic state near its triple point. To our knowledge, this is the first AIMD study carried out for bulk l-Ti.

The obtained results for the static structure show a very good agreement with the available experimental data as evinced by the comparisons provided for the pair distribution function, $g(r)$, and the static structure factor, $S(q)$. We point out that the calculated $S(q)$ shows an asymmetric shape in its second peak which exhibits a marked shoulder (in agreement with the recent XS data). A similar feature has been found in other liquid transition metals and has been related to the appearance of icosahedral short-range order. This latter point has been confirmed by a more detailed study of the liquid static structure by using the CNA method, which has shown a large abundance of five-fold structures, which are somewhat angle-distorted as compared to ideal icoshedral ones.

As for the single-particle dynamical properties, several quantities have been evaluated. Comparison with the quasielastic neutron scattering data of Horbach *et al.* [216]. has been reported for the self-intermediate scattering function $F_s(q, t)$, and for the self-diffusion coefficient.

An analysis of the microscopic mechanisms has been performed by evaluating the second-order memory functions of the AIMD results for the intermediate scattering functions, $F(q, t)$. Then, those second-order memory functions were fitted to a two exponentially decaying function aiming to describe a fast and a slow relaxation processes. An analysis of the physical origin of both relaxation processes has concluded that a generalized hydrodynamic model is adequate for describing the microscopic dynamics of l-Ti near the triple point. Moreover, we have obtained some insight into the behavior of the generalized specific heat ratio, $\gamma(q)$, which allowed to get an estimate of its hydrodynamic limit γ_0.

The AIMD dynamic structure factors, $S(q, \omega)$, show side-peaks which are indicative of collective density excitations. Their calculated lifetimes and dispersion relation closely follow the corresponding experimental IXS data.

Furthermore, a detailed analysis of the AIMD $S(q, \omega)$ has revealed some type of excitations which have similar features as the transverse-like excitation modes found by Hosokawa *et al.* [246] in their IXS data for some liquid metals (i.e. l-Ga, l-Cu, l-Sn and l-Fe) near their respective triple points.

The AIMD transverse current correlation functions, $C_T(q, t)$, exhibit clear oscillations around zero and the associated spectra, $C_T(q, \omega)$, have inelastic peaks which reflect the presence of shear waves in l-Ti. The calculated transport coefficients, namely the self-diffusion, adiabatic sound velocity and shear viscosity coefficients show a reasonable agreement with the available experimental data. We have also checked that the Stokes-Einstein-Sutherland relation still holds for l-Ti near melting.

6.3 AIMD SIMULATIONS OF LIQUID PD AND PT NEAR MELTING

We report a study on several static and dynamic properties of liquid Palladium (l-Pd) and Platinum (l-Pt) metals at thermodynamic conditions near their respective triple points. The calculations have been carried out by AIMD simulation technique. Results are reported for several static structural propertiess which are compared with the available X-ray diffraction data. As for the dynamic properties, results have been obtained for both single and collective dynamical magnitudes as well as for some transport coefficients which are compared with the corresponding experimental data.

6.3.1 *Introduction.*

Pd and Pt have not attracted as much attention as other transition metals and, to our knowledge, only a few CMD simulations have been carried out on these two liquid metals. Alemany *et al.* [250] have used CMD simulations,

combined with interatomic potentials constructed within the framework of the embedded atom model, in order to evaluate the static structure factor, $S(q)$, and some transport coefficients of l-Pd and l-Pt. A similar calculation was also performed by Kart *et al.* [251], but using a different interatomic potential. On the experimental side, we are only aware of the X-ray diffraction (XD) measurements of Waseda [192], who determined the $S(q)$ of l-Pd and l-Pt near their respective triple points. As for the dynamical structure, no measurements have been performed yet. This dearth of information has prompted us to perform AIMD simulations in order to evaluate several structural and dynamical properties as well as some transport coefficients. We emphasize that this is the first *ab initio* study on these two metals and, given the superior accuracy of the AIMD versus CMD simulations, we expect these results may stimulate further experimental and/or theoretical work.

In section 6.3.2 we briefly describe the theory underlying the present AIMD simulations, and in section 6.3.3 we report and discuss some structural and dynamical results which are compared with other previous studies and experimental data. Finally some conclusions are drawn.

TABLE 8: Input data for the different thermodynamic states studied in this work. ρ is the total ionic number density and T is the temperature. N_c is the total number of configurations.

	ρ (Å^{-3})	T (K)	N_c
Pd	0.0594	1873	21000
Pt	0.0577	2053	18500

6.3.2 Computational details.

The AIMD calculations for bulk l-Pd and l-Pt have been performed at a thermodynamic states near their respective melting points (see Table 8). The exchange-correlation energy, $E_{xc}[n]$, for which we have used the local density approximation, as parametrized by Perdew and Zunger [89, 91], including non-linear core corrections. The ion-electron interaction has been described by means of ultrasoft pseudopotentials [128] which were generated from a scalar-relativistic calculation of the atomic electron configurations [Kr]$4d^9 5s^1$ and [Xe]$5d^9 6s^1$ for Pd and Pt respectively. For both systems, we have used 120 atoms (i.e. $120 \times (9\ d+1\ sp) = 1200$ valence electrons) in a cubic supercell with the initial atomic positions taken at random.

Both systems were thermalized during 15.0 ps and therefrom, microcanonical AIMD simulations were performed with an ionic time step of 0.0055 ps, lasting a total simulation time of 115.5 ps for l-Pd and 101.75 ps for l-Pt.

The ionic configurations were generated under the BO approximation solving the Kohn-Sham equations on a plane-wave basis set for a given configuration of ions, calculating the forces on the ions using the Hellmann-Feynman theorem, and solving the corresponding Newton's equations for constant total energy, as implemented in the Quantum Espresso package [227]. The plane-wave representation with an energy cutoff of 25 Ryd and the single Γ point was used in sampling the Brillouin zone.

Finally, the 21000 configurations generated for l-Pd (18500 configurations for l-Pt) were used in the evaluation of the corresponding static and dynamic properties.

6.3.3 Results: Bulk Properties.

We have evaluated several liquid static properties (pair distribution function, static structure factor) and dynamic properties, both single-particle ones (velocity autocorrelation function, mean square displacement) and collective ones (intermediate scattering functions, dynamic structure factors, longitudinal and transverse currents). The calculation of the time correlation functions was performed by taking time origins every five time steps.

Static properties.

The AIMD simulations provide a direct evaluation of both the static structure factor, $S(q)$, and the pair distribution function, $g(r)$. Figure 6.16 shows the AIMD result for the $S(q)$ of l-Pd along with the XD data of Waseda [192]. The calculated $S(q)$ has a symmetric main peak located at $q_p = 2.79$ Å^{-1}, whose shape and amplitude practically coincide with experiment. As for the subsequent oscillations, we observe a very small mismatch concerning the position of the subsequent oscillations although its amplitude is well reproduced. The AIMD result for l-Pt is depicted in Figure 6.17 and we observe an excellent agreement of the calculated $S(q)$ with the XD data [192]. There is a symmetric main peak at $q_p = 2.77$ Å^{-1} and the following oscillations closely follow the experimental ones.
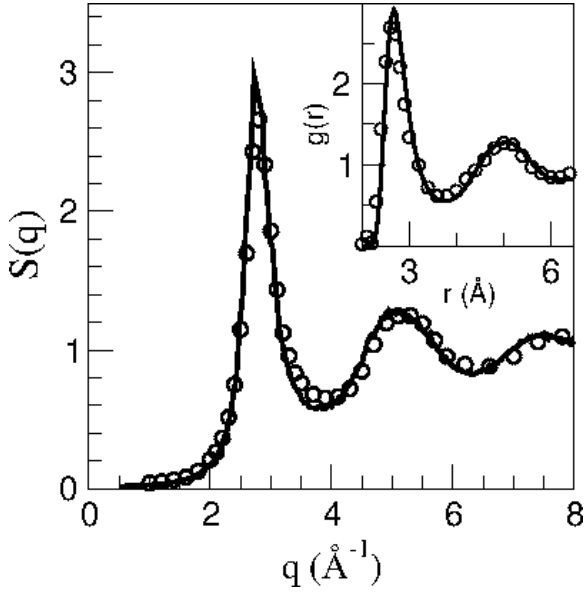
FIGURE 6.16: Static structure factor, $S(q)$, of l-Pd at $T = 1873$ K. Full line: AIMD calculations. Open circles: XD data from Waseda [192]. The inset shows the pair distribution function $g(r)$.
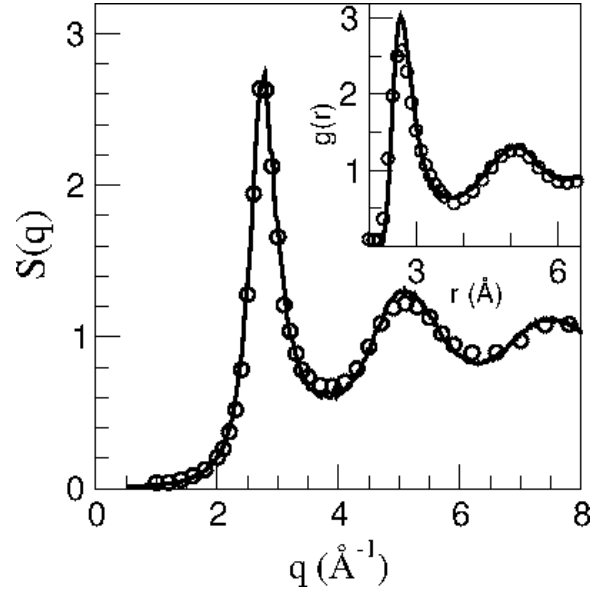
FIGURE 6.17: Same as the previous figure, but for l-Pt at $T = 2053$ K.

A similar good agreement is found for the AIMD calculated $g(r)$. The coordination number (CN) has been evaluated by integrating the $g(r)$ up to the position of its first minimum, which for both l-Pd and l-Pt stands at the same value $R_{min} = 3.77$ Å, yielding an identical result of CN ≈ 12.8 atoms, which is a typical value of the simple liquid metals near their triple point [23].

The isothermal compressibility, κ_T, has been estimated by using the relation $S(q \to 0) = \rho k_B T \kappa_T$ where k_B is Boltzmann's constant. The AIMD calculated $S(q)$ has been extrapolated to $q \to 0$, by using a least squares fit $S(q) = s_0 + s_2 q^2$ of the q-values for $q \leqslant 1.40^{-1}$. This scheme yielded $S(q \to 0) = 0.013 \pm 0.001$ and 0.0095 ± 0.0010 for l-Pd and l-Pt respectively. Therefrom, the following compressibility values (in units of 10^{11} m^2 N^{-1}) were obtained: $\kappa_T = 4.70 \pm 0.20$ for l-Pd and 1.80 ± 0.15 for l-Pt. Comparison with experiment, can only be performed for l-Pt for which there is a experimental data, $\kappa_T \approx 0.84 \pm 0.02$ [233].

Dynamic properties

Single particle dynamics

Figure 6.18 depicts the calculated $Z(t)$ along with the respective power spectrum (for the sake of comparison we have also included liquid Ni). The $Z(t)$ exhibit the typical backscattering behavior with a first minimum followed
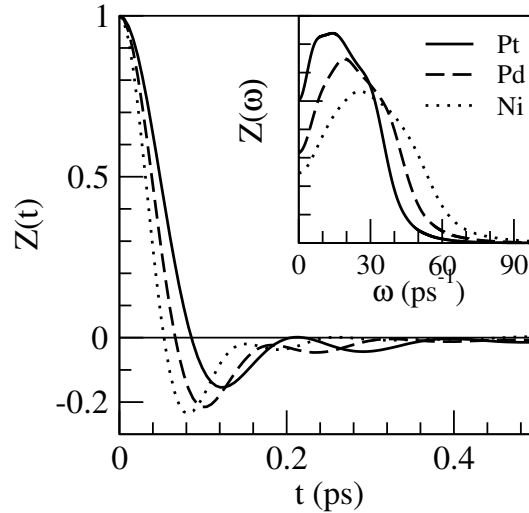
FIGURE 6.18: Normalized AIMD calculated velocity autocorrelation function of l-Pd, l-Pt and l-Ni near their respective melting points. The inset represents the corresponding power spectrum $Z(\omega)$.

by rather weak oscillations and the $Z(t)$ always remaning negative. Notice that the $Z(t)$ are qualitatively very similar and the minor differences are related to the increasing ionic mass when going from Ni to Pt.

The self-diffusion coefficient, D, evaluated from both $Z(t)$ and $\delta R^2(t)$ has yielded the same value which, moreover, coincides for both metals, i.e. $D_{AIMD}(Pd) = D_{AIMD}(Pt) = 0.27 \pm 0.02$ Å^2/ps. Unfortunately, the lack of experimental data implies that comparison can only be performed with the avaiable CMD simulations; thus Alemany *et al.* [250] have obtained $D_{CMD}(Pd) = 0.403 \pm 0.003$ Å^2/ps and $D_{CMD}(Pt) = 0.281 \pm 0.003$ Å^2/ps. On the other hand, the CMD study of Kart *et al.* [251] gave $D_{CMD}(Pd) = 0.496 \pm 0.006$ Å^2/ps.

Collective dynamics

Figure 6.19 depicts, for some q/q_p-values, the AIMD results for $F(q,t)$ and $S(q,\omega)$ in both l-Pd and l-Pt. For small q-values, the $F(q,t)$ show the typical oscillatory behaviour which lasts up to $q \approx (3/5) q_p$, with the amplitude of the oscillations becoming weaker with increasing q-values. Moreover, these oscillations are superposed on a discernible diffusive component. At $q \approx q_p$, the $F(q,t)$ exhibit the typical slow decay, giving rise to the mentioned "de Gennes narrowing" of the spectra.

The associated $S(q,\omega)$ show side-peaks, indicative of collective density excitations, up to $q \approx (3/5)q_p$; therefrom the side-peaks evolve into shoulders which last until $q \approx (4/5)q_p$ and for greater q's the corresponding $S(q,\omega)$ show a monotonic decreasing behavior.

Our AIMD calculated $C_L(q,\omega)$ show a peak for each q-value and from the frequencies of those peaks, the dispersion relation for the longitudinal modes, $\omega_l(q)$, has been obtained and is plotted in Figure 6.20.

In the low-q region, the slope of the $\omega_l(q)$ curve gives a q-dependent adiabatic sound velocity that in the limit $q \to 0$ reduces to the bulk adiabatic sound velocity, c_s. Using the $q \leqslant 1.2$ Å^{-1} values of our calculated $\omega_l(q)$, we have evaluated its slope at $q \to 0$ and obtained $c_s \approx 3450 \pm 150$ m/s (l-Pd) and $c_s \approx 3000 \pm 150$ m/s (l-Pt). The AIMD result for l-Pt compares well with the experimental data, $c_{s,exp} \approx 3053 \pm 150$ m/s [233].

For both l-Pd and l-Pt, we have found that the $C_T(q,\omega)$ already shows a peak for the smallest attainable q-value, i.e. $q_{min} = 0.18 q_p$ and it lasts up to $q \leqslant 3q_p$, which is typical of the simple liquid metals [23].

From the AIMD results for the $C_T(q,t)$, the shear viscosity coefficient, η, has been calculated. Details are given in References [23, 242].
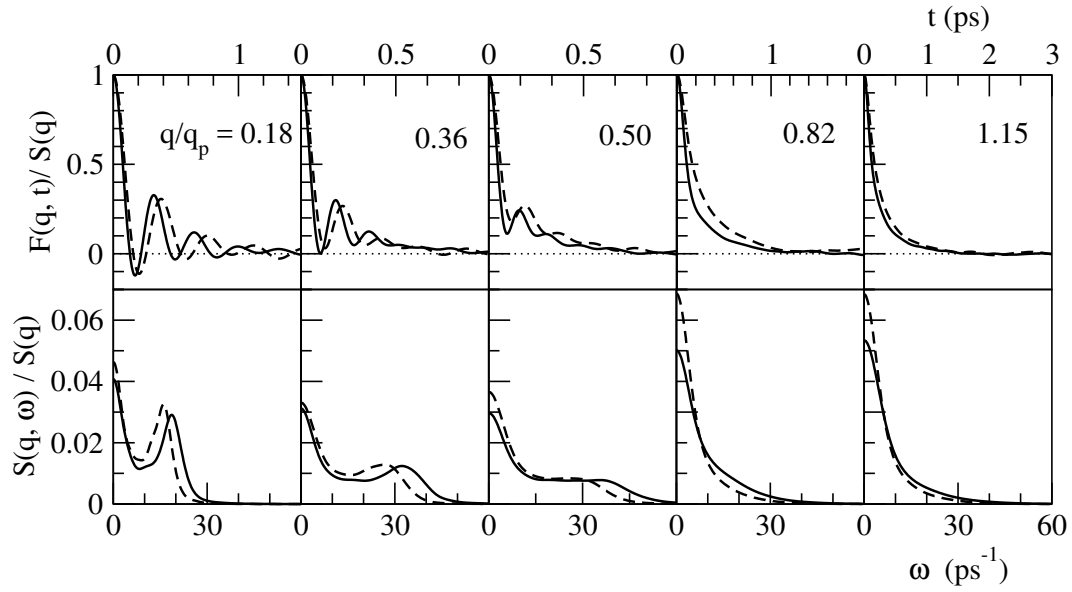
FIGURE 6.19: Upper part: Intermediate scattering functions, $F(q, t)$, of l-Pd at $T = 1873$ K (full lines) and l-Pt at $T = 2053$ K (dashed lines) at several values of q/q_p. Lower part: Same as before but for the dynamic structure factors, $S(q, \omega)$
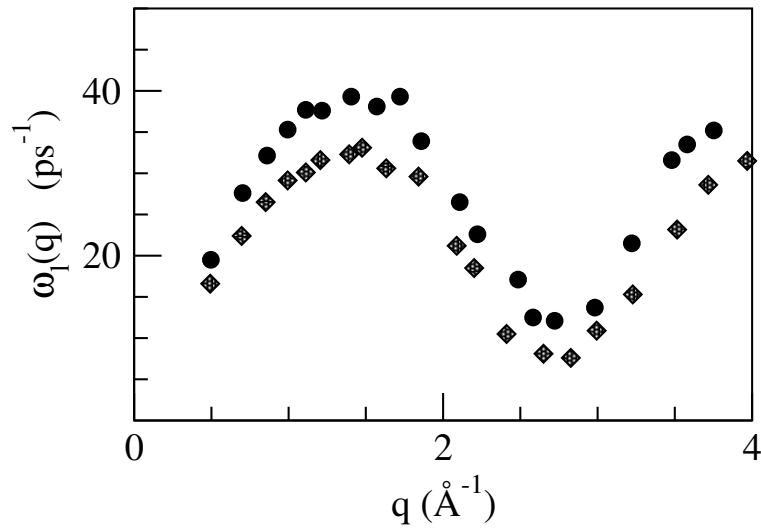
FIGURE 6.20: Longitudinal dispersion relation for l-Pd at $T = 1873$ K (circles) and for l-Pt at $T = 2053$ K (diamonds).

For l-Pd, we have obtained $\eta_{AIMD} \approx 4.57 \pm 0.15$ GPa ps which compares well with the experimental value of $\eta_{exp} = 4.22 \pm 0.15$ GPa ps [253]; moreover, the CMD simulation studies have yielded smaller values, i.e. $\eta \approx 3.68 \pm 0.50$ GPa ps [250] and $\approx 2.91 \pm 0.86$ GPa ps [251]. As for l-Pt, our result $\eta_{AIMD} \approx 4.90 \pm 0.25$ GPa ps is close to the smaller of the two available experimental data $\eta_{exp} = 4.82$ and 6.74 GPa ps [253]; moreover, the latter one is closer to the CMD simulation result $\eta \approx 6.08 \pm 0.95$ GPa ps [250].
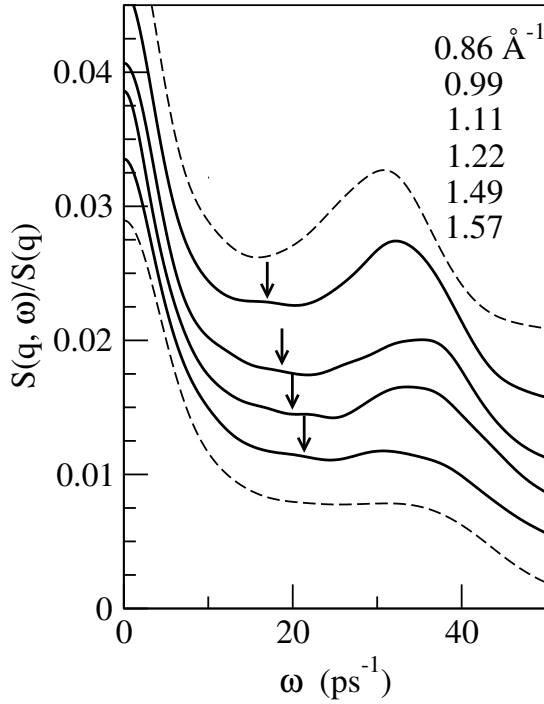
FIGURE 6.21: AIMD calculated dynamic structure factors $S(q, \omega)/S(q)$ of l-Pd at $T = 1873$ K and several q-values. The vertical scales are offset for clarity. The arrows point to the locations of the TA modes.
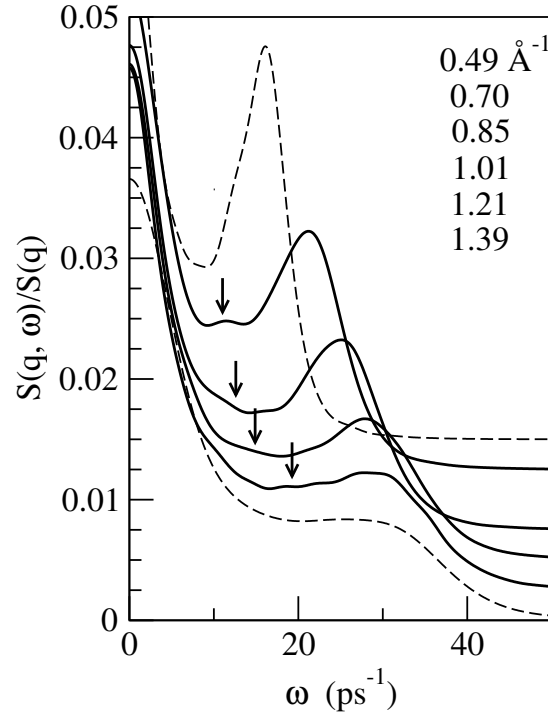
FIGURE 6.22: Same as the previous figure, but for l-Pt at $T = 2053$ K.

As previously observed in liquid Ni and liquid Ti, a close analysis of the AIMD results for $S(q, \omega)$ reveals that within the range $0.3q_p \leqslant q \leqslant \approx 0.5q_p$, some weak shoulders show up in the ω-region located between the quasielastic and the inelastic peaks. This is observed in Fig. 6.21 and Fig. 6.22. Outside the above q-range, those weak shoulders are no longer visible in the $S(q, \omega)$. .

Electronic properties.

We have also calculated the partial and total electronic density of states, $n(E)$. It has been obtained from the self-consistently determined eigenvalues, and averaged over five ionic configurations separated in time, sampling the Brillouin zone with six *k*-points. Figure 6.23 shows the obtained results for the electronic partial and total $n(E)$ associated to the outer ten valence electrons. It is clear to see that the $n(E)$ is greatly dominated by the 4d states in Pd and the 5d states in Pt and point to a metallic character.

6.3.4 *Conclusions.*

An AIMD simulation method has been used to calculate some static and dynamic properties of l-Pd and l-Pt near their respective triple point. These two metals have not attracted much attention and therefore there is not
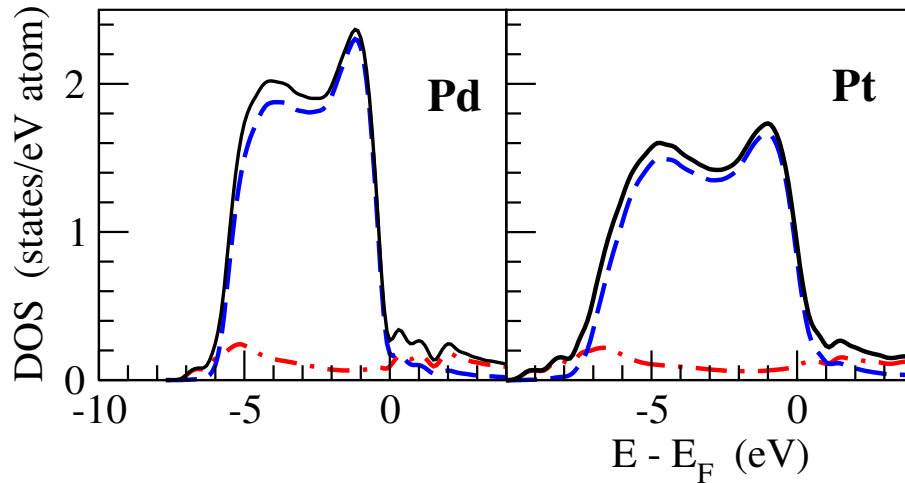
FIGURE 6.23: Total electronic DOS (black line) for l-Pd and l-Pt near their respective melting points, as obtained from the present AIMD calculations. The angular momentum decomposition of the DOS in *s* (red dashed line) and *d* (blue dashed line).

much theoretical and/or experimental information to compare with. Concerning the static structure, the *ab initio* results for the pair distribution function, $g(r)$, and the static structure factor, $S(q)$, are in good agreement with the experimental data. The calculations account for the shape and position of the main peak of $S(q)$ as well as the subsequent peaks. The obtained coordination numbers are typical of the simple liquid metals.

The intermediate scattering functions, $F(q,t)$, show at small q-values, strong oscillations superposed on a distinct diffusive component. The associated dynamic structure factors, $S(q,\omega)$, show side-peaks which are indicative of collective density excitations. The calculated transport coeffcients show good agrement with the available experimental data.

7

COLLECTIVE DYNAMICS COUPLING

In this chapter we show an analysis of the complex dynamics of two liquid metals, Zn and Sn. From the structural point of view they are very different. Solid Zn is close packed, while the structure of solid Sn is rather open. The liquid structures also differ correspondingly, both in their avarage structure ($g(r)$ and $S(q)$), and in the local atomic environment, with totally different properties in their common neigbour analysis. However, in both systems inelastic scattering experiments have revealed fingerprints of low energy excitations in the dynamic structure factor for wavevector regions around half the position of the main peak of $S(q)$. These have been ascribed to the existence of some type of coupling with transverse propagating waves. However, such connection is purely phenomenological, based on the similarity between the corresponding frequencies. In other systems, as liquid Ni describes in the preceeding chapter, double modes have also been observed in different wavevector regions, in particular in the transverse current spectra. Again there is not a theoretical explanation so far for the origin of the extra excitation in this region.

We try to shed some light into this problem by using the mode-coupling theory for both systems. For liquid Zn we have performed standard KS AIMD simulations using 90 atoms, whereas for liquid Sn we have increased the sample size to 1000 atoms by using orbital free simulations.

We show that some aspects of the complex dynamics of these systems are well described by the mode-coupling theory considered, whereas some other features still need some improvement in the theory in order to understand their origin.

7.1 LIQUID ZN: AB INITIO STUDY AND THEORETICAL ANALYSIS.

We perform an AIMD simulation of liquid Zn near the melting point in order to study the longitudinal and transverse dynamic properties of the system. We find two propagating excitations in both of them in a wide range of wavevectors. This is in agreement with some experimental observations of the dynamic structure factor in the region around half the position of the main peak. Moreover, the two-mode structure in the transverse and longitudinal current correlation functions had also been previously observed in high pressure liquid metallic systems. We perform a theoretical analysis in order to investigate the possible origin of such two components by resorting to mode-coupling theories. They are found to describe qualitatively the appearance of two modes in the dynamics, but their relative intensities are not quantitatively reproduced. We suggest some possible improvements of the theory through the analysis of the structure of the memory functions. We also analyze the single-particle dynamics embedded in the velocity autocorrelation function, and explain its characteristics through mode-coupling concepts.

7.1.1 *Introduction*

The dynamic behavior of a liquid at long times (compared to interatomic collision times) and large lengthscales (compared to atomic sizes), can be well understood in terms of continuum theories, namely hydrodynamics. This indicates that only two mechanisms are required to understand longitudinal dynamics: thermal relaxation and adiabatic propagation of attenuated pressure waves (sound). Transverse stress can however only be relaxed via shear viscosity, since the lack of elasticity prevents the propagation of shear waves. In this hydrodynamic regime the dynamic structure factor of the liquid, $S(q, \omega)$, has the form of a Rayleigh-Brillouin triplet, with a central Lorentzian peak, whose width is related to the thermal diffusivity, and a pair of stretched-Lorentzian side peaks

at positive and negative frequencies, whose position is dictated by the adiabatic sound velocity and whose width is related to the sound attenuation. The transverse spectrum is also Lorentzian, and its width is related to the shear viscosity [23, 26].

This picture changes when the explored legthscales and times decrease, abandoning thr hydrodynamic regime. Additional mechanisms can appear in the longitudinal dynamics (for instance, structural relaxation), leading to a more complex behavior, and viscoelasticity of the liquid can lead to the emergence of shear waves for wavevectors larger than a critical one [23, 26].

If lengthscales become smaller than interatomic distances and times shorter than collision times, the dynamics are dictated by free-particle like motion (lacking therefore any type of collective wave propagation), which is characterized simply by the thermal velocity of the particles. In this regime the correlation functions take a gaussian form [23, 26].

The intermediate regime is by far the one less well understood, and this has prompted experimental as well as theoretical studies of liquid dynamics in this regime, which comprises wavevectors, q, spanning typically the range from 10^{-1} to 10^{1-1} and frequencies, ω), in the THz range. Experimental techniques include inelastic scattering of radiation, either x-rays or neutrons, which exchange energy and momentum with the density fluctuations in the liquid. These studies only probe longitudinal dynamics, and have shown that, in general, the shape of the dynamic structure factor evolves from the Rayleigh-Brillouin hydrodynamic form by changing the positions of the peak frequencies, reflecting the dispersion of the collective longitudinal excitations, and varying the widths of the central and side peaks. This type of behavior has been reproduced by molecular dynamics simulation studies, and also by different theoretical approaches. Transverse dynamics is, on the other hand, not accessible directly to experimental techniques for liquids, and their study relies on molecular dynamics simulations and/or theoretical approaches. The general behavior obtained through these methods is, as mentioned before, the transition from pure relaxation at small q values, to a propagating scenario above a critical q. Upon increasing the wavevector (decreasing the lengthscale explored) the dynamics eventually become free-particle like and propagation again disappears.

Recently, however, a careful analysis of the measured scattering intensities in several liquid metals has unveiled the existence of a second propagating excitation in a wavevector region around $q_p/2$, where q_p is the position of the main peak of the static structure factor, $S(q)$, of the liquid [191, 231, 245–247, 249, 254–256]. Interestingly, the frequency associated to this excitation is similar to the one associated to transverse waves at the same wavevector. This fact prompted the interpretation of this second contribution as a fingerprint of transverse excitations in the longitudinal spectrum. Such interpretation is merely based on the similarity of the corresponding frequencies, but it is not backed by any theoretical approach that may explain such coupling between transverse and longitudinal excitations.

A similar situation appears in relation with the transverse dynamics. Recent studies of high pressure liquid Li, Fe and Na have unveiled the existence of two (and not just one) propagating excitations in the transverse dynamics [257], now for wavevectors around q_p. In this case a tentative interpretation would be to attribute the second mode to the coupling with longitudinal propagating excitations. Moreover, analysis of the longitudinal currents in this region also suggest the existence of two propagating modes. It was first assumed that this type of behavior was a pressure-induced effect, but more recent calculations for liquid Ni at room pressure have unveiled a quite similar behavior [231]. Again, the association of these phenomena to coupling between longitudinal and transverse modes has not been backed by theoretical schemes yet.

In this study we try to make some advance into the explanation of such couplings as responsible for the two-mode structure of the longitudinal and transverse spectra, using in particular mode-coupling ideas. Mode-coupling theories were developed starting in the 1970's and, since then, they have been mostly applied in simplified forms to the study of the dynamic glass transition [72]. There have been some applications to the study of the longitudinal dynamics of a few liquid metals but none for the transverse dynamics yet. The basic idea of mode-coupling approaches is to separate the dynamics into two contributions with different decay rates. A fast one is related mostly to binary collisions, although it can also include couplings with fast-decaying modes. A

second, slowly decaying, contribution is due to the coupling of the quantity studied with hydrodynamic modes, which vary slowly for small wavevectors. This decomposition is performed at the level of the memory functions, as introduced by Mori and Zwanzig [23, 258].

Our study is here applied to the dynamics of liquid Zn (l-Zn). This system is among those for which a second mode in $S(q, \omega)$ around $q_p/2$ has been suggested by experimental observation. In fact it has been found both in IXS experiments [246] and in INS experiments [255]. Zinc has a full d-shell that contributes in an essential way to its properties. The structure of Zn systems is quite peculiar in all phases, from clusters [259], to the hcp solid phase, where a very large c/a ratio is observed [260], to the liquid, where an asymmetric main peak is found [192, 261, 262]. Most of these characteristics are shared only with Cd, which is immediately below in the periodic table. Such complexities obviously demand the use of highly accurate methods to describe the interatomic interactions.

We have determined the dynamic properties of liquid Zn (l-Zn) through MD simulations, where the total energy and the forces on the atoms are evaluated *ab-initio* on the fly using DFT [1, 2]. This AIMD simulation is very accurate, but also very costly computationally, and therefore the simulated samples are relatively small. We have, however, performed rather long simulation runs in order to keep the statistical noise as small as possible.

Single-particle dynamics can also be computed from molecular dynamics runs, and we will show the results for the VACF and the power spectrum. The motion of a particle in a dense fluid is influenced by the motion of the "cage" of neighbours that surround it, against which it bounces, and therefore it can be easily understood that the behavior of collective quantities has some effect on the single-particle dynamics. This influence can be described in a way similar to that considered previously for the collective dynamics, i.e., the memory function of the VACF can be separated into fast and slow components, with the latter determined by the coupling with slow modes [74, 76]. We have found more convenient to follow a different route that includes the coupling of the particle velocity with longitudinal and transverse currents directly in the VACF [85]. This type of theory has already been applied to several liquids and yielded a good description of the VACF [167, 256], so we check if it still holds in the complex dynamics scenario of l-Zn.

The layout of the study is as follows: in section 7.1.2 we describe briefly the AIMD simulation setup, in section 7.1.3 we define the quantities studied and the theoretical approaches used, in section 7.1.4 we show the results obtained for collective dynamics from both the simulation and the theoretical approach. The last section is devoted to the analysis of the velocity autocorrelation function obtained through the simulation and from the theoretical approach. Some conclusions are finally drawn, and possible improvements in the theoretical analysis are discussed. The full mathematical expressions used in the theoretical study can be found in Appendix A.

7.1.2 *Computational details*

We have enclosed 90 Zn atoms into a cubic simulation cell of side $L = 11.35$, so that the ionic number density is $\rho = 0.06155$ atoms/^{3}. We have considered explicitly 12 valence electrons per atom (10 d + 2 s), and their interaction with ionic cores has been modeled through an ultrasoft pseudopotential taken from the dataset included within the VASP package [184]. This code has been used in order to perform the molecular dynamics run, evaluating for each configuration the ground state energy from DFT and the forces on the atoms through the Helmann-Feynmann theorem. The exchange and correlation energy has been treated within the generalized gradient approximation using the PBE parametrization and non-linear core corrections have also been included. The cutoff for the planewave expansion of the orbitals has been 300 eV. The ionic equations of motion have been solved using a time-step of 4 fs.

After the equilibration period, when the temperature has stabilized at 723 K, we have let the system evolve for 36000 configurations (144 ps), and these configurations have been used in order to sample the properties of interest which were subsequently analyzed as described below.

The atomic positions and velocities at each timestep are directly available from the simulations, so that any function depending on them can be computed straightforwardly. Moreover, the periodic boundary conditions

associated to the simulation box fix the wavevectors compatible with the imposed periodicity, and consequently $\vec{q}$-dependent functions can only be obtained for such set of wavevectors. In particular the minimum feasible wavevector is $q_{min} = 2\pi/L = 0.55^{-1}$.

7.1.3 *Theory*

Rotational symmetry in the system implies that the two polarizations of the current correlation functions (i.e. longitudinal and transverse) are independent and do not mix directly, and that the correlation function between any two coordinate components of the current vector is uniquely determined by C_L and C_T. The instantaneous configuration of atoms in a liquid is not spherically symmetric (even more so in simulations where a periodicity of the simulation cell is imposed) so that some transverse-longitudinal mixing might occur, but such direct mixing should be expected to be quite small. The existence of transient structures (such as "dimers") that destroy rotational symmetry has been suggested to justify the mixing, but the argument is not totally convincing, since the lifetime of such structures is very short, and, moreover, not all liquids exhibit them.

We propose below a different approach, where the coupling between longitudinal and transverse modes does not occur directly, at the same wavevector, but indirectly, through all possible wavevectors, using mode-coupling ideas. These are routinely posed in terms of memory functions of the autocorrelation functions, which are described next.

Memory functions

The memory function of the intermediate scattering function can be defined either in the time domain or in the Laplace Transform (LT) domain:

$$\dot{F}(t) = -\int_0^t d\tau M(\tau)F(|t-\tau|) \quad ; \quad \tilde{F}(z) = \frac{F_0}{z + \tilde{M}(z)} \, , \tag{157}$$

where $F_0 = F(t = 0)$, is the initial value of the function, and the tilde denotes the LT, $\tilde{F}(z) = \int_0^\infty dt F(t) \exp[-zt]$.

The same procedure can be followed for any time-dependent function, so we also define $N(q, t)$ as the memory function of $M(q, t)$, i.e., the second order memory function of $F(q, t)$, and $M_T(q, t)$ as the memory function of $C_T(q, t)$.

Note that the short time behavior of the correlation functions and the memory functions (also related to their frequency moments) is dictated by static properties which can be directly evaluated from atomic positions, velocities, accelerations and, if necessary, higher order derivatives of the positions. Also note that the odd-order initial time derivatives of the correlation functions and memory functions must vanish due to time reversal symmetry.

An interesting feature of memory functions is that usually their time decay is faster than that of the original function. Therefore at some point in the memory function hierarchy it is possible to invoke a Markovian approximation, according to which the decay of a certain order memory function is instantaneous, thus leading to a simplified model for the previous lower order memory function, namely an exponential function,

$$f_{Ex}(t) = a \exp[-bt] \quad , \quad \tilde{f}_{Ex}(z) = \frac{a}{z + b} \, . \tag{158}$$

The particular form of the LT of an exponential function (a rational function of z of first degree in the denominator) means that all the previous lower order memory functions are also rational functions of z (of higher degrees in the denominator). These can then be separated into simple fractions, leading therefore to a sum of several exponential functions in the time domain. The number of exponential functions increases by one for each level one moves up in the hierarchy of memory functions. In the next subsection we mention several models of this type, frequently used in the analysis of MD or experimental data. We note however that exponential functions do not behave correctly for short times, since the odd-order derivatives are different from zero. Consequently we also propose some modified models that behave as exponentials for long times but whose odd-order initial time derivatives vanish.

Models

As previously commented in Chapter 3, the hydrodynamic model for $F(q, t)$ and $C_T(q, t)$ can be cast as models for $N(q, t)$ and $M_T(q, t)$ respectively [66]. On one hand $N(q, t)$ is modeled by the sum of a Dirac-delta function due to an instantaneous viscous relaxation and an exponential function due to a slower thermal relaxation. This leads to an $M(q, t)$ with two exponentials and finally an $F(q, t)$ with three exponential functions. On the other hand $M_T(q, t)$ is modeled by a Dirac-delta function due to instantaneous shear relaxation, leading to an exponential $C_T(q, t)$.

Since all the coefficients in the LT of the memory functions are real numbers, the roots of the denominator must appear either as real numbers or as complex conjugate (cc) pairs, and the same happens to the corresponding amplitudes in the partial fraction decomposition. A pair of cc exponentials is in fact a damped oscillatory function of time. The three exponentials in $F(q, t)$ in the hydrodynamic model turn out to be a real one and a pair of cc ones, which represent respectively relaxing and propagating contributions to the longitudinal dynamics, as mentioned in the introduction. In $S(q, \omega)$ the real root leads to the central line of the Rayleigh-Brillouin triplet, while the pair of cc roots leads to the positive and negative frequency side peaks.

The immediate generalization of the hydrodynamic model consists in substituting the instantaneous relaxations by exponential ones, so that $N(q, t)$ is then the sum of two exponentials (three for $M(q, t)$ and four for $F(q, t)$, respectively), whereas $M_T(q, t)$ is modeled by one exponential, and consequently $C_T(q, t)$ by the sum of two exponential functions. Out of the four exponentials in $F(q, t)$ two turn out to be a cc pair, and the other two real ones. Consequently, there are two central lorentzian lines and the positive and negative frequency side peaks in $S(q, \omega)$. Such model is usually named as either generalized hydrodynamic model or viscoelastic model, depending on the physical interpretation for the fast and slow components of $N(q, t)$. Regarding the transverse dynamics it turns out that for small q the two roots are real, while for wavevectors larger than some critical q they become a cc pair, so that propagation of shear waves sets in. This model for the transverse dynamics is again usually named as viscoelastic model.

Further models can be easily constructed by including more exponentials. For instance, if one wants to describe two different propagating modes and a relaxation mode in $F(q, t)$, as suggested by the appearance of fingerprints of transverse modes in the measured or computed $S(q, \omega)$ near $q \approx q_p/2$, then at least five exponentials are needed in $F(q, t)$ (a real one and two pairs of cc roots), which means that $N(q, t)$ must be represented by at least three exponentials. These three could either be all real or be one real and one cc pair. Note that in the second case $N(q, t)$ should show an oscillatory behaviour. Similarly, if one wants to have two propagating modes in $C_T(q, t)$ as observed around $q \approx q_p$ for several systems, then at least two cc pairs are needed, leading to an $M_T(q, t)$ with at least three exponential functions, which again may be all real or else a real one and an oscillatory term due to a cc pair. Therefore we may say that the presence of an oscillatory component in the memory functions $N(q, t)$ or $M_T(q, t)$ hints towards the possible existence of two propagating modes in the longitudinal or transverse dynamics respectively.

The particular properties of the LT of exponential functions justifies their use in models, but it is important not to forget that these functions do not behave analytically as correlation functions or memory function should, namely they do not have null odd order derivatives at $t = 0$. Obviously a combination of such functions can be forced to fulfill these (or at least some of these) requirements. One particular case of such a combination is the DHO model, widely used in the interpretation of experimentally measured IXS and INS spectra to represent propagating excitations. As shown in section 3.2.1, it consists of a pair of cc exponentials with particular coefficients that nullify the first derivative at $t = 0$, namely,

$$f_{DHO}(t) = a \exp[-\gamma t] \left(\cos(\omega_o t) + \frac{\gamma}{\omega_o} \sin(\omega_o t) \right) . \tag{159}$$

While the first derivative behaves correctly, one runs into problems for higher order derivatives. For instance, the $C_L(q, t)$ function corresponding to such mode in $F(q, t)$ would contain a term of the form $-\ddot{f}_{DHO}(t)$, and it is easy to verify that such function violates the condition of initial null derivative (the third derivative of $f_{DHO}(t)$ at $t = 0$ is nonzero).

While forcing the correct derivatives is possible when including a sufficient number of exponentials [263], using such approach it may be complicated to disentangle if the presence of a particular exponential function is due to a physical process that decays/oscillates with that particular rate/frequency, or is just due to the mathematical requirement of nullifying the odd derivatives at short times. It therefore seems useful to introduce some modifications into these model functions so as to guarantee the correct time behaviour, while still mantaining the long time behavior of the exponential functions. We propose here the following models to replace the exponential and DHO ones:

$$f_{mEx}(t) = \frac{a}{\cosh(bt)} \,, \tag{160}$$

$$f_{mDHO}(t) = c \left(\frac{\cos(\omega_o t)}{\cosh(\gamma t)} + \frac{\gamma}{\omega_o} \frac{\sin(\omega_o t)}{\sinh(\gamma t)} \right) \,. \tag{161}$$

This type of models will be used later in order to check the q-range where two propagating modes can be found and to analyze the structure of the memory functions obtained from our simulations.

7.1.4 Collective dynamics

AIMD simulation results

As a previous validation of the input parameters of the simulation, we have compared the static structure factor obtained from the simulations with the available experimental ones [192, 261, 262] (which agree well among themselves) as shown in Fig. 7.1. We find an excellent description of $S(q)$, including the asymmetric shape of the main peak, located at $q_p \approx 3.0 \text{ Å}^{-1}$, and the amplitude and phase of the subsequent oscillations. The pair correlation function, $g(r)$, also compares favourably with the corresponding experimental data [192, 262].
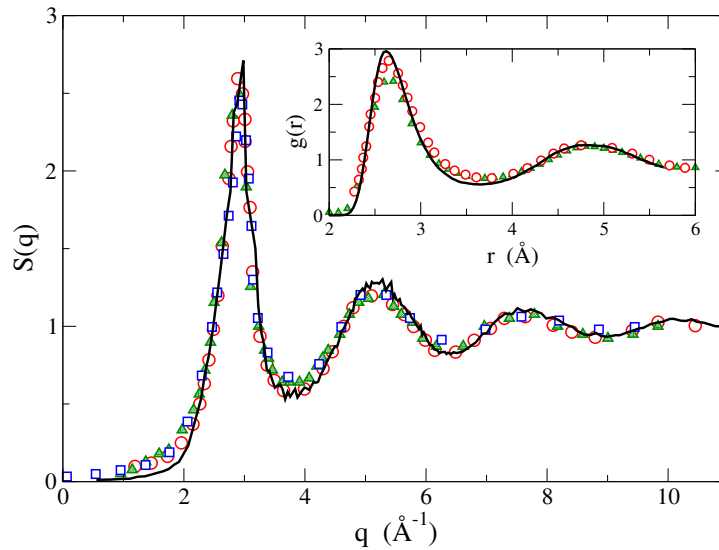
FIGURE 7.1: $S(q)$ for l-Zn near melting. Full lines: simulation results. The symbols denote experimental measurements, triangles: x-ray data from Ref. [192], circles: x-ray data from Ref. [262], squares: neutron data from Ref. [261]. The inset shows $g(r)$ with the same meaning for lines and symbols.

Transverse dynamics

Traditionally, the behavior of transverse dynamics in liquids has been studied in the small q-region, where a transition between relaxation and propagation has been observed for many liquids. Only in recent years some

attention has been paid to the behavior of transverse dynamics at higher q-values, but still not as high as required to reach the free-particle regime. Surprisingly double peak structures in $C_T(q, \omega)$ have been found for liquid metals under pressure for wavevectors around q_p [191, 256, 257]. Liquid Ni at room pressure has been also found to exhibit a similar picture [231]. Based on these premises, we have undergone a detailed study of the transverse current correlation functions and corresponding spectra for l-Zn in an extended q-range.

The lowest q-value allowed by the simulation setup is already outside the hydrodynamic region, since $C_T(q, t)$ already displays a negative minimum (and the spectrum shows a peak) indicating that propagation of shear waves already takes place at this q. An interesting phenomenon that we have observed is the presence of a negative tail in the $C_T(q, t)$ functions. An example is shown for q = 1.84 and 3.71 Å^{-1} in Fig. 7.2 where it is clearly visible due to the small amplitude of the oscillations, but we have found it in the whole q-range studied.
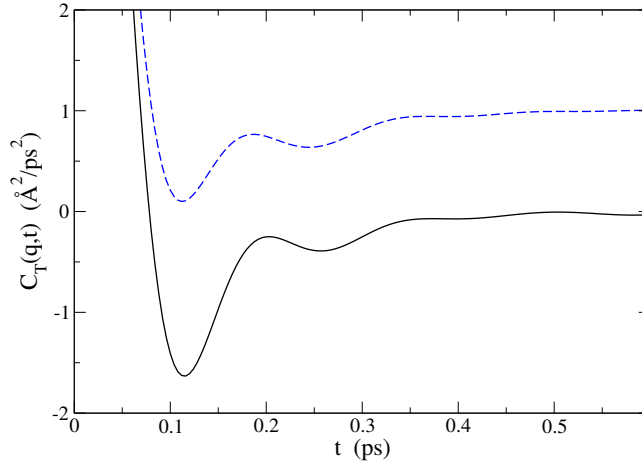
FIGURE 7.2: Detail of $C_T(q, t)$ for q = 1.84 (full line) and 3.71^{-1} (dashed line). The latter has been shifted up by one unit.

In Fig. 7.3 we display a general view of the behavior of $C_T(q, \omega)$ for $q_{min} \leqslant q \leqslant 5$ Å^{-1}. Here, and in the rest of the work, the "simulation" frequency-dependent functions shown in the figures have been obtained by numerical FT of the time-dependent functions which were obtained directly from the simulations, and not through the FT of a fit to such functions. In some figures we will indeed compare both routes, which have always led to very similar results. The numerical FT only required the use of a window function to alleviate the statistical noise present for long times. Figure 7.3 shows a transition between a single mode and two modes that occurs around 1.7 Å^{-1}, somewhat above $q_p/2$. Around q_p the shape is very flat, but for higher q the two-mode structure is clearly visible again. The results for several q below and above q_p are displayed in Fig. 7.4 for increased clarity. We have made a fit of $C_T(q, t)$ using one mDHO for the high frequency component, and the sum of a mDHO and a negative mEx (due to the negative tail) for the rest. The results of this decomposition are also shown in Fig. 7.4 for q = 2.54 and 3.37 Å^{-1}. The results of the fit reveal also the appearance of the second, high-frequency, mode around 1.7 Å^{-1} (for smaller q the amplitude of the high-frequency term found in the fit is negligible).

We can therefore conclude that l-Zn, as well as Ni and Ti, presents this double mode structure in the transverse dynamics in a wide range of wavevectors starting somewhat above $q_p/2$, even at normal pressures.

Longitudinal dynamics

The double mode structure of $C_T(q, \omega)$ was also observed in $C_L(q, \omega)$ in the case of liquid Fe and Na under pressure [191, 256]. We therefore analyze here the properties of this quantity for l-Zn also in the same extended q-range considered for the transverse counterpart. It is however important to perform this study taking into account at the same time the dynamic structure factor $S(q, \omega)$. First because being directly related they should
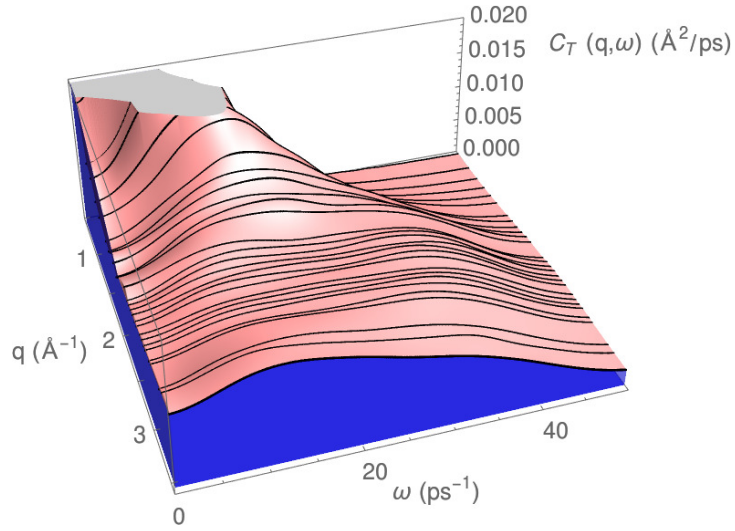
FIGURE 7.3: Transverse current spectra, $C_T(q, \omega)$, in a wide q-range.
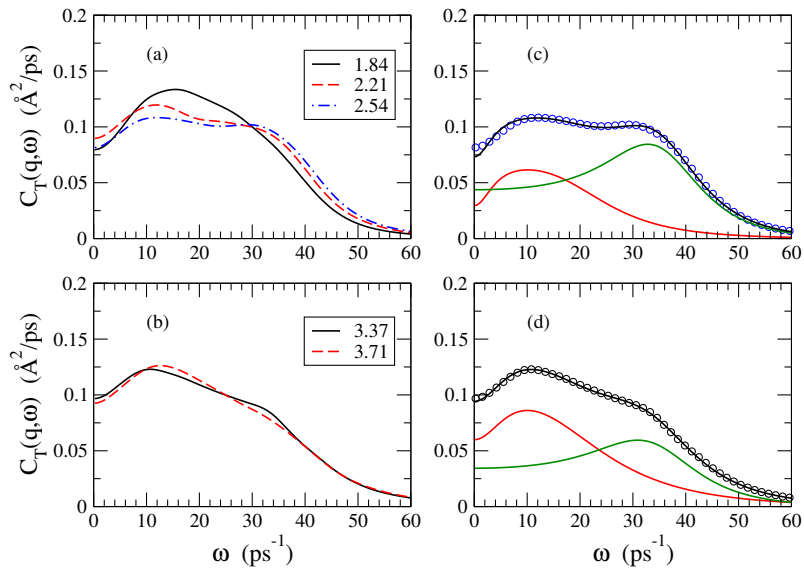
FIGURE 7.4: $C_T(q, \omega)$ for wavevectors shown in the graphs. (a) Below q_P. (b) Above q_P. (c) Results for $q = 2.54$ Å^{-1}; circles: simulation data, lines: fit results and its two components. (d) Same as (c), but for $q = 3.37$ Å^{-1}.

be described by the same terms if any decomposition into different contributions is performed: if a mEx or mDHO term is present in $F(q,t)$, its second derivative must be present in $C_L(q,t)$. And second because of the possible presence of peaks in $C_L(q,\omega)$ unrelated to propagating excitations. This is due to the fact that for small ω the function increases (starting at least as ω^2 according to its definition) and for large ω it decays to zero (as dictated by the null initial time derivative of $C_L(q,t)$), so that somewhere inbetween a maximum must exist, irrespective the presence or absence of propagating excitations. This property is however specific to $C_L(q,\omega)$ and, consequently, the comparison with $S(q,\omega)$ can be useful to discriminate the origin of the peak. For instance, in the free particle regime, for large q, $S(q,\omega)$ has a monotonic gaussian form of width related to the thermal velocity, but $C_L(q,\omega)$ has a peak at a frequency related to this thermal velocity, totally unrelated to propagating collective excitations.
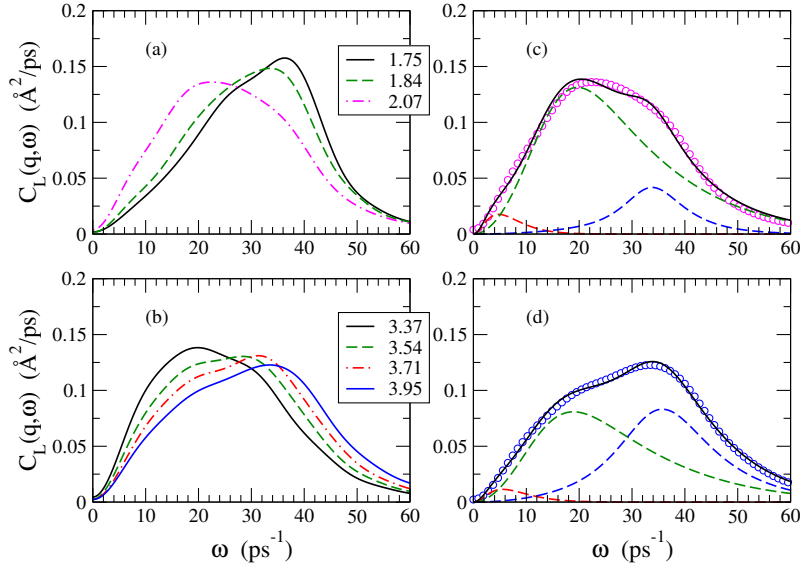
FIGURE 7.5: $C_L(q,\omega)$ for wavevectors shown in the graphs. (a) Below q_p. (b) Above q_p. (c) Results for $q = 2.07\,\text{Å}^{-1}$; circles: simulation data, lines: fit results and its three components. (d) Same as (c), but for $q = 3.95\,\text{Å}^{-1}$.

The separation into different contributions common to both $F(q,t)$ and $C_L(q,t)$ can be complicated for some wavevectors because of the different amplitudes of the corresponding terms in the two functions. For instance in the region around q_p a relaxing term is overwhelmingly dominant in $F(q,t)$ because of the structural correlations that lead to the de Gennes narrowing of $S(q,\omega)$. However such a term alone describes poorly the longitudinal current correlation function, and propagating terms are indeed needed, even if their contribution to $F(q,t)$ is insignificant. So when we consider below the components coming from a separation into contributions it must be understood that we have fitted jointly $F(q,t)$ and $C_L(q,t)$ to a given common model and using obviously the same parameters. We note in this respect the convenience of using models that fulfill directly the zero initial derivative of both $F(q,t)$ and $C_L(q,t)$ (as the mEx and mDHO ones) so as to obtain the correct short time behavior of both functions.

In Fig. 7.5 we plot the AIMD calculated $C_L(q,\omega)$ for several wavevectors below and above q_p. The behavior observed is rather similar to the one found in the transverse case. A two mode character of the functions is clearly observed. When approaching q_p from below the high-frequency component hardly changes its position, but its amplitude decreases strongly. On the contrary, the amplitude of the low-frequency component increases, while its position decreases. The switch from the high to the low frequency dominance in amplitudes produces a sharp decrease in the frequency corresponding to the maximum of $C_L(q,\omega)$ for q between 1.84 and 2.07 Å^{-1}. For wavevectors above q_p the opposite trend is found, with the amplitude of the low-frequency mode decreasing with q in favor of the high-frequency component, and a steep change in the position of the maximum from low

to high frequencies. The decomposition of $C_L(q, \omega)$ into contributions is shown for two q values on the right panels of Fig. 7.5. Two mDHOs and one mEx were used in the common fits of $F(q, t)$ and $C_L(q, t)$ and it is interesting to observe the contribution of the relaxing mEx mode at small ω, which introduces a kind of bump in C_L at low frequencies.
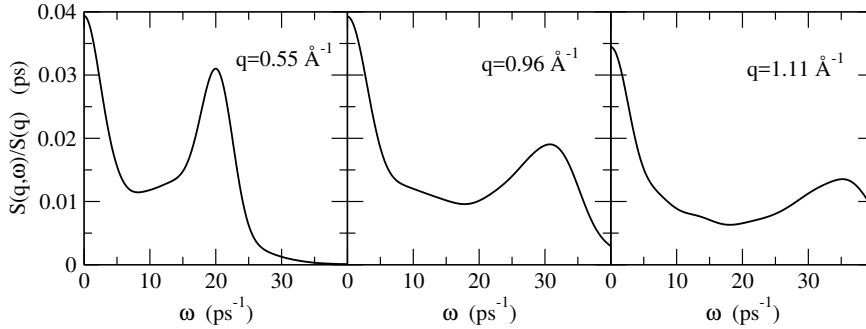
FIGURE 7.6: $S(q, \omega)$ for some q values in the 1psBZ.

Note that the analysis performed above includes the region of wavevectors larger that $q_p/2$, where the two-mode structure of the transverse and longitudinal currents is more visible. However, experimental measurements of $S(q, \omega)$ were performed in the q-range below $q_p/2$, usually called first pseudo Brillouin zone (1psBZ), and it is in this region where the measurements have suggested the existence of two propagating modes, with a low frequency one that produces a small signal in the measured intensity at an energy located roughly between the quasielastic line and the usual intense inelastic one.

Fig. 7.6 shows the results obtained from our simulations, for a few q values in this range. We clearly observe an unusual shape of $S(q, \omega)$ between the quasielastic and inelastic lines, which is qualitatively consistent with the IXS and INS results [246, 255]. A more detailed comparison with experiments requires the conversion from the calculated $S(q, \omega)$ to the equivalent measured $I(q, E)$, which comprises the application of the detailed balance correction, convolution with experimental resolution function and scaling (to arbitrary units as given in experiments). We show such comparison in Fig. 7.7, where we see a general overall agreement between the IXS experiment [246] and simulation, except for the height of the quasielastic line. However, the specific inter-line region shows indeed a similar shape, which was attributed in the experimental study to fingerprints of the influence of transverse excitations into the longitudinal dynamics. This was due to the good fitting of the experimental data obtained using a central Lorentzian line and two DHOs, suggesting the existence of two propagating excitations [246]. The INS experiments led to a similar conclusion, although the model used in fitting the $I(q, E)$ was different [255].

We show in Fig. 7.8 the AIMD results for the three functions $S(q, \omega)$, $C_L(q, \omega)$ and $C_T(q, \omega)$, scaled so as to fit in the same graph, in order to attest (i) the coincidence of the "features" in $S(q, \omega)$ with those of the longitudinal current spectra, which also display an "odd" shape in the corresponding frequency region, and (ii) the proximity between the frequencies of these features and the single maximum of C_T. Both q values shown are within the 1psBZ.

The global situation is summarized in Fig. 7.9, where we plot in several ways the results of the fits of the AIMD data to sums of one mEx and two mDHO models to all the functions considered, as discussed previously. For each mDHO we obtain an oscillation frequency, ω_o, and a damping rate, γ. We define the natural oscillator frequency (that is, the one if there were no damping) as $\Omega_+ = \sqrt{\omega_o^2 + \gamma^2}$. This value is very close to the position of the maximum of the product of ω^2 and the FT of the mDHO. We also define the apparent frequency as $\Omega_- = \sqrt{\omega_o^2 - \gamma^2}$, which is very close to the position of the maximum of the FT of the mDHO (assuming that $\gamma < \omega_o$, otherwise the maximum occurs at $\omega = 0$). Therefore, if the mDHO would be the only mode present one should see a maximum in $S(q, \omega \approx \Omega_-^L)$ and in $C_L(q, \omega \approx \Omega_+^L)$ for the $\Omega_\pm^L$ obtained in the common fit to
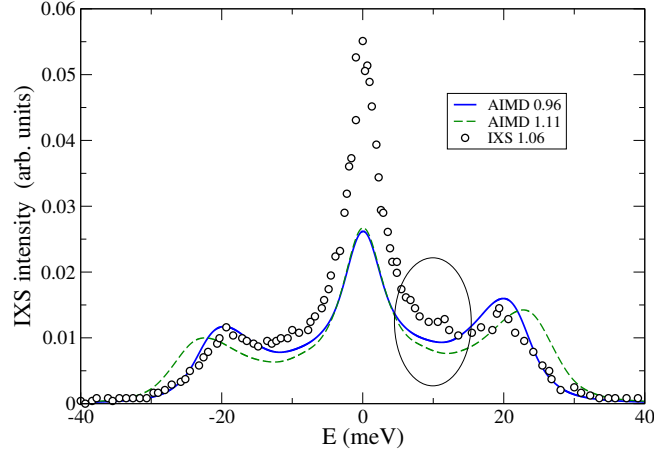
FIGURE 7.7: Comparison of IXS measurements at $q = 1.06$ Å^{-1} and AIMD $I(q, E)$ obtained from the properly modified $S(q, \omega)$ (see text) for $q = 0.96$ and 1.11 Å^{-1}.

these functions. Similarly one should find a maximum in $C_T(q, \omega \approx \Omega_-^T)$ for the Ω_-^T found in the fit. Note that no special feature would be seen at the natural transverse frequency Ω_+^T. In fact, the existence of other modes, with varying frequencies, damping coefficients and amplitudes, can result in changing somewhat the position of the maxima, turning the individual peaks into shoulders or even masking them completely if the amplitudes are small.

We have plotted in Fig. 7.9 the natural frequencies in the left panel and the apparent frequencies in the right panel, for both the longitudinal and the transverse dynamics. We see that up to a wavevector around 1.2 Å^{-1} the dynamics is well described with just one mDHO, but for larger q a two mode model describes better the AIMD data. Moreover, between 1.0 and 1.8 Å^{-1}, there is a coincidence between the low energy longitudinal natural frequency and either the unique or the low energy transverse natural frequency. On the other hand, the positions of the low frequency maxima of $S(q, \omega)$ and $C_T(q, \omega)$, when they exist, occur at similar, but not so much coincident positions, due to the different dampings of the longitudinal and transverse modes. It is remarkable that the high frequency transverse modes, after they appear, disperse very little, and both their natural and their apparent frequencies stay rather close to the largest frequency of the high energy longitudinal mode, which occurs around $q_p/2$.
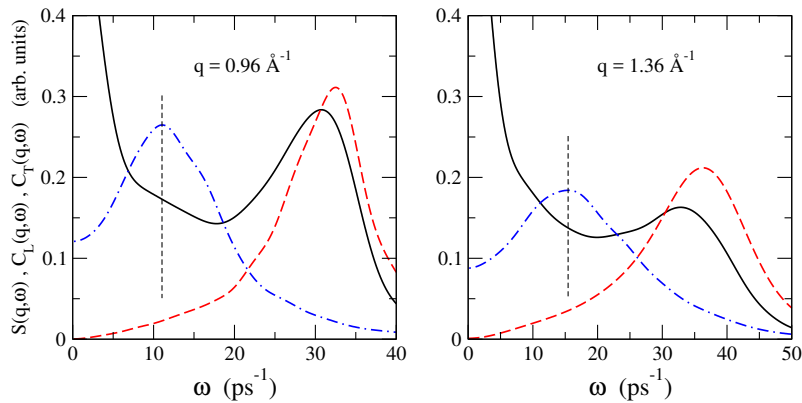
FIGURE 7.8: Comparison among $S(q, \omega)$ (full line), $C_L(q, \omega)$ (dashed line) and $C_T(q, \omega)$ (dash-dotted line), scaled so as to fit in the same graph, for two q values in the 1psBZ. The vertical lines denote the position of the maximum of $C_T(q, \omega)$.
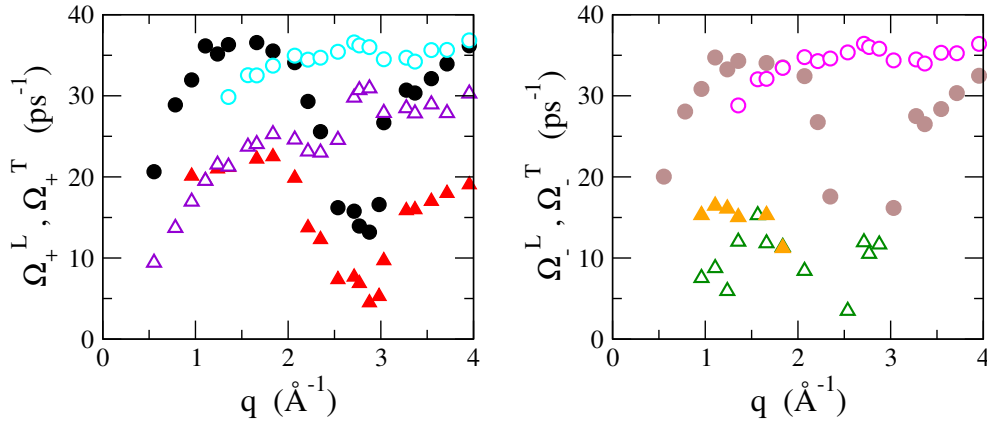
FIGURE 7.9: Left panel: longitudinal and transverse natural frequencies. Circles: high energy modes. Triangles: low energy modes. Full symbols: longitudinal modes. Open symbols: transverse modes. Right panel: corresponding apparent frequencies. Symbols have the same meaning as in the left panel.

Mode-coupling analysis

From the AIMD calculated $F(q,t)$ and $C_T(q,t)$ we have evaluated the corresponding AIMD memory functions, $N(q,t)$ and $M_T(q,t)$ solving the integrodifferential equations that define them (equation 157).

We have also used the expressions provided in Appendix A in order to compute the fast and MC components. The initial values and curvatures of the fast terms are equal to those of the full functions, which have been obtained from the simulation $N(q,t)$ and $M_T(q,t)$ by fitting the short time region with a form $a_0 - a_2 t^2 + a_4 t^4$. The integrals that define the MC component involve the whole wavevector range from zero to infinity. Obviously we have evaluated them only in the range in which we have computed the $F(q,t)$ functions, which goes from q_{min} up to a maximum vector $q_{max} \approx 2q_p$. Moreover, since the set of wavevectors is established by the periodic boundary conditions, the functions are obtained in an uneven grid of q-values. The integrals have therefore been performed using the trapezoidal rule, which is convenient for such a type of grid. All these limitations have an influence on the accuracy of the computed MC integrals, but we do not expect a qualitative change in the form of the results as a consequence of these limitations. We instead consider that the accuracy of the whole theory has a much greater influence on the goodness of the results. For instance, the inclusion of additional slow modes or a more fundamental treatment of the fast components that appear in the theory could lead to more marked, even qualitative changes. We will consider this point below, after the presentation of the results.

We finally point out that we have evaluated $S(q,\omega)$ and $C_L(q,\omega)$ from the sine and cosine Fourier Transforms of $N(q,t)$, and $C_T(q,\omega)$ from those of $M_T(q,t)$, through the memory function equations in the Laplace domain and the relation between Fourier and Laplace transformations. The explicit formulas are detailed in Appendix A.

Transverse dynamics

The results obtained through the MC formalism for $C_T(q,\omega)$ are compared with the AIMD ones in Fig. 7.10, for $q = 0.96, 2.35$ and 3.28 Å^{-1}. The first wavevector corresponds to the region where only one mode appears, whereas the other two lie below and above q_p in the two-mode region. We observe a qualitative agreement between MC and AIMD results, in particular regarding the one- or two-mode feature. This means that the present MC formalism captures the main mechanisms responsible for the double-mode structure, so that indeed the coupling with density fluctuations gives rise to such features. However, as mentioned above, the coupling is indirect, with all posible wavevectors, and not just the specific $\bar{q}$ being considered, and occurs at the level of the memory function through an integration over wavenumbers k and p.

The weight for the coupling with different wavevectors is dictated by the function $\gamma(q, k, p)$ defined in Appendix A. It is interesting to analyze how this function depends on its parameters (k, p). The function γ factorizes into a product of a structural term, $(S(k) - S(p))^2/(S(k)S(p))$ and a "geometric" factor that depends only on the magnitude of the wavevectors. The form of the structural term favors (k, p) regions where the structure factor has a small magnitude, and values of k and p that lead to large differences between $S(k)$ and $S(p)$. This term therefore is largest for $k \to 0$ and p around q_p, with further, but lower, maxima at the positions of the subsequent peaks of the structure factor (and interchanging k and p since the function is symmetric). Note that the structural term is zero for $k = p$. The geometric term, on the other hand, is zero at the limits of the integration region (a strip around the diagonal) and is maximum at $k = p$. The general structure of the weighting function will therefore be dictated by the compromise between the differing behavior of each term, leading to maxima, in general, for "small" k and near $p \approx q_p$, assuming such values of k are within the integration region (which approximately means that q is between $q_p/2$ and the first minimum of $S(q)$, located around 3.75 Å^{-1}, which we will refer to as the intermediate q region).
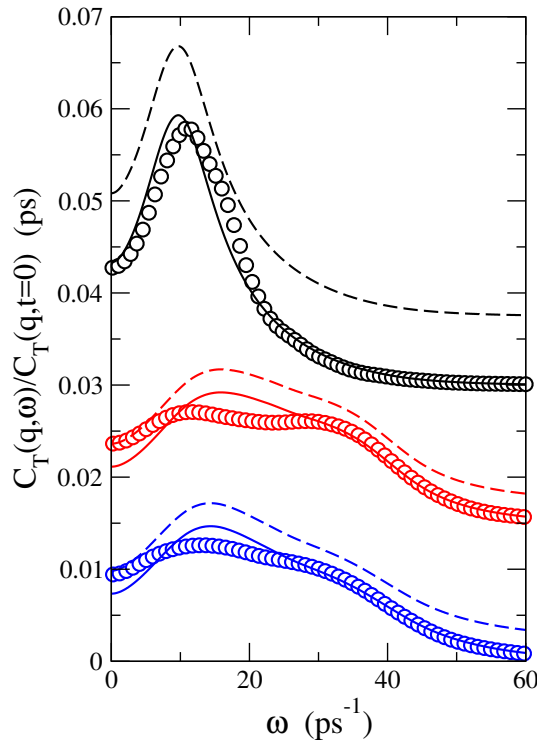
FIGURE 7.10: Comparison between AIMD calculated $C_T(q, \omega)$, shown by symbols, and MC results, shown as lines. The q values shown are 0.96 Å^{-1} (displaced 0.03 units upwards), 2.35 Å^{-1} (displaced 0.015 units upwards), and 3.28 Å^{-1}. The lines are repeated slightly displaced above (dashed lines) in order to observe more clearly the double-mode structure where it exists.

We show a glimpse of the weighting function $\gamma(q, k, p)$ in Fig. 7.11 for q values below $q_p/2$, around $q_p/2$, around q_p, and for a q-value beyond the first minimum of $S(q)$. It can be observed that the structure of the weight function changes little in the intermediate q region, but is qualitatively different outside. Remarkably, the clipping due to the geometric factor leads to maxima of the weight function that occur in the vicinity of $k = q_p/2, p = q_p$ for wavevectors in the intermediate q region. Therefore the structure of $M_T^{MC}(q, t)$ is basically the same in such region and consequently this can explain the lack of dispersion of the modes in $C_T(q, \omega)$ as observed in the AIMD simulations.

Although the presence of two modes is correctly described, the amplitude of the main, low-energy, one seems to be overestimated by the theory. In order to track down the origin of this problem we have compared directly
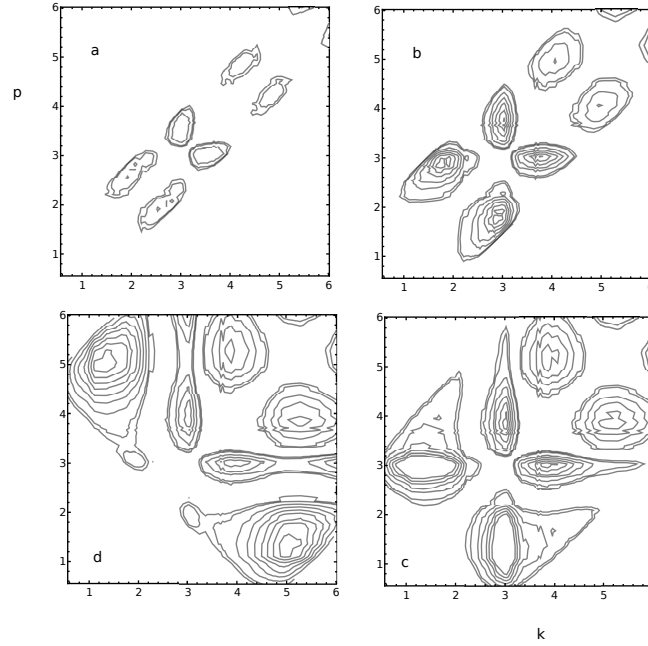
FIGURE 7.11: Isolines for the weighting function $\gamma(q, k, p)$ at $q = 0.96$ (a), 1.57 (b), 2.98 (c), and 4.63 (d) Å^{-1}. The plotted contours correspond to 35 (closest to the diagonal), 50, 100, 150, $\cdots$, units.

the AIMD and MC memory functions, as shown in Fig. 7.12. The general shape, including the positions of maxima and minima when present, is reproduced. However, we find two weak points in the theory. The first is that the tail amplitude is in some cases overestimated, reflecting possibly the need to include additional slow variables in the MC contribution. The second problem is due to the fact that the mode-coupling component is always found to be positive, and the fast term, by construction, is also positive. Consequently the theory cannot reproduce the AIMD data whenever they show a negative minimum, which also coincides with the q-region where the amplitude problem in $C_T(q, \omega)$ appears. A similar failure of the MC formalism to represent negative values in molecular dynamics data has been observed for the velocity autocorrelation function in liquid Pb [80], and in liquid Sn and Ge near the melting point and liquid Na at high temperatures [81].
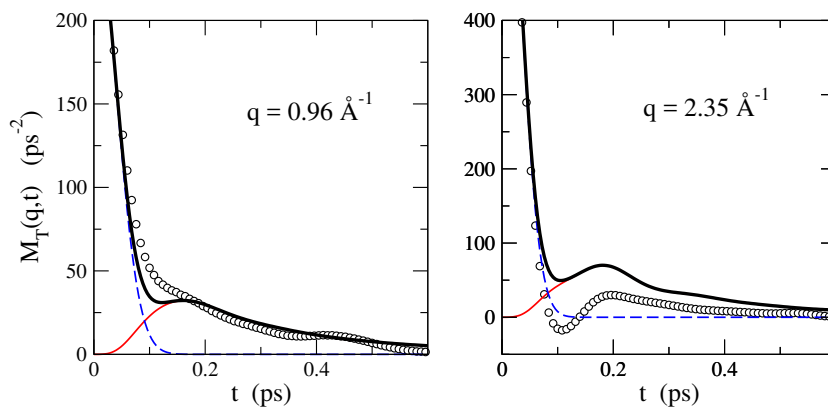
FIGURE 7.12: $M_T(q, t)$ for the wavevectors shown. Circles: AIMD results. Dashed line: fast part. Thin solid line: MC component. Thick solid line: total theoretical function.

We believe that the way towards the solution of these problems lies in a better treatment of the fast part of the memory function. As mentioned above, it includes not only the effects of binary collisions, but also the coupling with fast-decaying modes not included in the MC integral. These could indeed give rise to a negative minimum that would be reflected in an improved agreement with AIMD data. We therefore suggest the modification of the theory through the use of ansätz for the fast term, different from the one used here, that incorporate a negative minimum in order to check the impact these would have in the quantitative description of the two-mode structure of $C_T(q, \omega)$. In fact, already in the seminal work of Levesque and Verlet on LJ systems [77] the second order memory function of the intermediate scattering function was modeled using a fast term that has a negative minimum. Moreover, the ansatz propsed by Wahnström and Sjögren for this same function [76] also becomes negative, as shown explicitly by Canales and Padró in their studies of liquid Li and LJ systems [83]. Even though we are considering here a different correlation function it seems plausible that a similar ansatz may be useful.

In connection with this point, we have tried to fit $M_T(q, t)$ with the models mentioned in the text above, and found that indeed one mEx and one mDHO describe well the AIMD data in the two-mode region. Curiously, the mDHO turns out to be the fast term (which oscillates and takes negative values) while the mEx term decays slowly, but does not go to zero for small times. We expect this information can also be useful in considering possible modifications to the MC theory in order to improve its accuracy.

In this context, as a final note, we also mention a diagramatic formulation of the kinetic theory of fluctuations in equilibrium classical fluids, developed by Andersen and collaborators, who studied in particular the short time behavior of the memory functions (akin to the fast term discussed here) [264] The calculation of this short time part for a LJ liquid within such approach [265] indeed produced terms with a fast decay, but they do not account for the total value of the memory function at $t = 0$.

Longitudinal dynamics

We show in Fig. 7.13 $C_L(q, \omega)$ as obtained through the MC formalism, compared with the AIMD results in the q-range where the double-mode feature is visible in the simulations. Clearly, the theory describes correctly the mechanisms behind the appearance of this two-mode structure, including their frequencies and also the variation of the amplitudes with q, as evinced by the shifts in the main peak position in small intervals of q below (left panel) and above q_p (right panel), that was described previously.
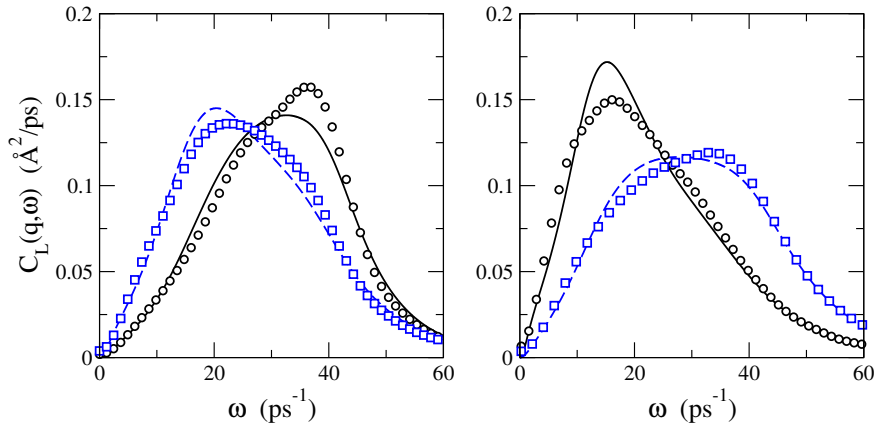
FIGURE 7.13: Comparison between AIMD calculated $C_L(q, \omega)$, shown by symbols, and MC results, shown as lines. The q values shown are 1.75 Å^{-1} (full line and circles), and 2.07 Å^{-1} (dashed line and squares) in the left panel, and 3.27 Å^{-1} (full line and circles) and 4.07 Å^{-1} (dashed line and squares) in the right panel.

The dynamic structure factor obtained from the AIMD simulations also showed traits of two propagating modes for some q values in the 1psBZ. The corresponding MC results are compared with the AIMD ones in
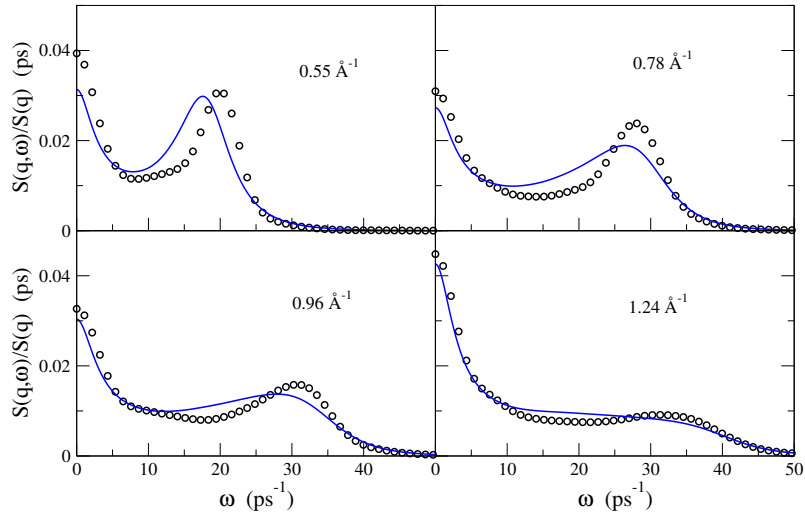
FIGURE 7.14: Comparison between AIMD calculated $S(q, \omega)$, shown by symbols, and MC results, shown as lines. The q values are shown in the graphs.

Fig. 7.14. Here the theory basically misses the second propagating mode, and even the usual sound mode appears at too low a frequency in the MC data at the smallest q allowed by the simulation setup, although this can be due to the absence of coupling with temperature fluctuations in the theory, which is important for small q. Only for $q \approx 0.96 \text{ Å}^{-1}$ the theory starts showing some hints of an additional mode in the expected frequency region, but there is still much room for improvement in this important wavevector region. Taking into account that only the density has been considered as a slow mode to couple with, it seems natural to conclude that further modes need to be included in the MC formalism, out of which the most obvious one would be the transverse current mode. Such possibility will be explored elsewhere and reported in due course.

One could also consider the possible existence of a problem with the fast component of $N(q, t)$ similar to the one found in $M_T(q, t)$, namely, the presence of negative values in the AIMD memory function, not reproducible using the gaussian ansatz. In fact, this is not the case for q values in the 1psBZ. For much larger q very shallow negative minima appear, but they cannot be discarded to be due to numerical noise in the calculation of the second order memory functions. In any case, this does not appear to be the main problem in the theory regarding the longitudinal dynamics.

As a short note we mention that the weight function for density-density coupling, $\alpha(q, k, p)$, displays a complicated behavior because it is not separable into structural and geometric terms, and it is not straightforward to relate the q-variation of $C_L(q, \omega)$ to the changes in $\alpha(q, k, p)$.

7.1.5 *Velocity autocorrelation function*

The AIMD calculated $Z(t)$ is shown in Fig. 7.15 together with the one calculated through the MC approach of Gaskell and Miller [85], previously seen in Chapter 3. The longitudinal and transverse components of $Z_{GM}(t)$ are also displayed in the figure. We observe that both $Z_{GM}^L(t)$ and $Z_{GM}^T(t)$ show damped oscillations, with the former dominating for larger times because of the smaller damping. The theory is able to describe very well the simulation results, except in the region near $t = 0$, where we observe some problems related to the limited integration range available.

In the power spectrum, $Z(\omega)$, we find two clear peaks, well separated in frequency. The MC results show that the low frequency peak comes from the contribution of tranverse currents, while the high frequency one corresponds to the longitudinal contribution. Interestingly, the peak frequencies for $Z_{GM}^T(\omega)$ and $Z_{GM}^L(\omega)$ ($\approx$

10 and 35 ps^{-1} respectively) are near the values where $C_T(q, \omega)$ and $C_L(q, \omega)$ show maxima for $q \approx q_p/2$. Note that the second maximum of $Z(\omega)$ occurs at somewhat lower frequency that that of $Z^L_{GM}(\omega)$, due to the addition of the tail of the transverse part.
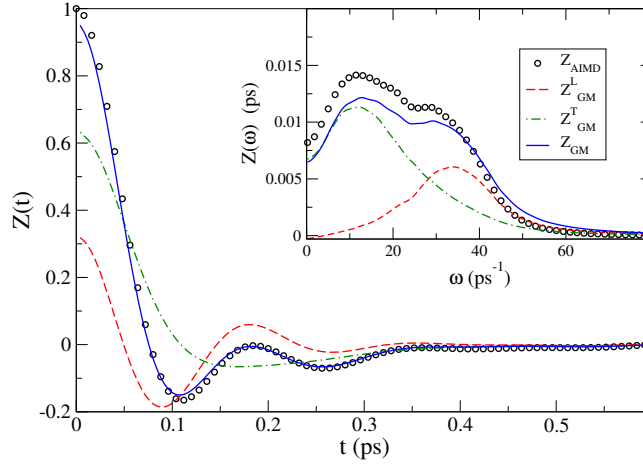
FIGURE 7.15: Normalized velocity autocorrelation function for l-Zn. Symbols denote the AIMD results. The full line is the theoretical MC function, with the dashed and dash-dotted lines representing its longitudinal and transverse components, respectively. The inset shows the corresponding power spectra.

As a final note, the diffusion coefficient obtained from the simulations, $D_{AIMD} = 0.23 \pm 0.01$ Å^2/ps, is very close to the experimental value [266], $D_{exp} = 0.236 \pm 0.006$ Å^2/ps.

7.1.6 *Conclusions*

The present AIMD simulations provide additional support to the experimental suggestion of complex dynamics in liquid Zn, as measured using IXS and INS in the q range within the 1psBZ. Moreover we have shown that this complex dynamics extends to larger q values, above the main peak of $S(q)$, through the appearance of a double mode structure in both the longitudinal and transverse dynamics, a feature previously observed in liquid metals at high pressure and in liquid Ni at room pressure.

Up to now, the origin of such behavior was attributed to couplings between transverse and longitudinal propagation modes, but no theoretical justification had been given. Through the use of mode-coupling concepts we have been able to relate the double-mode structure in $C_T(q, \omega)$ to the coupling of the transverse current with density fluctuations at all wavevectors $\vec{k}$, and not only at $\vec{q}$. The analysis of the weight of the different wavevectors in the sum can explain the dispersionless feature of the modes in the range from $q_p/2$ to the first minimum of $S(q)$. Similarly, the double mode-structure in $C_L(q, \omega)$ has been traced back to density-density couplings, again including all wavevectors in the integral.

However, the theory in its present form is still not able to explain the experimental and computational evidence of an additional mode in $S(q, \omega)$ in the vicinity of $q_p/2$.

We suggest that the inclusion of other coupling modes, particularly the transverse current, will be needed in order to explain the behaviour of $S(q, \omega)$ in this region. It is important from a theoretical point of view to remark again that the mode-coupling formulation takes into account the coupling modes for all wavevectors and not just the one corresponding to the function being studied, so that even if direct coupling is forbidden by symmetry requirements, the mode coupling is still possible. Finally we also suggest that a better treatment of the fast decaying term in the theory may be necessary in order to reproduce quantitatively the structure of the transverse current correlation functions for higher values of q.

The single particle dynamics, on the other hand, is well described by the mode-coupling theory of Gaskell and Miller. The power spectrum shows two well separated peaks, and this may serve as an hint towards the possible appearance of a double-mode structure in the transverse and longitudinal currents, as is indeed the case for l-Zn.

7.2 COLLECTIVE DYNAMICS IN LIQUID SN WITH OF-AIMD

The appearance of a second excitation mode in the longitudinal and transverse collective dynamics in some liquid metals has recently been observed either experimentally or computationally. However, the origin of the phenomenon is still inconclusive. For l-Sn, the second excitation mode in the dynamic structure factor and longitudinal current spectrum has been observed in IXS by Hosokawa *et al.* [J. Phys.: Condens. Matter 25, 112101 (2013)]. By performing OF-AIMD simulations on liquid Sn, we confirm the existence of a second excitation mode in the longitudinal and transverse collective dynamics and provide a theoretical explanation to this feature by means of mode coupling theories. This work has been carried out in collaboration with Prof. Carter's group at Princeton University.

7.2.1 *Introduction*

Much research in recent years has focused on the study of collective dynamics of non-simple liquid metals. It has been a challenging area to be studied experimentally for a number of years due to the available experimental techniques. However, the appearance of a new generation synchrotron facilities and the ability to energetically discriminate X-rays with high resolution has made IXS a reliable method to study collective dynamics in disordered systems. As a result, new experimental studies suggesting complex collective dynamic behaviors have been observed in the last few years. One such behavior is the appearance of a second propagating mode in the longitudinal dynamics.

The first experimental study suggesting the existence of a second mode in the intermediate scattering function and longitudinal current at small frequencies was carried out by Hosokawa *et al.* [245] on l-Ga. Since then, other simple liquid metals, such as Sn, iron Fe, zinc Zn and Cu [246, 247], have been found in experiments to exhibit this feature. Experimental results only sampled small wave vectors, lower than half of the position of the main peak in S(q), and related this second mode to a mixing of the transverse current with the longitudinal current. Later AIMD calculations performed on l-Li, l-Fe and l-Na [191, 256, 257] at high pressures revealed the existence of a second mode also on the transverse current correlation functions. This second mode on the transverse dynamics was visible in the wave vector region around the main peak in S(q) and at high frequencies. This effect was thought to be specific of high pressure dynamics. However, recent AIMD studies in our group have releaved this behavior on l-Ni and l-Zn at zero pressure [267].

The present study analyzes the second propagating mode in collective dynamics of l-Sn at zero pressure and the theoretical explanation for this feature. Previous AIMD calculations on l-Sn by Kresse [268] and Itami *et al.* [269] limited themselves to the study of the static properties and single particle properties. Due to the small number of particles used, i.e., 96 and 64 respectively, the obtained results presented some deficiencies. The S(q) near the melting point in Kresse's study exhibited a too high main peak slightly shifted from the correct position. The calculated S(q) in Itami's work also presented some deficiencies along with diffusion coefficients smaller than experiment. Calderín *et al.* [228] carried out an AIMD study on the collective dynamic properties of l-Sn. The calculation used 205 particles at the thermodynamic states of 573 K, near the melting point, and at a higher temperature of 1273 K. Their results showed good agreement with available experimental results although they did not report the appearance of any second mode on either intermediate scattering function, longitudinal nor transverse current correlation functions. Later, Munejiri *et al.* [270] performed an AIMD simulation at different pressures and temperatures on 64 atom cells of l-Sn. They only reported on the observation of a second propagating mode in the spectrum of the longitudinal current correlation function and connected it with the main transverse mode. This effect was later demonstrated experimentally by Hosowaka *et al.* [247].

However, in all the previous cited works, the use of KS-AIMD and therefore, a small number of particles along with short simulation time, may have resulted in high uncertainty in the results for collective dynamics. This deficiency may have masked [228] or made unclear [270] the appearance and study of this second mode at normal pressure. In order to alleviate the constraints imposed by KS-AIMD, we have used OF-AIMD in the present work. The studied samples consist of 1000 particles, which facilitates a detailed study of the collective dynamics. The simulation was performed at the thermodynamic state of 573 K near the melting point. We observe the second mode in the dynamic structure factor and the longitudinal current spectrum, previously hinted by experimental IXS data of Hosokawa *et al.* [247]. Moreover, we report on the existence of a second mode in the transverse current correlation function spectrum at high frequencies.

The main purpose of this study is to confirm the theoretical explanation provided previously in l-Zn for the existence and connection between all the modes in the collective dynamics based on mode coupling theories. From a theoretical standpoint, mode-coupling (MC) theories, and in particular Sjögren *et al.*'s [74, 75, 78] and Gaskell and Miller's [85] formulations, have provided considerable insight into the atomic dynamics of liquids. Moreover, their application to simple liquids has yielded reasonable estimates for several dynamic properties [23]. Within Gaskell and Miller's approach, we have evaluated the velocity autocorrelation function (VACF) in terms of the longitudinal and transverse current correlation functions and compared it to simulation results. The theory gives a correct representation of VACF and provides insight as to how each of the two main peaks in the power spectrum are related to a longitudinal and a transverse contribution, respectively. To study the possible coupling between the two different collective modes, we had to use Sjögren *et al.*'s formulation. We have evaluated the longitudinal and transverse autocorrelation functions in reciprocal space and compared them to the simulation results. The theory gives a correct representation of these quantities and provides support to the conclusions from l-Zn's work in the previous section.

7.2.2 *Computational details*

All calculations were performed using OF-AIMD implemented in the PROFESS 3.0 package [185]. The Smargiassi-Madden KEDF [110, 112] was chosen. The local pseudopotential was constructed through force-matching, starting from a BLPS pseudopotential. The atomic density at each temperature was obtained through an NPT simulation with 512 particles. Each simulation lasted 40 ps and the density was calculated averaging values from the last 20 ps. The obtained number densities (Table 9) are higher than the available experimental data of Waseda [192, 271]. One reason for this slight increase in the ionic density may be related to the exchange and correlation potential (XC) used to describe Sn: LDA. LDA tends to overbind atoms, giving rise to higher densities than experiment. However, GGA substantially overestimates equilibrium volumes for Sn and that is why LDA, among other reasons, has been claimed to be better in describing Sn and used in almost all previous AIMD studies [228, 268, 269, 272]. Another reason for the discrepancies in the densities could be associated to the KEDF used, which is another source of possible error in all OF-DFT calculations. Lastly, the final systems studied were formed by 1000 atoms in a cubic simulation box with dimensions as to comply with the given atomic density at each temperature in Table 9. The timestep used is 0.004 ps and each system was first relaxed for 20 ps and afterwards studied through a total time of 80 ps. The validation of the OF-AIMD method along with the LPS constructed for l-Sn was performed through the evaluation of different static and dynamic properties at various temperatures and is included in Appendix E. We will focus in the next section on the evaluation of the possible origin of the second propagating mode.

7.2.3 *Collective dynamics.*

OF-AIMD simulation results.

We have evaluated the dynamic structure factor, $S(q, \omega)$, through the Fourier Transform (FT) into the frequency domain of the intermediate scattering function, $F(q, t)$. The scattered intensity obtained in an IXS experiment is directly related to $S(q, \omega)$, although a proper comparison between the AIMD results and IXS data requires

TABLE 9: Comparison between calculated number densities and experimental densities by Waseda [192, 271] at temperatures ranging from 573 K to 1873 K.

T (K)	573	673	773	873	973	1073	1273	1873
ρ_{OFAIMD}	0.0411	0.0399	0.0394	0.0390	0.0386	0.0381	0.0375	0.0351
ρ_{exp}	0.0352	—	—	—	0.0337	0.0335	0.0325	0.0309

taking into account the difference between the simulations, where the ions are treated like classical particles, and the photon scattering which is a quantum process. Therefore, to compare with the IXS experimental results, the $S(q, \omega)$ obtained from our simulations is corrected so as to fulfill the detailed balance condition [23, 63]

$$S_Q(q, \omega) = \frac{\hbar \beta \omega}{1 - e^{-\hbar \beta \omega}} S(q, \omega) \tag{162}$$

where $S(q, \omega)$ is the dynamic structure factor calculated in the simulation and $\beta = \frac{1}{k_B T}$ with k_B the Boltzmann constant and T the temperature. Moreover, the experimental setup is characterized by an energy resolution, which is taken into account in our simulation results through the convolution of $S_Q(q, \omega)$ with the experimental resolution function,

$$I(q, \omega) = E(q) \int d\omega' \quad S_Q(q, \omega') R(\omega - \omega') \tag{163}$$

where $R(\omega)$ is the experimental resolution function and $E(q)$ is a normalization factor which takes into account the scattering geometries and the experimental setup. In the case of the IXS experiments performed by Hosokawa *et al.* for l-Sn [247] the experimental resolution factor takes the following form,

$$R(\omega) = \frac{c}{\pi \left(\omega^2 + c^2 \right)} \tag{164}$$

with $c = \frac{\Delta E}{2}$ where ΔE is the FWHM energy resolution in the experiment.

The normalization factor $E(q)$ is introduced through a proper rescaling in the final AIMD vs IXS comparison. Figure 7.16 depicts the $I(q, \omega)$ for different wavevectors along with experimental IXS results by Hosokawa *et al.* [247]. We observe, for different wave vectors, a very good agreement with experiment, especially concerning the position and amplitude of the side-peaks. However, we also observe some discrepancy around the central peak. It must be recalled that the accurate experimental determination of the spectral features around $\omega = 0$ is delicate task and possible discrepancies between AIMD calculations and experimental data may be caused by deconvolution corrections and impurities in the sample. Therefore, discrepancies in this region are to be expected.

Moreover, we have evaluated the longitudinal and transverse current correlation functions along with their spectra and calculated their dispersion relations, Fig. 7.17. As in l-Zn, a second high frequency mode appears in the dispersion relation of $C_T(q, \omega)$ as a second peak around $q = q_p$. Outside this small region, the second mode appears as a side shoulder. $S(q, \omega)$ and $C_L(q, \omega)$ also present a second mode as a side shoulder in their spectra.

To obtain information on the dispersion relation of these second modes, it is necessary to fit the correlation functions to a model. For this purpose, we have used the same mDHO model as for the previous study of l-Zn. The dispersion relations obtained from the maxima of the spectra of each mode are depicted in Fig. 7.18. The left hand side graph shows the apparent frequencies from the two longitudinal modes, $h_L^{(1)}$ and $h_L^{(2)}$, (which follows the dispersion relation of $S(q, \omega)$) along with the natural frequencies, $\Omega_L^{(1)}$ and $\Omega_L^{(2)}$ which follows the dispersion relation of $C_L(q, \omega)$. The right hand side of Fig. 7.18 depicts the apparent frequencies from the two transverse modes, $h_T^{(1)}$ and $h_T^{(2)}$, which follows the dispersion relation of $C_T(q, \omega)$, $\omega_{T,1}$ and $\omega_{T,2}$, also plotted for comparison.
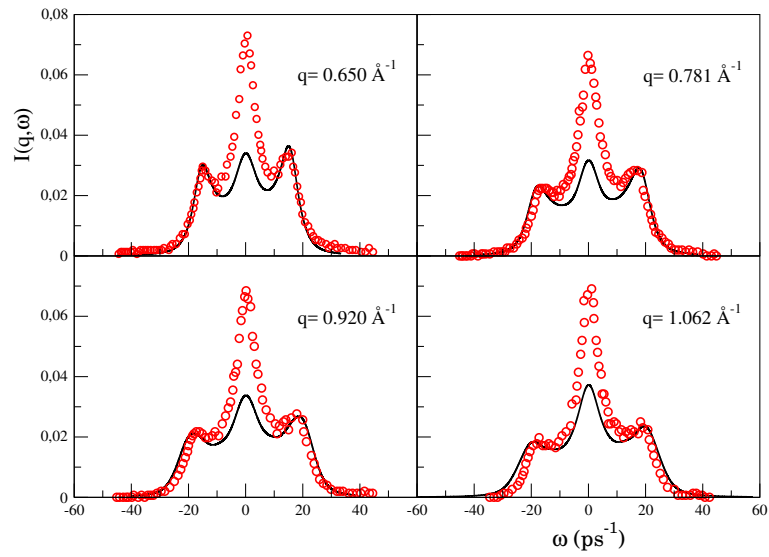
FIGURE 7.16: Comparison of OF-AIMD $I(q, \omega)$ obtained from the properly modified $S(q, \omega)$ (full line) and IXS measurements by Hosokawa *et al.* (open circles) [247] for q=0.66, 0.79, 0.92 and 1.06 Å^{-1}.
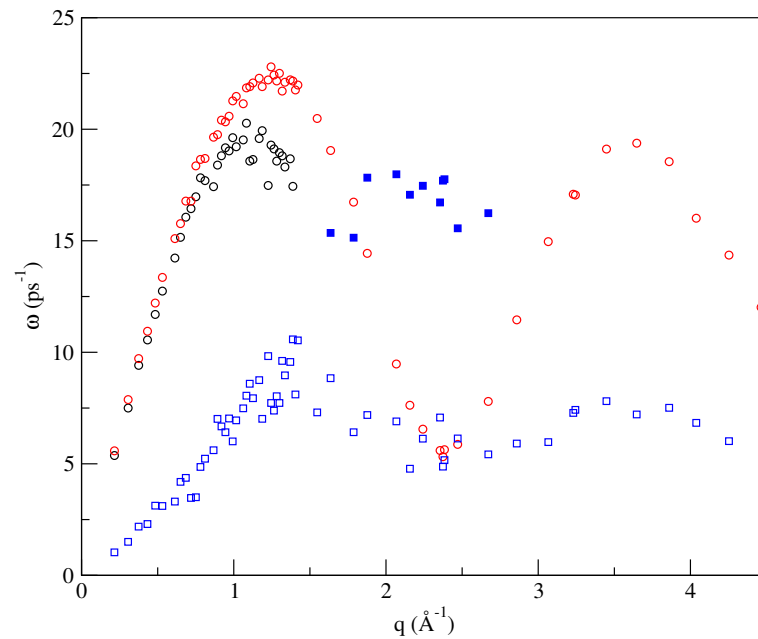
FIGURE 7.17: OF-AIMD dispersion relations for l-Sn at T=573 K. Black circles: $S(q, \omega)$ dispersion. Red circles: $C_L(q, \omega)$ dispersion. Blue squares: $C_T(q, \omega)$ dispersion. The second propagating mode in $C_T(q, \omega)$ is displayed as filled squares.
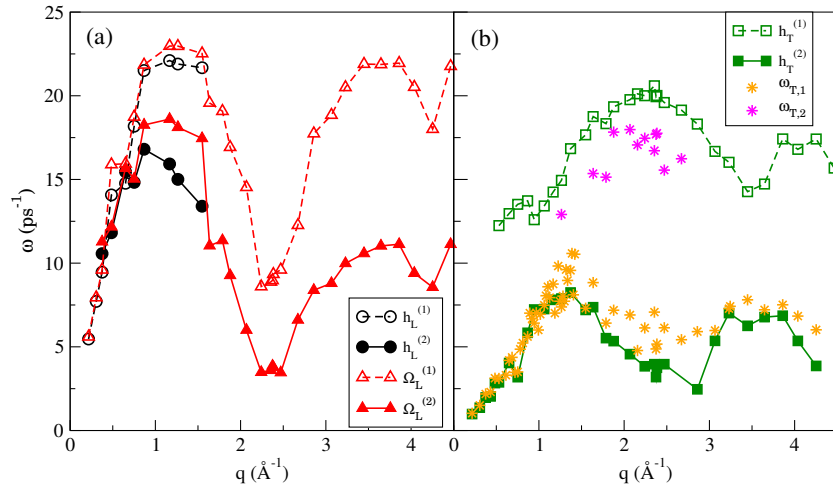
FIGURE 7.18: Dispersion relations of the maximums using the mDHO model. (a) $F(q, t)$ fit (black circles) and $C_L(q, t)$ fit (red triangles). (b) $C_T(q, t)$ fit (green squares). Open and closed symbols differentiate between first and second mode. Stars represent both modes obtained from $C_T(q, \omega)$ directly.

In Fig.7.19 (a) we compare the natural frequencies from the longitudinal modes with the frequencies obtained directly from the analysis of $C_L(q, \omega)$. Fig.7.19 (b) shows both natural frequencies from the longitudinal and transverse currents to observe any possible relation among any of their two modes.
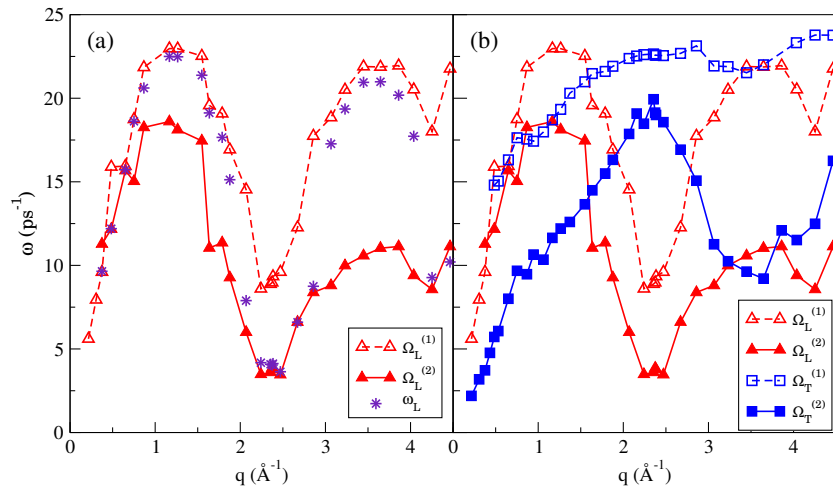
FIGURE 7.19: a) Dispersion relation of the maximums of each mDHO in the $C_L(q, \omega)$ (red triangles) and the total $C_L(q, \omega)$, which is the sum of both mDHO and the diffusive term (purple stars). (b) Dispersion relation of the natural frequencies of each mDHO in $C_L(q, \omega)$ (red triangles) and $C_T(q, \omega)$ (blue squares). Open and closed symbols differentiate between first and second mode.

Three important observations can be made by comparing Fig. 7.17, 7.18, and 7.19. First, the frequency of the unique peak of $C_L(q, \omega)$, i.e. $\omega_L(q)$, oscillates between that of the two modes $\Omega_L^{(1)}(q)$ and $\Omega_L^{(2)}(q)$ as a consequence of the amplitude of one mode decreasing and the amplitude of the other mode increasing. This is clearly seen in Fig. 7.19 (a). Second, there is a large difference between the position of the peaks in $C_T(q, \omega)$, shown in Figure 7.17 and in Figure 7.18 (b) using the mDHO, and the natural frequencies, shown in Figure 7.19 (b). This is due to the large damping coefficients of the transverse modes, that makes the frequency of the oscillation

smaller than the natural frequency. Finally, we observe in Figure 7.19 (b) that the natural frequencies of the low-energy longitudinal mode have a numerical value, for $q < 1.2$ Å^{-1}, very close to the natural frequency of the second, high energy transverse mode. This last point may suggest that the second modes appearing in all the collective dynamic functions are all related and may all have the same origin. To study such an origin, we turn to analyze our results with the MC theory.

Mode Coupling Theory

Single particle dynamics

For liquid systems, information about transport properties can be extracted from the VACF of a tagged ion in the fluid and, as in l-Zn, additional physical insight into the features of $Z(t)$ is provided by the MC approximation of Gaskell and Miller [85], which provides information about the relative importance of the coupling between the single-particle motion and the collective longitudinal and transverse currents. Using Eq. 113, both longitudinal and transverse contributions to VACF have been calculated.
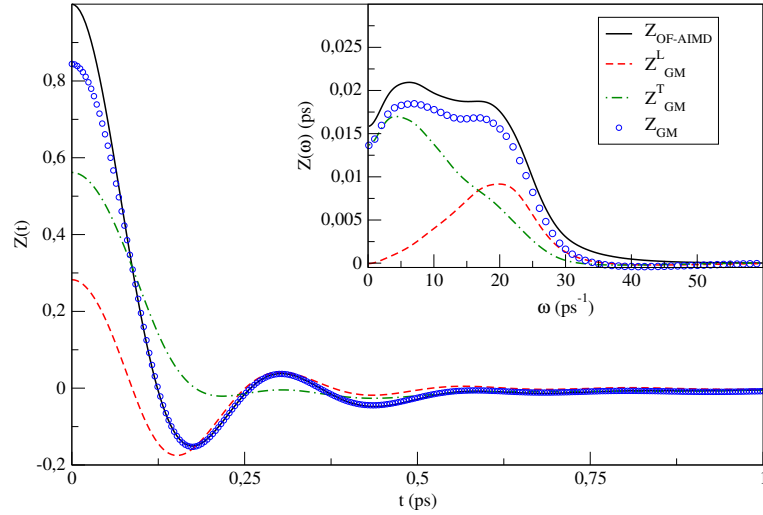
FIGURE 7.20: Solid line: normalized velocity autocorrelation function, $Z(t)$, obtained for l-Sn at T=573 K. The inset represents the power spectrum $Z(\omega)$. Dashed and dotted lines represent the longitudinal and transverse components of $Z(t)$ and $Z(\omega)$, respectively.

Figure 7.20 depicts both contributions, which show damped oscillations. It is found that the longitudinal component is less damped, so that it contributes over a wider time interval, although the crossing through zero of $Z(t)$ is determined by a balance between both components. An estimate of the frequency at which a given atom/ion is vibrating within the cage [23, 26] can be achieved through the second order Taylor expansion $Z(t) = 1 - \omega_E t^2/2$ where ω_E is the so-called Einstein frequency of the system. A short time fitting of the $Z(t)$ curve gives $\omega_E \approx 16.01$ ps^{-1}. The inset of Figure 7.20 shows the FT of $Z(t)$, the power spectrum or $Z(\omega)$. Each $Z_L(\omega)$ and $Z_T(\omega)$ show a peak and the combination of the two curves leads to a double-peak structure of the total $Z()\omega$, with the corresponding ω_E located between the two peaks.

Marques *et al.* study of l-Na at high pressures [256], where a second propagating mode appeared in the transverse current correlation dispersion relation, both components of $Z()\omega$ were evaluated. However, at zero pressure, where no second propagating mode was observed, the power spectrum presented just one peak and the longitudinal component of $Z(\omega)$ was completely covered by the transverse component. As pressure was increased, both components start to separate and two separated peaks start to appear in $Z(\omega)$. The fact that l-Sn's

VACF at zero pressure presents the same behaviour as l-Na's VACF at high pressures is in accordance with having the second propagating mode in l-Sn at zero pressure while l-Na only presented it at high pressures. This behaviour suggests a connection between the appearance of a second mode in the collective dynamic properties and the separation of both components of $Z(\omega)$ giving rise to two peaks, independent of working at zero or high pressure.

Collective dynamics

To study the possible coupling between the longitudinal and transverse current correlation functions, we apply Sjögren and co-workers MC approach [23, 74, 75, 78, 273–275] which is based on a combination of kinetic theories concepts with the Mori memory function approach, already described in Appendix A.

Figures 7.21 and 7.22 show the obtained $C_L(q, \omega)$ and $C_T(q, \omega)$, respectively, for different wave vectors as obtained directly from OF-AIMD or by using Sjögren's MC approach. We observe that the MC theory is capable of showing the appearance of two propagating modes in both cases (as a main peak and a shoulder) and both propagating modes appear at the correct position (or frequency) when compared to the direct OF-AIMD results.
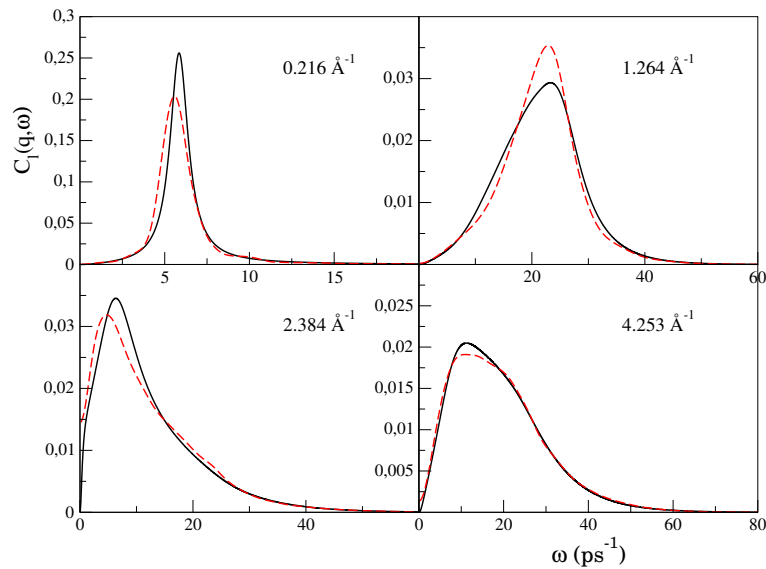
FIGURE 7.21: FT of the longitudinal current correlation functions at different wave vectors. Black line: results obtained from MC theory. Red dashed curve: results obtained directly from OF-AIMD.

From Figures 7.21 and 7.22, we notice that in the longitudinal case the theory reproduces better the OF-AIMD results than in the transverse case. This problem was already observed in the MC analysis of l-Zn. The reason in that case was the inability of the MC theory to reproduce the negative minimum present in the first memory function of $C_T(q, t)$. Fig. 7.23 depicts this first memory functions of the transverse current correlation functions obtained from OF-AIMD and from the MC theory of Sjögren *et al.*

The MC theory correctly predicts the position of the side peak as well as the decay behavior in the first memory function of the transverse correlation function at different q. However, we still find problems in the theory related to an incorrect representation of the negative minima in the first memory function. Similar problems appeared when trying to use Sjögren *et al.* MC theory in l-Zn.

7.2.4   *Conclusions*

To test MC theory as the appropriate tool to explain the two mode behavior previously observed both experimentally and in AIMD studies in various systems, which has already been successful in treating l-Zn, we decided
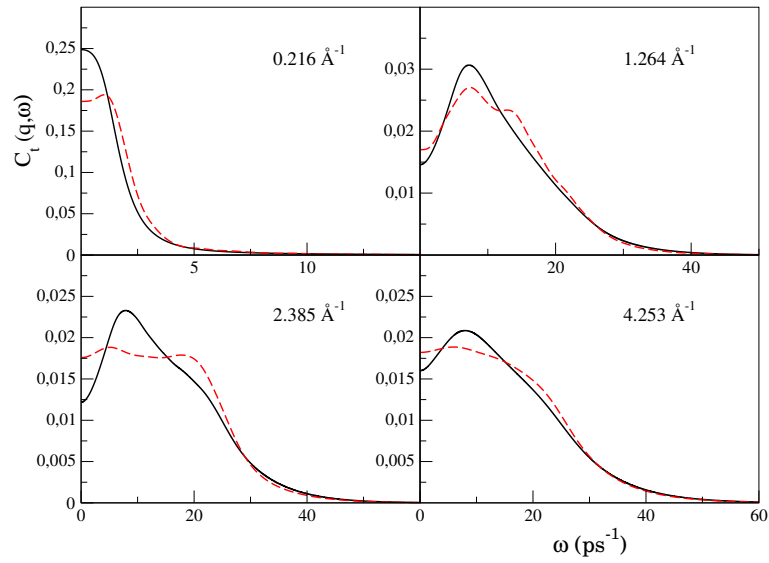
FIGURE 7.22: FT of the transverse current correlation functions at different wave vectors. Black line: results obtained from MC theory. Red dashed curve: results obtained directly from simulation.
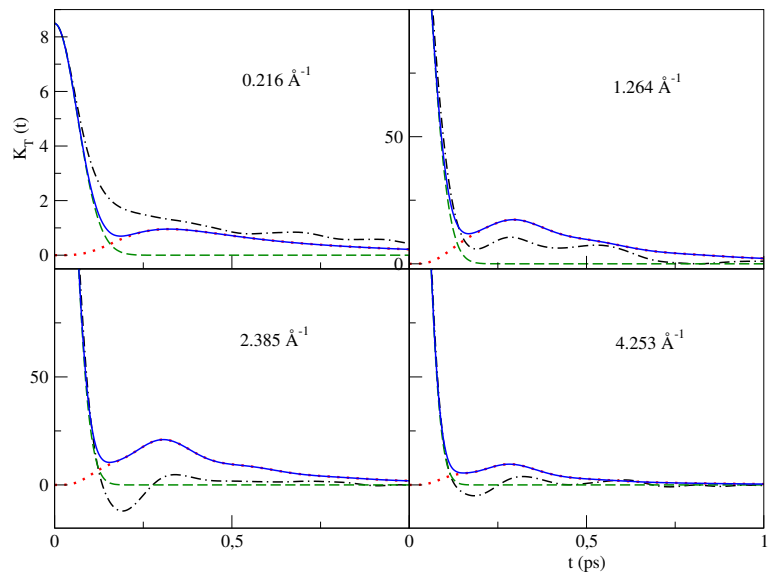
FIGURE 7.23: First memory function of the transverse current correlation functions at different wave vectors. Dashed-dotted line: OF-AIMD results. Dotted line: MC component. Dashed line: binary component. Full line: First memory function obtained from theory as the sum of the binary and MC components.

to use it in l-Sn. The reason for studying l-Sn is that it also presents a second dispersive mode in longitudinal and transverse dynamics, while being a very different system from l-Zn: 1) Sn belongs to another group in the Periodic Table and 2) the liquid phase presents a more open shell atomic arrangement whereas transition metals like l-Zn have a more closed shell structure, where icosahedral ordering dominates. However, apart from these important differences between one system and another, we observe again that the use of mode coupling theory succeeds in explaining the appearance of the second mode in collective dynamics and relates it to a coupling among longitudinal and transverse modes. This coupling is always taking place although the second mode which appears from it can only be observed at some cases. An indication of the possible observation of this mode in collective dynamics may be obtained from decomposition of the velocity autocorrelation function into its longitudinal and transverse components, following Gaskell and Miller's MC theory formulation. There appears to be a correlation between the magnitude of the separation between the peaks of the two components of $Z(\omega)$ and the ease of observation of the second mode in the longitudinal and transverse dynamics.

8

LIQUID ALLOYS.

In this chapter we make a short incursion into the realm of alloys, in particular binary alloys. The selected system is Ag-Sn. This choice is motivated by (1) the study that had already been performed for the pure components, Sn and Ag, (2) the existence of some experimental measurements of its static structure in a wide composition range, and (3) the technological interest of this particular alloy in the field of Pb-free soldering.

The existence of an additional dynamic variable, the concentration density, as compared to one-component liquids, introduces new aspects in the behavior of collective dynamics, and we have explored them in this study.

8.1 LIQUID AG-SN ALLOY. AN *AB INITIO* MOLECULAR DYNAMICS STUDY.

We report an *ab initio* molecular dynamics study of the static and dynamic properties of the liquid Ag_xSn_{1-x} alloy, which is a complex binary system with a mild tendency to heterocoordination. The calculated total static structure factors are in good agreement with the corresponding experimental data. The partial dynamic structure factors and the longitudinal current correlation spectra exhibit side peaks, some of which are indicative of propagating density fluctuations, while others are due to interdiffusion processes. We have also evaluated other dynamical properties such as the diffusion coefficients, including self- and inter-diffusion, the shear viscosity, and the adiabatic sound velocity. The electronic density of states shows that the liquid Ag_xSn_{1-x} alloy has a metallic character, although with strong deviations from the free-electron parabolic curve.

8.1.1 *Introduction*

The traditional Sn–Pb eutectic solder alloy has been widely used in electronic and communication components in the last decades. However, the inherent toxicity of Pb has prompted the search of suitable "Pb-free" solder alloys and several Sn-based eutectics containing Ag, Zn or/an Cu have been suggested because of their good mechanical properties. Furthermore, ternaries (SnAgCu, SnZnAg, Sn–Zn–In, etc) and even quaternary alloys (SnZnAgAl, SnAgBiCu, SnInAgSb) have also been considered as candidates for lead-free solders [276]. All those developments have aroused interest in the study of the physical/chemical properties associated to those candidate alloys. The main aim would be to find an alloy which could provide a similar (or better) performance as that of the Sn-Pb solders. Therefore, fundamental research into the physical/chemical properties of liquid Sn-based alloys are of paramount importance.

Within the above mentioned alloys, the Sn–Ag solder alloys stand among the most promising candidates because of their compatible properties with the Sn–Pb solder [277]. More specifically, the eutectic Ag-Sn alloy (3.5 wt. %Ag, melting temperature is $\approx$ 494 K) appears as an excellent alternative because its good mechanical strength, creep resistance and electrical properties even though it has a higher melting point and poorer fluidity than the traditional Sn-Pb solders. Therefore, it is no wonder that a considerable amount of work has already been focused on the study of a range of several thermophysical, structural, dynamical and electronic properties of the Ag-Sn alloy both in the solid and liquid states.

On the experimental side, we stress that several works have measured the density and surface tension of the liquid Ag-Sn alloy at several temperatures and compositions although special attention has focused on compositions around the eutectic composition [278–280]. Also, the liquidus and solidus temperatures as well as the enthalpy of fusion along the whole composition range have been determined [281]. Measurements of some transport coefficients such as interdiffusion coefficients and viscosity have been performed for a range of compositions and

temperatures [279, 282, 283]. Finally, we mention that Plevachuk *et al* have measured the electrical conductivity and thermoelectric power of the eutectic Ag-Sn liquid alloy at several temperatures [283].

As for the structural properties, we note that the first experimental study on the structure of this alloy was carried out by Wagner *et al* [284], who performed XD measurements for various concentrations at 100 K above the liquidus temperature. More recently, this alloy has been studied by Kaban *et al* [285], who have performed XD measurements of the total static structure factor for several concentrations and T = 1273 K. From their subsequent analysis, Kaban *et al* have suggested that the structural properties in the whole concentration range can be explained by assuming the existence of some substructures such as clusters with compositions akin to $Ag_{0.75}Sn_{0.25}$ and $Ag_{0.35}Sn_{0.65}$.

Most theoretical studies on the liquid Ag_xSn_{1-x} alloy have addressed several thermodynamic and static structural properties and the usual approach has been to characterize the liquid system by effective interatomic potentials constructed either empirically by fitting to experimental data or derived from some approximate theoretical model.

Gopala Rao *et al* have calculated several static structural properties [286], including the partial and total structure factors, as well as the partial diffusion coefficients of this alloy by using Lebowitz's analytical solution of the hard-spheres (HS) model with a square-well attractive tail. By a proper choice of the parameters in the model, they achieved a good description of the experimental total static structure factors for several concentrations and temperatures. Bhuiyan *et al* have calculated the mixing entropy, diffusion coefficients and shear viscosities of the alloy by using interatomic pair potentials which were used in the framework of a perturbation theory with the HS model taken as a reference system [287, 288]. The results were in fair agreement with experimental data. A similar theoretical approach has been followed by Terzieff [289] to calculate the viscosities of several Au- and Ag-based alloys.

Besides its intrinsic interest and prompted by the availablity of the above mentioned experimental structural data [284, 285], we have carried out a study of several static and dynamic properties of the liquid Ag_xSn_{1-x} alloy at several concentrations and a temperature T = 1273 K. We have used an AIMD simulation method based on DFT. For the specific case of liquid alloys, this approach has already provided a significant amount of information about the structural, dynamical and thermodynamic properties.

The layout of the study is as follows: In section 8.1.2 we briefly recall the theory underlying the AIMD simulation method and we describe some technical details. In section 8.1.3 we report and discuss the obtained structural and dynamical results which are compared with other previous studies as well as with the available experimental data. Finally, we summarize our main conclusions.

8.1.2   *Technical details*

For a given atomic configuration the ground state electronic energy plays the role (within the Born-Oppenheimer approximation) of the potential energy for the atomic motion. This ground state electronic energy is calculated using DFT. For the exchange and correlation energy we have used the local density approximation (LDA) [89, 91].

The ionic core of the Sn atom has been described by a norm-conserving scalar-relativistic Troullier-Martins [126] LDA pseudopotential with non-linear core corrections. This was generated [227] from the atomic electron configuration [Kr] $4d^{10}$ $5s^2$ $5p^2$ $5d^0$, pseudizing the all-electron potential to generate the local part and using cutoff radii (in a.u.) of $r_c(local) = 2.5$, $r_c(s) = 2.02$, $r_c(p) = 2.5$ and $r_c(d) = 3.0$. The calculations were performed considering as valence electrons the 4 outermost ones. In the case of Ag we have considered 11 valence electrons. Due to the presence of valence d electrons we have chosen an ultrasoft scalar-relativistic pseudopotential; it was generated from the atomic electron configuration [Kr] $4d^9$ $5s^2$, and the cutoff radii were of $r_c(local) = 2.3$, $r_c(s) = 2.3$, $r_c(p) = 2.7$ and $r_c(d) = 2.4$. Again LDA and nonlinear core corrections were considered. During and after the construction of the pseudopotentials the usual tests were performed to check its quality, such as the reproduction of the all-electron logarithmic derivatives, the results for different electronic configurations of the atom and the equilibrium distance of the solid. Finally the absence of ghost states was also confirmed.

TABLE 10: Thermodynamic input data of the liquid Ag_xSn_{1-x} alloy at $T = 1273$ K, used in the present AIMD simulation study. The total ionic number density, ρ, was taken from Ref. [278].

x_{Ag}	ρ (Å^{-3})
0.0	0.03298
0.27	0.03662
0.35	0.03778
0.50	0.03926
0.64	0.04308
0.75	0.04528
1.0	0.0517

We performed AIMD calculations for the liquid alloy Ag_xSn_{1-x} at five concentrations and a temperature $T = 1273$ K; more details are specified in Table 10. For each concentration, a total of 120 atoms were placed in a cubic supercell with the initial atomic positions taken at random. The systems were thermalized during 10 ps of simulation time. Therefrom, microcanonical AIMD simulations were performed over 16500 time steps, which amounted to 107.3 ps of simulation time, with ionic dynamics being generated using the Verlet algorithm with HF forces, as implemented in the Quantum-ESPRESSO package [227]. We used a plane-wave representation with an energy cutoff of 25 Ryd and the single Γ point was used in sampling the Brillouin zone. For all concentrations, those 16500 configurations have been used in the evaluation of the respective static, dynamic and electronic properties.

8.1.3 *Results*

Structural properties

The simulations allow a direct evaluation of the partial pair distribution functions, $g_{ij}(r)$ as well as the corresponding partial Ashcroft-Langreth (AL) structure factors $S_{ij}(q)$. Figure 8.1 shows the AIMD calculated $g_{ij}(r)$ for the liquid Ag_xSn_{1-x} alloy at four concentrations. For all concentrations the SnSn partial pair correlation function shows a behaviour different from the other two partials, with the main peak and the subsequent oscillations located at larger distances that those corresponding to AgAg and AgSn pairs. Notice that for concentrations $x_{Ag} \leqslant 0.50$, the main peak in $g_{AgSn}(r)$ is clearly higher than the main peaks in $g_{AgAg}(r)$ and $g_{SnSn}(r)$; on the other hand, for $x_{Ag} \geqslant 0.50$, it is comparable to the highest one, i.e. the $g_{AgAg}(r)$. This feature points to the existence of heterocoordinating tendencies, i.e. each atom tends to be surrounded, in its first coordination shell, by atoms of the other species.

In order to quantify the aforementioned ordering tendencies, we have calculated the Wagner [27] short range order (SRO) parameter for the first neighbour shell, α_1, along with n_{ij}, the number of j-type particles around an i-type located within a sphere of radius R_{ij}. The n_{ij} have been calculated [28–30] from the partial pair distribution functions, $g_{ij}(r)$, by integrating the corresponding radial distribution function, $4\pi r^2 g_{ij}(r)$ up to the position of its first minimum, R_{ij}.

Table 11 displays the results for the coordination numbers and α_1 . As already seen in Chapter 2, for a random distribution of atoms, the $\alpha_1 = 0$ whereas a positive (negative) value for α_1 suggests a homocoordinating (heterocoordinating) tendency. The α_1 take small negative values in all cases which clearly suggest the existence of heterocoordinating tendencies.

The obtained AL partials $S_{ij}(q)$, are depicted in Figure 8.2 for several concentrations. An interesting feature is the existence of a prepeak in the $S_{AgAg}(q)$ at the concentrations $x_{Ag} = 0.27$ and 0.50 whereas for the concentration $x_{Ag} = 0.75$ we observe another prepeak in the $S_{SnSn}(q)$. Notice that the position of the prepeak for each
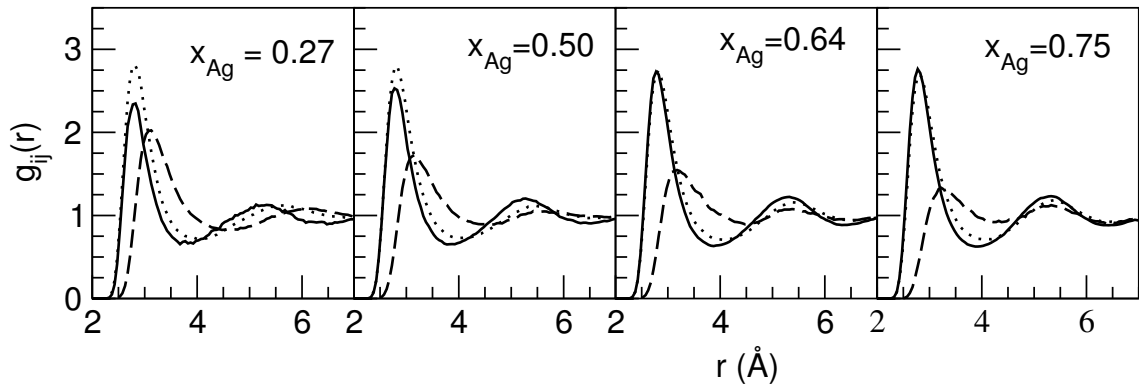
FIGURE 8.1: Partial pair distribution functions $g_{ij}(r)$ of the liquid Ag_xSn_{1-x} alloy at $x = 0.27$, 0.50, 0.64 and 0.75. Full, dashed and dotted lines correspond to $g_{AgAg}(r)$, $g_{SnSn}(r)$ and $g_{AgSn}(r)$, respectively.
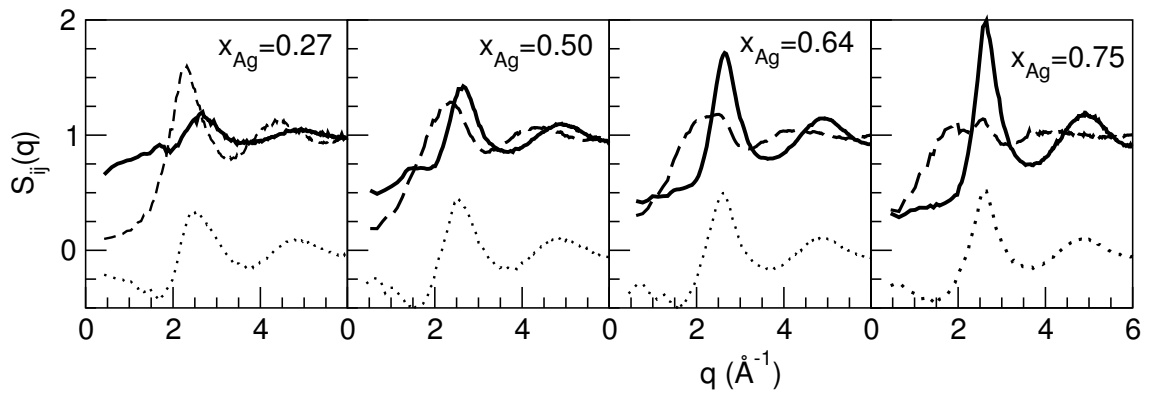
FIGURE 8.2: Ashcroft-Langreth partial static structure factors $S_{ij}(q)$ of the liquid Ag_xSn_{1-x} alloy at $x = 0.27$, 0.50, 0.64 and 0.75. Full, dashed and dotted lines correspond to $S_{AgAg}(q)$, $S_{SnSn}(q)$ and $S_{AgSn}(q)$, respectively.

TABLE 11: Calculated coordination numbers n_{ij} and the Warren SRO parameter α_1 for the liquid Ag_xSn_{1-x} alloys at the thermodynamic states given in Table 10.

x_{Ag}	n_{AgAg}	n_{AgSn}	n_{SnSn}	n_{SnAg}	α_1
0.27	1.8	6.6	7.3	2.4	-0.03
0.50	4.0	4.8	4.3	4.8	-0.07
0.64	6.2	3.8	2.8	6.8	-0.09
0.75	7.5	2.7	1.9	8.2	-0.07

concentration coincides with the position of the first minimum of $S_{AgSn}(q)$. The appearance of a prepeak has usually been related to the existence of some kind of intermediate range order in the alloy, which may be induced by the existence of some substructures such as clusters or polyatomic ions. At this point, we recall that from the analysis of their experimental total structure factor, Kaban *et al* have suggested that the structural properties of the the Ag_xSn_{1-x} liquid alloy can be explained in terms as a mixture of some special alloys (so-called reference alloys) made up of atomic micro-formations or clusters of one type. Although the appearance of prepeaks in some of our calculated AL partials $S_{ij}(q)$ may provide some support for Kaban *et al*'s suggestions, however our present AIMD calculations do not allow us to conclude anything about the existence and/or composition(-s) of those presumptive clusters. In fact, given the existence of an intermetallic compound with the $Ag_{0.75}Sn_{0.25}$ composition, the existence in the liquid phase of some remnant clusters with this same composition can not be ruled out. However, the appearance of clusters with the $Ag_{0.35}Sn_{0.65}$ composition, appears more difficult to justify.

From the AL partials, we have also evaluated the Bhatia-Thornton (BT) concentration-concentration, $S_{CC}(q)$, number-number, $S_{NN}(q)$, and number-concentration, $S_{NC}(q)$, partial structure factors (Chapter 2), and we have also evaluated the total X-ray weighted static structure factor, $S_T(q)$, given as

$$S_T(q) = \sum_{i,j=1}^{2} (x_i x_j)^{1/2} \frac{f_i(q)f_j(q)}{\langle f^2(q) \rangle} S_{ij}(q) \tag{165}$$

where $f_i(q)$ are the atomic scattering factors and $\langle f^2(q) \rangle = \sum_{i=1}^{2} x_i f_i^2(q)$.

In terms of the BT partial structure factors the X-ray weighted one can also be written as

$$S_T(q) = \frac{\langle f(q) \rangle^2 S_{NN}(q) + \delta f(q) \langle f(q) \rangle S_{NC}(q) + \delta f(q)^2 S_{CC}(q)}{\langle f^2(q) \rangle} , \tag{166}$$

where $\langle f(q) \rangle = \sum_{i=1}^{2} x_i f_i(q)$, and $\delta f(q) = f_2(q) - f_1(q)$. In the particular case of Ag-Sn alloys the atomic scattering factors of the two species are rather similar (their atomic numbers differ by only 3 units), so that $\delta f(q)$ is much smaller than $\langle f(q) \rangle$, and consequently $S_T(q)$ is basically determined by $S_{NN}(q)$.

The BT partial structure factors provide information about the topological and chemical order in the alloy. Figure 8.3 depicts the calculated BT partial structure factors for several concentrations. We observe that, for all concentrations, the corresponding $S_{NN}(q)$ displays a typical oscillatory shape, with no visible topological features like prepeaks, low-q divergences or shoulders. The main peak of $S_{CC}(q)$ roughly coincides with the position of the shoulders in the AL partials, reinforcing their interpretation as being induced by chemical ordering. On the other hand, the long-wavelength limit, $S_{CC}(q \to 0)$, provides information about the short range order in the alloy. In the present system, we have obtained that $S_{CC}(q \to 0)/x_{Ag}x_{Sn}$ takes, for all concentrations, values which are smaller than unity which suggests the existence of heterocoordinating tendencies in the alloy.

Figure 8.3 shows a comparison of the calculated $S_T(q)$ at several concentrations with the corresponding XD experimental ones [285]. The experimental $S_T(q)$ shows the typical oscillatory shape and with increasing Ag concentration its main peak which becomes higher and its position moves towards greater q-values. Notice that
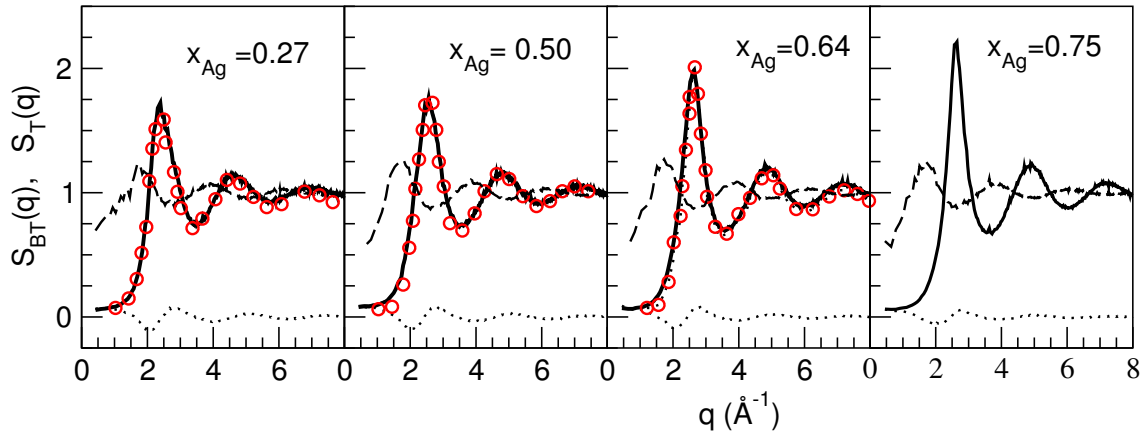
FIGURE 8.3: Bhatia-Thornton partial static structure factors and total structure factor of the liquid Ag_xSn_{1-x} alloy at x_{Ag} = 0.27, 0.50, 0.64 and 0.75. Continuous, dashed and dotted lines correspond to $S_{NN}(q)$, $S_{CC}(q)$ and $S_{NC}(q)$, respectively. The thick continuous lines stand for the calculated $S_T(q)$, whereas the open circles are the corresponding experimental data of Kaban *et al*. [285] Note that $S_{NN}(q)$ is indistinguishable from $S_T(q)$ in the scale of the graph.

the present AIMD calculations lead, for all concentrations, to an $S_T(q)$ which closely reproduces the experimental one.

At this stage we recall that Kaban *et al* have suggested that the structural properties of the Ag_xSn_{1-x} liquid alloy may be analyzed in terms of the micro-heterogeneous structure (MHS) model [285]. According to this model, the structure of the binary alloy is explained by assuming the existence of three concentration intervals bounded by the reference alloys Ag-$Ag_{0.75}Sn_{0.25}$, $Ag_{0.75}Sn_{0.25}$-$Ag_{0.35}Sn_{0.65}$ and $Ag_{0.35}Sn_{0.65}$-Sn. Moreover, inside each concentration interval, the Ag_xSn_{1-x} alloy is composed of a mixture of clusters of two kinds whose composition is that of the boundary reference alloys. The MHS model provides, for any concentration, an expression for the $S_T(q)$ of the binary alloy in terms of those of the nearest reference alloys. Therefore, by using the experimental $S_T(q)$ corresponding to the reference alloys Ag-$Ag_{0.75}Sn_{0.25}$, $Ag_{0.75}Sn_{0.25}$-$Ag_{0.35}Sn_{0.65}$ and $Ag_{0.35}Sn_{0.65}$-Sn, Kaban *et al* [285] showed that they could accurately reproduce the $S_T(q)$ for any other concentration; this was understood as a support for the existence of those specific clusters in the alloy.

However, we have checked the soundness of the MHS model by using our calculated AIMD $S_T(q)$ results. Specifically, we have considered different choices of reference alloys (i.e. varying their concentrations) and, by using the MHS model, we have evaluated the $S_T(q)$ for other intermediate concentrations; then the results have been compared with its AIMD counterparts. We have considered three different choices of reference alloys: (1) Ag-$Ag_{0.27}Sn_{0.73}$ and $Ag_{0.27}Sn_{0.73}$-Sn, (2) Ag-$Ag_{0.50}Sn_{0.50}$ and $Ag_{0.50}Sn_{0.50}$-Sn, (3) Ag-Sn, and we have used the AIMD $S_T(q)$ for these reference alloys. Now, by using the MHS model we have evaluated the $S_T(q)$ of the alloy for some concentrations between those of the reference alloys. Tellingly, the thus evaluated $S_T(q)$ were practically identical to those obtained by a direct AIMD evaluation of the $S_T(q)$, notwithstanding the specific concentrations chosen for the reference alloys. Therefore, the assumption of a link between the reference alloys and the composition of some remnant clusters is not supported by the present AIMD calculations.

Dynamic properties

In one component liquids the most important dynamic variables, which in the hydrodynamic limit determine the dynamic behaviour of the liquid, are the mass density, the energy density and the mass current. They lead to a dynamic structure factor with a central line due to heat diffusion and side lines due to sound propagation. In binary mixtures, as the Ag-Sn alloy, an extra dynamic variable appears, namely the concentration density, which leads to additional terms in the description of the dynamic structure. The new process is basically interdiffusion, which contributes with an additional central line to the dynamic structure factors.

In MD simulations the interdiffusion process can be studied specifically, in terms of the velocities of the particles, together with the usual self-diffusion of each type of atoms. In the collective, wave-vector dependent, dynamics section we analyze the intermediate scattering functions, dynamic structure factors, current correlation functions, and some associated transport coefficients.

A particular characteristic of the Ag-Sn alloy is the similarity between the atomic masses of the components ($m_{Sn}/m_{Ag} = 1.1$). If the interactions between atoms were also similar we would obtain dynamic properties similar to those of a pseudo-binary alloy. However, this is not the case, since $g_{SnSn}(r)$ is quite different from the other two partial pair distribution functions. Most of the studies of the dynamic properties of binary mixtures performed so far have concentrated in systems with large difference between the atomic masses of the components, mainly because of the early discovery of the so-called fast sound phenomenon. No such feature is expected in the case of the Ag-Sn alloy considered here.

Diffusion.

The time correlation functions among the atomic velocities of the particles provide information about those transport properties related to the mobility of the particles in the system. In this section we report results for the relative velocity correlation functions (VCFs), $Z_{ij}(t)$, which are defined in Chapter 2 along with the different diffusion coefficients D_{ij}, D_{ij}^0, D_{ij}^d and D_i^s.
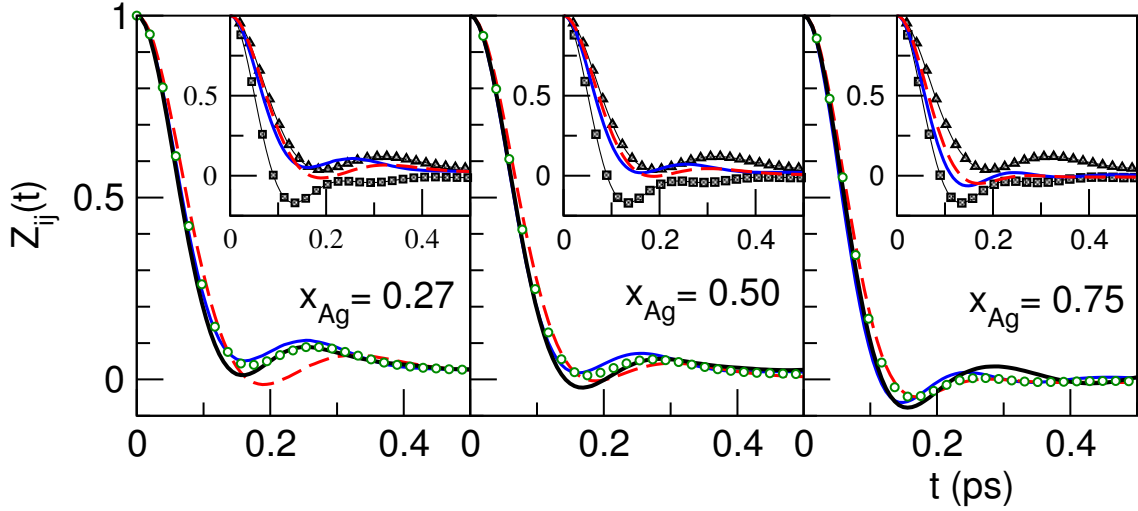
FIGURE 8.4: Normalized self, relative and ideal VACFs for the liquid Ag_xSn_{1-x} alloy at $T = 1273$ K and $x_{Ag} = 0.27$, 0.50 and 0.75. Full blue, dashed red, full thick black lines and green circles correspond to $Z_{Ag}^s(t)$, $Z_{Sn}^s(t)$, $Z_{AgSn}(t)$, and $Z_{AgSn}^0(t)$, respectively. The insets show the comparison between the self-VCFs of the alloy and those of pure liquid Ag (squares) and Sn (triangles) at the same temperature.

The present AIMD results for the normalized self and relative VCFs in the liquid Ag_xSn_{1-x} alloy at some concentrations are plotted in Figure 8.4. First, we note that both self-VCFs, namely $Z_{Ag}^s(t)$ and $Z_{Sn}^s(t)$, have qualitatively similar shapes which may be explained by the fact that the Ag and Sn atoms have comparable atomic masses. However, the smaller mass of the Ag atom implies that the backscattering effect starts earlier than for the Sn atom and therefore the position of its main minimum is located at shorter times. For comparison we have also included in Figure 8.4 the VCFs corresponding to both concentration limits, namely pure l-Ag and l-Sn at the same temperature. The, $Z_{Sn}^s(t)$ in the alloy at $x_{Ag} = 0.27$ and 0.50 is similar to the VCF of pure l-Sn; this is so because, besides being at the same temperature, the ionic number densities are very similar in the alloy and in pure l-Sn. On the other hand, the $Z_{Ag}^s(t)$ in the alloy exhibits a mild backscattering effect when compared to the VCF of pure l-Ag, because the ionic number densities in the alloy are distinctly smaller

than that of pure l-Ag. Indeed, it is just at a high Ag concentration, i.e. $x_{Ag} = 0.75$, that the corresponding $Z_{Ag}^s(t)$ show similar qualitative features as those in pure l-Ag.

The $Z_{AgSn}^d(t)$ takes into account the effects of distinct correlations, either with particles of the same or different species. A quantitative measurement of the distinct effects is given by the γ_{AgSn}, defined in equation (53), with positive (negative) values of γ_{AgSn} denoting [34, 35, 290] that particles of the same (different) species have a greater tendency to diffuse together that those of distinct (same) species.

The calculated diffusion coefficients are given in Table 12 where we notice that D_{Ag}^s and D_{Sn}^s take similar values because of their very similar atomic masses. In fact, the ratio D_{Ag}^s/D_{Sn}^s remains practically constant over the whole concentration range. Niwa *et al* [291] measured the diffusivities of Ag in Ag-Sn alloys for $x_{Ag} = 0.2, 0.6$ and 0.8, in general for tempetatures lower than the one considered in the present study. Their measurement for D_{Ag}^s at $x_{Ag} = 0.8$ and $T = 1230$ K is $0.35 \pm 0.05 \times 10^{-4}$ cm^2/s, which follows the composition dependence of our data, taking also into account the temperature difference. For the other concentrations the temperature difference is even larger, but the measured diffusivities at constant temperature increase upon increasing the Sn content, in qualitative agreement with our results. Moreover, the AIMD calculations for pure l-Ag and pure l-Sn [228, 230] at the same temperature (which correspond to both concentration limits) gave for the respective self-diffusion coefficients (in the same units as before) the values $D_{Ag} = 0.26$ and $D_{Sn} = 1.10$ whereas the respective experimental data are $D_{Ag}^{expt} = 0.28 \pm 0.01$ [293] and $D_{Sn}^{expt} = 1.14 \pm 0.05$ [294]; this excellent agreement for the pure cases provides, in our opinion, additional reliability to the results obtained for the alloy. Concerning the interdiffusion coefficient, the only experimental data available [282] correspond to $x_{Ag} \approx 0.4$, but at temperatures sensibly lower than the present one, namely 775, 860 and 944 K, and therefore no reliable comparison can be made with our results.

TABLE 12: Diffusion coefficients (in 10^{-4} cm^2/s) and parameter γ_{AgSn} of the liquid Ag$_x$Sn$_{1-x}$ alloy at the thermodynamic states given in Table 10.

x_{Ag}	0.27	0.50	0.64	0.75
D_{Ag}^s	0.95	0.83	0.66	0.54
D_{Sn}^s	0.87	0.73	0.66	0.52
D_{AgSn}	0.77	0.75	0.66	0.56
D_{AgSn}^0	0.89	0.78	0.66	0.53
D_{AgSn}^d	-0.56	-0.12	0	0.16
γ_{AgSn}	-0.63	-0.15	0	0.06
$S_{CC}(0)D_{int}$	0.15	0.19	0.15	0.11
$S_{CC}(0)D_{int}^{Darken}$	0.18	0.20	0.15	0.10

The calculated values for γ_{AgSn} are negative for $x_{Ag} = 0.27$ and 0.50, which again suggests heterocoordinating tendencies in the alloy. We have also included in Table 12 the results for $S_{CC}(q \to 0) \cdot D_{int}$, which are compared with those predicted by Darken's semiempirical expression [292], i.e. $S_{CC}(q \to 0) \cdot D_{int} = x_1 x_2 D_{12}^0$; which is obtained by neglecting the distinct interparticle velocity correlations. Given the mild heterocoordinating tendencies in the alloy, it is no wonder that Darken's expression provides results similar to the AIMD ones.

Collective dynamics.

The collective dynamics of the density fluctuations in an alloy is usually described through the partial AL intermediate scattering functions (ISF) $F_{ij}(\mathbf{q}, t)$ (see Chapter 2). The time FT of the $F_{ij}(\mathbf{q}, t)$ into the frequency domain gives the partial dynamic structure factors $S_{ij}(\mathbf{q}, \omega)$.

Another interesting dynamical function is the *j*-type component particle current [29], $\mathbf{j}_j(\mathbf{q}, t)$, which is usually split into a longitudinal component $\mathbf{j}_j^L(\mathbf{q}, t)$, parallel to $\mathbf{q}$, and a transverse component $\mathbf{j}_j^T(\mathbf{q}, t)$, perpendicular to $\mathbf{q}$. The partial longitudinal and transverse current correlation functions, $C_{ij}^L(\mathbf{q}, t)$ and $C_{ij}^T(\mathbf{q}, t)$, are defined in terms of these as

$$C_{ij}^L(\mathbf{q}, t) = \langle \mathbf{j}_i^L(\mathbf{q}, t) \cdot \mathbf{j}_j^{L\,*}(\mathbf{q}, 0) \rangle \tag{167}$$

and

$$C_{ij}^T(\mathbf{q}, t) = \frac{1}{2} \langle \mathbf{j}_i^T(\mathbf{q}, t) \cdot \mathbf{j}_j^{T\,*}(\mathbf{q}, 0) \rangle, \tag{168}$$

and their time FT gives the respective spectra, $C_{ij}^L(\mathbf{q}, \omega)$ and $C_{ij}^T(\mathbf{q}, \omega)$. For isotropic systems, all the previous correlation functions depend only on $q = |\mathbf{q}|$.

Figure 8.5 shows, for three q-values, the calculated partial AL intermediate scattering functions, $F_{ij}(q, t)$, as well as the BT $F_{NN}(q, t)$. The time (or frequency) dependent BT partials are defined as a straightforward extension of the static counterparts (see appendix). Note in particular that separating the correlations that appear in $F_{CC}(q, t)$ into self and distinct terms (see Appendix F), we can write

$$\frac{F_{CC}(q, t)}{x_1 x_2} = x_2 F_1^s(q, t) + x_1 F_2^s(q, t) +$$
$$x_1 x_2 \left(F_{11}^d(q, t) - 2F_{12}^d(q, t) + F_{22}^d(q, t) \right), \tag{169}$$

which bears an interesting similarity with the definition of $Z_{12}(t)$ in equation (52). Noting that $Z_i^s(t)$ is directly related to the memory function of $F_i^s(q, t)$ for small q [23], we consider quite plausible that a similar relation exists between $Z_{12}(t)$ and $F_{CC}(t)$.

One of the q-values shown in figure 8.5 corresponds to the smallest value attainable in the present AIMD simulations (q_{min} = 0.42, 0.43 and 0.45 Å^{-1} for x_{Ag}= 0.27, 0.50 and 0.75 respectively). Notice that for these small q's, the partials $F_{AgAg}(q, t)$, $F_{SnSn}(q, t)$ and $F_{AgSn}(q, t)$ have a very slow decay as they are dominated by diffusive contributions, which have the effect of screening the oscillations associated with the propagating density fluctuations; moreover, the $F_{AgSn}(q, t)$ takes negative values. However, for increasing q-values the rate of decay becomes faster and for q's greater than ≈ 2.1 Å^{-1} the $F_{AgSn}(q, t)$ take positive values. On the other hand, within the range $q \leqslant 2.1$ Å^{-1}, the $F_{NN}(q, t)$ partials are one order of magnitude smaller than the previous ones because of the large cancellations among the other partials, as $F_{AgSn}(q, t)$ is of similar magnitude but opposite sign than $F_{AgAg}(q, t)$ and $F_{SnSn}(q, t)$.

The time FT of the $F_{ij}(q, t)$ gives the associated partial dynamic structure factors, $S_{ij}(q, \omega)$. We first notice that the $S_{NN}(q, \omega)$'s show, for the smallest q's, a kind of Rayleigh-Brillouin structure similar to that of the one-component systems close to the hydrodynamic regime, but with an enhanced central line due to interdiffusion processes. This is shown in figure 8.6 where the Brillouin peak is visible at the q_{min}. The three AL partials also show either a peak or a shoulder at the same position for $q = q_{min}$, indicating that all the particles oscillate in phase with the same frequency, which is characteristic of hydrodynamic sound propagation. With increasing q-values, the NN peak fades away and only remnant shoulders are visible; indeed, we found that for all concentrations, a peak can be discerned up to $q \approx 0.95$ Å^{-1}.

From the position of the Brillouin peak at q_{min}, $\omega_B(q_{min})$, we have used the relation $c_s = \omega_B(q_{min})/q_{min}$ to obtain an estimate for the adiabatic velocity of propagation of these modes. We have obtained the values $c_s \approx 1950 \pm 100$ m/s, 1850 ± 100 m/s, 2200 ± 100 m/s and 2350 ± 100 m/s for $x_{Ag} = 0.27, 0.50, 0.64$ and 0.75, respectively. We are not aware of any experimental measurement of the adiabatic sound velocity in this alloy; however, an indirect check on the reliability of these estimates is provided by the same AIMD calculations performed at the same temperature (T = 1273 K) for the limits of pure liquid Ag and Sn, where the AIMD calculations predict [228, 230] $c_s = 2800 \pm 100$ m/s and $c_s = 2330 \pm 100$ m/s respectively, which are close to the corresponding experimental values [253] of ≈ 2810 and 2284 m/s.
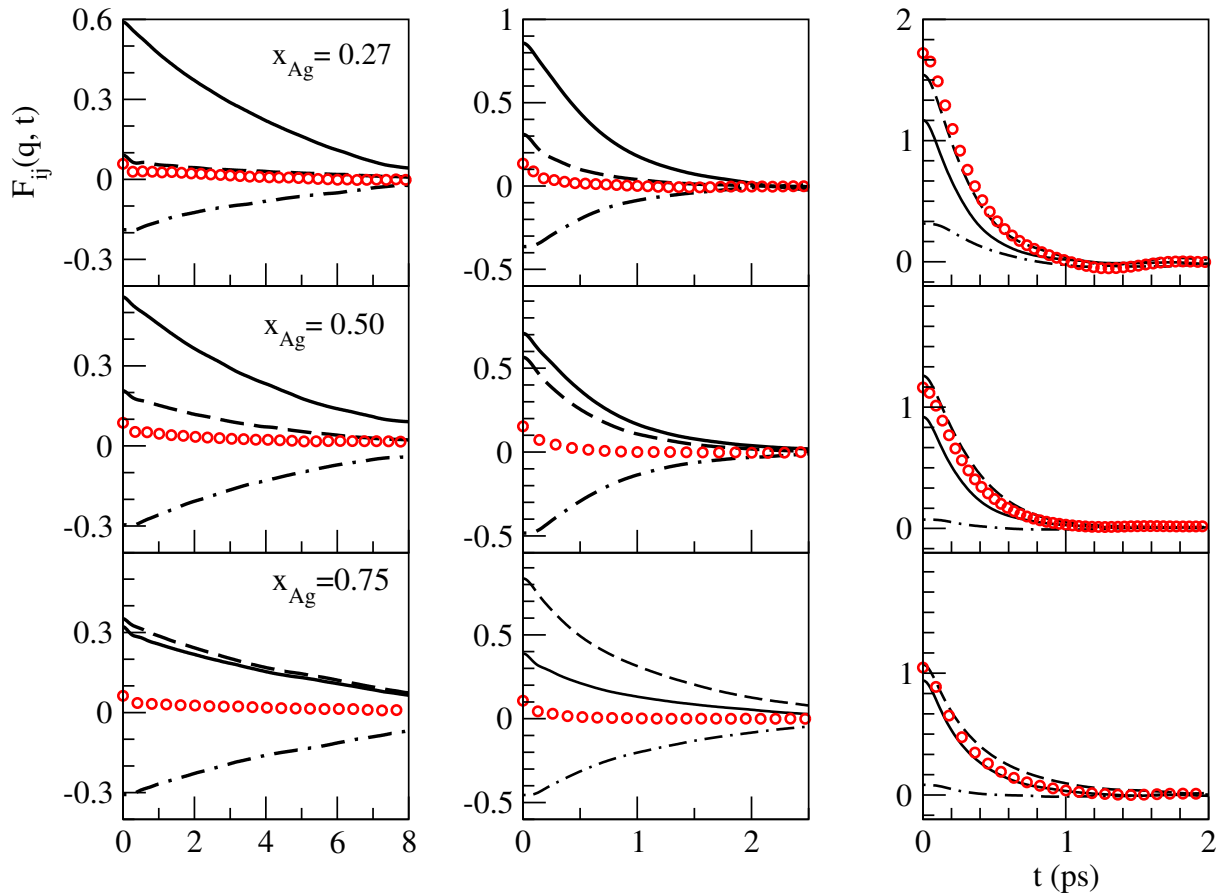
FIGURE 8.5: Partial intermediate scattering functions $F_{ij}(q, t)$ of the liquid Ag_xSn_{1-x} alloy at three concentrations. The left column depicts the $F_{ij}(q, t)$ at the corresponding q_{min}, i.e. $q = 0.42$ Å^{-1} ($x_{Ag} = 0.27$), $q = 0.43$ Å^{-1} ($x_{Ag} = 0.50$) and $q = 0.45$ Å^{-1} ($x_{Ag} = 0.75$). The center column is for $q = 1.34$ Å^{-1} ($x_{Ag} = 0.27$), $q = 1.35$ Å^{-1} ($x_{Ag} = 0.50$) and $q = 1.36$ Å^{-1} ($x_{Ag} = 0.75$). The right column is for $q = 2.20$ Å^{-1} ($x_{Ag} = 0.27$), $q = 2.20$ Å^{-1} ($x_{Ag} = 0.50$) and $q = 2.27$ Å^{-1} ($x_{Ag} = 0.75$). Full line, dashed line, dash-dotted line and circles correspond to $F_{AgAg}(q, t)$, $F_{SnSn}(q, t)$, $F_{AgSn}(q, t)$ and $F_{NN}(q, t)$ respectively.
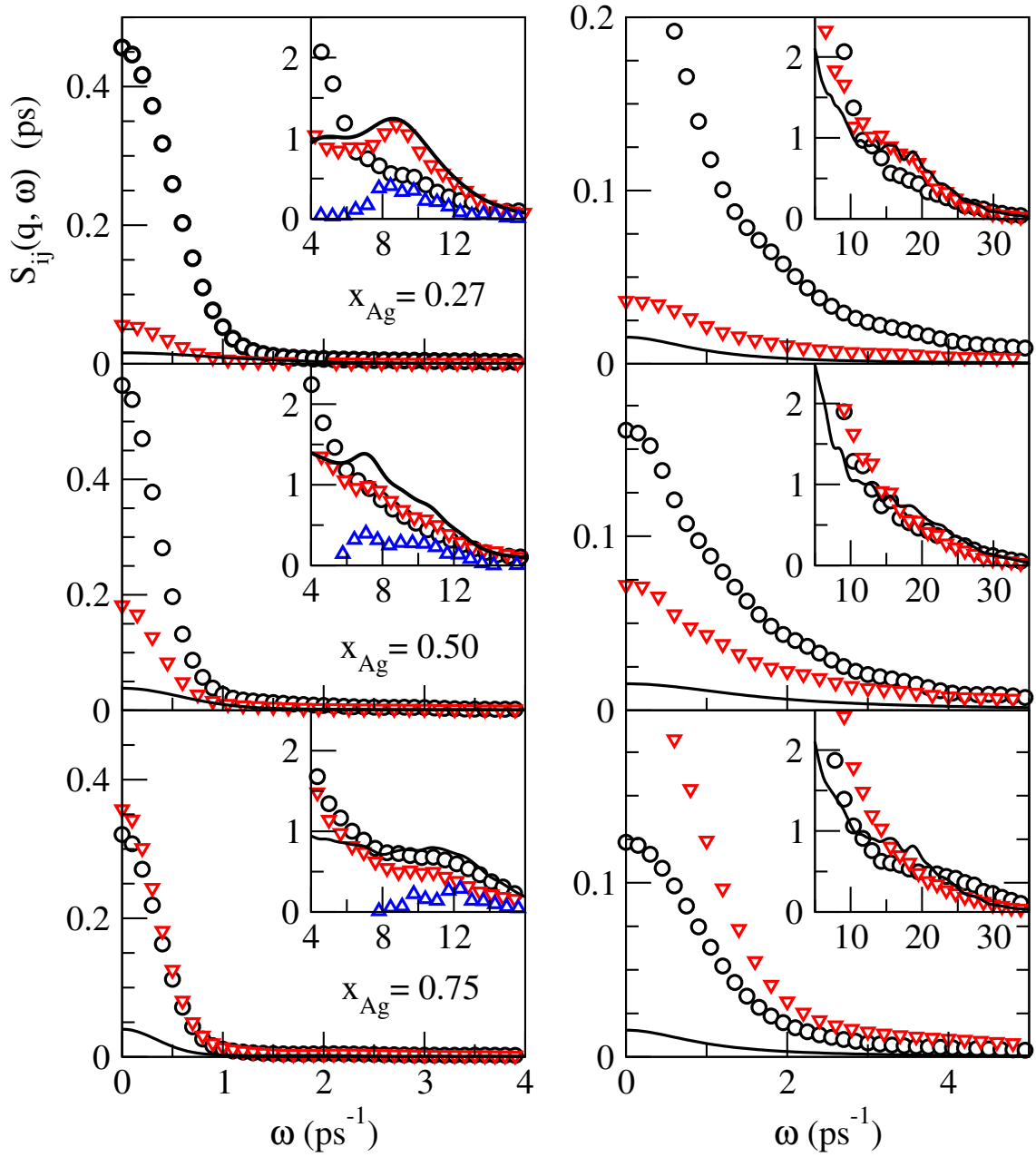
FIGURE 8.6: Partial dynamic structure factors $S_{ij}(q,\omega)$ of the liquid Ag_xSn_{1-x} alloy for $x_{Ag} = 0.27, 0.50$ and 0.75. Left panel: corresponding q_{min}, namely, $0.42 \text{ Å}^{-1}, 0.43 \text{ Å}^{-1}, 0.45 \text{ Å}^{-1}$ for $x_{Ag} = 0.27, 0.50$ and 0.75 respectively. Right pannel: $q = 1.03 \text{ Å}^{-1}$ ($x_{Ag} = 0.27$), $q = 1.06 \text{ Å}^{-1}$ ($x_{Ag} = 0.50$) and $q = 1.11 \text{ Å}^{-1}$ ($x_{Ag} = 0.75$). Circles, red down triangles, blue up triangles and lines correspond to $S_{AgAg}(q,\omega)$, $S_{SnSn}(q,\omega)$ $S_{AgSn}(q,\omega)$ and $S_{NN}(q,\omega)$, respectively. The insets show $10^3 S_{ij}(q,\omega)$. The $S_{AgSn}(q,\omega)$ for the q-values shown in the right pannel are not displayed because they are negative for all ω.

The appearance of clear side peaks, similar to those of $S_{NN}(q, \omega)$ in the AL partials, $S_{AgAg}(q, \omega)$ and $S_{SnSn}(q, \omega)$, is quite more retricted in q, as is observed in figure 8.6. In this way, whereas for $x_{Ag} = 0.75$ the $S_{AgAg}(q, \omega)$ shows side peaks up to $q \approx 0.91$ Å^{-1}, however when x_{Ag} decreases, the side peaks appear over a smaller q range and for $x_{Ag} = 0.27$ no side peaks are visible, even at q_{min}. As for the $S_{SnSn}(q, \omega)$, we observe that, for all concentrations, the side peaks show up to $q \approx 0.85$ Å^{-1}.

Additional information about the longitudinal collective modes in the alloy can be extracted from the partial longitudinal current correlation functions, $C_{ij}^L(q, t)$, whose spectra is related to the partial dynamic structure factors by $C_{ij}^L(q, \omega) = \omega^2 S_{ij}(q, \omega)/q^2$. Moreover, these functions often allow to uncover propagating longitudinal modes that are not visible in the $S_{ij}(q, \omega)$ either because of its small amplitude or because of they are shielded by the diffusive modes. Therefore, we have calculated the partial longitudinal current correlation functions according to equation (167) and using the configurations obtained in the AIMD simulations.

Nevertheless, some caution is necessary before assigning a peak in the longitudinal current spectra to a collective propagating mode, since any decreasing function of ω, when multiplied by ω^2 leads to a maximum at some frequency. This is well known to occur in any system in the large-q region, where single-particle like behaviour sets in and no collective motion exists, but a peak in the longitudinal current spectrum is indeed present. In the case of the Ag-Sn alloy we will observe a similar characteristic, but now in the opposite region, namely, low-q.

Figure 8.7 shows the calculated $C_{ij}^L(q, \omega)$ for several concentrations and q-values. We have found that, for any q-value, $C_{AgAg}^L(q, \omega)$, $C_{SnSn}^L(q, \omega)$ and $C_{NN}^L(q, \omega)$ exhibit at least one peak, although at some concentrations and q-ranges, two peaks may be observed. In the specific case of $C_{NN}^L(q, \omega)$, we obtain that for all concentrations there is only a peak.

A striking feature observed in figure 8.7 is the existence of a peak or a shoulder in $C_{AgAg}^L(q, \omega)$ and a minimum in $C_{AgSn}^L(q, \omega)$ at a very small frequency, lower than 5 ps^{-1}, in the low-q region, a feature that is still present at intermediate values of q. Looking at the BT longitudinal currents it is observed that these extrema in the AL partials correspond to the peak of $C_{CC}^L(q, \omega)$. Taking into account that the $S_{ij}(q, \omega)$ at low frequencies are overwhelmingly dominated by the central, diffusive, peaks, and that the concentration-concentration functions are expected to be especially sensitive to interdiffusion modes, as discussed previously, we deduce that these peaks do not, in fact, correspond to a propagating mode but to the relaxations associated to interdiffusion processes.

Other maxima in the longitudinal currents, common to all the AL partials and the NN one, appear at larger frequencies and clearly correspond to propagating acoustic modes where all the particles oscillate in phase. They define the dispersion relations, which are shown in figure 8.8. Finally, for small q-values, another special frequency seems to be present, around $\omega = 25$ ps^{-1}, for which $C_{AgSn}^L(q, \omega)$ has a minimum and some other partials may show a shoulder, but not a clear maximum. These may be related to an optic-like propagating mode where the different kinds of particles oscillate in opposite phase, but since no clearcut value can be assigned to the frequency we have refrained from plotting them in figure 8.8.

Note that for Sn-rich alloys the AgAg, SnSn and NN dispersion relations are basically determined by that of pure Sn, which shows that the average number density, similar in the alloys and in pure Sn, plays a very important role in the characteristics of acoustic propagation modes. Only when x_{Ag} increases, along with the density, the SnSn and AgAg dispersion relations start to deviate from each other, with the former remaining close to that of pure Sn, and the latter moving towards that of pure Ag.

Shear viscosity.

The shear viscosity, η, of the alloy can be evaluated by using the total transverse current correlation function $C_{tt}^T(q, t) = \langle j_t^T(q, t) j_t^{T*}(q, 0) \rangle$, where

$$j_t^T(q, t) = x_1^{1/2} m_1 j_1^T(q, t) + x_2^{1/2} m_2 j_2^T(q, t) \tag{170}$$
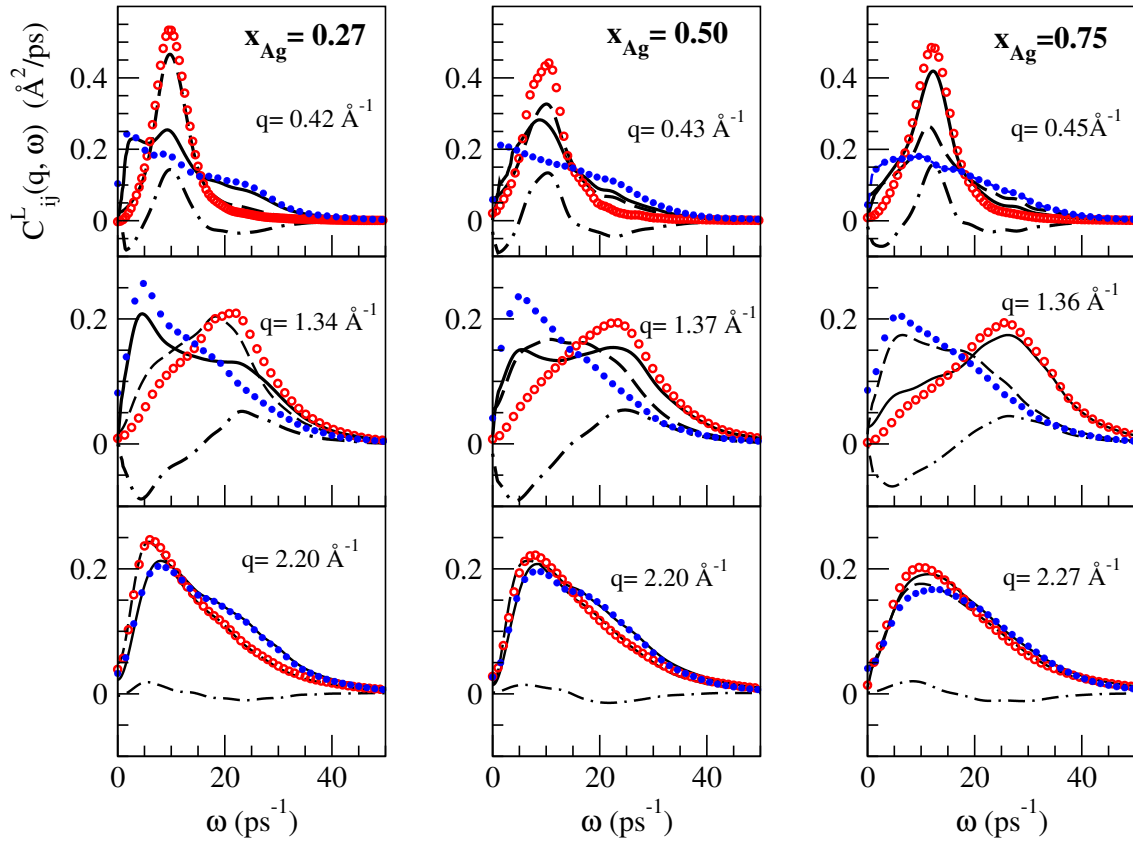
FIGURE 8.7: Partial longitudinal current correlation functions, $C_{ij}^L(q, \omega)$, for the liquid Ag–Sn alloy at $T = 1273$ K and three concentrations. The full, dashed and dot-dashed lines, and the red open circles and blue stars represent $C_{AgAg}^L(q, \omega)$, $C_{SnSn}^L(q, \omega)$, $C_{AgSn}^L(q, \omega)$, $C_{NN}^L(q, \omega)$, and $C_{cc}^L(q, \omega)/(x_{Ag}x_{Sn})$ respectively.
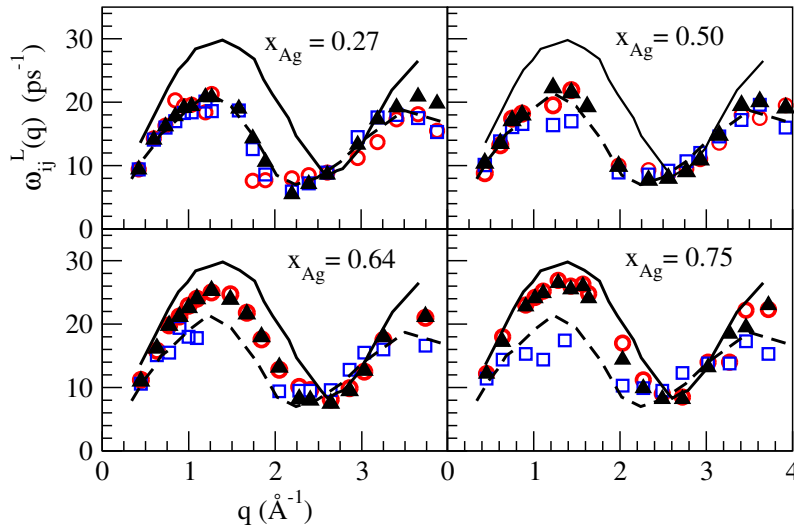
FIGURE 8.8: Longitudinal dispersion relations $\omega_{AgAg}^L(q)$ (red circles), $\omega_{SnSn}^L(q)$ (blue squares), and $\omega_{NN}^L(q)$ (black triangles), for the Ag_xSn_{1-x} liquid alloy at several concentrations. The continuous and broken lines show the longitudinal dispersion relations of pure liquid Ag and Sn at $T = 1273$ K, respectively.

is the total transverse current. For more details, we refer the reader to Refs. [295, 296]. For simple liquid alloys, η shows either a linear variation with concentration or a small negative deviation from linearity whereas positive deviations are usually found in those alloys with marked heterocoordination tendencies.

From the AIMD results for the $C_{tt}^T(q, t)$, we have evaluated the alloy shear viscosity and the results are reported in Table 13, along with the respective experimental data [297]. First, we notice that the AIMD results show the same qualitative behaviour as the experimental data, with both sets exhibiting negative deviation from linearity; indeed similar negative deviations appear in the experimental data for other Au- and Ag-based binary alloys [289]. We have also reported in Table 13 the AIMD results (and experimental data) for both pure Ag and Sn [228, 230] at the same temperature. The agreement is really good which can be considered as a benchmark for the reliability of the AIMD results for the alloy.

TABLE 13: Calculated values of the adiabatic sound velocity c_s (in m/s) and the shear viscosity η (in GPa ps) for the liquid Ag_xSn_{1-x} alloy at the thermodynamic states given in Table 10. For comparison, we also include the AIMD values obtained for pure liquid Ag and Sn.[228, 230] The experimental data were taken from Ref.[297].

x_{Ag}	T (K)	c_s	η	η_{exp}
0.0	1273	2300 ± 150	0.90 ± 0.10	0.80, 0.90
0.27	1273	1960 ± 150	0.92 ± 0.10	1.06 ± 0.10
0.35	1273	1980 ± 150	0.99 ± 0.10	1.12 ± 0.10
0.50	1273	2030 ± 150	1.05 ± 0.15	1.25 ± 0.10
0.64	1273	2250 ± 150	1.45 ± 0.15	1.69 ± 0.10
0.75	1273	2400 ± 150	1.90 ± 0.15	2.12 ± 0.10
1.0	1273	2800 ± 150	3.30 ± 0.15	3.65 ± 0.10

Electronic Density of States

Figure 8.9 shows the calculated electronic density of states (EDOS) of the liquid Ag_xSn_{1-x} alloy at three concentrations; for comparison we have also included the EDOS obtained for pure l-Ag and l-Sn by using the same AIMD method [228, 230]. Notice that the EDOS in the alloy smoothly recovers the pure l-Ag and l-Sn limits. Interestingly, the d states in pure Ag and in the alloys are located around the energy where pure Sn shows a pseudogap that separates mainly s from p states. According to these calculated EDOS, we observe that the liquid Ag_xSn_{1-x} alloy is a good metal, with a large EDOS at the Fermi level which has a predominant p-character. The experimental resistivity data for this alloy [298] show that, starting from pure l-Ag, the resistivity increases with the addition of Sn, up to a maximum at around a concentration $x_{Ag} \approx 0.75$; therefrom the resistivity continuously decreases up to the value of pure l-Sn. This behaviour qualitatively agrees with the present AIMD results for the EDOS at the Fermi energy.

8.1.4 Conclusions

In this study, we have reported an AIMD simulation study of several static, dynamic and electronic properties of the liquid Ag_xSn_{1-x} alloy at five concentrations.

The calculated total static structure factor $S_T(q)$ at x_{Ag}=0.27, 0.50 and 0.64 stands in a very good accordance with the experimental data. An analysis of the local arrangement of the atoms in the alloy shows the existence of some heterocoordinating tendencies for the whole concentration range which appear more marked for the smaller Ag concentrations. For some compositions, the partials $S_{ij}(q)$ show weak prepeaks which have been
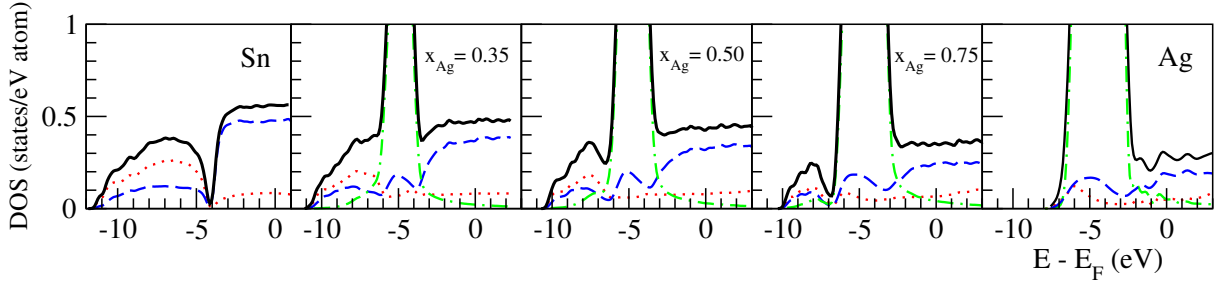
FIGURE 8.9: AIMD results for the total DOS (full line) of the liquid $Ag_x Sn_{1-x}$ alloy at three concentrations. The dotted, dashed and dash-dot lines refer to s, p, and d channels. For comparison we have also plotted the DOS for pure l-Sn and l-Ag at the same temperature as obtained by the same AIMD method.

correlated with the existence of some substructures such as clusters of a definite composition in the alloy. However, the present AIMD results do not provide any support for the asumptions behind the microheterogeneous structure model.

We have studied the single particle dynamics of the liquid alloy by evaluating the velocity correlation functions and computing several diffusion coefficients. Although there are no experimental data available for direct comparison, there are common trends in theory and in experiment, which support the reliablity of the data.

The calculated partial dynamic structure factors $S_{AgAg}(q, \omega)$, $S_{SnSn}(q, \omega)$ and $S_{NN}(q, \omega)$ exhibit clear side peaks which are indicative of the existence, for some q-range, of collective density fluctuations. The longitudinal current correlation functions have also been computed, and from their respective spectra we have obtained the longitudinal dispersion relations, which have been discussed in detail by analyzing the different origins of the peaks in the corresponding spectra.

The predicted values for the alloy shear viscosity show a negative deviation from linearity, which is a common feature in alloys with heterocoordination tendencies.

The EDOS curves obtained for the liquid $Ag_x Sn_{1-x}$ alloy suggest a good metallic behavior and qualitatively agree with the available resistivity data.

The results reported in this work provide a comprehensive information on the static, dynamic and electronic properties of the liquid $Ag_x Sn_{1-x}$ alloy at $T = 1273$ K. We expect that this information will contribute towards a better understanding of this alloy of particular technological interest. Moreover, based on the good description provided by the present theoretical approach, we expect that a similar study at concentrations and temperatures closer to the eutetic point will be able to provide accurate information about a range of properties of interest for lead-free soldering.

9
LIQUID SLABS.

In this chapter we consider the free liquid surface of several liquid metals: Ag, Hg, Pb, Bi, Sn and In. Due to computational convenience the simulated systems are in fact in a slab geometry, thus showing two equivalent free liquid surfaces. We describe the structure of the liquid in such geometry by two quantities: the density profile, $\rho(z)$, which describes how the liquid is distributed in the direction perpendicular to the interface, and the transverse pair distribution function, $g_T(r)$, that indicates the ionic distribution in planes parallel to the interface, which in principle can vary from the deep, bulk-like, regions of the slab to the outermost interfacial plane, due to the different environment that can lead to structural reorganizations.

The density profile in liquid metal surfaces has been found to exhibit layering, with $\rho(z)$ displaying large oscillations which decrease towards the bulk. The signature of such structure is a surface reflectivity that displays a peak at a wavevector related to the interlayer spacing. Experimental studies have however revealed a richer structure in the reflectivities of several liquid metals for intermediate wavevectors. In the first parts of this chapter we consider the calculation of these reflectivities from computer simulations, and report about the feasilibity and importance of a microscopic calculation of the so-called intrinsic density profile (where the influence of capillary waves is removed). This is exemplified in the first section of this chapter for the case of liquid Ag, where additionally bulk properties were calculated. The relevance of the extraction of the intrinsic profile is highlighted in the second section (Hg, Pb and Bi) where we show that the method is a must for small simulation samples, as required by standard KS AIMD calculations, that are also affected by high temperature and low surface tension, such as Pb and Bi. Finally, in the third section we consider the case of liquid Sn, where the sample is much larger (2000 atoms) because of the use of orbital-free methods.

The last two sections (on liquid Sn and In) deal with a study of the collective dynamic properties of the liquid metal in the presence of the surface. In the same way as the lateral structure can vary with the depth below the surface due to the different environment, the same can happen with the dynamic properties. The experimental extraction of this z-dependence of the dynamic and transport properties is extremely difficult, and has been pursued to our knowledge just for the case of liquid In, with which we compare our calculations. In spite of the great advance in the field achieved in this experimental investigation, we show that the measured properties still include large contributions from the bulk liquid, so that the surface dynamic properties are still too difficult to separate out, and in this respect simulations are much better suited.

9.1 AN *AB INITIO* STUDY OF BULK LIQUID AG AND ITS LIQUID-VAPOR INTERFACE

In the present study we evaluate some structural and dynamic properties of liquid Ag near melting in two different configurations: bulk liquid and free liquid surface. Silver is an important component in several liquid alloys of technological importance, especially in lead-free solders, such as liquid Ag-Sn, Chapter 8, and multicomponent alloys based on it, for instance Cu-Ag-Sn [299], or Cu-Ag-Sn-Bi [300].

On the other hand, some properties of pure l-Ag are of fundamental, rather than applied, scientific interest. The high melting temperature of Ag (and other related metals, such as Au, Pd or Pt) poses difficulties in their experimental study. Therefore, the feasibility of accurate simulation studies is important for the understanding of the properties of these liquids.

The second part of this work reports a study of the free liquid surface (FLS) of l-Ag. This is a topic which, in the last two decades, has attracted a considerable amount of both theoretical and experimental work. The principal experimental techniques used to extract information about the FLS are grazing incidence X-ray diffraction and

X-ray reflectivity. In these works the shape of the oscillatory density profiles (DPs) typical of liquid metal surfaces (Chapter 2) perpendicular to the interface were deduced by fitting the measured reflectivities to those predicted within a specific profile model, namely, the distorted crystal model, or variations thereof [302]. Although it would be desirable to obtain the DP in a model-independent way, the lack of phase information in the measurements renders this impossible. The use of MD simulations aids in this particular goal because the DP can be obtained directly from the simulation, without the need of models.

9.1.1   *Computational details*

AIMD simulations based on DFT have been performed for both the bulk and FLS case. We have used the local density approximation, as parametrized by Perdew and Zunger [89, 91], including non-linear core corrections [325]. We consider in the calculations 11 valence electrons per atom, i.e., the atomic d-electrons, as well as the s ones, are considered explicitly in the computation of the ground state density. The rather localized character of these orbitals would require large energy cutoffs in their Fourier representation, and this would make the calculations even more costly in computer time and memory. We used an ultrasoft pseudopotential generated from a scalar-relativistic calculation of the atomic electron configuration $[Kr]4d^9 5s^2$, following the procedure established by Kresse and Hafner [301].

The planewave cutoff has been set to 25 Ryd for the wavefunctions and 150 Ryd for the electron density. The Verlet's leapfrog algorithm was used to solve Newton equations with a timestep of 7.5 fs. For the bulk liquid a total of 19000 configurations were generated using 150 atoms in a cubic box side of 14.26 Å, corresponding to a number density of $\rho = 0.0517$ Å^{-1}. The temperature was set to 1273 K. In the FLS case a total of 15000 configurations were generated using 120 atoms in a tetragonal simulation box with $L_x = L_y = 11.465$ Åand $L_z = 32.676$ Å. The atoms form a slab of initial width corresponding to the experimental number density. The temperature was set to 1400 K

9.1.2   *Results and discussion*

For the bulk l-Ag case, different static and dynamic properties were evaluated and compared with the available experimental results with good agreement. The good representation of the bulk liquid prompted us to study the FLS of Ag, for which no experimental results are yet available. We evaluated the DPs and reflectivities using both the macroscopic and the microscopic method, highlighting their differences. The following paper reports on this part of our work.

An *ab initio* study of the structure and atomic transport in bulk liquid Ag and its liquid-vapor interface

Beatriz G. del Rio, David J. González, and Luis E. González
Departamento de Fisica Teorica, Facultad de Ciencias, Universidad de Valladolid,
47011 Valladolid, Spain

Several static and dynamic properties of bulk liquid Ag at a thermodynamic state near its triple point have been calculated by means of *ab initio* molecular dynamics simulations. The calculated static structure shows a very good agreement with the available experimental data. The dynamical structure reveals propagating excitations whose dispersion at long wavelengths is compatible with the experimental sound velocity. Results are also reported for other transport coefficients. Additional simulations have also been performed so as to study the structure of the free liquid surface. The calculated longitudinal ionic density profile shows an oscillatory behaviour, whose properties are analyzed through macroscopic and microscopic methods. The intrinsic X-ray reflectivity of the surface is predicted to show a layering peak associated to the interlayer distance. *Published by AIP Publishing.*
[http://dx.doi.org/10.1063/1.4966656]

I. INTRODUCTION

Ab initio molecular dynamics (AIMD) methods based on density functional theory[1] (DFT) are techniques commonly used for the study of a wide range of condensed matter systems. Starting with a collection of atoms at given nuclear positions, DFT enables to compute the ground state electronic energy and, via the Hellmann-Feynman theorem, it also yields the forces on the nuclei. It allows to perform molecular dynamics (MD) simulations whereby the nuclear positions evolve according to classical mechanics, whereas the electronic subsystem follows adiabatically. Most AIMD methods are based on the Kohn-Sham (KS) orbital representation of DFT, whose application demands considerable computational resources and consequently poses some significant constrains concerning the size of the systems under study as well as the extent of the simulation times. Nevertheless, the accuracy achieved for the energies and forces, and consequently, in the dynamics of the system, is very high. This paper reports an AIMD simulation study on several static and dynamic properties of liquid silver (l-Ag) at a thermodynamic state near its triple point and on its free liquid surface at a slightly higher temperature.

Silver is an important component in several liquid alloys of technological importance, especially in lead-free solders, such as liquid Ag-Sn,[2] and multicomponent alloys based on it, for instance, Cu-Ag-Sn[3] or Cu-Ag-Sn-Bi.[4] The theoretical study of this type of systems requires, as a prerequisite, the availability of suitable tools to describe the properties of the pure components, and the present study of l-Ag goes along this line.

On the other hand, some properties of pure l-Ag are of fundamental, rather than applied, scientific interest. The high melting temperature of Ag (and other related metals, such as Au, Pd, or Pt) poses difficulties in their experimental study. For instance, only very recently it has been possible to study the dynamic properties of liquid Au using neutron Brillouin scattering.[5] Therefore, the feasibility of accurate simulation studies is important for the understanding of the properties of these liquids.

The static structure of l-Ag has been experimentally studied by X-ray diffraction (XD)[6–9] and neutron diffraction (ND)[10] measurements. The static structure factors, $S(q)$, obtained by the different workers generally agree with each other, although some discrepancies may be observed in the height of the main peak as well as in the region near the first minimum (see Figure 1). Indeed, some discrepancies between ND and XD data should be expected because neutrons are scattered by the nuclei

---

28, 107105-1
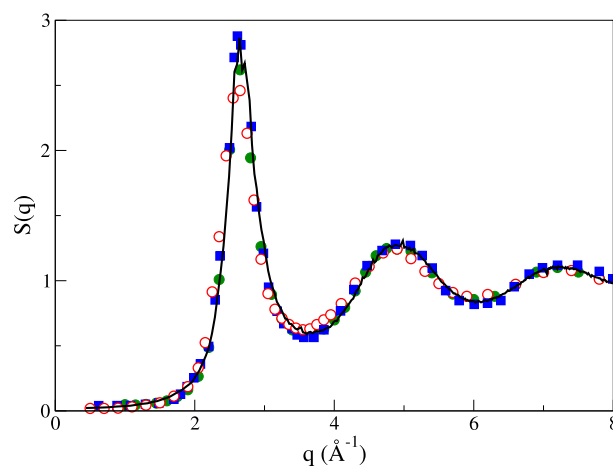
FIG. 1. Static structure factor, $S(q)$, of l-Ag at 1273 K. Continuous line: present calculations. Open circles: experimental XD data at 1273 K from Waseda.[8] Closed squares: experimental ND data[10] at 1323 K. Closed circles: experimental XD data at 1273 K from Kaban and Hoyer.[9]

and X-rays are scattered by all the electrons surrounding the nuclei. However, the more recent XD results of Kaban and Hoyer[9] show better agreement with the ND results of Bellissent *et al.*[10] than those of Waseda and Ohtani,[8] probably due to the availability of better X-ray sources and instrumentation. In some of these studies, the measured $S(q)$ was Fourier transformed into real space, so as to obtain the pair correlation function, $g(r)$. This "experimentally" determined $g(r)$ is subject to a greater uncertainty due to the limited q-range covered by the experiments, and therefore somewhat larger differences are observed between the XD data[8] and the ND results[10] (see Figure 2). The discrepancies appear both in the main peak's height and in the phase of the subsequent oscillations. In any case, it is possible to calculate the number of neighbors in the first coordination shell from the knowledge of $g(r)$ and the atomic number density. The coordination number so computed varies from 11.3 according to the XD data[8] to 11.9 as obtained from ND,[10] which corresponds to a quite compact structure.

Several thermophysical properties of l-Ag have also been measured experimentally, including the diffusion coefficient,[11] the shear viscosity,[11-14] and the adiabatic and isothermal sound velocities.[12,13]

Most theoretical studies on l-Ag have focused on its thermodynamics and its static structural properties. The usual approach has been to characterize the liquid system by effective interatomic potentials[15-17] that were constructed either empirically by fitting to some experimental data, or
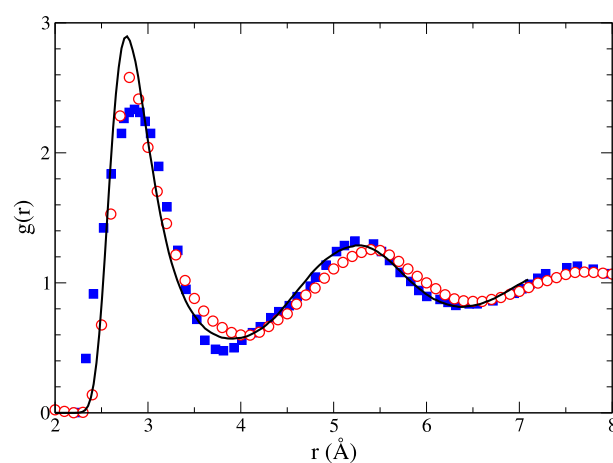
FIG. 2. Pair distribution function $g(r)$ of l-Ag at 1273 K. The full lines are the present AIMD results. Open circles correspond to experimental XD data[8] at 1273 K (non-zero values for small r are artifacts due to the limited extent of the experimental $S(q)$). Closed squares correspond to experimental ND data[10] at 1323 K.

derived from some approximate theoretical model. Therefrom, the liquid structure has been determined by resorting to either liquid state theories[18] or classical MD simulations.

Alemany *et al.*[15] have used the embedded atom model (EAM) in order to derive many-body potentials which were used in classical MD simulations so as to obtain information about various static and dynamic properties of the liquid noble metals, including l-Ag. Their calculated $S(q)$ for l-Ag showed an overall good agreement with experiment except for the position of the main and subsequent peaks which were somewhat displaced towards greater q-values.

More recently, Bhuiyan *et al.*[19] resorted to the orbital-free *ab initio* MD (OF-AIMD) method in order to calculate a range of static and dynamic properties of l-Ag at several thermodynamic conditions. The OF-AIMD method is based on the Hohenberg and Kohn version of the DFT, where the electronic orbitals are replaced by the total valence electronic density. This substantially reduces the number of variables describing the electronic states. However, it also includes some approximations which render it less accurate than the KS orbital representation of DFT. For l-Ag near its triple point, their calculated $S(q)$ showed a good agreement with experiment except for the main peak's height, which was $\approx 15\%$ higher. They also evaluated several dynamic properties and transport coefficients which showed a qualitative agreement with experiment.

However, the full orbital representation of the DFT has not yet been used to perform a molecular dynamics study of the static and dynamic properties of l-Ag.

The second part of this paper reports a study of the free liquid surface (FLS) of l-Ag. This is a topic which, in the last two decades, has attracted a considerable amount of both theoretical and experimental work.[20] Grazing incidence X-ray diffraction and X-ray reflectivity have been the principal experimental techniques used to extract information about the FLS. The data obtained for several liquid metals and binary alloys[21] have shown that the FLS exhibits an oscillatory surface-normal (longitudinal) density profile (DP) which extends several atomic diameters into the bulk liquid. In these works the shape of the DPs perpendicular to the interface was deduced by fitting the measured reflectivities to those predicted within a specific profile model, namely, the distorted crystal model, or variations thereof.[22] Although it would be desirable to obtain the DP in a model-independent way, the lack of phase information in the measurements renders this impossible.

Another route to calculate an ionic (or electronic) DP is by resorting to computer simulations which provide a detailed description of the ionic positions and therefore allow the direct evaluation of the ionic DP. This method has been used by several authors, and their calculated ionic DPs show features similar to those predicted by experiment.[23–30] Now, from the electronic DP the reflectivity can be directly computed and compared with experiments. A proper comparison must take into account the thermally induced capillary waves (CW) present in the samples. The amount of CW depends strongly on the surface area, and this is utterly different in experiments than in simulations, where the area is much smaller. The comparison is therefore conveniently performed in terms of the so-called intrinsic reflectivity, which is the one that would correspond to the absence of CWs. Such intrinsic reflectivity is obtained from the experimental measurements by correcting the raw reflectivity through the application of the macroscopic capillary wave theory, which boils down to the division by a Gaussian factor that involves the temperature, the surface tension of the system, and the atomic and sample sizes.[22] This same approach has also been customarily used to evaluate the intrinsic reflectivity from simulation results, although now the sample is not really macroscopic. A different type of approach was proposed some years ago by Chacón and Tarazona,[31] who extracted an intrinsic DP from the atomic positions in the simulation through a microscopic procedure, in which it was possible to define a rigged surface that represents the liquid-vapor separation surface, and use this surface as a reference for the calculation of the intrinsic profile. So far this type of analysis has been applied to simulations of metallic FLS only for the case of K, where it provided a very good agreement with the experimental intrinsic reflectivity.[32]

Here, we report the results of an AIMD simulation of the FLS of l-Ag at a temperature slightly higher than melting, and derive the DPs and reflectivities comparing both the macroscopic and the microscopic method, highlighting their differences. We notice that because of the high computational demands posed by this method, just a few AIMD studies on the FLS of liquid metals have been performed to date, namely for Si,[24] Na,[25] Sn,[27] Hg,[29] and Cd.[30]

The layout of the paper is as follows: In Section II we succinctly review the method applied in the present AIMD simulations, by describing some technical details and the ionic pseudopotential used to account for the electron-ion interaction. In Section III we report and discuss the obtained structural and dynamical results for bulk l-Ag, which are compared with other previous studies and the available experimental data. The structure of the FLS is calculated in Section IV, where several structural properties are evaluated and discussed. Finally some conclusions are drawn.

II. COMPUTATIONAL METHOD

The total potential energy of N ions with valence Z, enclosed in a volume Ω, located at positions $(\{\vec{R}_l\})$, and interacting with $N_e = NZ$ valence electrons is written, within the Born-Oppenheimer (BO) approximation, as the sum of the direct ion-ion Coulombic interaction energy, $E_{i-i}[\{\vec{R}_l\}]$, plus the ground state energy of the electronic system subjected to the external potential created by the ions, $V_{ext}(\{\vec{R}_l\})$,

$$E(\{\vec{R}_l\}) = E_{i-i}[\{\vec{R}_l\}] + E_g[n_g(\vec{r}), V_{ext}(\{\vec{R}_l\})], \tag{1}$$

where $n_g(r)$ is the ground state electronic density. According to DFT, the ground state electronic density minimizes the energy functional

$$E[n(\vec{r})] = T_s[n] + E_{ext}[n] + E_H[n] + E_{xc}[n], \tag{2}$$

where the terms represent the electronic kinetic energy, $T_s[n]$, of a non-interacting system with density $n(\vec{r})$, the electron-ion interaction energy, $E_{ext}[n]$, the classical electrostatic Hartree energy, $E_H[n]$, and the exchange-correlation energy, $E_{xc}[n]$, for which we have used the local density approximation, as parametrized by Perdew and Zunger,[33] including non-linear core corrections.[34] We consider in the calculations 11 valence electrons per atom, i.e., the atomic d-electrons, as well as the s ones, are considered explicitly in the computation of the ground state density. The rather localized character of these orbitals would require large energy cutoffs in their Fourier representation, and this would make the calculations even more costly in computer time and memory. Ultrasoft pseudopotentials[35] were devised specifically for the purpose of alleviating these shortcomings, and consequently we have used this type of pseudopotential to describe the interaction between ions and valence electrons. It was generated from a scalar-relativistic calculation of the atomic electron configuration [Kr]4d^{9}5s^2, following the procedure established by Kresse and Hafner.[36] First, an all electron calculation is performed. Then, a norm-conserving pseudopotential is constructed, with matching radii between all-electron and pseudized wavefunctions of 2.3 atomic units (a.u.) for the 5s atomic orbital, 2.7 a.u. for the 5p, and 1.8 a.u. for the 4d electrons. The s component was taken as the local part of the pseudopotential. Moreover, two projectors were considered for the p and d electrons, one at the all-electron energy eigenvalue and another one at 0.2 a.u. and -0.7 a.u. for the p and d electrons respectively. Finally the ultrasoft pseudopotential was constructed by using matching radii of 2.3, 2.7, and 2.4 a.u. for the s, p, and d pseudowavefunctions, respectively. During and after the construction of the pseudopotential, the usual tests were performed to check its quality, such as the reproduction of the all-electron logarithmic derivatives, the results for different electronic configurations of the atom, and the equilibrium distance of the solid. Finally the absence of ghost states was also confirmed.

In these AIMD calculations the planewave cutoff has been set to 25 Ryd for the wavefunctions and 150 Ryd for the electron density, the Newton equations have been solved using Verlet's leapfrog algorithm with a timestep of 7.5 fs, and the total number of equilibrium configurations generated amounts to 19 000 in the study of the bulk liquid, and to 15 000 in the liquid surface case. We have checked that these numbers of configurations were enough to obtain converged results for the magnitudes studied. The simulations have been performed using the Quantum-Espresso code.[37]

III. RESULTS: BULK PROPERTIES

The simulated sample contains 150 Ag atoms, enclosed in a cubic box of side 14.26 Å, which corresponds to a number density as given by experiments,[8] $\rho = 0.0517$ Å^{-3}.

We have evaluated several liquid static properties (pair distribution function, static structure factor) and dynamic properties, both single-particle ones (velocity autocorrelation function, mean square displacement) and collective ones (longitudinal and transverse currents). From these magnitudes we have also deduced several atomic transport properties of the liquid, such as the self-diffusion coefficient, the shear viscosity, and the adiabatic sound velocity.

A. Static properties

Figure 1 shows the AIMD result for $S(q)$ along with the XD data of Waseda,[8] the ND measurements of Bellissent *et al.*,[10] and the more recent XD data of Kaban and Hoyer.[9] The experimental $S(q)$ has a main peak located at $q_p \approx 2.64$ Å^{-1}, and its height is $S(q_p) \approx 2.8$. The calculated $S(q)$ shows an overall very good agreement with experiment, taking into account the experimental dispersion of the data. The simulation results reproduce correctly the height and position of the oscillations of $S(q)$, being in general closer to both the ND data and the more recent XD results. We note that previous studies based on the EAM model[15,16] or the OF-AIMD method[19] have predicted a $S(q)$ whose main peak was somewhat higher than experiment.

We have extrapolated our calculated $S(q)$ to $q \rightarrow 0$, in order to derive an estimate for the isothermal compressibility κ_T, by resorting to the relation $S(q \rightarrow 0) = \rho k_B T \kappa_T$, where k_B is Boltzmann's constant. A least squares fit $S(q) = s_0 + s_2 q^2$ of the computed $S(q)$ for q-values smaller than 1.1 Å^{-1} gives the result $S(q \rightarrow 0) = 0.0183 \pm 0.0005$, thus yielding the value $\kappa_T = 2.02 \pm 0.05$ (in units of 10^{-11} m^2 N^{-1}), which is close to the experimental data near melting of 2.11,[38] 1.92,[12] or 1.80.[13] For comparison, we note that the OF-AIMD calculation[19] gave a value $\kappa_T = 1.94 \pm 0.08$.

The Fourier Transform (FT) of $S(q)$ gives the pair distribution function, $g(r)$, which provides information about the short range order in the liquid. This is depicted in Fig. 2, along with the corresponding "experimental" data. It has a main peak located at $r_p = 2.77$ Å, whose height is somewhat higher than the experimental ones. This is followed by marked oscillations that coincide with the ones derived from ND.[10] The ratio between the positions of the main and the second peak is 1.90 which stands within the range 1.84–1.93 typical of the simple liquid metals (alkalis, alkali earths, and Al).

The coordination number (CN) has been evaluated by integrating $g(r)$ up to the position of its first minimum, which for our calculated $g(r)$ is located at $R_{\min} = 3.91$ Å, leading to CN ≈ 12.4 atoms. We note that this value for CN is typical of the simple liquid metals around their respective triple point.[39]

B. Dynamic properties

1. Single particle dynamics

Information about transport properties can be extracted from the normalized velocity autocorrelation function (VACF) of a tagged ion in the fluid, $Z(t)$. This is defined as

$$Z(t) = \langle \vec{v}_1(t) \cdot \vec{v}_1(0) \rangle / \langle v_1^2 \rangle, \tag{3}$$

with $\vec{v}_1(t)$ being the velocity of a tagged ion in the fluid at time t, and $\langle \ldots \rangle$ standing for the ensemble average.

Figure 3 depicts the calculated $Z(t)$ which displays the typical backscattering behavior with a shallow first minimum (in comparison with that of the simple liquid metals) which is followed by rather weak oscillations. This first minimum is related to the so-called "cage effect" by which a given particle rebounds against its surrounding cage, formed by its nearest neighbors. An estimate of the frequency at which a given particle vibrates within its near neighbor's cage[18] can be derived by the short time expansion $Z(t) = 1 - \omega_E^2 t^2/2 \ldots$, where ω_E is the so-called "Einstein frequency" of the system. A short time fitting of the $Z(t)$ curve in Fig. 3 gives $\omega_E \approx 18.8$ ps^{-1}. The inset of Figure 3 represents the power spectrum, $Z(\omega)$, which shows a maximum located at ≈ 13 ps^{-1} and a shoulder at ≈ 27 ps^{-1}. We note that ω_E stands between the two peaks (in fact, the peak and the shoulder) of $Z(\omega)$, which is a characteristic feature of the simple liquid metals.[39]
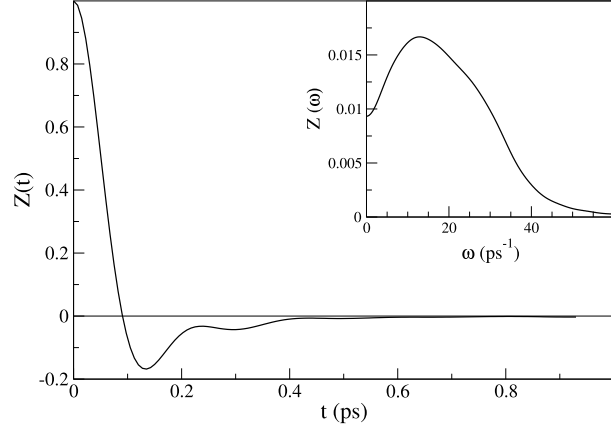
FIG. 3. Normalized velocity autocorrelation function of l-Ag at 1273 K. The inset represents its power spectrum $Z(\omega)$.

The self-diffusion coefficient, D, can be found by either the time integral of $Z(t)$ or from the slope of the mean square displacement $\delta R^2(t) \equiv \langle |\vec{R}_1(t) - \vec{R}_1(0)|^2 \rangle$ of a tagged ion in the fluid. In the present AIMD study, both routes lead to a value of $D_{AIMD} = 0.29$ Å^2/ps. The experimental result near melting ($T = 1235$ K) reported by Iida and Gutrhie[11] is 0.257 Å^2/ps, which when extrapolated to 1273 K yields $D_{exp} = 0.281$ Å^2/ps.

We notice that the OF-AIMD calculation[19] predicted a $Z(t)$ which is qualitatively different from the present one, i.e., it has a deeper first minimum and the subsequent maximum was above zero. Nevertheless, despite these differences, the OF-AIMD calculation gave a value $D_{OF} = 0.29$ Å^2/ps. On the other hand, the EAM calculation[15] yielded a somewhat smaller value $D_{EAM} = 0.24$ Å^2/ps.

2. Collective currents

The current due to the overall motion of the particles is defined, in reciprocal space, as

$$\vec{j}(q,t) = \sum_{a=1}^{N} \vec{v}_a(t) \, \exp[i\vec{q} \cdot \vec{R}_a(t)]. \tag{4}$$

It is usually split into a longitudinal component $\vec{j}_L(q,t)$, parallel to $\vec{q}$, and a transverse component $\vec{j}_T(q,t)$, perpendicular to $\vec{q}$. The longitudinal and transverse current correlation functions are obtained as

$$C_L(q,t) = \frac{1}{N} \langle j_L(q,t) j_L^*(q,0) \rangle, \tag{5}$$

and

$$C_T(q,t) = \frac{1}{2N} \langle \vec{j}_T(q,t) \cdot \vec{j}_T^*(q,0) \rangle. \tag{6}$$

The corresponding time FTs give the associated spectra $C_L(q,\omega)$ and $C_T(q,\omega)$, respectively. The longitudinal spectrum takes a zero value at $\omega = 0$, shows a maximum at a frequency $\omega_L(q)$, and finally decays to zero for large frequencies. A glimpse of the behavior of $C_L(q,\omega)$ is observed in Figure 4 where this function has been plotted for several wavevectors. In the long wavelength region ($q \to 0$) the existence of the maximum is related to the propagation of sound waves, and the phase velocity $\omega_L(q)/q$ tends in this region to the value of the adiabatic sound velocity, c_s. Certainly, the q values obtainable in AIMD simulations are not very small because of the size limitations imposed by the computational demands. In particular the minimum attainable wavevector is $q_{min} = 0.44$ Å^{-1}, which is not small enough so as to allow a precise quantitative estimate of c_s. Nonetheless, a qualitative guess may be extracted from the position of the peak in $C_L(q_{min},\omega)$ which yields a value $c_s = 2770 \pm 150$ m/s, whereas the experimental (hydrodynamic) value is[12] $c_{s;exp} = 2751$ m/s. An evaluation of c_s can also be obtained from the expression[18] $c_s = [\gamma k_B T / m S(q \to 0)]^{1/2}$, where m
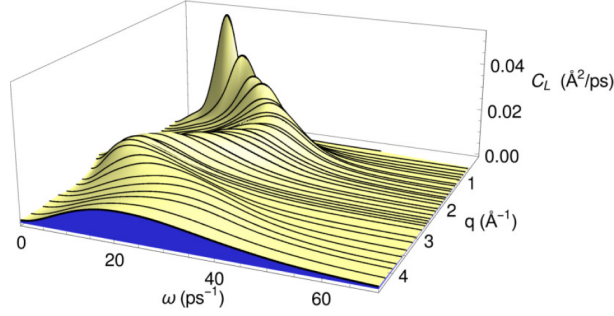
FIG. 4. Longitudinal current spectra for several wavevectors in the range from $q = 0.44$ to 4.49 Å^{-1}.

is the atomic mass. Using for the ratio of the specific heats $\gamma = 1.39$[12] and our calculated value $S(q \to 0) = 0.018$, the previous expression gives $c_s = 2750 \pm 100$ m/s, which attests to the consistency between the static and dynamic results obtained in the present AIMD study. We note that the OF-AIMD calculation[19] gave a somewhat greater value, namely $c_s = 2930 \pm 120$ m/s.

The dispersion relation of the density fluctuations, $\omega_L(q)$, is depicted in Figure 5 along with a straight line that corresponds to sound propagation in the hydrodynamic regime.

The transverse current correlation function, $C_T(q,t)$, cannot be measured directly in experiments, but it can be evaluated by means of computer simulations or by using some theoretical model. Shear waves are not supported by fluids for long wavelengths, where instead viscous damping is observed. In this hydrodynamic region, $C_T(q,\omega)$ decays as a Lorentzian function whose width is related to the shear viscosity. However, when the wavevector increases and less particles are involved in the response, some kind of solid-like elasticity sets in and shear waves start being supported. This is observed as a peak in $C_T(q,\omega)$ at a non-zero frequency, $\omega_T(q)$. For very short wavelengths (large values of q), the response becomes atomic-like. This amounts to a transverse spectrum that shows a Gaussian shape (without peaks at non-zero frequency) whose width is related to the average velocity of the particles in the system, i.e., to the temperature. Therefore, $C_T(q,\omega)$ provides information on the existence of propagating shear waves upon observation of non-zero
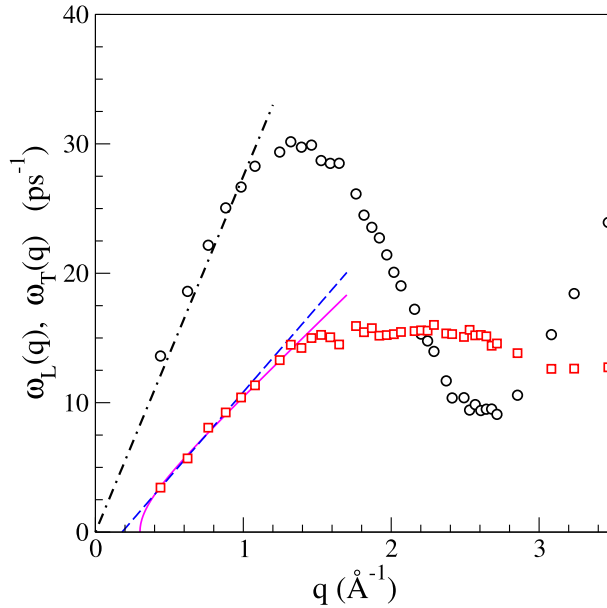
FIG. 5. Dispersion relations for l-Ag at $T = 1273$ K. Open circles: peak positions, $\omega_L(q)$, of the maxima of the calculated longitudinal current spectra. Open squares: peak positions, $\omega_T(q)$, of the maxima of the transverse current spectra. Dashed-dotted line: linear dispersion with the hydrodynamic sound velocity, $c_s = 2751$ m/s. Dashed line and full line correspond to fits of $\omega_T(q)$ to the linear and non-analytic expressions, respectively.
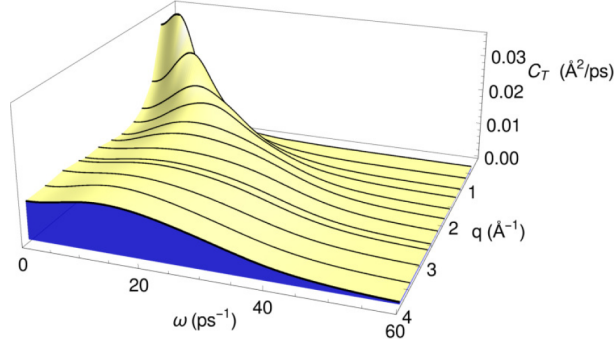
FIG. 6. Transverse current spectra for several wavevectors in the range from $q = 0.44$ to 3.87 Å^{-1}. Note the appearance of a peak at a non-zero frequency in $C_T(q,\omega)$ for all the q-ranges shown.

values of $\omega_T(q)$. Figure 6 depicts the behavior of $C_T(q,\omega)$ for several wavevectors. The peaks appear for a wide range of q-values, namely, $0.2q_p \leq q \leq 2.3q_p$, which is comparable to what has been found in simple liquid metals.[39] In passing, we note that at $q_{min}(0.44$ Å$^{-1})$, the corresponding $C_T(q,\omega)$ shows a peak, which means that q_{min} is already beyond the hydrodynamic regime. From the position of the maximum in the $C_T(q,\omega)$ a dispersion relation for the transverse modes, $\omega_T(q)$, can be obtained. We already mentioned that the q-value where from shear waves are supported (q_T) is smaller than the q_{min} of the simulation. Even though the behavior of $\omega_T(q)$ at the onset of shear wave propagation is predicted to be non-analytic,[39] it is nevertheless possible to define a "transverse sound velocity" in terms of the slope of $\omega_T(q)$ near q_T. It has been observed that the dispersion there is quasi-linear, i.e., it is well described by the formula $\omega_T(q) = c_T(q - q_{T,lin})$, where c_T is the transverse velocity of sound and $q_{T,lin} < q_T$ is the parameter of the proposed formula. We obtain (using the smallest four q-values allowed in the simulation) the estimates $q_{T,lin} \approx 0.18$ Å^{-1} and $c_T \approx 1320$ m/s. A fit to the non-analytic formula[39] $\omega_T = \alpha\sqrt{q^2 - q_T^2}$ leads to $q_T \approx 0.30$ Å^{-1}. The previous OF-AIMD calculation[19] yielded a substantially greater value, namely $c_T = 1950 \pm 150$ m/s. The transverse dispersion relation is also shown in Figure 5 along with the fitted formulas.

Another interesting property of the transverse correlation functions is that they enable to obtain a q-dependent shear viscosity coefficient, $\eta(q)$, which goes over to the macroscopic shear viscosity coefficient, η, in the limit $q \to 0$,[40–42] as shown in Figure 7. The present AIMD calculations yield an estimate $\eta_{AIMD} = 3.36 \pm 0.15$ GPa ps. The q_{min} allowed in our simulations is not really small, and for this reason the extrapolation towards $q = 0$ produces a relatively large uncertainty. The experimental recommended value for l-Ag at $T = 1273$ K, according to the review of Assael et $al.$, is[14] $\eta_{exp} \approx 3.90$ GPa ps. For comparison, we mention that the EAM and OF-AIMD calculations gave $\eta = 4.20$ and 3.65 GPa ps, respectively.

Within the context of the Brownian motion of a macroscopic particle with a diameter d in a liquid of viscosity η, the Stokes-Einstein relation $\eta D = k_B T/2\pi d$ establishes a connection between η and the self-diffusion coefficient D. Although not intended for atoms, this relation has been used to estimate η (or D) by identifying d with the position of the main peak of $g(r)$. The present calculations give $d = 2.77$ Å, and combined with the previous AIMD value $\eta = 3.36 \pm 0.15$ GPa ps yields $D = 0.30 \pm 0.02$ Å^2/ps, which is close to the calculated AIMD value and experimental results. Indeed, a similar level of agreement has already been found for a variety of liquid metals near melting which highlights the capability of the Stokes-Einstein relation to provide reasonable estimates when extrapolated to the atomic realm.

IV. RESULTS: FREE LIQUID SURFACE

In order to study the free liquid surface, we placed 120 Ag atoms in a tetragonal simulation box with $L_x = L_y = 11.465$ Å and $L_z = 32.676$ Å, in which the atoms formed a slab of initial width that
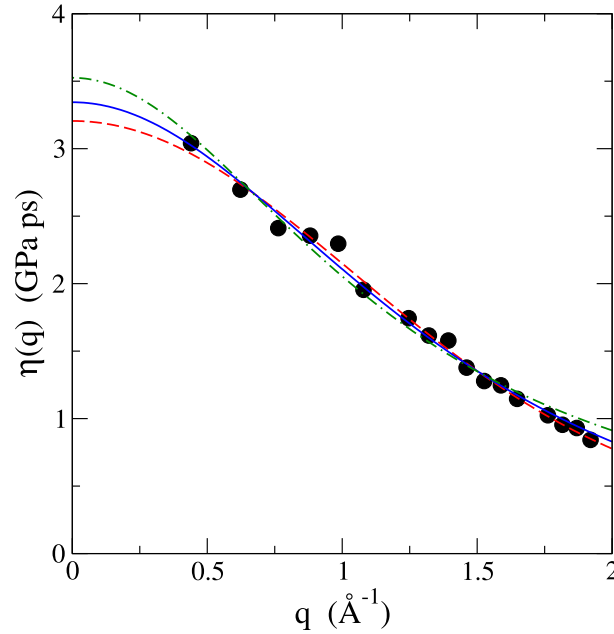
FIG. 7. Wavevector dependent shear viscosity. Circles are results from the AIMD simulations, and lines correspond to different fitting functions.

corresponds to the experimental number density. The temperature was set to 1400 K and the system was allowed to evolve until equilibrium is reached. After equilibration, 15 000 configurations were generated and the properties of the slab were analyzed as reported below.

By using the atomic configurations generated in the simulation box, we have calculated, for each configuration, the corresponding center of mass; therefrom a histogram of the atomic positions relative to the slab's center of mass was obtained after representing each atom's position with a Gaussian distribution whose width was taken as one third of the ionic radius. Finally the average of the previously obtained histograms was performed to obtain the average ionic DP.

Figure 8 shows the results obtained for the average ionic DP. A clear stratification is observed, and we can estimate the interlayer distances as those between consecutive maxima in the profile.
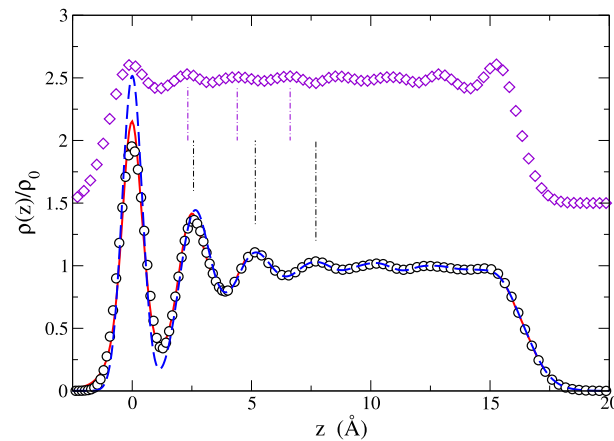
FIG. 8. Density profiles for the FLS of l-Ag. Diamonds: Average ionic DP (displaced upwards by 1.5 units) as obtained directly from a histogram of particle positions along the simulation. Dashed line: Intrinsic DP obtained using the most rigged separation surface in the computation. Circles: Intrinsic DP obtained using the separation surface with a truncated Fourier expansion. Full line: Electronic intrinsic density profile obtained using the same separation surface as in the ionic profile shown by circles. All the densities have been plotted relative to their respective bulk values.

The spacing between the outermost layer and the first inner one is $\lambda_{\text{out}} = 2.35$ Å, whereas the inner interlayer distances are somewhat shorter, namely, $\lambda_{\text{in}} = 2.07$ Å. The existence of two different spacings had already been observed in other AIMD studies of the FLS of l-Hg[29] and l-Cd[30] at thermodynamic conditions near their respective triple points. In l-Hg we obtained the same behavior as in l-Ag, namely $\lambda_{\text{out}} > \lambda_{\text{in}}$, whereas the opposite behavior was observed in l-Cd.

Additional information concerning the local structure in the slab is provided by the z-dependent coordination number, $\text{CN}(z)$, defined as the average number of neighbors within a distance $R_{\text{min}} = 3.91$ Å, which is the position of the first minimum of the bulk pair distribution function. (See Section III.) Our results show that for most of the slab, $\text{CN}(z)$ takes a value ≈ 12.3, which is almost the same as obtained for the bulk liquid. Indeed, this number remains practically constant up to the region where the outermost layer begins; therefrom $\text{CN}(z)$ begins decreasing and at the position of the first peak of the profile, it attains a value $\text{CN}(z) \approx 8.7$. This reduction of $\approx 30\%$ is similar to what we have already found for a wide range of simple liquid metals.[26] The outermost atoms, which stand at the region where the tail of the profile becomes very small, show a substantially smaller coordination number namely $\text{CN}(z) \approx 4.5$.

As already mentioned in the Introduction, the density profile described above is somewhat blurred because of the existence of CW in the simulation, and also because of the statistical fluctuations associated to the small number of particles. In order to calculate the X-ray reflectivity, it is most convenient to consider the intrinsic profile, which would correspond to the absence of CW. The CWs cause height fluctuations in the separation surface between the liquid and vapor phases, which is described by the function $z = \xi(x, y)$, so their elimination boils down to computing the histogram of the particle positions relative to this separation surface, i.e., computing the histograms according to the values of $z_{i;\text{rel}} = z_i - \xi(x_i, y_i)$, where i runs over all the particles of the sample. It is therefore crucial to define a method to compute $\xi(x, y)$ from the simulation. We have followed the prescription put forward by Chacón and Tarazona,[31] which we describe here briefly.

For each configuration of the simulation run we select 9 atoms, which are those whose z coordinate is the smallest within the 9 prisms obtained by partitioning the simulation cell in 3×3 across the xy plane. Next we proceed to compute a surface that passes through these pivot atoms and has a minimum area. Then we locate the atom closest to this surface and incorporate it as a new pivot, proceeding to the recalculation of the minimum area surface that passes through all of the pivots. The procedure is repeated until a specified target number of pivots is obtained, which in our simulation of the FLS of Ag is 18 atoms.

Note that the existence of two interfaces leads to two separation surfaces, and consequently two intrinsic profiles. The results shown below correspond to their average.

In order to satisfy the periodicity inherent to the simulation, $\xi(x, y)$ is represented by its Fourier series. From a physical point of view, it is not acceptable that the separation surface undulates within an atomic diameter, and therefore the Fourier series is terminated at the wavevector that corresponds to the atomic size. The Fourier coefficients are then obtained through the minimization of the area of the surface (computed up to second order in the wavevector) constrained to satisfying $z_\ell = \xi(x_\ell, y_\ell)$ with ℓ running through all the pivots selected. The surface so obtained is the most rigged minimum area surface, that we use as separation surface, and the relative z coordinate of all the pivot atoms with respect to this surface is zero. Consequently, if we considered the atoms as point particles, the intrinsic DP would contain a Dirac delta function at $z = 0$. However, it is possible to truncate the Fourier expansion further, by ignoring the higher order coefficients, thus obtaining a smoother surface, which however, does not go through the pivot atoms. These smoothed surfaces can again be used to obtain different intrinsic DPs, whose first layer would no more be a delta function, but rather a smooth function peaked at $z = 0$. Given the small size of our simulation box, it is only possible to apply this truncation once, i.e., eliminating only the highest Fourier coefficients of $\xi(x, y)$. In Figure 8 we show the intrinsic density profiles obtained from both possible separation surfaces, although now describing the atoms as Gaussian distributed, as we did in the calculation of the average DP. The difference between the two profiles is negligible after the second layer, where it is already small. Obviously the first layer is narrower and sharper if no truncation is performed (dashed line in the figure).

We recall that the separation surface that is calculated in order to obtain the intrinsic profile is specific to each interface. It gives rise to a sharp peak at the position of the interface being considered but not at the other interface; this means that the slab is in fact wide enough so as to rule out correlations between the two interfaces.

The layered structure of the interface is much more clearly observed in the intrinsic profiles. Moreover, the obtained interlayer distances are significantly modified from those found in the average DP. Now all the interlayer distances take the same value of $\lambda = 2.57$ Å, which is larger than both distances λ_1 and λ_2 corresponding to the average DP. This interlayer distance is in fact closer to the maximum of the liquid's $g(r)$ obtained in Section III, which on physical grounds appears as a sensible correlation.

The X-ray reflectivity, which is the property amenable to experimental observation, is related to the electronic density profile. We have therefore calculated the intrinsic electron density profile, as obtained from a superposition of atomic electron densities centered at each ionic position, and using the smoothed separation surface. This is depicted in Figure 8, and it looks very similar to the ionic one. This justifies somehow the width of the Gaussian distribution used to obtain the ionic profiles. The intrinsic reflectivity is calculated as $R_{\text{int}}(q_z) = |\Phi(q_z)|^2$, where

$$\Phi(q_z) = \frac{1}{\rho_{e0}} \int_0^\infty dz \, \exp[-i\,q_z z] \frac{d\rho_{e;int}(z)}{dz}, \tag{7}$$

where ρ_{e0} is the average bulk electron density. The results obtained are shown in Figure 9, where we see a characteristic peak located at $q_z = 2.50$ Å^{-1}, which is close to $2\pi/\lambda = 2.44$ Å^{-1}, and is related to the layering of the DP. Moreover, we find that for smaller q_z the intrinsic reflectivity decreases uniformly towards its value at $q_z = 0$. This behavior is similar to that found experimentally for liquid Ga, In, or K.[43]

We proceed now to analyze the structure of the different layers of the slab. The absence of neighbors at one side of the interface can in principle induce some rearrangement of the surface atoms, due to the different forces they experience as compared to atoms in the bulk. Such rearrangements can be visualized in terms of the pair correlation function between atoms within particular slices of the slab, $g_T(r)$. We define the outermost slice as that from the vacuum region to the first minimum in the ionic DP, and other slices comprise the regions between minima. The average ionic density observed within the different slices changes very little as compared to the bulk one. Only the outermost layer shows a minor decrease of 4.4% with respect to the average density. Figure 10 shows $g_T(r)$ for the outermost slice, for the first inner slice, and for a 4.40 Å wide region in the slab's center, which we qualify as the "bulk region." It is observed that there is basically no atomic relaxation at the outermost slice, as $g_T(r)$ is practically coincident with those of the inner slice and the bulk region. Moreover, they all are very close to the pair correlation function in the bulk liquid as obtained in Section III.
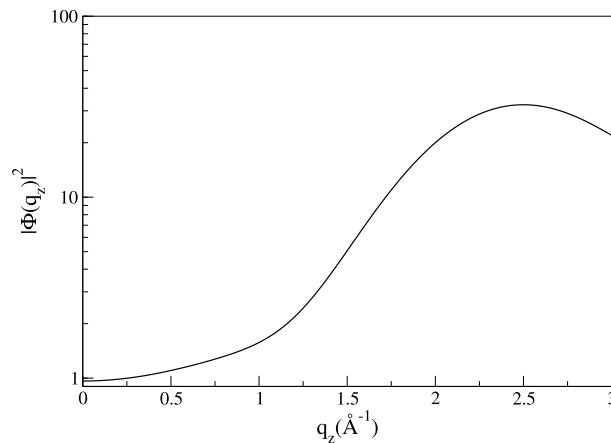
FIG. 9. Intrinsic X-ray reflectivity of the FLS of l-Ag at 1400 K. The layering peak is located at $q_z \approx 2.50$ Å^{-1}.
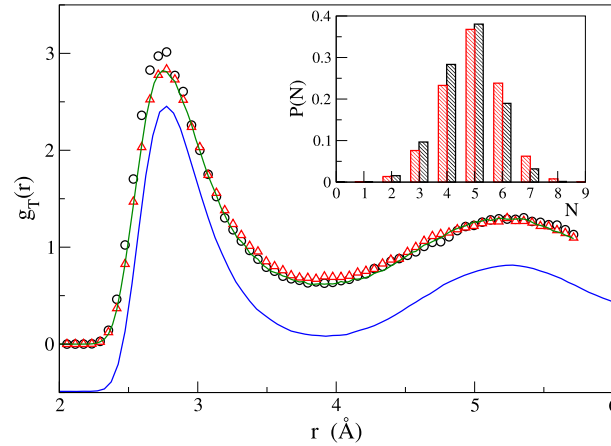
FIG. 10. Transverse pair correlation functions for different slices of the slab. Circles: outermost slice, triangles: first inner slice, line: bulk region. The $g(r)$ obtained in the study of the bulk liquid (see Figure 2) is also shown displaced downwards by 0.5 units. The inset shows the distribution of in-layer neighbors at the slab's center (right bars) and at the interface layer (left bars).

We have additionally studied the distribution of near neighbors of an atom within a layer, and compared the results at the outermost interface layer with those in inner regions. The results are also displayed in Figure 10, and again show very little relaxation at the interface. The most probable number of in-layer neighbors is 5, whereas the average value is 5.0 at the interface, slightly higher than the average value in the slab's center, namely, 4.7 neighbors. The distribution at the interface is typical of liquid surface metallic layers, as similar results have been found in other systems.[27,29,30]

As for the transport properties in the FLS, we have analyzed the in-plane diffusion coefficient in the different layers. The procedure followed is the same that was used to study this property at the FLS of a variety of liquid metals and a Lennard-Jones system.[44] The basic idea is to compute the mean square displacements within the given layer of particles that stay in that layer for a time long enough as to attain a diffusive motion. It is important to follow the behavior of each particle and select only the ones that comply with the conditions mentioned, because in general the particle motion in the direction perpendicular to the interface can be viewed as a series of oscillations within a layer and jumps from one layer to another, and therefore a particle that changes its position to a different layer before attaining a diffusive in-plane motion must be discarded.

The results for the FLS of l-Ag are shown in Figure 11, and follow the same trends as observed in a previous study for other metals,[44] namely, the diffusion coefficient increases from the bulk
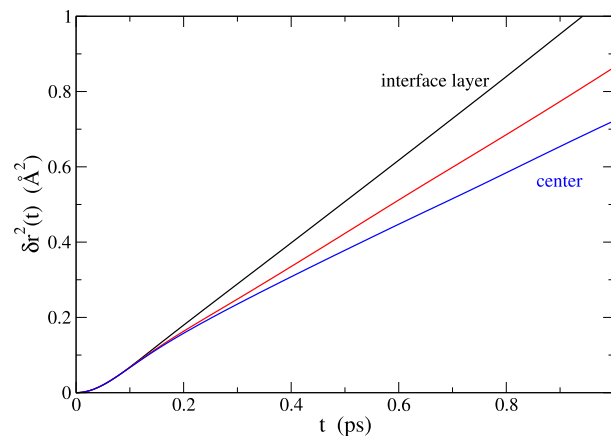
FIG. 11. Mean squared displacements parallel to the interface for different layers. The lower curve corresponds to the slab's center, the middle one to the first inner layer, and the upper curve corresponds to the outermost layer.

value as the interface is approached, and at the outermost layer this increase is close to 100%. Specifically, at the slab's center $D_{center} = 0.33$ Å^2/ps, which is larger than the value obtained in Section III because of the higher temperature considered for the slab. This value increases to 0.44 at the first inner layer and to $D_{surf} = 0.57$ Å^2/ps at the interface layer. We ascribe such a large increase in diffusivity to the reduced number of neighbors of a given particle at the outermost layer, which allows further mobility to the atoms due to a weakened cage effect. Even though the atoms in the first inner layer are surrounded by neighbors, those located at the outermost layer have higher mobility than the bulk ones, and this again depletes the cage effect, although less than the total absence of neighbors. Consequently, the diffusion coefficients in the inner layers stand between the interface and bulk values.

V. CONCLUSIONS

We have reported results of *ab initio* simulations for several bulk properties as well as for the free liquid surface of l-Ag at a thermodynamic state near its triple point.

Concerning bulk l-Ag, the results obtained for the static structure are in good agreement with the available experimental data. In this way, the present AIMD calculation accounts for the height and position of the main peak in the experimental $S(q)$ as well as for the position and amplitude of the subsequent oscillations.

As for the calculated dynamical properties, we note that the calculated $Z(t)$ shows the typical oscillatory behavior characteristic of the simple liquid metals near melting. Moreover, the associated self-diffusion coefficient, which is related to the integral of the $Z(t)$, shows a very good agreement with experiment. Other transport coefficients such as the adiabatic sound velocity or shear viscosity coefficient, which are closely related to the longitudinal and transverse current correlation functions, respectively, provide a very good estimate of the corresponding experimental data.

Therefore, it may be asserted that the present AIMD method yields a rather accurate description of a range of static and dynamic properties of bulk l-Ag at thermodynamic conditions near its triple point. This fact has prompted us to undertake the study of the free surface of l-Ag, for which no experiments have been performed yet. First we notice that the free liquid surface exhibits surface layering which is a typical feature in liquid metals. In our analysis of the simulation results we have carried out a microscopic calculation of the intrinsic density profile, from which we have derived the corresponding intrinsic reflectivity; this magnitude shows a behavior which is qualitatively similar to that experimentally found for liquid Ga, In, and K. Our analysis of the atomic motion within the layers parallel to the interface has shown an enhancement with respect to the bulk, which yields an almost two-fold increase of the diffusion coefficient at the outermost layers.

Finally, we acknowledge that a more accurate calculation of the different properties associated to the liquid free surface would be achieved by using of a greater number of atoms in the simulation box, i.e., several hundreds or even thousands. However, this is not yet feasible within the context of the present KS-AIMD simulation method. Nevertheless, we think that the main qualitative features of the free liquid surface of l-Ag are already accounted for in the present simulation results.

ACKNOWLEDGMENTS

[1] P. Hohenberg and W. Kohn, "Inhomogeneous electron gas," Phys. Rev. **136**, B864 (1964); W. Kohn and L. J. Sham, "Self-consistent equations including exchange and correlation effects," Phys. Rev. **140**, A1133 (1965).

[2] W. R. Osório, D. R. Leiva, L. C. Peixoto, L. R. Garcia, and A. Garcia, "Mechanical properties of Sn-Ag lead-free solder alloys based on the dendritic array and Ag$_3$Sn morphology," J. Alloys Compd. **562**, 194 (2013).

[3] H. Nishikawa and N. Iwata, "Formation and growth of intermetallic compound layers at the interface during laser soldering using Sn-Ag-Cu solder on a Cu pad," J. Mater. Process. Technol. **215**, 6 (2015).

[4] A. A. El-Daly, A. M. El-Taher, and S. Gouda, "Development of new multicomponent Sn–Ag–Cu–Bi lead-free solders for low-cost commercial electronic assembly," J. Alloys Compd. **627**, 268 (2015).

[5] E. Guarini, U. Bafile, F. Barocchi, A. De Francesco, E. Farhi, F. Formisano, A. Laloni, A. Orecchini, A. Polidori, M. Puglini, and F. Sacchetti, "Dynamics of liquid Au from neutron Brillouin scattering and *ab initio* simulations: Analogies in the behavior of metallic and insulating liquids," Phys. Rev. B **88**, 104201 (2013).

[6] O. Pfannenschmid, "Atomverteilung in flüssigem quecksilber, geschmolzenem silber und gold," Z. Naturf. A **15**, 603 (1960).

[7] C. N. J. Wagner, H. Ocken, and M. L. Joshi, "Interference and radial distribution functions of liquid copper, silver, tin and mercury," Z. Naturf. A **20**, 325 (1965).

[8] Y. Waseda and M. Ohtani, "Static structure of liquid noble and transition metals by x-ray diffraction," Phys. Status Solidi B **62**, 535 (1974); Y. Waseda, *The Structure of Non-Crystalline Materials* (McGraw-Hill, New York, 1980).

[9] I. Kaban and W. Hoyer, "Interplay between atomic and electronic structure in liquid noble–polyvalent metal systems," J. Non-Cryst. Solids **312–314**, 41 (2002).

[10] M. C. Bellissent, P. Desre, R. Bellissent, and G. Tourand, "Neutron diffraction studies of liquid silver and liquid Ag-Ge alloys," J. Phys. **37**, 1437 (1976).

[11] T. Iida and R. I. L. Gutrhie, *The Thermophysical Properties of Metallic Liquids* (Oxford University Press, New York, 2015).

[12] S. Blairs, "Review of data for velocity of sound in pure liquid metals and metalloids," Int. Mater. Rev. **52**, 321 (2007).

[13] R. N. Singh, A. Arafin, and A. K. George, "Temperature-dependent thermo-elastic properties of s-, p- and d-block liquid metals," Physica B **387**, 344 (2007).

[14] M. J. Assael, A. E. Kalyva, K. D. Antoniadis, R. M. Banish, I. Egry, J. Wu, E. Kaschnitz, and W. A. Wakeham, "Reference data for the density and viscosity of liquid antimony, bismuth, lead, nickel and silver," High Temp.-High Pressure **41**, 161 (2012).

[15] M. M. G. Alemany, C. Rey, and L. J. Gallego, "Transport coefficients of liquid transition metals: A computer simulation study using the embedded atom model," J. Chem. Phys. **109**, 5175 (1998); M. M. G. Alemany, O. Dieguez, C. Rey, and L. J. Gallego, "Molecular-dynamics study of the dynamic properties of fcc transition and simple metals in the liquid phase using the second-moment approximation to the tight-binding method," Phys. Rev. B **60**, 9208 (1999); M. M. G. Alemany, M. Calleja, C. Rey, L. J. Gallego, J. Casas, and L. E. González, "A theoretical and computer simulation study of the static structure and thermodynamic properties of liquid transition metals using the embedded atom model," J. Non-Cryst. Solids **250–252**, 53 (1999); M. M. G. Alemany, L. J. Gallego, L. E. González, and D. J. González, "A molecular dynamics study of the transport coefficients of liquid transition and noble metals using effective pair potentials obtained from the embedded atom model," J. Chem. Phys. **113**, 10410 (2000); J. I. Akhter, E. Ahmed, and M. Ahmad, "Study of diffusion coefficients in liquid noble metals," Mater. Chem. Phys. **93**, 504 (2005).

[16] G. M. Bhuiyan, M. Silbert, and M. J. Stott, "Structure and thermodynamic properties of liquid transition metals: An embedded-atom-method approach," Phys. Rev. B **53**, 636 (1996); A. Z. Ziauddin Ahmed and G. M. Bhuiyan, "Application of the EAM potentials to the study of diffusion coefficients of liquid noble and transition metals," Int. J. Mod. Phys. B **16**, 3837 (2002); R. C. Gosh, M. R. Amin, and G. M. Bhuiyan, "Atomic transport for liquid noble and transition metals using scaling laws," J. Mol. Liq. **188**, 148 (2013).

[17] H. W. Sheng, M. J. Kramer, A. Cadien, T. Fujita, and M. W. Chen, "Highly optimized embedded-atom-method potentials for fourteen fcc metals," Phys. Rev. B **83**, 134118 (2011).

[18] J. P. Hansen and I. R. McDonald, *Theory of Simple Liquids* (Academic Press, London, 1986); J. P. Boon and S. Yip, *Molecular Hydrodynamics* (Dover, New York, 1991).

[19] G. M. Bhuiyan, L. E. González, and D. J. González, "Orbital free *ab initio* molecular dynamics simulation study of some static and dynamic properties of liquid noble metals," Condens. Matter Phys. **15**, 33604 (2012).

[20] J. S. Rowlinson and B. Widom, *Molecular Theory of Capillarity* (Clarendon, Oxford, 1982); J. Penfold, "The structure of the surface of pure liquids," Rep. Prog. Phys. **64**, 777 (2001).

[21] P. S. Pershan, "X-ray scattering: Liquid metal/vapor interfaces," Eur. Phys. J.: Spec. Top. **196**, 109 (2011).

[22] P. S. Pershan and M. L. Schlossman, *Liquid Surfaces and Interfaces. Synchrotron X-ray Methods* (Cambridge University Press, New York, 2012).

[23] S. A. Rice, "What can we learn from the structures of the liquid-vapor interfaces of metals alloys?," Mol. Simul. **29**, 593 (2003), and references therein.

[24] G. Fabricius, E. Artacho, D. Sanchez-Portal, P. Ordejon, D. A. Drabold, and J. M. Soler, "Atomic layering at the liquid silicon surface: A first-principles simulation," Phys. Rev. B **60**, R16283 (1999).

[25] B. G. Walker, C. Molteni, and N. Marzari, "*Ab initio* molecular dynamics of metal surfaces," J. Phys.: Condens. Matter **16**, S2575 (2004); "*Ab initio* studies of layering behavior of liquid sodium surfaces and interfaces," J. Chem. Phys. **124**, 174702 (2006); "In-plane structure and ordering at liquid sodium surfaces and interfaces from *ab initio* molecular dynamics," J. Chem. Phys. **127**, 134703 (2007).

[26] D. J. González, L. E. González, and M. J. Stott, "Surface structure of liquid Li and Na: An *ab initio* molecular dynamics study," Phys. Rev. Lett. **92**, 085501 (2004); "Liquid-vapor interface in liquid binary alloys: An *ab initio* molecular dynamics study," Phys. Rev. Lett. **94**, 077801 (2005); "Surface structure in simple liquid metals: An orbital-free first-principles study," Phys. Rev. B **74**, 014207 (2006); L. E. González and D. J. González, "Structure and dynamics of bulk liquid Ga and the liquid-vapor interface: An *ab initio* study," Phys. Rev. B **77**, 064202 (2008).

[27] L. Calderín, L. E. González, and D. J. González, "First-principles study of the layering at the free liquid Sn surface," Phys. Rev. B **80**, 115403 (2009).

[28] J.-M. Bomont, J.-L. Bretonnet, D. J. González, and L. E. González, "Computer simulation calculations of the free liquid surface of mercury," Phys. Rev. B **79**, 144202 (2009).

[29] L. Calderín, L. E. González, and D. J. González, "*Ab initio* molecular dynamics study of the free surface of liquid Hg," Phys. Rev. B **87**, 014201 (2013).

[30] L. Calderín, L. E. González, and D. J. González, "An *ab initio* study of the structure and dynamics of bulk liquid Cd and its liquid-vapor interface," J. Phys.: Condens. Matter **25**, 065102 (2013).

[31] E. Chacón and P. Tarazona, "Intrinsic profiles beyond the capillary wave theory: A Monte Carlo study," Phys. Rev. Lett. **91**, 166103 (2003); P. Tarazona and E. Chacón, "Monte Carlo intrinsic surfaces and density profiles for liquid surfaces," Phys. Rev. B **70**, 235407 (2004).

[32] E. Chacón, P. Tarazona, and L. E. González, "Intrinsic structure of the free liquid surface of an alkali metal," Phys. Rev. B **74**, 224201 (2006).

[33] D. M. Ceperley and B. J. Alder, "Ground state of the electron gas by a stochastic method," Phys. Rev. Lett. **45**, 566 (1980); J. P. Perdew and A. Zunger, "Self-interaction correction to density-functional approximations for many-electron systems," Phys. Rev. B **23**, 5048 (1981).

[34] S. G. Louie, S. Froyen, and M. L. Cohen, "Nonlinear ionic pseudopotentials in spin-density-functional calculations," Phys. Rev. B **26**, 1738 (1982).

[35] D. Vanderbilt, "Soft self-consistent pseudopotentials in a generalized eigenvalue formalism," Phys. Rev. B **41**, 7892 (1990).

[36] G. Kresse and J. Hafner, "Norm-conserving and ultrasoft pseudopotentials for first-row and transition elements," J. Phys.: Condens. Matter **6**, 8245 (1994).

[37] P. Gianozzi *et al.*, "QUANTUM ESPRESSO: A modular and open-source software project for quantum simulations of materials," J. Phys.: Condens. Matter **21**, 395502 (2009).

[38] M. Shimoji, *Liquid Metals* (Academic Press, London, 1977).

[39] U. Balucani and M. Zoppi, *Dynamics of the Liquid State* (Clarendon, Oxford, 1994).

[40] D. J. González, L. E. González, J. M. López, and M. J. Stott, "Orbital free *ab initio* molecular dynamics study of liquid Al near melting," J. Chem. Phys. **115**, 2373 (2001); "Dynamical properties of liquid Al near melting: An orbital-free molecular dynamics study," Phys. Rev. B **65**, 184201 (2002); M. M. G. Alemany *et al.*, "*Ab initio* molecular dynamics simulations of the static, dynamic, and electronic properties of liquid Pb using real-space pseudopotentials," Phys. Rev. B **76**, 214203 (2007).

[41] B. J. Palmer, "Transverse current autocorrelation function calculations of the shear viscosity for molecular liquids," Phys. Rev. E **49**, 359 (1994).

[42] U. Balucani, J. P. Brodholt, P. Jedlovszky, and R. Vallauri, "Viscosity of liquid water from computer simulations with a polarizable potential model," Phys. Rev. E **62**, 2971 (2000); J. Blanco, D. J. González, L. E. González, J. M. López, and M. J. Stott, "Collective ionic dynamics in the liquid Na-Cs alloy: An *ab initio* molecular dynamics study," Phys. Rev. E **67**, 041204 (2003).

[43] O. Sphyrko *et al.*, "X-ray study of the liquid potassium surface: Structure and capillary wave excitations," Phys. Rev. B **67**, 115405 (2003).

[44] L. E. González and D. J. González, "*Ab initio* study of the atomic motion in liquid metal surfaces: Comparison with Lennard-Jones systems," J. Phys.: Condens. Matter **18**, 11021 (2006).

9.2 INTRINSIC PROFILES OF LIQUID METALS AND THEIR REFLECTIVITY.

The free surfaces of liquid metals are known to exhibit a stratified profile that, in favourable cases, shows up in experiments as a peak in the ratio between the reflectivity function and that of an ideal step-like profile. This peak is located at a wave-vector related to the distance between the layers of the profile. In fact the surface roughness produced by thermally induced capillary waves causes a depletion of the previous so called intrinsic reflectivity by a damping factor that may hinder the observation of the peak. The behaviour of the intrinsic reflectivity below the layering peak is however far from being universal, with systems as Ga or In where the reflectivity falls uniformly towards the $q \to 0$ value, others like Sn or Bi where a shoulder appears at intermediate wavevectors, and others like Hg which show a minimum. We have performed extensive ab initio simulations of the free liquid surfaces of Bi, Pb and Hg, that yield direct information on the structure of the profiles and found that the macroscopic capillary wave theory usually employed in order to remove the capillary wave components fails badly in some cases for the typical sample sizes affordable in ab initio simulations. However, a microscopic method for the determination of the intrinsic profile is shown to be successful in obtaining meaningful intrinsic profiles and corresponding reflectivities which reproduce correctly the qualitative behaviour observed experimentally.

9.2.1 *Introduction.*

Since the original prediction of D'Evelyn and coworkers that free liquid surfaces (FLS) of metals would exhibit surface layering in the density profile (DP) perpendicular to the interface [42], $\rho(z)$, almost a decade had to elapse until this expectation was realized experimentally for the case of liquid Hg [43, 54], through the analysis of the x-ray reflectivity of the FLS, $R(q_z)$, which showed a peak related to the layering. Since then, up to 2009 [48], measurements have been performed for other five pure liquid metals, namely Ga, In, K, Sn and Bi [302]. All these studies were possible due to the advent of x-ray sources intense enough and reflectometers precise enough to measure reflectivities that decay by as much as 9/10 orders of magnitude as the wavevector increases above the position of the reflectivity peak. The experimental requirements to make such experiments feasible, as discussed in [302], basically limit the set of pure liquid metals candidates to these studies to those already mentioned, plus liquid Pb and possibly liquid Ge. A particular source of complications due to the liquid nature of the samples is the presence of thermally induced capillary waves (CW) which blur the so-called intrinsic profile, $\rho_{int}(z)$, leading to an average profile, $\rho_{av}(z)$, and deplete even more the measured reflectivity, $R_m(q_z)$. The effects of CW are removed from $R_m(q_z)$ through the use of the macroscopic CW theory, that boils down to a division of $R_m(q_z)$ by a gaussian, Debye-Waller-like, factor that depends on a capillary roughness, σ_{cw}, leading to the intrinsic reflectivity, $R_{int}(q_z)$. In most cases, this is further divided by the Fresnel reflectivity, $R_F(q_z)$, that corresponds to a sharp flat surface and accounts for the overall decay of $R_{int}(q_z)$. The resulting quantity is called the surface structure factor, $|\Phi_{int}(q_z)|^2$, which is directly related to the Fourier Transform of the electronic DP. Note that the capillary roughness depends on the temperature, T, and the surface tension, γ, of the liquid, on the atomic size, and on the lateral resolution of the detector.

The systems studied can be classified in three groups so far: those whose $|\Phi_{int}(q_z)|^2$ decays monotonously from the layering peak towards $q_z \to 0$ (Ga, In and K), those that display a shoulder at an intermediate q_z (Sn and Bi) and those that display a minimum at an intermediate q_z (Hg). The origin of such different behaviors must lie in the different electronic DPs, but these are not directly available to experiments. Instead model profiles are proposed and the corresponding reflectivities are fitted to the measurements. The systems in the first group can be adequately described by a simple model named distorted crystal model (DCM), in which the DP is described by layers of equally dense and equispaced gaussians of linearly increasing variance as the bulk is approached. The other groups require some modifications to this model, changing either the positions or the density of some layer(s), in particular the outermost one. However the lack of uniqueness of model profiles that reproduce a given reflectivity poses a note to take into account in the interpretation.

An alternative route to study the FLS of metals is the use of computer simulations. These, however, rely on the availability of methods to describe properly the interaction among ions immersed in a valence electron sea, as adequate for a metal. In this respect, ab initio methods are certainly advantageous, since the underlying density

TABLE 14: Simulation details.

	ρ_i (Å^{-3})	T (K)	N	$L_x = L_y$ (Å)	L_z (Å)	N_c
Hg	0.0403	300	116	13.03	17.10	8000
Bi	0.0288	800	160	13.57	38.69	27000
Pb	0.0309	850	160	13.57	37.33	27000

functional theory (DFT) [1, 2] shows a high degree of accuracy. Moreover, simulations give access to the atomic positions, so the DPs can be directly computed, and through them, the reflectivity. In fact, ab initio simulations have already been performed for the FLS of Si [303], Na [304], Sn [305], Hg [306] and Cd [190].

The sample size in simulations is utterly smaller than in experiments and consequently the abundance of CW is much reduced, but it is not null. It is therefore important to take into account this difference for proper comparison with experimental data. In previous studies the procedure adopted has been the same macroscopic CW theory as used in experiments, except for the aforementioned size differences. However a more direct access to the intrinsic profile and reflectivity is desirable, considering that the simulation samples are very far from being macroscopic. One such method was proposed by Chacon and Tarazona (CT) [57]. It relies on the calculation of a surface that separates the liquid and vapour phases, and sample the atomic positions with respect to this surface in order to obtain the intrinsic profile. The surface is computed so as to be the one that goes through the "surface atoms" and has "minimum area".

In this contribution we report a reanalysis of previous ab initio molecular dynamics (MD) simulations of the FLS of Hg, as well as new calculations for Pb and Bi. We discuss the differences between the average and intrinsic profiles as obtained through the CT procedure, highlighting the advantages of the latter. Also, when available, we compare our reflectivities with the measured ones.

9.2.2 Theory.

The energy and the forces on the atoms for each MD configuration were computed through the use of DFT and pseudopotentials to describe the interaction between ions and valence electrons. The simulations for Hg [306] were performed using the Quantum Espresso (QE) code [227], and an ultrasoft pseudopotential with 12 valence electrons. In the cases of Pb and Bi we used the PARSEC code [307] along with norm-conserving pseudopotentials with 4 and 5 valence electrons respectively [308, 309].

For the study of the FLSs we used N atoms in a slab geometry of initial width adequate to the experimental density, ρ_i, located in a tetragonal simulation box with $L_z > L_x = L_y$ and periodic boundary conditions. The vacuum region separating the replicas of each slab is taken large enough so that the inter-slab interaction can be safely neglected. After equilibration at the desired temperature N_c microcanonical configurations were generated from which the different properties were sampled. The particular values used for the different systems are shown in table 14.

The average electronic DP is obtained from the evaluation of a histogram of the z-coordinates of the particles, after representing each particle by the projection of the atomic electron density onto the z-direction.

The CT procedure to obtain the intrisic DP for a FLS relies on the computation, for each MD configuration, of a liquid-vapour separation surface, $z = \xi(x, y)$, so that the intrinsic DP is obtained from a histogram of the particles distances to this surface along the z-direction, i.e., according to their values of $z_{i;rel} = z_i - \xi(x_i, y_i)$, where i runs over all the particles of the sample. The separation surface must comply with the periodic boundary conditions (PBC) of the simulation cell, so it is represented by its Fourier series. The separation surface should not oscillate within an atomic diameter. Therefore the series is terminated at q-values correponding to this size and compatible with the PBC, and consequently has a finite number of coefficients. These coefficients are determined by a constrained minimization of the surface area. The constraints imposed consist in the requirement that the separation surface passes through the surface atoms (pivots), i.e., $z_\ell = \xi(x_\ell, y_\ell)$, with ℓ running through the

pivots. For each configuration 9 atoms are initially selected as pivots, by taking those whose z-coordinate is smallest among the atoms in each of the 3×3 prisms obtained by partitioning the simulation cell equally across the xy plane. After computing the minimal surface that passes through these pivots we locate the atom closest to this surface and include it as a new pivot. Further recalculations of minimal surfaces that pass through the pivots and inclusions of the closest atom as pivot are repeated until a specified number of pivots is reached, which is 21 atoms for Hg and 19 atoms for Pb and Bi. This number is self-consistently obtained from the method (and of course depends on the sample sizes), because the use of a different number of final pivots leads to intrinsic profiles with strange shapes that include shoulders at either the outermost layer or the first inner one. After the Fourier coefficients have been obtained one can optionally truncate the series, while keeping the coefficients, at lower cutoff wavevectors. This leads to a smoother separation surface which does not go exactly trough all the pivots, but close to them. Such separation surface is more physically appealing, since in the liquid there are not only capillary waves, but also other types of excitations that influence the vertical motion of the surface atoms, for instance transverse waves that propagate parallel to the surface. Due to the limited size of the samples used in ab initio simulations this further truncation of the series can only be performed one level, down to the next lower q compatible with the PBC.

Finally, after the DPs have been computed the reflectivities are obtained from the relations

$$\Phi(q_z) = \int_0^\infty dz \, \exp[-iq_z z] \frac{d\rho(z)/\rho_0}{dz} \qquad \frac{R(q_z)}{R_F(q_z)} = |\Phi(q_z)|^2. \tag{171}$$

where ρ_0 is the density of the bulk liquid. When $\rho(z)$ is the intrinsic profile these relations lead to the intrinsic reflectivity. However, when $\rho(z)$ is the average profile the resulting reflectivity function includes the CW present in the simulation. From this the corresponding intrinsic reflectivity, within the macroscopic CW theory, is obtained through the relation

$$\frac{R_{int}^{CWT}(q_z)}{R_F(q_z} = \frac{R_{av}(q_z)/R_F(q_z)}{\exp[-\sigma^2 q_z^2]} \tag{172}$$

where σ^2 includes the capillary roughness and also an intrinsic roughness, not really well defined but related to the atomic size [306].

9.2.3 *Results and discussion.*

Liquid Hg

The experiments on liquid Hg at several temperatures [54], without correcting for CW, yielded a $R_m(q_z)/R_F(q_z)$ with a layering peak at $q_z = 2.2$ Å^{-1} and a minimum at intermediate q between 0.6 and 1.2 Å^{-1} depending on the sample measured. A first attempt to fit the data with the DCM lead to an interlayer spacing of $\lambda = 2.72$ Å, but the fit was not good. Two modifications were proposed. The first one included a quite broad ad-layer of very small density (0.1 to $0.3\rho_0$) located a few Å into the vapour region. The second one corresponded to an interface layer broadened and a little depleted and with an expanded distance to the next layer. This second model was more in line with the one used in the first measurements [43], for which the first interlayer distance was $\lambda_1 = 3.05 \pm 0.15$ Å, and the rest were $\lambda = 2.76 \pm 0.20$ Å. The surface roughness was estimated as $\sigma \approx 1.0$ Å.

Our simulations [306] led to an average profile, shown in fig. 9.1, with $\lambda_1 \approx 2.95$ and $\lambda \approx 2.75$, in qualitative agreement with experiment. Moreover, the reflectivity, modified through the CWT to be directly comparable to the measured one, showed a peak at a similar q_z as the experiment but did not reproduce the intermediate minimum. The intrinsic electronic profile computed through the CT procedure is also shown in fig. 9.1 and leads to the same λ_1 as the average profile, whereas the inner interlayer distance increases a little to $\lambda \approx 2.84$ Å. The layers are however narrower and higher than in $\rho_{av}(z)$. The layer positions correlate very well with the available pair distribution function of the bulk liquid [310]. It is interesting to note that $\rho_{int}(z)$ cannot be fit by the models used by experimentalists, since the first two layers don't have a gaussian shape, although they can
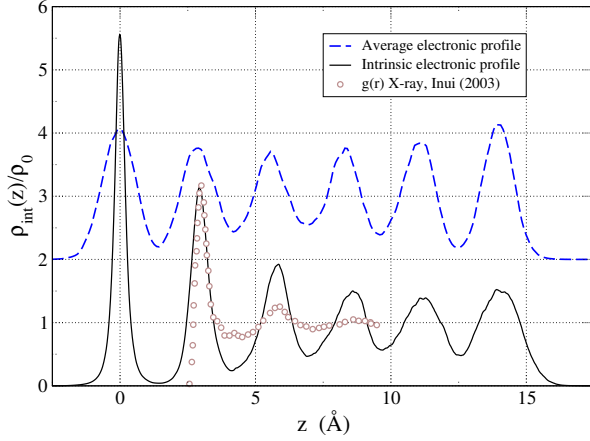
FIGURE 9.1: Intrinsic and average electronic density profiles for Hg at 300 K. Also shown is the experimental pair correlation function of the bulk liquid.
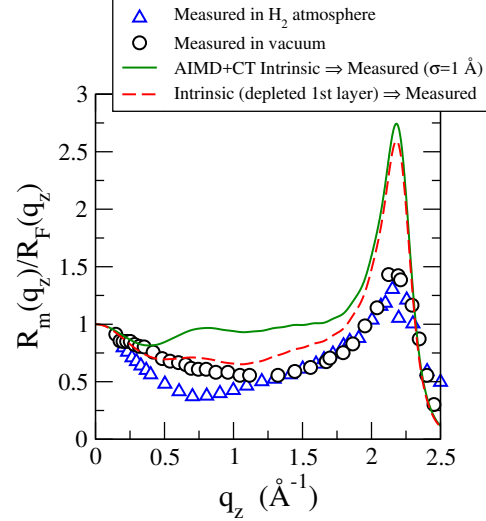
FIGURE 9.2: Reflectivities for Hg at 300 K. Symbols correspond to experimental data using a hydrogen atmosphere or in vacuum. Continuous line: AIMD results obtained from the intrinsic profile. Dashed line: AIMD results obtained by depleating by 10% the height of the first layer in the intrinsic profile.

be reproduced as the sum of two gaussians for each layer. The resulting intrinsic reflectivity has been modified through the same procedure and using the same parameters as in experiment [54] and is shown in fig. 9.2. It keeps the correct peak position, although the height is overestimated, but it still does not produce the dip found in the measurements. Nevertheless, the form of the reflectivity is very sensitive to small details in the profile, and a 10 % reduction of the height of the first layer does produce a correct minimum in the q_z region where it was experimentally observed. Therefore we can conclude that the expanded distance and a small depletion of the fist layer are behind the appearance of the minimum, in line with the second experimental model.

Liquid Pb and Bi

In table 14 one can observe a much higher number of configurations for these two systems than those for Hg. The main reason was the lack of convergence of the average DP as obtained directly from the simulations. We observed that further increase in N_c did not lead to any substantial improvement in the convergence. We performed several tests, using different simulation cells, different pseudopotentials (ultrasoft vs norm-conserving) and/or different computer codes (QE and VASP vs PARSEC), but the lack of convergence persisted in all cases. We consider that such problems in the simulation, not present in Hg, are due to the combination of a high temperature and low surface tension, both favouring large fluctuations in the height of the surface atoms, which are enhanced even more by the small number of them at the surface layer.

No experiments have been performed for the FLS of Pb. On the contrary, Bi (together with Sn) is one of the systems whose measured reflectivity, when transformed into the intrinsic one, shows a shoulder at intermediate q values [48] between 0.6 and 1.4 Å^{-1}. The authors constructed several models that could fit the measured reflectivity, with an adlayer on top of a DCM. The main conclusion was that the adlayer should be denser than the bulk in order to produce the shoulder, but different values of the width, position and density of the adlayer could do the job. The inner interlayer distance, as obtained from the DCM, was $\lambda \approx 2.83 \pm 0.05$ Å.

The intrinsic electronic DP obtained for Bi and Pb are shown in fig. 9.3, along with the corresponding experimental $g(r)$ [192, 311]. The shape of the layers is not DCM-like, requiring several gaussians for a proper fit. The

layer positions in general agree with the maxima of $g(r)$ although some relaxation towards smaller distances is observed in the profile. Moreover, specific features as the shoulder of $g(r)$ in Bi, are reflected also in the shape of $\rho_{int}(z)$. The inner interlayer distance in Bi is found to be ≈ 3.12 Å, somewhat larger than the one experimentally determined through the fit to $R_m(q_z)$. Despite the many non-DCM features of the profile, its form is in line with one of the possible models put forward by Pershan and coworkers, with a very narrow outmost layer, at a slightly contracted distance to the inner layer ($\lambda_1 = 3.02$ Å) and with a slightly enhanced integrated density.

The corresponding intrinsic reflectivities are displayed in fig. 9.4 along with the experimental one for Bi [48]. In Pb we find a monotonous function, akin to those of Ga, In and K. For Bi we find, in agreement with experiments, a shoulder at intermediate q_z, although the magnitude of the reflectivity is rather overshot. To check the experimentalists suggestion that an enhanced first layer is responsible for the shoulder, we decreased the density of this layer, obtaining still a reflectivity with a shoulder. However, including one by one layers from the bulk towards the surface for computing $R_{int}(q_z)$ we find that the shouldered structure appears after the first inner layer is included. Consequently we can conclude that the two first layers are responsible for this kind of behaviour.
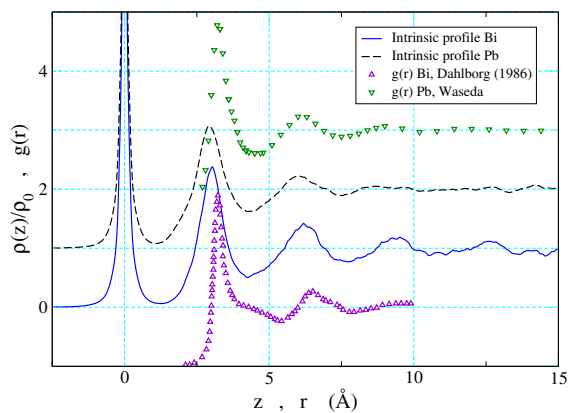
FIGURE 9.3: Intrinsic electronic density profiles for Bi and Pb. Also shown are the experimental pair correlation functions of the bulk liquids. The different functions are shifted vertically for clarity.
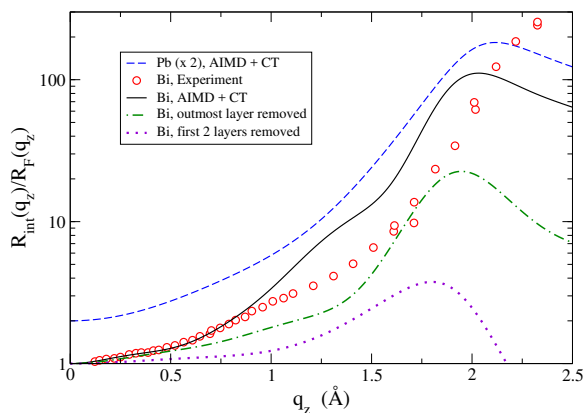
FIGURE 9.4: Reflectivities for liquid Bi and Pb (multiplied by two for clarity).

9.2.4 Conclusions.

The first important point to note is that the CT procedure leads to converged DPs, which is not always the case for the average profile, possibly due to a combination of high temperature and low surface tension.

The combination of AIMD simulations and the CT procedure leads to reflectivities which, either directly or with small modifications, agree qualitatively with experiments.

The profiles obtained are not in general well described by the DCM or variations thereof, but the general characteristics of the intrinsic profiles are similar to the models proposed by the experimentalists. We observe a high degree of correlation between the bulk $g(r)$ and the characteristics of the intrinsic profile, although with some relaxation in the distances, which become somewhat smaller. The particular behaviour of the reflectivities has been traced back to the depletion of the first layer in the case of Hg, and to a combined effect of the first two layers in the case of Bi.

9.3 COLLECTIVE DYNAMICS IN THE FREE LIQUID SURFACE OF SN.

We report results of an orbital-free ab initio molecular dynamics (OF-AIMD) study of the free liquid surface (FLS) of Sn at 600 K and 1000 K. A key ingredient in the OF-AIMD method is the local pseudopotential describing the ions-valence electrons interaction. We have used a force-matching method to derive a local pseudopotential suitable to account for the variation of the forces from the bulk to the FLS. We obtain very good results for structural properties, such as the reflectivity, including the characteristic shoulder it presents in x-ray experiments. Moreover we have studied ab initio for the first time the evolution in some dynamical properties as we move from the central region, where the system behaves like the bulk liquid, to the FLS, at 600 K.

9.3.1 *Introduction*

Liquid metals reveal a great number of intriguing surface phenomena, such as atomic layering, density fluctuations perpendicular to the surface (capillary waves), or peculiar ordering phenomena in alloys [43, 45, 312]. In particular, the static (time-averaged) aspects of the structure of liquid metals have been the subject of numerous studies and are well documented, both for the bulk and the surface [313]. On the other hand, the influence of these surface phenomena in the dynamics in the near-surface region is largely unknown, in particular, at short length scales.

The collective dynamics of a bulk liquid metal encompasses the existence of longitudinal and transverse waves, where acoustic and shear modes, respectively, are allowed to disperse, like phonons in the solid phase. However, when the slab configuration is considered, another type of waves may appear. One type of collective excitation typical of free liquid surfaces are the capillary waves (Rayleigh waves in solids) [302], in which particles perform a circular movement as a combination of both longitudinal and transverse to the surface oscillations. Another type of waves present in both solid and liquid surfaces is the guided- or Lamb waves corresponding to longitudinal waves suffering multiple reflections in both surfaces of the slab. These type of waves propagate parallel to the surface and form a standing wave in the direction perpendicular to the surface. It is limited by the surface geometry (more specifically, its width), thus the prefix 'guided'.

Experimental techniques like INS and IXS allow the study of the dynamics in bulk liquids at interatomic length scales. These studies have provided important insights concerning the nature of propagating excitations (sound modes), their relation to the local atomic structure, and the influence of relaxation phenomena on the excitation spectrum [63, 314]. However, the high-frequency dynamics of liquid surfaces and interfaces has not been experimentally studied due to the lack of suitable experimental techniques.

The first (and only) MD study of the dynamical properties of a liquid surface was performed by Iarlori and coworkers [315] on a liquid gold metal slab. The study was done with CMD at different temperatures above the melting point. They predicted: 1) a sound velocity 20-30% smaller than in the bulk liquid; 2) the dispersion relation of transverse currents normal to the surface exhibits two distinct curves, one corresponding to capillary waves at small wavevectors and another to Rayleigh-type shear waves at larger wavevectors; 3) at small q, there are also weak high- frequency "optical" modes. The presence of capillary waves at the surface dynamics has also been observed experimentally in recent experiments on liquid In [316], but not the presence of transverse "optical" modes. Optical transverse modes have never been observed in monatomic liquid metals and therefore Iarlori and coworker's conclusion seems unlikely.

From the point of view of AIMD simulations, the study of the collective dynamics of FLS has never been performed. The reason for this is the high computation demand imposed to run this type of calculation because of the high number of particles needed: due to the oscillating nature of the DP in liquid metals, the correct analysis of the collective dynamics cannot be performed by selecting the entire slab, but independent calculations in each layer or in small regions in the slab are required in order to observe special features due to the interface. By using OF-AIMD, we have been able to simulate a big sample (2000 particles) for tenths of picoseconds making it possible to study the collective dynamics of the systems at different depths.

The present *ab initio* study on the dynamical properties of the FLS of Sn the same behavior on the dispersion curves of both longitudinal and transverse currents is observed. Capillary waves appear as well as a high frequency contribution at small q vectors in the dispersion relation of the transverse current correlation functions perpendicular to the surface. We propose a different origin for this last interesting feature.

9.3.2 *Computational details*

We have performed an OF-AIMD study where the exchange-correlation energy, $E_{xc}[n]$, has been described by the LDA, as parametrized by Perdew and Zunger [89]. To represent the kinetic energy of the non-interacting electrons, $T_s[n]$, we have used the average density model [119–122].

The ion-electron interaction is described by means of a local pseudopotential. The construction of the local pseudopotential for our system has two steps. We start from an initial local pseudopotential proposed for Sn by Bhuiyan *et al* [317] which, in combination with the OF-AIMD method, has provided a good description of the static properties of liquid Sn at thermodynamic conditions near its triple point. However, the method used to construct the pseudopotential is not completely optimal, since it only tries to represent the static behavior but not the dynamical one, where the interaction between the different particles is taken into account at different time and length scales. A more realistic method should explicitly account for the presence of atoms around the central one and their effect on the force it feels. For this purpose, we have used the FM method [153] to obtain a more accurate LPS. Using as benchmark the results of a KS-AIMD calculation for l-Sn [305], in figure 9.6 we have plotted the differences in the x and z components of the forces felt by the atoms as obtained in the OF and in the KS calculations at a particular liquid configuration before and after the FM process. In figure 9.5 we have plotted the local pseudopotential before and after the force-matching process. We can observe how, in order to better represent the interactions, the pseudopotential has to adopt a higher value in reciprocal space near $q = 0$. We can observe how with the initial local pseudopotential we can recover reasonably well the forces in the bulk region, but not at the surface (particles are sorted according to their z coordinate). However, after the force matching process, these forces are recovered and the ones in the bulk are improved.
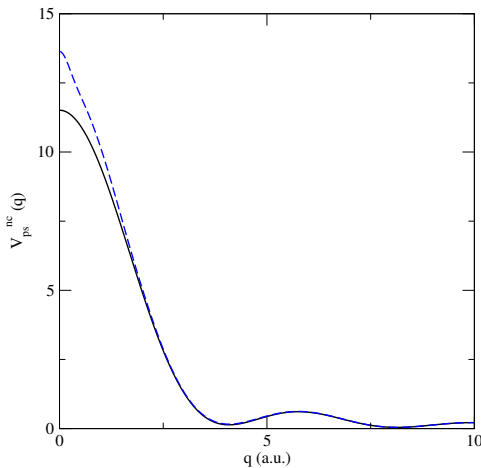
FIGURE 9.5: Non coulombic part of the local pseudopotential before (full curve) and after (dashed curve) force-matching.
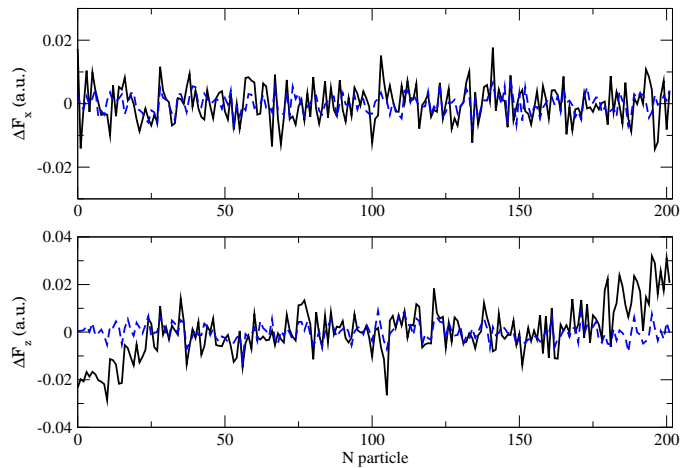
FIGURE 9.6: Difference between the x and z components of the forces as computed with KS-AIMD simulations [305] and OF-AIMD calculations, before (solid line) and after (dashed line) force-matching.

We have performed OF-AIMD simulations for the free liquid surface of Sn at two thermodynamic conditions: 1000 K and 600 K. For each system we have considered a slab containing 2000 atoms in a supercell with two free surfaces normal to the z axis. The dimensions of the slab were $L_0 \cdot L_0 \cdot L_z(L_z = \alpha L_0)$, with L_0 and α chosen so that the average number density of the slab coincides with the experimental bulk ionic number density of

TABLE 15: Calculation details for each of the thermodynamic states studied.

Temperature (K)	ρ (Å^{-3})	L_0 (Å)	α
600	0.0350	33.80	1.95
1000	0.0341	34.25	1.93

the system at the same temperature: additional details about the thermodynamic states are given in Table 15 along with several simulation parameters. A further 8 Å of vacuum were added both above and below the slab. Therefore we are dealing with liquid slabs which are wide enough to rule out interference effects between the two free surfaces and with supercells which are large enough to discard slab-slab interactions. Although the periodic boundary conditions require that a particle moving out of the cell in the z direction reappears on the other side of the slab, we did not observe such an event during the present simulations. Given the ionic positions at time t, the electron density was expanded in plane waves and the energy functional was minimized with respect to the plane wave coefficients yielding the ground state electronic density, energy, and the forces on the ions, and therefrom the ionic positions and velocities were updated according to Newton equations, i.e., the simulations are performed in the NVE ensemble. For both systems equilibration runs were previously performed for 1000 configurations. Therefrom, the N_{Conf} ensuring configurations were those used in the evaluation of the slab's physical properties. During the simulations each slab contracted or expanded and the average ionic density varied in response to the condition of zero external pressure so that the ionic density in the central region of the slab changed by an amount of $\approx -2.9\%$ at 600 K and $\approx -2.6\%$ at 1000 K.

9.3.3 *Results and discussion.*

Static properties and reflectivity.

The transverse pair correlation function, $g_T(r)$, has been calculated for the first (or outmost) and second layers of the slab and compared to the bulk pair correlation function evaluated inside a 15 Å wide central section of the slab. The result is depicted in Fig.9.7 at both temperatures, showing very good agreement with its experimental counterparts [269] at T = 573K and T = 1073K. At both temperatures we observe an important increase of the height of the main peak of $g_T(r)$ of the first layer in comparison with the bulk value. Moreover, there is a displacement of the position of the main peak in the first layer to smaller values, meaning a smaller first neighbour distance. All these results indicate an increase of the density in the outer layer of the slab, as suggested previously [47, 305].

The $g_T(r)$ for the second slab presents the same position of the main peak as the bulk $g_T(r)$. However, at T = 600 K the height of the main peak of $g_T(r)$ of the second slab is still higher than the bulk counterpart, not so at T = 1000 K, where both $g_T(r)$ present the same shape. This evidence suggest that at lower temperatures, the density increase does not only affect the first layer but it goes deeper into the slab to even the second layer, although to a lesser degree.

Next, we have proceeded to analyze the in-plane order within the slices, especially the outer slice for which different works have uncovered the predominance of five- and sixfold coordination. For example, MD simulations of supercooled Au surfaces [318] have found in the outer slice a preference of sixfold coordinated sites. Moreover, experimental [319] and AIMD [320] studies of l-Pb in contact with a solid Si wall have shown the existence of fivefold symmetry for the Pb atoms. Also, AIMD simulations of the free surface of l-Na [321] and l-Sn [305] have shown the predominance at the outer slice of fivefold coordinated atoms. Therefore, we have carried out a similar study of l-Sn at both temperatures, and the obtained results are plotted as an inset in Fig. 9.7. The so-called bulk values have been obtained by using a slice with the same width as the outermost one but located at the center
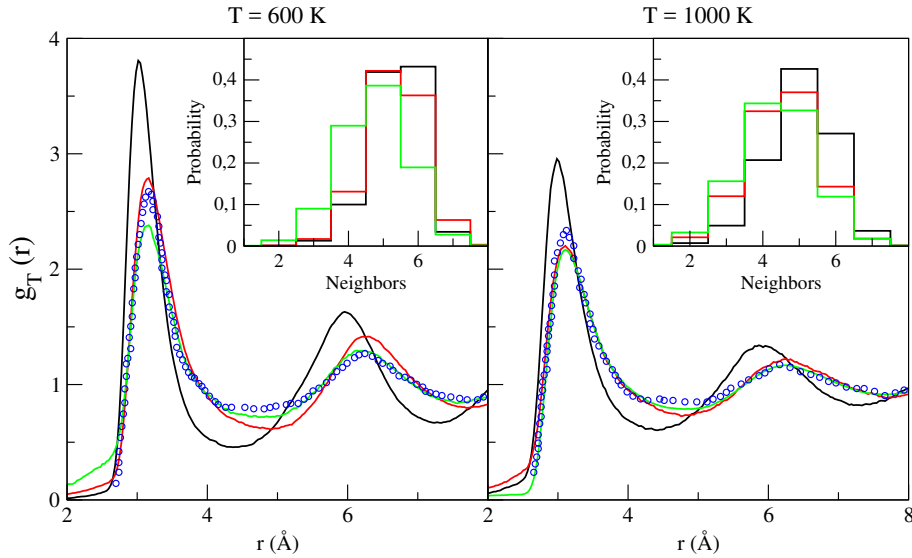
FIGURE 9.7: Transverse pair correlation function for different layers at the free liquid surface of l-Sn at T= 600 K and T= 1000 K. Open circles: bulk experimental data of Itami *et al.* [269]. Black line: $g_T(r)$ calculated at the outmost layer. Red line: $g_T(r)$ calculated at the second layer. Green line: $g_T(r)$ calculated at the central layer. Insets: distribution of the number of in-plane neighbours for different regions of the slab.

of the slab. The results show that in the outer slice, more than 40% of the atoms have sixfold coordination and another 30% − 40% present fivefold coordination. Notice that when going inside the slab, there is an important reduction in the fractions of five- and sixfold coordinations along with a substantial increase in the fractions of three- and fourfold coordinations, especially at T = 1000 K.

The average ionic DP was computed from a histogram of the particle positions relative to the slab's center of mass, so that both halves of the slab are being averaged. The obtained results are shown in figure 9.8, where we observe stratification for at least four layers into the bulk liquid. The spacing between the outermost layer and the first inner one is $\lambda_{out} = 2.83$ Å, whereas the inner interlayer distances are somewhat larger, namely, $\lambda_{in} = 2.97$ Å at 1000 K. It should be noted that the average DP obtained through the KS-AIMD [305] led to equal interlayer distances of 3.1 Å, which highlights the dependence of the average DP on the conditions of the simulation, in particular the lateral size of the box. At the lower temperature of 600 K the interlayer distances obtained are essentially all equal, with $\lambda_{out} \approx \lambda_{in} = 2.86$ Å.

In order to compute the reflectivity and compare with the experimental reported results, capillary waves have to be substracted from the system. The most convenient method is to obtain the intrinsic density profile through the calculation of the separation surface between the liquid and vapor phases, which is smoothed afterwards, following the procedure of Chacon and Tarazona. In figure 9.8 we show the intrinsic DP along with the average DP for the two temperatures studied. The layered structure of the interface is more marked in the intrinsic profiles. Moreover, the obtained interlayer distances are modified from those in the average DP. The outermost interlayer distance is $\lambda_{out} = 2.96$ Å, with the inner interlayer distances being $\lambda_{in} = 3.02$ Å at 1000 K. At the lower temperature of 600 K the difference between the outermost and inner interlayer distances is more emphasized, with $\lambda_{out} = 2.83$ Å and $\lambda_{in} = 3.01$ Å. It is important to note that, despite the differences between the average DPs obtained in this work and the one obtained in the KS-AIMD study, the corresponding intrinsic DPs practically coincide (see figure 9.8).

The x-ray reflectivity, which is the property amenable to experimental observation, is related to the electronic DP. We have calculated the intrinsic electron DP, as obtained from a superposition of atomic electron densities
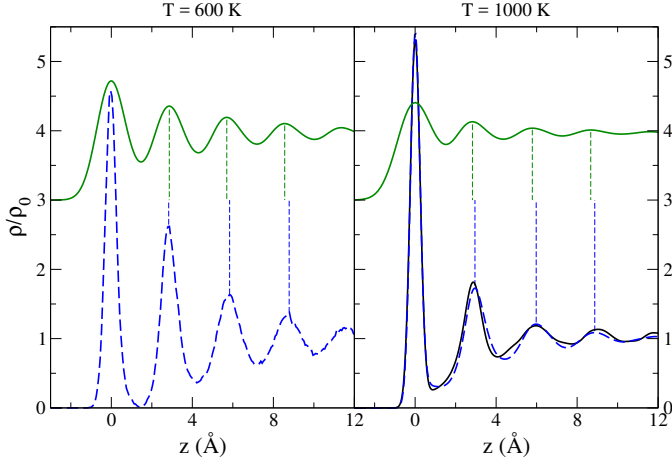
FIGURE 9.8: Average ionic DP (full curve, shifted upwards by 2.5 units) and intrinsic ionic DP (dashed curve) at T=600 K and 1000 K. At 1000 K the lower full curve corresponds to the intrinsic ionic DP obtained using the simulation data from [305].
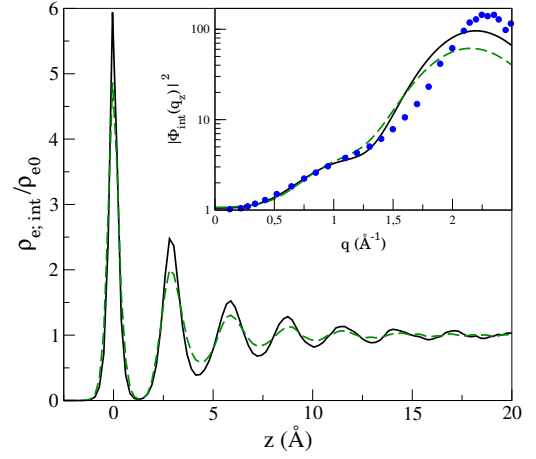
FIGURE 9.9: Comparison of the intrinsic electronic density profiles and reflectivities at 600 K (full line) and 1000 K (dashed line) with the experimental reflectivity (dots) [47].

centered at each ionic position, using the smoothed separation surface. The intrinsic reflectivity is calculated as $R_{int}(q_z) = |\Phi_{int}(q_z)|^2$, where

$$\Phi_{int}(q_z) = \frac{1}{\rho_{e0}} \int_0^\infty dz \exp[-iq_z z] \frac{d\rho_{e;int}(z)}{dz} \tag{173}$$

where ρ_{e0} is the average bulk electron density. The results obtained are shown in figure 9.9, where we see a characteristic peak located around $q_z \simeq 2.2$ Å^{-1}, which is close to $2\pi/\lambda_{in,600K} \simeq 2.1$ Å^{-1}, and is related to the layering of the DP. Morever, at around $q_z \simeq 0.8$ Å^{-1} we obtain a shoulder, more emphasized at 600 K than at 1000 K, which also appears in the experimental measurements perfomed by Shpyrko *et al* [47] at melting. The experimentalists ascribed the origin of the shoulder to an increased density in the outermost layer related to its smaller interlayer distance. However this interpretation may be biased by the model that was used and a deeper analysis would be of value and will be performed in the future.

Collective dynamics

In order to study the collective dynamic properties at different depths in the slab at $T = 600$ K, we had to restrict the particles to be used in each case. The contribution of each particle to a dynamic variable (particle density, particle current, particle number) is weighted by a function that is one inside the region of interest and falls down smoothly to zero outside. Explicitly, we have used,

$$\text{weight}(z) = \begin{cases} 0 & \text{if} \quad z < z_{min} - z_w \\ 0.5 + 0.5\cos\left(\frac{z-z_{min}}{z_w}\pi\right) & \text{if} \quad z_{min} - z_w < z < z_{min} \\ 1 & \text{if} \quad z_{min} < z <_{max} \\ 0.5 + 0.5\cos\left(\frac{z-z_{max}}{z_w}\pi\right) & \text{if} \quad z_{max} < z < z_{max} + z_w \\ 0 & \text{if} \quad z > z_{max+z_w} \end{cases} \tag{174}$$

where z_{min} is the left end of the layer (taken as the position of left minimum of the layer in the DP), z_w is the width of the layer, and z_{max} is the right end of the layer (taken as the right minimum of the layer in the

DP). The number of particles that intervene in each collective dynamic calculation for one layer is around ~ 120, guaranteeing good statistics.

The symmetry of the system defines a special direction, the z-axis, around which the properties must show cylindrical symmetry. We are particularly interested in waves that propagate parallel to the interface, and therefore among the $\vec{q}$ vectors allowed by the periodic boundary conditions, only those that are perpendicular to the z-axis have been used, i.e. with $q_z = 0$. In the averages involved in the correlation function we consider all vector orientations that fulfill this condition.

Figure 9.10 displays the $S(q, \omega)$ at different depths in the slab. All of them show side-peaks, indicative of collective density excitations, up to $q \approx 1.4 \text{ Å}^{-1}$. Moreover, as one approaches the interphase region coming from the bulk, the frequency of the side peaks increases, while the corresponding widths also increase, making the peaks less marked. This increase in frequency suggests a higher adiabatic sound velocity in outer layers than in the bulk region, probably due to an increase in the density. Also, at small q vectors, the height and width of the central peak increases in the interface region, indicating a higher thermal diffusivity at the interface.
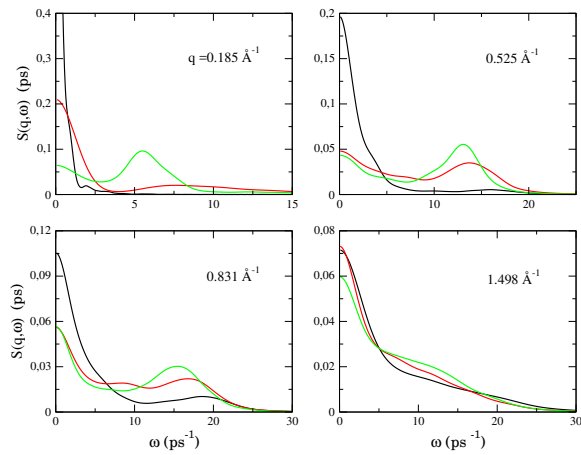
FIGURE 9.10: $S(q, \omega)$ at different q values and depths: bulk region (green curve), second layer (red curve) and first layer (black curve).
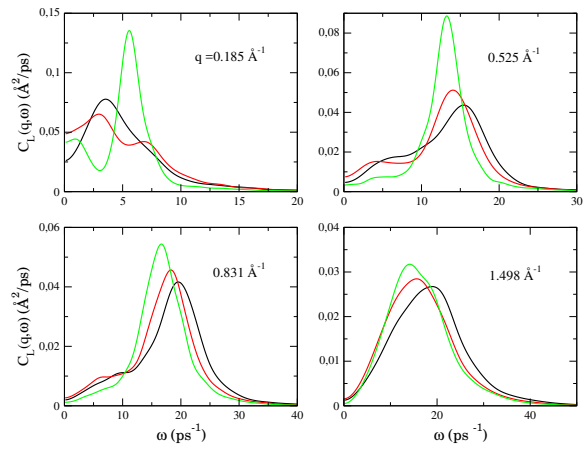
FIGURE 9.11: $C_L(q, \omega)$ at different q values and depths. Same legend as Fig. 9.10

To gain insight into the longitudinal dynamics in the slab, we have plotted in Fig. 9.11 the calculated $C_L(q, \omega)$ at different depths in the slab. The most outstanding feature at small q values is the appearance of a second low-frequency peak, which is more predominant as we approach the interface. At the lowest attainable q vector in the simulation and at the outmost layer, the low frequency peak covers the peak related to the dispersion of pressure waves and only one peak appears, at intermediate frequencies. Moreover, the position of the high frequency peaks related to the dispersion of pressure waves is displaced to higher frequencies as we approach the interface, as in $S(q, \omega)$.

We were also interested in the transverse current correlation functions. Due to the symmetry of the system, we differentiated between those perpendicular to the interface (in the z-axis), $C_{T_z}(q, t)$, and those in the x-y plane perpendicular to the q-vector, $C_{T_p}(q, t)$. Fig. 9.12 shows the FT of $C_{T_p}(q, t)$ at different depths. At the smallest attainable q vector in the simulation, there is no side peak indicative of collective shear wave propagation, regardless of the depth studied. Once the wavevector is increased, side peak appear. In all cases we observe the already mentioned behavior of a small displacement towards high frequencies as we approach the interface. Already, at $q = 1.498 \text{ Å}^{-1}$ we start to observe the two mode shape in transverse collective dynamics previously observed in bulk l-Sn in Chapter 7. However, no special effect due to the interface is observed in the case of $C_{T_p}(q, \omega)$.
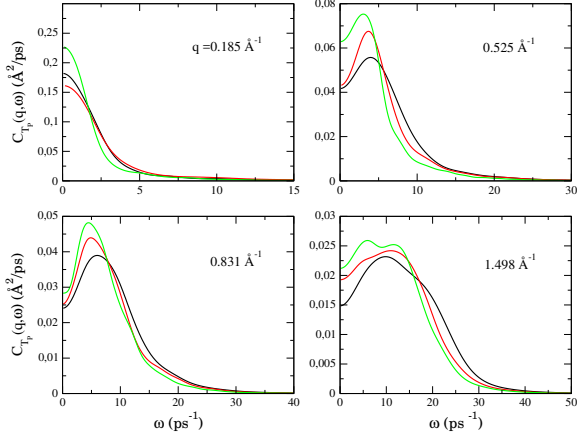
FIGURE 9.12: FT transverse in XY plane current correlation functions at different q values and depths. Same legend as Fig. 9.10
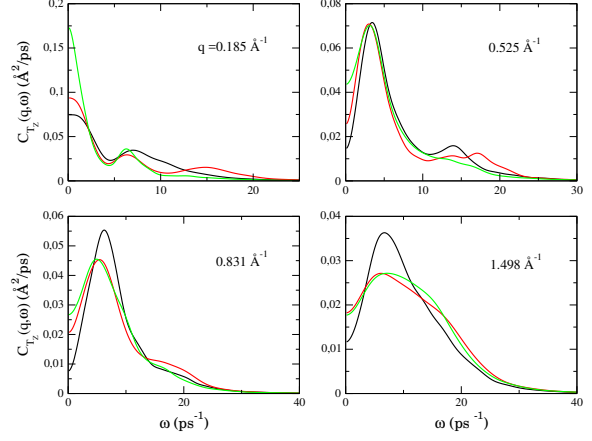
FIGURE 9.13: FT transverse perpendicular to the surface current correlation functions at different q values and depths. Same legend as Fig. 9.10

Figure 9.13 presents the FT of $C_{T_z}(q,t)$. The most striking feature is that already at the smallest attainable q-vector, there appears side peaks, at all depths, in contrast to what happened in the FT transverse current correlations functions in the x-y plane. Therefore, these peaks cannot be associated with the propagation of collective shear waves. At higher q-vectors, where the main side peak corresponds to shear waves, there is still the presence of these high frequency peaks until q-values of ~ 1.498 Å^{-1}, where the two mode peak of bulk l-Sn appears. Iarlori *et al.* hypothesis [315] relates these high frequency peak at low q to internal vibrations of the very dense double layer characteristic of their model. However, is not clear whether these type of 'optical' modes represent genuine observable features for real liquid surface.

To understand the origin of the low frequency peaks in Fig.9.11 and of the high frequency peaks in Fiq. 9.13, we have performed a fit of the corresponding functions to a model. With this fit, we will be able to obtain the different dispersion relations of each mode, even in the cases when they appear as side shoulders in the FT of the functions.

The fitting model used corresponds, in the case of $F(q,t)$ to an elastic mode characterized by an exponential decay and one or two DHOs for the inelastic modes,

$$
\begin{aligned}
F(q,t) = A\exp(-\alpha t) + B\exp(-\beta t)\left(\cos(\omega_1 t) + \frac{\beta}{\omega_1}\sin(\omega_1 t)\right) + \\
+ C\exp(-\gamma t)\left(\cos(\omega_2) + \frac{\gamma}{\omega_2}\sin(\omega_2 t)\right)
\end{aligned}
\tag{175}
$$

For $C_L(q,t)$ we used as a model the second derivative with respect to time of Eq. 175, due to the relation $C_L(q,t) = -\frac{1}{q^2}\frac{\partial^2 F(q,t)}{\partial t^2}$. For $C_{T_p}(q,t)$ and $C_{T_z}(q,t)$ we used a model composed of two or three DHOs.

The inset of Fig. 9.14 shows the dispersion relation obtained with the fit of $F(q,t)$ for the main mode. It can be seen that it follows very closely the results obtained directly from the FT of $F(q,t)$. One advantage in performing the fit is that we can expand the dispersion relation of the first layer to lower q values, which allows a more precise calculation of the adiabatic sound velocity, c_s. Fig. 9.14 depicts the calculated q-dependent adiabatic sound velocity, $c_s(q)$, at different scattering depths along with Hosokawa and coworkers' experimental results at 593 K [322], obtained by fitting the inelastic component of their measured $S(q,\omega)$ to the same damped harmonic oscillator model as we have used. We obtain very good comparison with the experimental data. Moreover, we observe a significant discrepancy with the available experimental value for the adiabatic sound velocity of

$c_s = 2448$ m/s [324]. The reason for this could be related to a significant *positive dispersion*, i.e., an increase with respect to the hydrodynamic adiabatic speed of sound. Independent of the reason for this behavior, we observe that at the first layer the effect is considerably increased, resulting in a higher adiabatic sound velocity and/or positive dispersion.
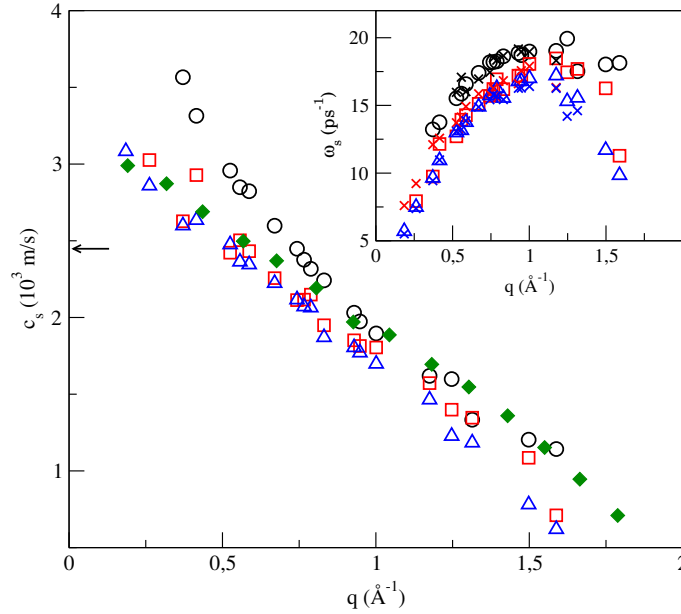
FIGURE 9.14: q-dependent adiabatic sound velocity, $c_s(q)$, in l-Sn at 600 K. Black circles: First layer. Red squares: Second layer. Blue triangles: Bulk region. Filled green diamonds: IXS data for bulk l-Sn at 593 K by Hosokawa *et al.* [322]. Inset: Dispersion relation of the intermediate scattering function. Open symbols: Results from the fit to the model 175. X: OF-AIMD results from the direct FT. The horizontal arrow at $q = 0$ stands at the experimental adiabatic sound velocity [324]

Fig. 9.15 displays the $C_L(q, \omega)$ dispersion relation. We can observe two different dispersive modes at all the depths studied, represented by the open and full symbols. The discontinuous line represents the theoretical dispersion relation of the capillary waves in the system, which is given by [323],

$$\omega_{CW} \cong \sqrt{\frac{\gamma}{\rho}} q^{3/2} \tag{176}$$

with γ the experimental surface tension of 560 mN/m [47] and ρ the number density. The low frequency mode in the dispersion relation from the second layer clearly follows the dispersion relation of the capillary waves. However, the dispersion relation of the first layer appears displaced to slightly higher frequencies. One possibility for this behavior could be because of the high contribution of the thermal diffusion component that, while in the $S(q, \omega)$ appears as a peak centered at $\omega = 0$, in $C_L(q, \omega)$ has a small contribution at frequencies $\neq 0$. Given the predominance of the thermal diffusion component in the first layer, the final dispersion relation of the low frequency dispersion relation of the capillary waves may be affected.

Regarding the dispersion relation in the bulk region, the low frequency mode corresponds to the same low frequency mode that appears in bulk l-Sn studied in Chapter 7. In Fig. 9.16 we have plotted the dispersion relation of $C_L(q, \omega)$ in the bulk region of the slab obtained from the fit along with the dispersion relation from the fit of bulk l-Sn studied in Chapter 7. Both sets of results are displaced in frequency one from the other but in both cases it can be seen that the behavior of the high and low energy modes is the same. The reason for the displacement in energy could be related to the difference in number density, LPS and KEDF used.
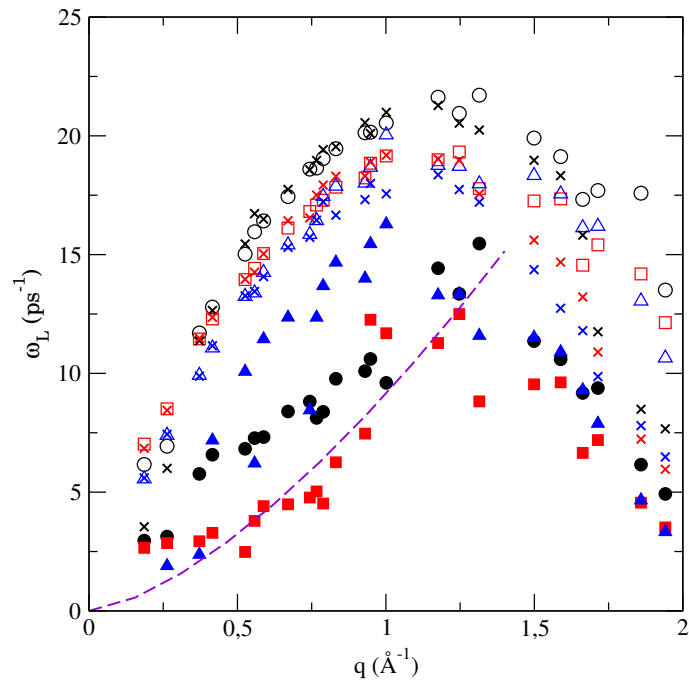
FIGURE 9.15: Dispersion relation of $C_L(q, \omega)$ at different scattering depths. Open and full symbols: High and low energy modes respectively. Black circles: First layer. Red squares: Second layer. Blue triangles: Bulk region. Dashed line: theoretical dispersion relation of the capillary waves in the system [323].
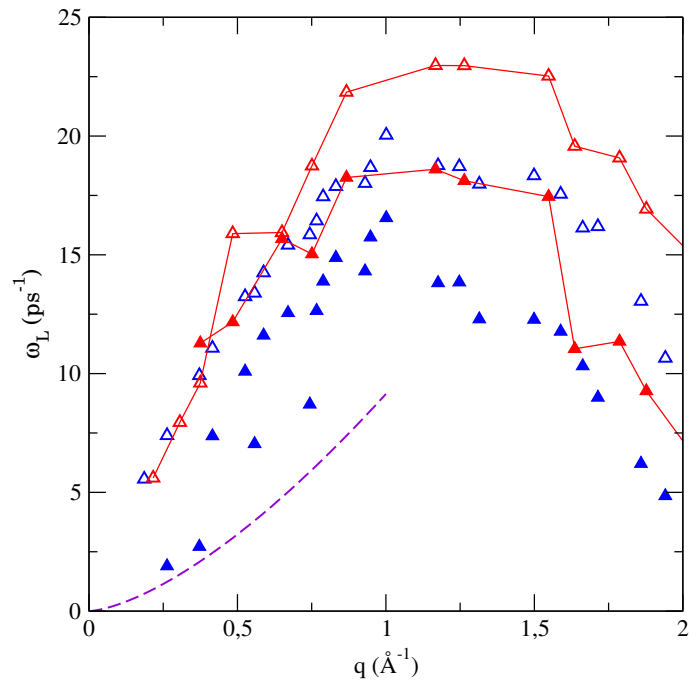
FIGURE 9.16: Comparison of dispersion relations for $C_L(q, \omega)$ in the bulk region of the slab (blue triangles) and in bulk l-Sn from Chapter 7 (red triangles).
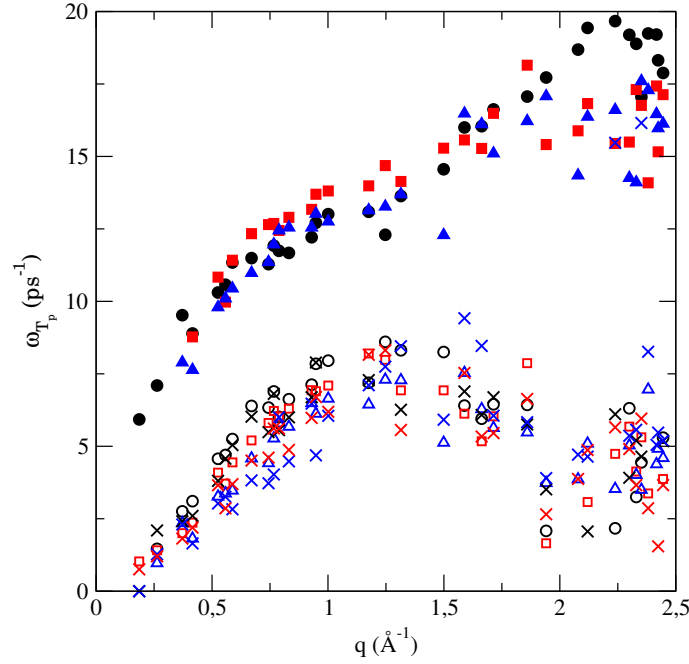
FIGURE 9.17: Dispersion relations for $C_{T_p}(q, \omega)$ at different depths. Open and full symbols: low energy and high energy modes, respectively. Black circles: First layer. Red squares: Second layer. Blue triangles: Bulk region. X: OF-AIMD results from the direct FT.

The dispersion relations for $C_{T_p}(q, \omega)$ at the different depths studied are depicted in Fig. 9.17. All the dispersion relations from both modes follow the same behavior as already studied in bulk l-Sn in Chapter 7. The low frequency mode is only related to shear wave dispersion since there is no capillary waves' contribution in this case. Fig. 9.19 compares the dispersion relation of $C_{T_p}(q, \omega)$ along with the dispersion relation of $C_T(q, \omega)$ of bulk l-Sn obtained in Chapter 7. From this figure, it is clear that both contributions in the slab correspond to the two contributions present in the bulk liquid.

Fig. 9.18 depicts the dispersion relation of $C_{T_z}(q, \omega)$. At high q-values, their behavior is the same as the dispersion relation of $C_{T_p}(q, \omega)$, with two modes corresponding to the two modes present in the liquid bulk, as can be observed in Fig. 9.20.

However, at small q-values there appear high frequency contributions, as those previously observed by Iarlori *et al.* [315] in their CMD study of the liquid surface of Au, which do not have an analogue in the bulk liquid. Our reasoning for their appearance is based on the combination of longitudinal currents not parallel to the XY plane, as obtained from multiple reflections in the two parallel interfaces that limit the slab (see Fig. 9.21). If a longitudinal current of q vector $\vec{q}_2$, not in the XY plane, combines with another longitudinal current with same q module (therefore same frequency ω_L) and angle with respect to the horizontal, such that $|\vec{q}_1| = |\vec{q}_2|$, the result is a wave that propagates parallel to the XY plane with module q_{xy} and, if an appropriate angle is taken, a stationary wave perpendicular to the surface. The superposition of these two waves induces atomic vibrations with a component perpendicular to the surface, and therefore contribute to $C_T(q, t)$. This type of waves in which the particles vibrate perpendicular to the surface and propagate parallel to the surface are called Lamb (or guided) waves in solids. The module of both initial longitudinal currents can be written in terms of q_{xy} and q_z, and the particles oscillation frequency takes the form,

$$\omega_L \left(\sqrt{\left(\frac{q_{xy}}{2}\right)^2 + q_z^2} \right) = \omega_L \left(\sqrt{\left(\frac{q_{xy}}{2}\right)^2 + \left(\frac{n\pi}{d}\right)^2} \right) \tag{177}$$

with d the width of the slab and $n = 1, 2, \ldots$ the number of half wavelengths of the standing wave inside the slab. By increasing n we obtain different dispersion relations which span a limited region at small q values that englobe all the high frequency contributions we obtain at small q vectors.
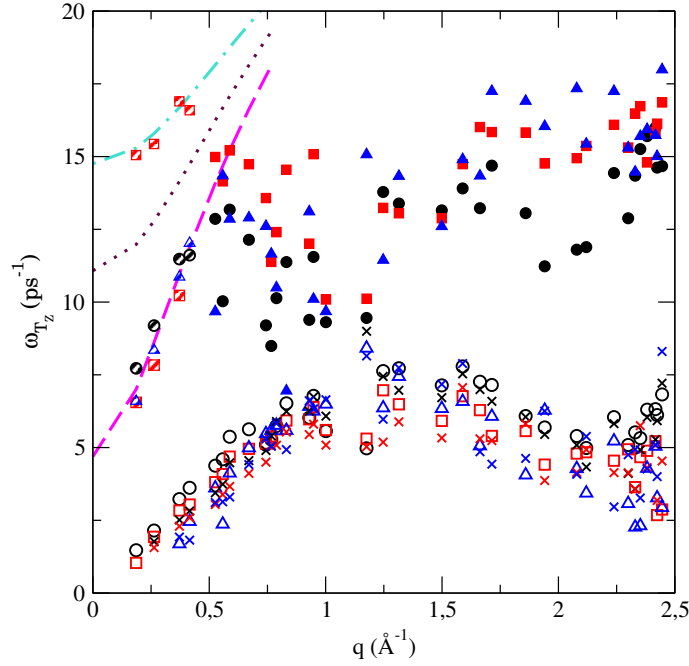
FIGURE 9.18: Dispersion relations for $C_{T_z}(q, \omega)$ at different depths. Open, dashed and full symbols: low energy, Lamb wave modes and high energy modes, respectively. Black circles: First layer. Red squares: Second layer. Blue triangles: Bulk region. X: OF-AIMD results from the direct FT. Dashed, dotted and dashed-dotted lines: Lamb waves dispersion relation corresponding to n=4, 5 and 6, respectively.

Capillary waves should also be present in $C_{T_z}(q, t)$. However, in the dispersion relation of $C_{T_z}(q, \omega)$, there is no distinct low frequency branch that can be related to their dispersion relation. In Fig. 9.20 we have plotted the dispersion relation for $C_{T_z}(q, \omega)$ in the second layer (region where capillary waves are clearly observed in $C_L(q, \omega)$) along with the dispersion relation of $C_T(q, \omega)$ of bulk l-Sn from Chapter 7. Moreover, we have included the dispersion relation of capillary waves which closely follows the dispersion of shear waves, making it impossible to distinguish one from the other.

9.3.4 Conclusions

Using OF-AIMD and the FM method to obtain an accurate LPS we have been able to study *ab initio* for the first time the collective dynamics in a FLS of Sn from the central region, where the system behaves like the bulk to the outmost layer. We have studied some structural properties of the liquid slab at 600 K and 1000 K. The calculated reflectivity in both cases presented a small shoulder, more marked at 600 K, and in very good comparison with the available experimental data.

The most outstanding result is the appearance of capillary waves which can clearly be observed as a low energy contribution at small wavevectors to the dispersion relation of $C_L(q, \omega)$. Their appearance in the dispersion relation of $C_{T_z}(q, \omega)$ is difficult to distinguish since the main dispersive mode due to shear waves has a contribution at the same energy. Moreover, in the dispersion relation of $C_{T_z}(q, \omega)$ we have been able to identify the high energy contribution at small wavevectors as originated from a combination of $C_L(q, t)$ not in the XY plane,
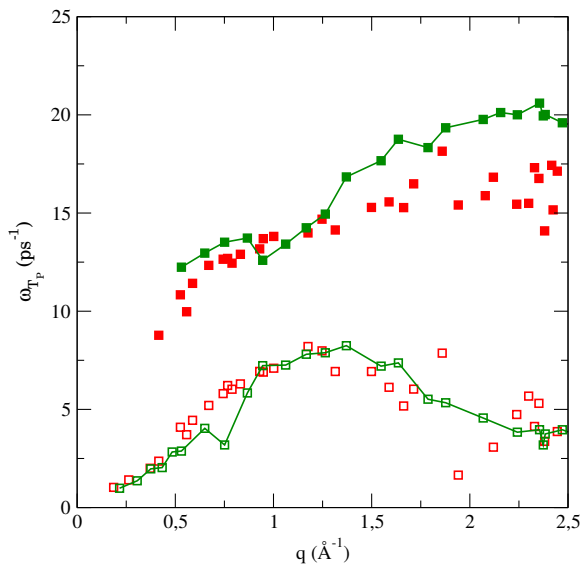
FIGURE 9.19: Comparison of dispersion relations for $C_{T_p}(q, \omega)$ in the second layer (red squares) and the $C_T(q, \omega)$ in bulk l-Sn from Chapter 7 (green squares).
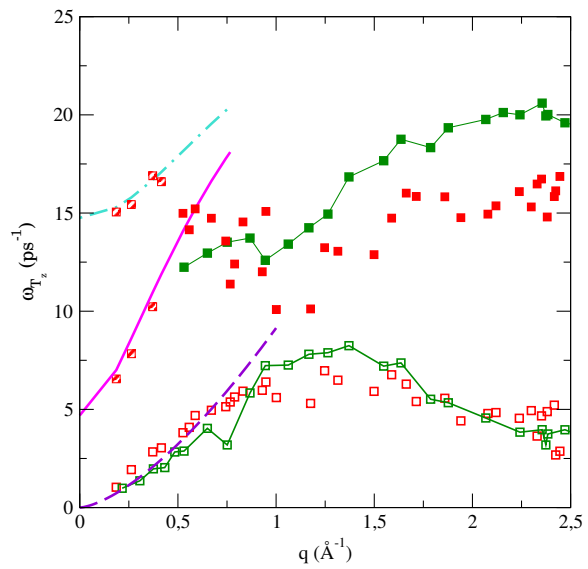
FIGURE 9.20: Comparison of dispersion relations for $C_{T_z}(q, \omega)$ in the second layer (red squares) and the $C_T(q, \omega)$ in bulk l-Sn from Chapter 7 (green squares). Discontinuous line: dispersion relation of capillary waves. Continuous and dash-dotted lines: Lamb waves dispersion relation corresponding to n=4 and n=6, respectively.
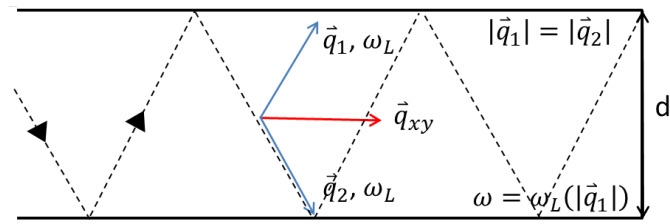
FIGURE 9.21: Scheme representing the combination of two $C_L(q, t)$ not in the XY plane giving rise to a wave propagating in the XY plane and oscillating perpendicular to the surface.

similar to Lamb waves. In addition, we have studied the evolution of the q-dependent adiabatic sound velocity at different depths in the slab. The behavior at the outmost layer indicates an increase in the value of the adiabatic sound velocity as well as in the positive dispersion, present at all the depths sampled.

9.4 COLLECTIVE DYNAMIC PROPERTIES IN LIQUID INDIUM SLAB.

We report results of an OF-AIMD study of the free liquid surface (FLS) of In at T=550 K. A key ingredient in the OF-AIMD method is the local pseudopotential describing the ion-valence electrons interaction. We have used the previously developed force-matching method to derive a local ionic pseudopotential suitable to account for a rapidly varying density system, such as a free liquid surface. We obtain good results for structural properties, such as the reflectivity. Moreover, we have also studied the evolution in some dynamical properties when going from the central region, where the system behaves like the bulk liquid, to the FLS and they are compared to the available experimental data.

9.4.1 *Introduction.*

Despite centuries of research, the study of the liquid state continues to provide us with new insights. In particular, surprising phenomena occur at the surface of liquids metals, i.e. layering at liquid metal surfaces or thermally excited height fluctuations (capillary waves). Understanding the surface phenomena of liquid metals is of fundamental scientific interest, and there are also technical applications [21].

However, the study of the microscopic dynamics at the liquid metal surface (which would involve inelastic scattering experiments) is a largely unexplored research field. Up to our knowledge there is only one recent experimental work that, using IXS in grazing angle geometry, has allowed the investigation of the microscopic dynamics at the liquid surface of In [316]. Moreover, by varying the incident angle around the critical angle of total reflection, they have been able to selectively study the bulk and surface dynamics from a probing depth of 4 nm to 180 nm. They reported the influence of capillary waves in the spectra as an additional contribution with a Lorentzian shape, especially for small momentum transfers and the smallest probing depth of 4 nm. They also reported on an increase of the longitudinal viscosity by a factor two in the near surface region but no significant change in the adiabatic sound velocity.

This experimental study, the first of its kind, has prompted us to perform an OF-AIMD study of the FLS of In. We have analyzed the collective dynamics in different regions of the slab and compared them with their experimental data. The results bring up some limitations of the experimental method that restrict the observation of some special features characteristic of the collective dynamics of the FLS.

9.4.2 *Computational details.*

We have performed an OF-AIMD study where the exchange-correlation energy, $E_{xc}[n]$, has been described by the local density approximation, as parametrized by Perdew and Zunger [89]. To represent the kinetic energy of the non-interacting electrons, $T_s[n]$, we have used the average density model [119–122].

The ion-electron interaction is described by means of a local pseudopotential. The construction of the local pseudopotential for our system has two steps. First, we start from an initial local pseudopotential obtained through the NPA method (in sec. 4.2.1) which, in combination with the OF-AIMD method, has provided a good description of the static properties of various liquid metals. To improve the local pseudopotential to better represent the liquid surface we have used the FM method to obtain a more accurate LPS. As benchmark a KS-AIMD calculation for l-In slab of 205 particles lasting 4.28 ps at 450 K was used. The calculation was performed with the Quantum Espresso package. In figure 9.22 we have plotted the local pseudopotential before and after the force-matching process. We can observe how, in order to better represent the interactions, the pseudopotential has to adopt a higher value in reciprocal space near $q = 0$. In figure 9.6 we have plotted the differences in the x and z components of the forces felt by the atoms as obtained in the OF and in the KS calculations at a random

liquid configuration before and after the force matching process. As in the previous study of the FLS of Sn, we can observe how after the force matching process, the surface forces are recovered.
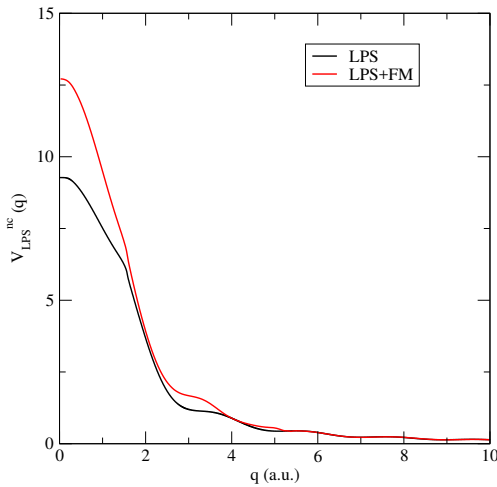
FIGURE 9.22: Non coulombic part of the local pseudopotential before (black curve) and after (red curve) force-matching.
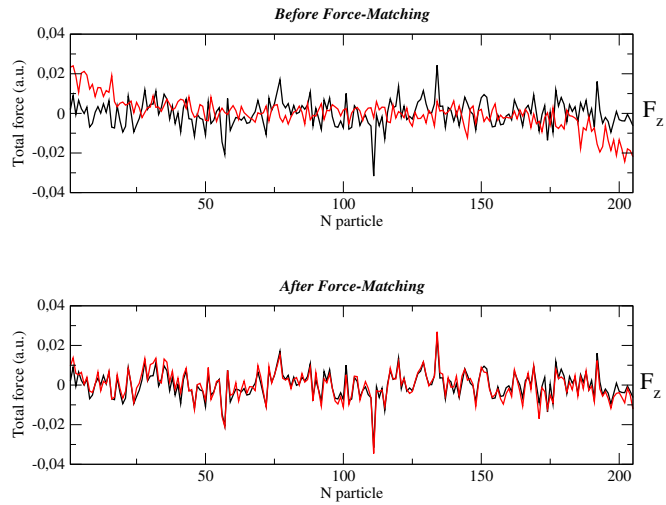
FIGURE 9.23: Comparison of the z components of the forces as computed with KS-AIMD simulations (black curve) and OF-AIMD simulation (red curve), before and after force-matching.

We have performed OF-AIMD simulations for the free liquid surface of In at the thermodynamic state of 550 K, close to the melting point of 429 K. We considered a slab containing 3000 atoms in a supercell with two free surfaces normal to the z axis. The dimensions of the slab were such that we had $L_z = 95$ Å, which would allow us to reach a sampling depth of 47.5 Å and compare our results with those from the experiment at their lowest probing depth. We performed 20000 timesteps of 0.004 ps each. The initial ionic density of the system is $\rho = 0.0369$ Å^{-3}. We included a vacuum of 12.5 Å in the upper and lower limit of the slab along the z-axis. Periodic boundary conditions were applied in the x and y directions.

9.4.3 Results and discussion.

Reflectivity

In this study we have focused our attention to evaluating the dynamic structure factors at different probing depths as well as other collective dynamic properties. Nevertheless, we have evaluated the static structure by calculating its reflectivity. In order to compute the reflectivity and compare with the experimental reported results, capillary waves have to be substracted from the system. As in previous studied cases in this thesis, we have followed the procedure of Chacon and Tarazona where the intrinsic density profile is obtained through the calculation of the separation surface between the liquid and vapor phases. In figure 9.24 we show the IDP. The interlayer distance is $\lambda = 2.68$ Å, in very good agreement with the experimental data of 2.69 Å [316].

The x-ray reflectivity, which is the property amenable to experimental observation, is related to the electronic DP. We have calculated the electronic IDP, as obtained from a superposition of atomic electron densities centered at each ionic position, using the smoothed separation surface. The results obtained are shown in figure's 9.24 inset, where we see a characteristic peak located around $q_z \simeq 2.3$ Å^{-1}, which coincides with the corresponding peak due to the interlayer distance from the IDP, $2\pi/\lambda \simeq 2.34$ Å^{-1}. This very good comparison assures us of the good static representation of l-In with OF-AIMD.
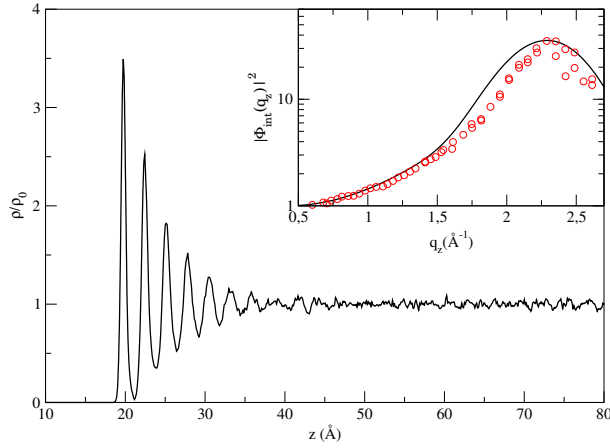
FIGURE 9.24: OF-AIMD calculated IDP. Inset: intrinsic surface structure factor from OF-AIMD (black line) and experimental data [316] (open circles).

Collective dynamic properties.

To select the particles inside each region of interest we have multiplied their contribution to the dynamic variables by weighting them with a window function. To evaluate the evolution of the properties at different depths, or layers in the slab, we applied the weight function previously used in the study of the free liquid surface of Sn, Eq. 174. However, to make a proper comparison with the IXS experimental data we used a weight function with an exponential decay which mimics the exponential decay of the IXS signal inside the sample. The rate of the exponential decay is chosen so as that it has decayed to $1/e$ when reached the probing depth desired, which in our case is 40 Å.

As with the FLS of Sn, due to the symmetry of the system, among the $\vec{q}$ vectors allowed by the periodic boundary conditions, we have chosen only those that are perpendicular to the z-axis. In the averages involved in the correlation function we consider all vector orientations that fulfill this condition.

First, we have evaluated the dynamic structure factors at different q-vectors and depths and compared them to the available experimental data at 40 Å. After the numerical FT of $F(q, t)$, we had to apply the detailed balance condition and afterwards convolute the resulting dynamic structure factors with the experimental resolution function, Eqs. 162 and 163 in Chapter 7.

Fig. 9.25 shows the results. At first glance we observe that the $I(q, \omega)$ obtained by using an exponential decay window compares very well with the direct IXS experimental results, in both height of the central peak and in the position and height of the side peaks. This good comparison confirms the good representation of the liquid's dynamics, which was the goal for performing the FM on the LPS. There is one discrepancy at the highest wavevector sampled between the heights of the main peak. However, as in the case of bulk l-Sn, this discrepancy should not be directly ascribed to poor OF-AIMD representation.

It is also interesting to analyze and compare the results from different layers in the slab obtained with different windows. The results from the first or outmost layer stand out from the rest, especially at the two lowest wavevectors. At $q = 0.429$ Å^{-1} the height and width of the main peak from the first layer surpasses the rest, indicating a much higher thermal diffusion, as with the FLS of Sn. Moreover, it does not present any side peaks. At $q = 0.644$ Å^{-1} the comparison is still the same, although an indication of collective sound waves appear with the presence of small side shoulders at frequencies slightly higher (in absolute value) than the rest.

Regarding the results from the second slab and those from the bulk region, the results are more similar to those from experiment with the exponential decay window. At $q = 0.429$ Å^{-1} there is still some difference in the frequency position of the side peaks between the results from the second slab and those from the bulk

region, the IXS experimental data and the exponential decay window. This discrepancy indicates still a higher adiabatic sound velocity at the second layer than at the central region. Moreover, it indicates that the smallest experimental probing depth is already very deep into the FLS, and most of the signal is sampling a region that is already behaving like the bulk.

The most interesting result extracted from the experimental data in the paper [316] is that capillary waves affect mainly the height and width of the central peak. However, this is not what our OF-AIMD study reveals to us, but rather an effect of experimental resolution. Fig. 9.26 displays the OF-AIMD results at the same wavelengths and depths, before convolution with the experimental resolution.
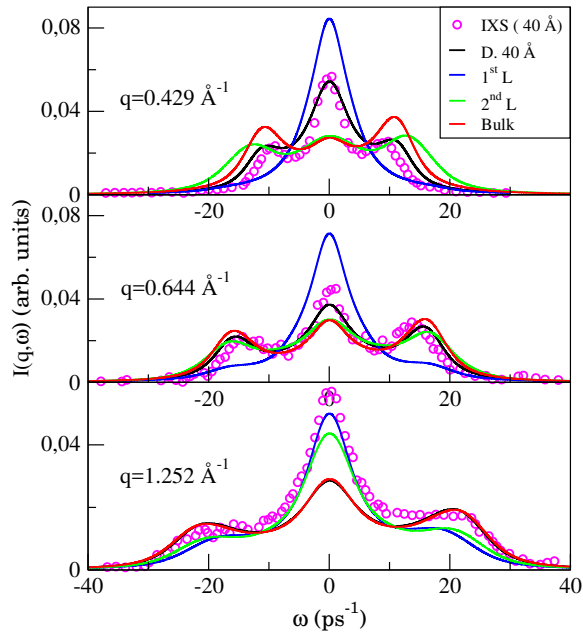
FIGURE 9.25: Dynamic structure factor after detailed balance condition and experimental convolution, $I(q, \omega)$, at several wave vectors in all the regions studied. Continuous lines: OF-AIMD results. Open circles: IXS experimental results at the smallest possible probing depth, 40 Å [316].
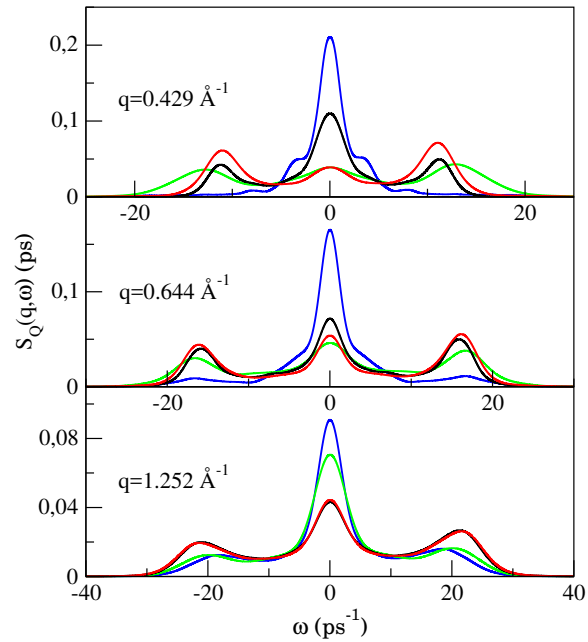
FIGURE 9.26: OF-AIMD dynamic structure factor after detailed balance condition, $S_Q(q, \omega)$, at several wave vectors in all the regions studied.

The results most affected by the convolution with the experimental resolution function are those from the first layer, region where capillary waves are more predominant. At this depth, their presence is indicated by side shoulders close to the central peak. As we go deeper into the slab, these shoulder are less marked and only appear as very subtle shoulders or flat regions between the central and side peaks. However, all these hints of dispersive modes from capillary waves disappear once the function is convoluted with the experimental resolution.

Nevertheless, a better way to observe capillary waves is in $C_L(q, \omega)$ where there is no central peak that can mask the presence of capillary waves.

In fig. 9.27 the presence of capillary waves as a dispersive side peak is evident at all wavevectors and probing depths. In the first layer, their contribution to $C_L(q, \omega)$ is of the same weight as pressure or sound modes, resulting in only one wide peak at low wavevectors which, as q increases, transforms into a main sound mode with a side shoulder at smaller frequencies corresponding to capillary waves.

At the second layer, the weight of the capillary is always lower than that of the sound mode which results in two clear peaks. In this case is easy to see how the frequency of the sound mode at low wavevectors is higher than in the bulk region or at a probing depth of 40 Å. Moreover, the signal from a probing depth of 40 Å and
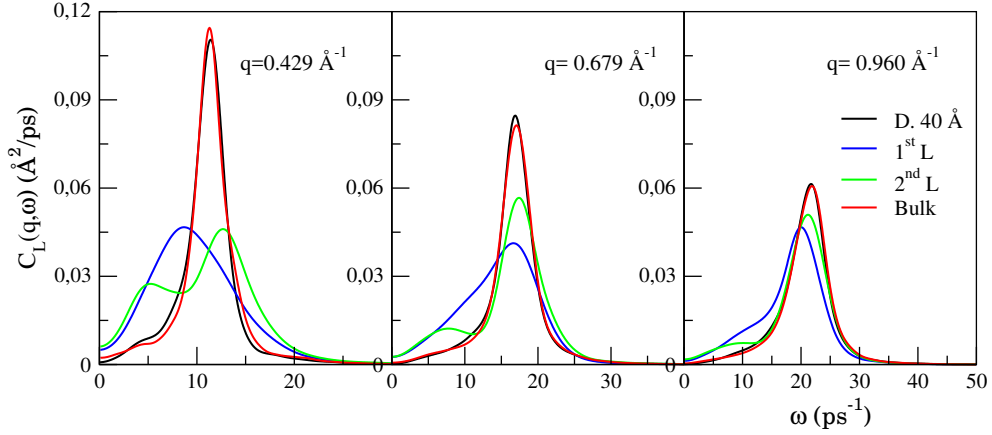
FIGURE 9.27: $C_L(q,\omega)$ at different wavevectors and probing depths.

from the bulk region are almost identical at all wavevectors, supporting the previous conclusion that the lowest experimental probing depth of 40 Å is already very deep into the slab as to obtain significantly different results.

We have evaluated two different properties related to collective dynamics to shed light on how microscopic dynamics in different regions of the slab will affect experimentally measurable properties. In addition, we compare our OF-AIMD results with those obtained at the smallest probing depth in the experiment [316] and draw some conclusions.

Longitudinal viscosity

The longitudinal viscosity was obtained by performing a fitting of the intermediate scattering function, $F(q,t)$, following the generalized hydrodynamic model in sec. 3.2.1. In this model, the elastic central peak is modeled by an exponential decay in $F(q,t)$ which gives a Lorentzian function in $S(q,w)$, and the propagating sound waves are modeled by a shifted Lorentzian peak. We have included an extra shifted Lorentzian expression into the model to take into account the dispersion of capillary waves,

$$\frac{F(q,t)}{F(q,0)} = Ae^{-\alpha t} + Be^{-\beta t}\frac{\cos(\omega_1 t - \varphi)}{\cos\varphi} + Ce^{-\gamma t}\frac{\cos(\omega_2 - \theta)}{\cos\theta} \qquad (178)$$

The expression for the longitudinal viscosity can be easily deduced from the relationship of the model parameters with different thermodynamic properties [66],

$$\eta_L(q) = \frac{1}{q^2}\left(\alpha + 2\beta - \alpha\left(1 - A\frac{(\alpha-\beta)^2 + \omega_1^2}{\beta^2 + \omega_1^2}\right)^{-1}\right) \qquad (179)$$

with B, β and ω_1 corresponding to the term describing the pressure waves.

The model used in the experimental analysis of the results in Ref. [316] was the "two-times" viscoelastic model, differing in the description of the central peak in $S(q,\omega)$ by two central Lorentzians . Due to their conclusion from the measured dynamic structure factors where capillary waves only contribute to the central peak, their modification of the model was the addition of an extra exponential decay which would correspond to an additional central Lorentzian contribution to the central peak in the dynamic structure factor, ending in a signal with three central Lorentzians (capillary, heat and viscoelastic) and one lateral line associated to pressure waves.

Fig. 9.28 displays the results obtained from the fitting of OF-AIMD results at different depths along with the experimental fitting results from Ref.[316] at the smallest and biggest probing depths in the IXS experiment. The longitudinal viscosity results from the smallest and biggest experimental probing depths are very similar, indicating again that at 40 Å the microscopic dynamics are very similar to those in the bulk region. These
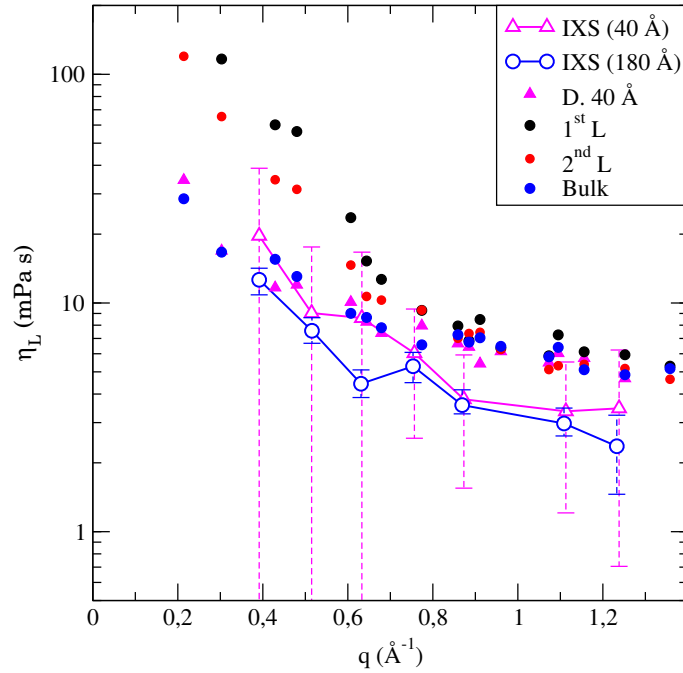
FIGURE 9.28: Longitudinal viscosity at different wavelengths and depths.

results compare very well to our OF-AIMD results from the bulk region and from the depth of 40 Å, especially at small wavevectors. The similarity in both results even when two different fitting models were used for the capillary waves, implies that the observance of the dispersive nature of capillary waves in experiments is a very difficult task.

The most outstanding results are those from the first and second layers. At high wavevectors, their behavior is very similar to those from the bulk region as well as those from experiment. However, the value that would be measured in an experiment corresponds to the extrapolation to $q \rightarrow 0$ which means that, by seeing the behavior of all curves at small wavevectors, the longitudinal viscosity in the first and second layer will more than double the values in the bulk region and those obtained experimentally.

Adiabatic sound velocity

The model used for the fitting of $F(q, t)$, Eq. 178, allows us to obtain the dispersion relation of $S(q, \omega)$ at each sampled depth and, therefore, the q-dependent adiabatic sound velocity. Fig. 9.29 depicts both functions.

The dispersion relation of $S(q, \omega)$ in inset of Fig. 9.29 shows the same behavior for the results from the bulk region and at 40 Å from OF-AIMD results and experiment whereas the dispersion relation from the first and second layers present clear differences until $q = 0.75 \text{ Å}^{-1}$. These differences result in a much higher adiabatic sound velocity in the two outmost layers than in the bulk region. This conclusion is clearly observed in Fig. 9.29 when the q-dependent adiabatic sound velocity curves are extrapolated to $q \rightarrow 0$. The experimental results indicated by open symbols as well as the OF-AIMD results from the bulk region and a depth of 40 Å are close to the experimental value of $c_s = 2320 \text{m/s}$. However, data from the first and second layers result in an almost 80 % higher adiabatic sound velocity. One difference with previous results for the FLS of Sn is that the increase in the adiabatic sound velocity in this case extends also to the second layer but, in l-Sn, only affected the first layer.
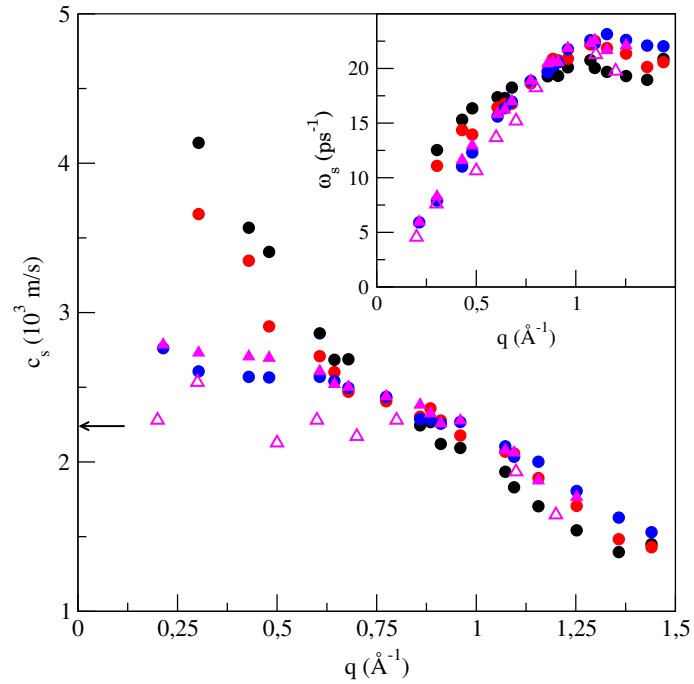
FIGURE 9.29: q-dependent adiabatic sound velocity at different depths in the FLS. Same legend as Fig. 9.28. The horizontal arrow indicates the experimental value at melting [253].

9.4.4 *Conclusions*

This work clearly demonstrates the value of OF-AIMD simulations for the investigation of collective dynamic properties at the FLS, region which IXS experiments still cannot sample correctly. The experimental work on the FLS of In opens a very interesting field of research. However, much research is still need to reduce the probing depth to a few Å to be able to measure the effect of the interface on the properties with respect to the bulk. In addition, higher resolution would be needed to observe experimentally the dispersive nature of capillary waves.

10

FINAL CONCLUSIONS AND FUTURE WORK

The present thesis has focused on the *ab initio* molecular dynamics (AIMD) study of liquid metals in a wide variety of situations, i.e. bulk pure liquids, alloys and free liquid surface (FLS). For these studies we have used the DFT in its two versions: KS and OF, depending on the characteristics of the specific liquid metal/alloy.

The most salient contributions and improvements of this thesis to the field of liquid metals are:

- In Chapter 5 an improved method to construct LPS has been reported, which takes into account the disordered array of atoms in the liquid system. This method has allowed us to study, using OF-AIMD, liquid alkaline-earth metals, l-Sn in bulk and FLS configuration and the FLS of In. In addition, collaboration with Prof. Carter's group at Princeton University has resulted in an improved LPS construction procedure for both solid and liquid applications. The main goal is to create an open access library of available goLPSs for as many elements as possible, to be used with the open access OF-DFT package, PROFESS.

- Chapter 6 was dedicated to the study of different bulk liquid metals with the goal of providing information complementary to the experimental one and to serve as benchmark for future development of OF schemes for this type of systems. In the case of l-Ni, a close analysis of the dispersion relation of $S(q, \omega)$ and the models used to fit the IXS and INS results, helped to understand the discrepancy between both experimental dispersion relations. Moreover, $S(q, \omega)$ displayed the existence of a second low frequency peak previously observed in other liquid metals (not yet Ni) through IXS by Hosokawa and coworkers. Another interesting result has been the observation of a second high frequency mode in $C_T(q, \omega)$ which has only been observed previously in a few liquid metals under pressure, but never at zero pressure.

  The AIMD study of l-Ti is the first to date. The $S(q)$ available experimental curves for l-Ti presented marked difference among them and this study has provided insight into which are the correct ones. In addition, the calculated AIMD $S(q)$ displays an asymmetric second peak which has been linked in some experimental results with the presence of some type of icosahedral ordering. This study has provided confirmation on this hypothesis as well as exactly which type of icosahedral ordering and its abundance in the system. Analysis of the decaying channels in the system's collective dynamics has provided information on the value of some properties like the ratio of specific heats γ_0, for which no experimental value is still available. The spectra of $F(q, t)$ and $C_T(q, t)$ also display the existence of a second dispersive mode. Future work on l-Ni and l-Ti involve the study of these second dispersive modes in collective modes using the same procedure as in Chapter 7.

  The last study of bulk systems involved l-Pd and l-Pt. The reason to study them was the dearth of information concerning their liquid state since this is also the first AIMD on l-Pd and l-Pt. Only the static structure has been studied through the evaluation of $g(r)$ and $S(q)$, for which we obtain good comparison with our AIMD results. Our study provides important information regarding the collective dynamics of these systems, useful for future experimental research. The next step of this study will be the evaluation of the liquid slabs of these two systems.

- The feature of complex collective dynamics which has started to be observed in both experimental and AIMD studies of different liquid metals has been the theme of Chapter 7. We selected two very different elements, Zn and Sn, for which experimental results of Hosokawa and coworkers have confirmed the existence of a second mode in longitudinal dynamics. The difference between these two systems regards their atomic ordering in liquid state, because while l-Zn adopts an icosahedral order, l-Sn does not. In addition, both systems have been studied with different DFT versions: for l-Zn we used KS-AIMD with

a NLPS while for l-Sn we used OF-AIMD with a LPS. For both systems the collective dynamic spectra, longitudinal and transversal, presented two different dispersive modes. The explanation of the appearance of the second mode in both cases is described by the use of mode-coupling (MC) theories. However, we found important limitations in the theory in both cases and have provided some insight into possible solutions. Future work in this aspect regards the application of this theory to other systems which display this same behavior (like l-Ni and l-Ti) as well as possible improvements to the theory.

• Liquid alloys are briefly treated in Chapter 8 with the study of the liquid Ag-Sn alloys at different concentrations. Two main conclusions can be highlighted: 1) the present study does not support the assumptions behind the microheterogeneous structure (MHS) model, and 2) the presence of a peak or shoulder in $C_{AgAg}^{L}(q,\omega)$ and a minimum in $C_{AgSn}^{L}(q,\omega)$ at very small frequency correspond to relaxations associated to interdiffusion processes and not to propagating modes.

• Finally, Chapter 9 contains different studies of FLS of different liquid metals. For l-Ag, we performed a combined study of both the bulk and the FLS configuration. We have introduced the evaluation of the intrinsic density profile as the best path to eliminate in a microscopic way the presence of capillary waves from the density profile, to compute the surface structure for comparison with experimental results. In the case of l-Ag, no experimental reflectivity data is available yet since the experimental procedure has important limitations in the type of liquid systems possible to study.

The relevance of the elimination of capillary waves through the calculation of the intrinsic density profile is highlighted in section 9.2, where three very different reflectivities are studied with this method: l-Hg, l-Bi and l-Pb. One first important result of the study is that the use of the intrinsic density profile provides a converged profile with clear oscillations characteristic of FLS of metals, which sometimes, due to high temperatures and low surface tensions, are impossible to obtain with the average density profile calculation, independently of the number of configurations used in the study. l-Hg reflectivity has a particular minimum which we have related to a depletion of the first layer in the intrinsic density profile. On the other hand, the particular reflectivity curve of l-Bi, with a side shoulder, cannot be ascribed to the first layer only, but to a relation between the first and second layers in the intrinsic density profile

The last two studies of the chapter regard the calculation, for the first time, of the collective dynamics in different regions of the FLS of Sn and In by using an AIMD approach: from the central section where it behaves like the bulk, to the surface. This type of study requires the use of a high number of particles and therefore, can only be performed with first principles theory through OF-AIMD. In both cases, the construction of an accurate LPS for the treatment of the slab was obtained through the use of the FM method previously developed in Chapter 5. In the case of the FLS of Sn, we concentrated on the dispersion relation of the spectra of all the collective dynamic functions and to characterize the different branches obtained, such as dispersion relation of the capillary waves, or the existence of Lamb-type waves. In the FLS of In, for which IXS experimental data at different probing depths are available, we mainly concentrated on the comparison of our AIMD results with experiment as well as providing insight on different limitations on the experimental technique: 1) even the lowest probing depth is already too deep into the sample to observe differences in properties like longitudinal viscosity or adiabatic sound velocity when comparing their value at the surface with their value deep under the FLS; and 2) better experimental resolution would be necessary in order to observe fine details like the dispersive nature of capillary waves.

Overall, the present thesis has provided insight into liquid metals research concerning features such as: (i) new methods in the construction of accurate LPS essential to the study of liquid systems with OF-AIMD, (ii) the explanation of one of the most recent features observed in liquid metals, which may affect the collective dynamics of all liquid metals, and (iii) the importance of the use of an improved method to eliminate capillary waves from FLS of metals which allows the correct evaluation of characteristic features of the density profile and the reflectivity.

A

MODE COUPLING THEORY. FURTHER EXPRESSIONS.

We recall that the memory functions are decomposed as the sum of a fast-decaying contribution and a slowly decaying one associated to couplings with slow variables, as specified in equations 111 and 112. The MC theory applied in this work includes couplings with the density mode, which decays slowly not only for $q \to 0$, because of its conserved character, but also in the vicinity of q_p, due to structural correlations. The MC integrals are then written as

$$N^{MC}(q,t) = \int d\vec{k} \, \nu_{\rho\rho}(\vec{q},\vec{k},\vec{q}-\vec{k}) \left[F(k,t)F(|\,\vec{q}-\vec{k}\,|,t) - F^f(k,t)F^f(|\,\vec{q}-\vec{k}\,|,t) \right] , \tag{180}$$

$$M_T^{MC}(q,t) = \int d\vec{k} \, \nu_{T\rho}(\vec{q},\vec{k},\vec{q}-\vec{k}) \left[F(k,t)F(|\,\vec{q}-\vec{k}\,|,t) - F^f(k,t)F^f(|\,\vec{q}-\vec{k}\,|,t) \right] , \tag{181}$$

where $F^f(k,t)$ denotes the fast component of $F(k,t)$, and $\nu_{\rho\rho}$ and $\nu_{T\rho}$ are the so called vertex functions corresponding to the density-density coupling and the transverse current-density coupling respectively. Selecting the z direction as that of $\vec{q}$, their expressions are given by[23]

$$\nu_{\rho\rho}(\vec{k},\vec{q}-\vec{k}) = \frac{\rho k_B T}{16\pi^3 m} \left[k_z c(k) + (q - k_z)c(|\,\vec{q}-\vec{k}\,|) \right]^2 , \tag{182}$$

$$\nu_{T\rho}(\vec{k},\vec{q}-\vec{k}) = \frac{\rho k_B T}{16\pi^3 m} k_x^2 \left[c(k) - c(|\,\vec{q}-\vec{k}\,|) \right]^2 . \tag{183}$$

The function $c(q)$ is the direct correlation function, related to the structure factor through the relation $S(q) = [1 - \rho c(q)]^{-1}$. The substraction of the product of the fast components in the integrals has the effect of nullifying the short time contribution of the integrals to the total function, so that $N^{MC}(q, t \to 0) \to at^4$, and the same applies to $M_T(q, t \to 0)$. However these terms decay fast and have no influence on the long time behavior of the functions. In fact the original formulation of MC theories, which focused on the long-time tails, did not include such terms, as we discussed in the text.

In any case, the expressions used imply that the short time characteristics of the memory functions (initial value and first three derivatives) are fully accounted for by the fast contributions. This property is used in the reverse direction, so that an ansatz is formulated for the analytic form of the fast contributions that incorporates the initial value and derivatives of the full memory functions. In this work we use a gaussian ansatz,

$$N^f(q,t) = N(q,0)\exp[-\frac{|\,\ddot{N}(q,0)\,|\,t^2}{2N(q,0)}] , \tag{184}$$

with an equivalent expression for $M_T^f(q,t)$. For the fast part of $F(q,t)$ we use as different type of ansatz, following Sjögren, given in terms of the single-particle intermediate scattering function, $F_s(q,t)$, which we compute from the AIMD simulations, and the free particle expression, F_0 of the form $F_0(q,t) = \exp[-k_B T q^2 t^2/(2m)]$,

$$F^f(q,t) = F(q,t)\frac{F_0(q,t)}{F_s(q,t)} . \tag{185}$$

Introducing the normalized intermediate scattering function, $F_N(q,t) = F(q,t)/S(q)$, which has initial value equal to one for any q, and the same for its fast part, we finally arrive to mode-coupling integrals in which the time dependence is common to both memory functions, but whose weights for a given $\vec{k}$ vector are different, dictated by the vertex functions, which depend on the structure factor of the liquid and on q, k and $|\,\vec{q}-\vec{k}\,|$.

Using two-center bipolar coordinates (Fig. A.1), so that $p = |\,\vec{q}-\vec{k}\,|$, and performing the ϕ-angular integration explicitly, the final MC integrals read

$$N^{MC}(q,t) = \frac{\rho k_B T}{8\pi^2 m} \frac{1}{q} \int_0^\infty dk \int_{|q-k|}^{q+k} dp \, \alpha(q,k,p) F_N(k,t) F_N(p,t) \left[1 - \frac{F_0(k,t)F_0(p,t)}{F_s(k,t)F_s(p,t)} \right] , \tag{186}$$

$$M_T^{MC}(q,t) = \frac{\rho k_B T}{16\pi^2 m} \frac{1}{q} \int_0^\infty dk \int_{|q-k|}^{q+k} dp \, \gamma(q,k,p) F_N(k,t) F_N(p,t) \left[1 - \frac{F_0(k,t)F_0(p,t)}{F_s(k,t)F_s(p,t)} \right] , \tag{187}$$
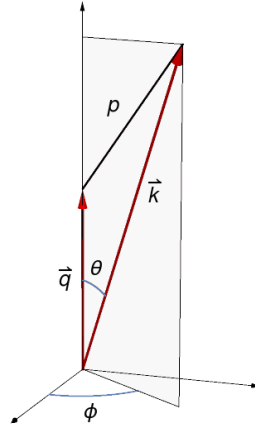
FIGURE A.1: Two-center bipolar coordinates

where

$$\alpha(q,k,p) = kS(k)pS(p) \left[\frac{q^2+p^2-k^2}{2q} \left(\frac{S(k)-1}{S(k)} \right) + \frac{q^2+k^2-p^2}{2q} \left(\frac{S(p)-1}{S(p)} \right) \right]^2 \tag{188}$$

and

$$\gamma(q,k,p) = -\frac{kp\,[S(k)-S(p)]^2}{S(k)S(p)} \frac{(q-k-p)(q-k+p)(q+k-p)(q+k+p)}{4q^2} \tag{189}$$

Note that the integration region for a given q is a strip in the (k,p) plane, symmetric with respect to its diagonal, $p = k$, whose width depends on q. Moreover, both $\alpha(q,k,p)$ and $\gamma(q,k,p)$ are symmetric with respect to interchanging k and p, i.e., both functions are symmetric with respect to the diagonal.

These functions quantify the degree of coupling between the functions at wavevector $\vec{q}$ and at given values of k and p, i.e. at wavevector $\vec{k}$, and both are non-negative (the product of the latter four terms in $\gamma(q,k,p)$ is always negative or zero in the integration strip). The function $\gamma(q,k,p)$ factorizes into a structural term and a "geometric" term purely dependent on the wavenumbers. The geometric factor is zero at the borders of the strip, and the structural term is zero at the diagonal, so $\gamma(q,k,p)$ takes null values in several parts of the integration region, somehow reflecting the "difficulty" for transverse-longitudinal coupling. On the contrary, $\alpha(q,k,p)$ only becomes zero for particular (k,p) pairs that nullify the term inside brackets, for instance in the diagonal $p = k$ at k values where $S(k) = 1$. This basically reflects that longitudinal-longitudinal couplings are much easier than transverse-longitudinal ones. Once the fast terms (Eq. 184) and MC terms (Eqs. 186 and 187) have been evaluated, the full memory functions are obtained and, from these, using the memory function equation in Laplace space and the relation between FT and LT, we obtain

$$C_T(q,\omega) = \frac{k_B T}{\pi m} \Re \left[\frac{1}{i\omega + \tilde{M}_T(q,i\omega)} \right] , \tag{190}$$

where $\Re$ denotes the real part. Since the LT is a complex magnitude we write $\tilde{M}_T(q,i\omega) = M_{T,c}(q,\omega) - iM_{T,s}(q,\omega)$, where the labels c and s denote integration of the function multiplied by $\cos(\omega t)$ and $\sin(\omega t)$ respectively. After taking the real part we get

$$C_T(q,\omega) = \frac{k_B T}{\pi m} \frac{M_{T,c}(q,\omega)}{M_{T,c}^2(q,\omega) + \left(\omega - M_{T,s}(q,\omega) \right)^2} . \tag{191}$$

Following exactly the same approach for $N(q,t)$, we can directly obtain $S(q,\omega)$ and $C_L(q,\omega)$ from $N_c(q,\omega)$ and $N_s(q,\omega)$.

B

AVERAGE KINETIC ENERGY DENSITY FUNCTIONAL.

We consider the kinetic energy functional

$$T_s[\rho] = T_W[\rho] + T_\beta[\rho] \tag{192}$$

where

$$T_\beta[\rho] = \frac{3}{10} \int d\vec{r}\, \rho(\vec{r})^{5/3 - 2\beta} \tilde{k}(\vec{r})^2 \tag{193}$$

$$\tilde{k}(\vec{r}) = (2k_F^0)^3 \int d\vec{s}\, k(\vec{s})\, \omega_\beta\left(2k_F^0|\vec{r} - \vec{s}|\right) \equiv k(\vec{r}) * \omega_\beta\left(2k_F^0 r\right) \tag{194}$$

$$k(\vec{r}) = (3\pi^2)^{1/3} \rho(\vec{r})^\beta \tag{195}$$

In the limit of small deviations from a uniform system, we wish to recover the LRT result. Equating the Fourier transform (FT) of the second functional derivative of $T_s[\rho]$ with respect to $\rho(\vec{r})$ for $\rho(\vec{r}) = \rho_0$, to the inverse of the Lindhard response function, gives for the weight function

$$\left(6\beta^2 - \frac{20}{3}\beta + \frac{10}{9}\right) + 4\beta \left(\frac{5}{3} - 2\beta\right) \overline{\omega}_\beta(\eta) + 2\beta^2\, \overline{\omega}_\beta(\eta)^2 = \frac{10}{9}\left(1/\pi_L(\eta) - 3\eta^2\right) \tag{196}$$

where $\eta = q/2k_F^0$, $\overline{\omega}_\beta$ is the FT of ω_β and

$$\pi_L(\eta) = \frac{1}{2}\left(1 + \frac{1 - \eta^2}{2\eta} \ln\left|\frac{1 + \eta}{1 - \eta}\right|\right). \tag{197}$$

is the noninteracting homogeneous electron gas response function. Taking in eqn. (196) the solution which satisfies the normalization condition $\overline{\omega}_\beta(\eta = 0) = 1$, and with β within the range $0 \leqslant \beta \leqslant 5/6$ so that the power of $\rho(\vec{r})$ in eqn. (193) is positive, the weight function is given by

$$\overline{\omega}_\beta(\eta) = 2 - \frac{5}{3\beta} + \frac{1}{3\beta}\sqrt{(5 - 3\beta)^2 + 5(\pi_L^{-1}(\eta) - 1 - 3\eta^2)}. \tag{198}$$

Requiring $\overline{\omega}_\beta$ to be real places a stricter limit on β: $\beta \leqslant 0.5991$. With this choice of weight function, the functional recovers the LRT limit, and in the limit of uniform density it reduces to the Thomas-Fermi functional. In the limit $\eta \to \infty$ we have

$$\overline{\omega}_\beta(\eta) \to C_1 + A/\eta^2 + \cdots \tag{199}$$

where

$$C_1 = 2 - \frac{5}{3\beta} + \frac{1}{3\beta}\sqrt{17 - 30\beta + 9\beta^2} \tag{200}$$

The constant C_1 gives rise to a Dirac delta function in the real space; therefore it is convenient to define a "modified" weight function

$$\tilde{\omega}_\beta(\eta) = \overline{\omega}_\beta(\eta) - C_1 \tag{201}$$

so that every convolution involving ω_β, such as in eqn. (194), becomes

$$G(\vec{r}) * \omega_\beta\left(2k_F^0 r\right) = C_1 G(\vec{r}) + G(\vec{r}) * \tilde{\omega}_\beta\left(2k_F^0 r\right). \tag{202}$$

An important limit is when the mean electron density, and therefore k_F^0, vanishes as for instance in a finite system. Now, the convolutions involving the "modified" weight function vanish because $\eta = q/2k_F^0 \to \infty$ and $\tilde{\omega}(\eta)$ vanishes. Consequently, $\tilde{k}(\vec{r}) = C_1 k(\vec{r})$, and the kinetic energy functional becomes $T_s[\rho] = T_W[\rho] + C_1^2 T_{TF}[\rho]$, and when $\beta = 4/9$, $C_1 = 0$.

C

LI BLPS CREATION AND FINAL GOLPS

C.1 LITHIUM (LI) BULK-DERIVED LOCAL PSEUDOPOTENTIAL (BLPS) CONSTRUCTION.

For all Kohn-Sham density functional theory (KSDFT) and Orbital-free density functional theory (OFDFT) calculations in this work, we used the Perdew-Burke-Ernzerhof (PBE) electron exchange-correlation (XC) functional [92] with non-linear core-corrections [325–327] (NLCC) and a core radius of $r_{core} = 0.89$ Å. The two parameters required to build the BLPS; i.e., 1) the value of the non-Coulombic part of the Fourier-transformed BLPS at $q = 0$ and 2) the position in real space beyond which a Coulomb tail is enforced are chosen to best reproduce the KSDFT with a non local pseudopotential (NLPS) ("KSDFT/NLPS") energy ordering for body-centered-cubic (bcc), face-centered-cubic (fcc), simple cubic (sc), and cubic diamond (cd) phases of Li. These structures are chosen because they span a wide range of coordination-number environments in the solid. When building the BLPS, Troullier-Martin NLPSs [126] are generated with the FHI98PP [186] code using default cutoff radii. Fermi-Dirac smearing with a width of 0.1 eV is used, and the plane-wave basis kinetic energy cutoff is 1200 eV for all cases to obtain accurate target KSDFT/NLPS electron densities used in the BLPS construction scheme, the details of which are given in ref. [151]. The k-point mesh used during the BLPS construction is 20x20x20 for bcc, fcc, and sc and 12x12x12 for cd. The number of atoms per primitive unit cell is one for bcc, fcc, and sc and two for cd. The BLPS is then tested on the ground state of Li and its properties compared to other phases. In these tests, a plane-wave kinetic energy cutoff of 900 eV and same k-point meshes as described above are used to converge the total energy per cell to within 1 meV. Table 16 shows the KSDFT/NLPS and KSDFT/BLPS energy orderings, equilibrium volumes, and bulk moduli for all four Li structures studied.

C.2 FINAL GLOBALLY OPTIMIZED LOCAL PSEUDOPOTENTIALS (GOLPSS).

Figure C.1 shows the non-Coulombic part of the initial BLPS used for both gallium (Ga) and Li and of the initial local channel of the NLPS used for calcium (Ca), compared to the final goLPSs obtained for each element. For Ga and Ca in which fitting to only crystal properties was performed, the final goLPSs tend to be 'harder' or have higher maximum values. On the other hand, for Li, where liquid phase forces were also included in the fitting process, the final goLPS is 'softer' and reduced the value of its maximum, as expected.
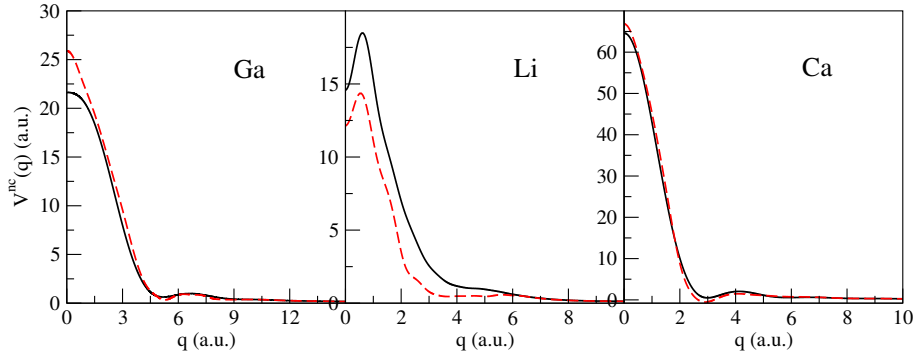
FIGURE C.1: Non-Coulombic parts of the initial BLPS (for Ga and Li) and local channel of NLPS (for Ca) (black curves), and the final goLPSs (dashed red curves).

195

TABLE 16: Comparison of NLPS and BLPS KSDFT-PBE bulk properties of the bcc, fcc, sc, and CD phases of Li. The bulk modulus (B) is in GPa, the equilibrium volume per atom (V0) is in Å, and the equilibrium total energy (E0) is in eV/atom. All total energies are listed relative to bcc-Li equilibrium total energy.

	bcc	fcc	sc	cd
V_0 (Å^3/atom)				
NLPS	20.205	20.163	20.375	25.792
BLPS	21.099	21.056	22.132	25.214
B_0 (GPa)				
NLPS	12.1	13.8	13.1	6.4
BLPS	14.8	15.1	14.9	10.3
ΔE_{min} (eV/atom)				
NLPS	0.000	-0.002	0.121	0.517
BLPS	0.000	-0.002	0.133	0.502

D

GENERALIZED HYDRODYNAMIC MODEL.

We begin with the hierarchy of memory functions of $F(q, t)$ and this is most conveniently achieved through the use of the Laplace Transform technique, $\tilde{f}(z) = \int_0^\infty f(t) \exp[-zt] \, dt$. In this way, the first, $M(q, t)$, and second order, $N(q, t)$, memory functions of $F(q, t)$ are defined as

$$\tilde{F}(q,z) = \frac{F_0(q)}{z + \tilde{M}(q,z)} \quad , \quad \tilde{M}(q,z) = \frac{M_0(q)}{z + \tilde{N}(q,z)},$$ (203)

where $F_0(q)$ and $M_0(q)$ are the initial ($t = 0$) values of $F(q, t)$ and $M(q, t)$ respectively, and their values are $F_0(q) = S(q)$ and $M_0(q) = -\ddot{F}(q, 0)/F_0(q) = k_B T q^2/(mS(q))$, the dot denoting time derivative, with k_B the Boltzmann constant and m the atomic mass. Moreover, since $F(q, t)$ is a real even function of time, its second derivative can be related to the second frequency moment of the $S(q, \omega)$, so that $M_0(q) = \langle \omega^2(q) \rangle / S(q) = \int_{-\infty}^\infty \omega^2 S(q, \omega)/S(q) \, d\omega$.

The second order memory function, $N(q, t)$, accounts for all the relaxation processes in the collective dynamics and it is a basic magnitude in most theoretical models for $F(q, t)$. Usually, the $N(q, t)$ has been written as a sum of a rapidly decaying term, which aims to describe the interations of a particle with its nearest neighbors, plus a slowly decaying term to account for the cooperative motion of large number of particles. A convenient mathematical description is provided by writing the $N(q, t)$ as a sum of two exponentially decaying functions (a slow and a fast one), namely

$$N(q,t) = A_s(q)e^{-t/\tau_s(q)} + A_f(q)e^{-t/\tau_f(q)}$$

$$\tilde{N}(q,z) = \frac{A_s(q)}{z + \tau_s(q)^{-1}} + \frac{A_f(q)}{z + \tau_f(q)^{-1}}.$$ (204)

As previously explained in Chapter 3, this model can present two possibilities, i.e. the slow decaying exponential represents the thermal relaxation (generalized hydrodynamics) or the viscoelastic relaxation (generalized viscoelastic). The decay rates behave different, with the thermal channel going to zero for small q and the visoelastic channel going to a nonzero value. However, the amplitude variation of each channel is easier to use as a distinguishing term between both channels. The value of the generalized heat capacity ratio, $\gamma(q)$, derived from the amplitudes of the exponentials always behaves very different when assuming that the slow term is the thermal one than when assuming that the viscoelastic term in the slow one. If the slow channel is ascribed to the thermal decay channel, the amplitude is $(\gamma(q) - 1)M_0(q)$ and the relaxation time is $(\gamma(q)D_T(q))^{-1}$ whereas, if the slow exponential accounts for a viscoelastic decay channel, the amplitude is $\omega_L^2(q) - \gamma(q)M_0(q)$ and the relaxation time is $\tau_\nu(q)$. The values of the amplitudes are such that $N(q, t = 0)$ recovers its correct value in terms of the second and fourth derivatives of $F(q, t)$ at $t = 0$ or alternatively in terms of the second and fourth frequency moments of $S(q, \omega)$, where in particular $\omega_L^2(q) = \langle \omega^4(q) \rangle / \langle \omega^2(q) \rangle$. The other q-dependent magnitudes, namely $\gamma(q)$ and $D_T(q)$, are generalizations of the thermophysical parameters $\gamma_0 = C_P/C_V$ (the ratio between specific heats at constant pressure and at constant volume) and the thermal diffusivity D_T. In the generalized hydrodynamics model we obtain $\gamma(q) = 1 + \frac{A_s(q)}{M_0(q)}$, whereas in the generalized viscoelastic model $\gamma(q) = \frac{\omega_L^2(q) - A_s(q)}{M_0(q)}$.

E

LIQUID SN TEMPERATURE-DEPENDENT PROPERTIES.

E.1 STATIC STRUCTURE FACTOR.

The pair distribution function, $g(r)$, and the static structure factor $S(q)$ can both be obtained directly from the simulation. The latter is plotted in figure E.1 for different temperatures along with the x-ray diffraction data of Waseda et al. [192] and the inelastic neutron scattering of Itami et al. [269]. The OF-AIMD $S(q)$ has a main peak that goes from $q_p \approx 2.39$ Å^{-1} at T=573 K to $q_p \approx 2.34$ Å^{-1} at T=1873 K. The second peak's position goes from ≈ 4.58 Å^{-1} at T= 573 K to ≈ 4.61Å^{-1} at T=1873 K. The subsequent oscillations are rather weak for all temperatures. We obtain some discrepancies with experimental results at the lower temperatures of 573 K and 973 K related to the main ad second peak's position. However, the OF-AIMD $S(q)$ accounts for the height and amplitudes of the main and second peak. Moreover, the shoulder on the high-q side of the main peak, which is the most distinctive feature of the measured $S(q)$ for l-Sn, is also reproduced by the simulation at all the temperatures studied.
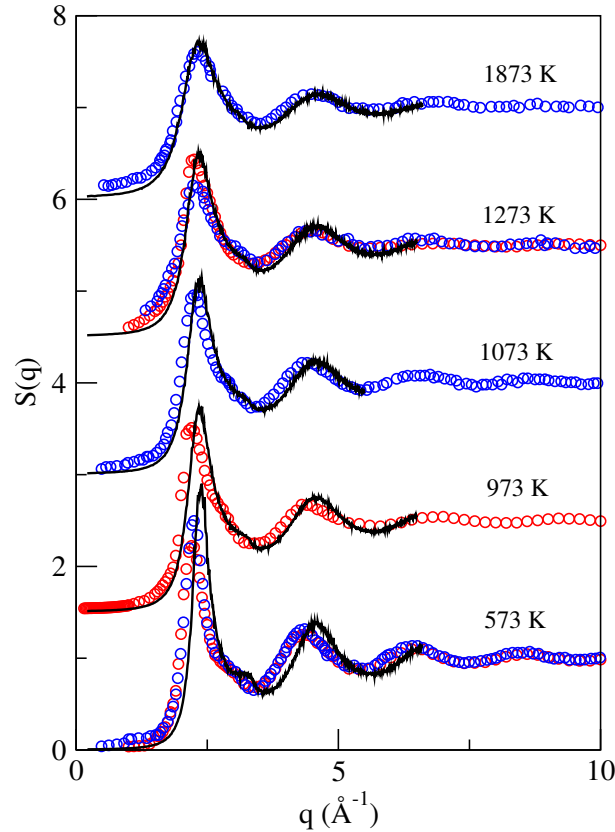
FIGURE E.1: Static structure factor, $S(q)$, at different temperatures. Full lines: OFDFT results. Red circles: experimental X-ray (XR) results by Waseda [192]. Blue circles: neutron scattering (NS) by Itami [269].

E.2 SINGLE PARTICLE DYNAMICS.

In figure E.2 we display the calculated self diffusion coefficients at different temperatures. We obtained good results that follow the same trend as experimental results as the temperature increases. Even though we obtain better results than those obtained by Itami et al. with KSDFT [269], ours are still lower than all the experimental results. This may be related to system size effects as previously studied by Chen and co-workers [328]. From their results we can predict that for a bigger system size we would obtain even better results when comparing to experiment.
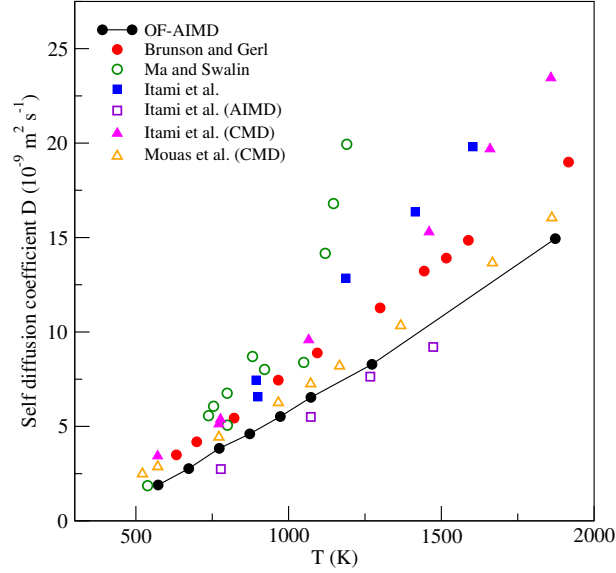
FIGURE E.2: Self diffusion coefficients at different temperatures. Black line: OFDFT results. Full circles: Experimental results by Brunson and Gerl [294]. Open circles: Experimental results by Ma and Swalin [329]. Full squares: Experimental results under microgravity by Itami et al. [330]. Open squares: AIMD results by Itami et al. [269]. Full triangles: Classical MD (CMD) results by Itami et al. [269]. Open triangles: CMD results by Mouas et al. [331].

E.3 COLLECTIVE DYNAMICS.

Figure E.3 depicts the calculated OFDFT $F(q,t)$'s along with KSDFT results of Calderín and co-workers [228] at two different temperatures, T= 573 K and T= 1273 K. Both studies show similar oscillation frequencies and amplitudes.

The frequencies where the maxima of the side-peaks in $S(q,\omega)$ appear define the dispersion relation $\omega_m(q)$. In the limit of small wavevectors ω_m should vary linearly with q and the slope corresponds to the adiabatic sound velocity, c_s. Figure E.4 shows the obtained adiabatic sound velocities in comparison with experimental results.

Figure E.5 shows the calculated shear viscosity coefficients at different temperatures. The obtained results compare good to experimental and classical molecular dynamics results.
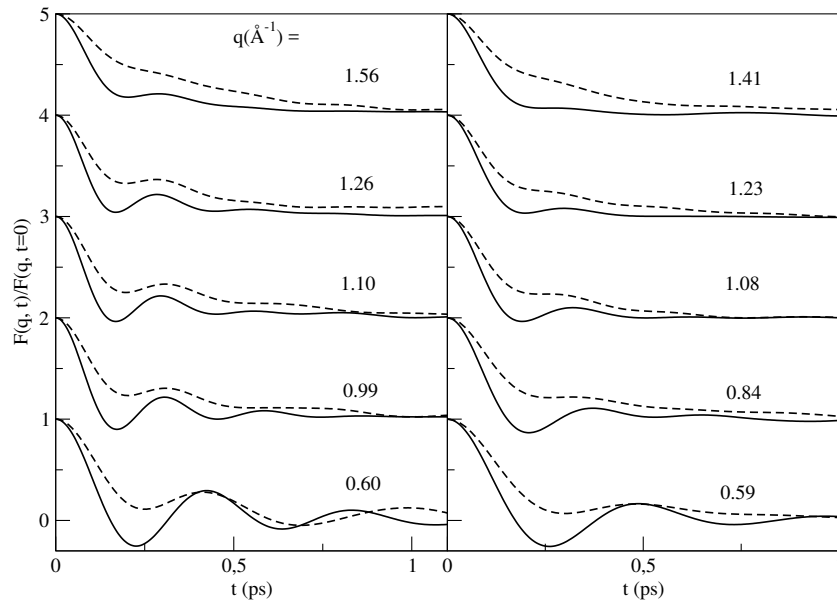
FIGURE E.3: Intermediate scattering function, $F(q, t)$, for several q-values at T= 573 K (left) and T= 1273 K (right). Full line: OFDFT results. Dashed line: KSDFT results by Calderín and co-workers [228].
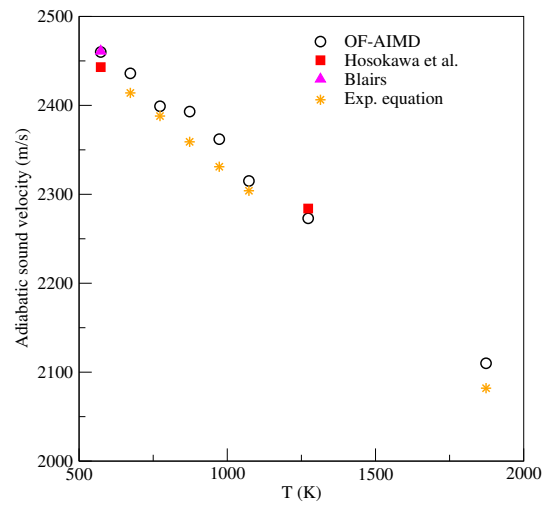
FIGURE E.4: Adiabatic sound velocity, c_s, at different temperatures. Full circles: OFDFT results. Full squares: experimental results from Hosokawa and coworkers [322]. Full triangle: experimental result from Blairs [233]. Stars: extrapolated results using experimental equation from [233].
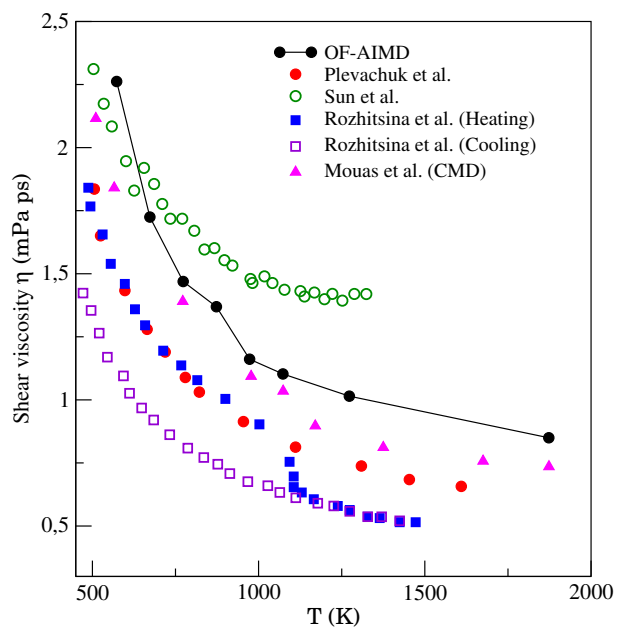
FIGURE E.5: Shear viscosity coefficients at different temperatures. Black line: OFDFT results. Full circles: Experimental results by Plevachuk et al. [283]. Open circles: Experimental results by Sun et al. [332]. Full squares: Experimental results from heating by Rozhitsina et al. [333]. Open squares: Experimental results from cooling by Rozhitsina et al. [333]. Full triangles: Classical MD results by Mouas et al. [331].

F

COLLECTIVE DYNAMICS IN LIQUID ALLOYS.

We give here the definitions of the magnitudes used throughout the paper. Some of them are quite standard and can be found in many excellent references. We consider a binary system, with N_1 and N_2 particles of each type, and concentrations $x_i = N_i/(N_1 + N_2) = N_i/N$, occupying a volume V, with total number density $\rho = N/V$.

We start with the partial microscopic number densities in Fourier space

$$\rho_j(\mathbf{q}, t) = \frac{1}{\sqrt{N_j}} \sum_{\ell=1}^{N_j} \exp[-i\mathbf{q} \cdot \mathbf{r}_\ell^{(j)}(t)] \quad (j = 1, 2). \tag{205}$$

The AL partial intermediate scattering functions, $F_{ij}(q, t)$ are defined as

$$F_{ij}(q, t) = \langle \rho_i(\mathbf{q}, t + t_0)\rho_j(-\mathbf{q}, t_0) \rangle =$$
$$= \frac{1}{\sqrt{N_i N_j}} \left\langle \sum_{\ell=1}^{N_i} \exp[-i\mathbf{q} \cdot \mathbf{r}_\ell^{(i)}(t + t_0)] \sum_{n=1}^{N_j} \exp[i\mathbf{q} \cdot \mathbf{r}_n^{(j)}(t_0)] \right\rangle, \tag{206}$$

where the average is taken over time origins and over wavevectors with the same module.

The initial values of these functions are the static AL partial structure factors, $S_{ij}(q) = F_{ij}(q, t = 0)$, and these are related to the partial pair distribution functions, $g_{ij}(r)$, through FT,

$$S_{ij}(q) = \delta_{ij} + (x_i x_j)^{1/2} \rho \int d\mathbf{r} \left[g_{ij}(r) - 1 \right] \exp[-i\mathbf{q} \cdot \mathbf{r}]. \tag{207}$$

A similar separation can be performed for the intermediate scattering functions, as

$$F_{ij}(q, t) = \delta_{ij} F_j^s(q, t) + (x_i x_j)^{1/2} F_{ij}^d(q, t), \tag{208}$$

where $F_j^s(q, t)$ denotes the self part, which corresponds to the autocorrelation of the single-particle j-type density, $\rho_j^s(\mathbf{q}, t) = \exp[-i\mathbf{q} \cdot \mathbf{r}_n^{(j)}(t)]$. Here n can take any value from 1 to N_j, and $F_j^s(q, t) = \left\langle \rho_j^s(\mathbf{q}, t + t_0)\rho_j^s(-\mathbf{q}, t_0) \right\rangle$ includes an extra average over particles of the same type. The second term in Eq. 208 corresponds to those terms in $F_{ij}(q, t)$ that share no particle in the double sum that defines it (Eq. 206).

The FT into frequency domain defines the AL partial dynamic structure factors,

$$S_{ij}(q, \omega) = \frac{1}{2\pi} \int dt \, F_{ij}(q, t) \exp[i\omega t]. \tag{209}$$

From the AL partial magnitudes, the BT partials are defined as

$$\begin{aligned}
S_{NN}(q) &= x_1 S_{11}(q) + x_2 S_{22}(q) + 2(x_1 x_2)^{1/2} S_{12}(q) \\
S_{CC}(q) &= x_1 x_2 [x_2 S_{11}(q) + x_1 S_{22}(q) - 2(x_1 x_2)^{1/2} S_{12}(q)] \\
S_{NC}(q) &= S_{11}(q) - S_{22}(q) + (x_2 - x_1)/(x_1 x_2)^{1/2} S_{12}(q).
\end{aligned} \tag{210}$$

The extension to finite times is straightforward,

$$
\begin{aligned}
F_{NN}(q,t) &= x_1 F_{11}(q,t) + x_2 F_{22}(q,t) + 2(x_1 x_2)^{1/2} F_{12}(q,t) \\
\frac{F_{CC}(q,t)}{x_1 x_2} &= x_2 F_{11}(q,t) + x_1 F_{22}(q,t) - 2(x_1 x_2)^{1/2} F_{12}(q,t) \\
F_{NC}(q,t) &= F_{11}(q,t) - F_{22}(q,t) + \frac{x_2 - x_1}{(x_1 x_2)^{1/2}} F_{12}(q,t) \, .
\end{aligned}
$$

$$(211)$$

Their FT into frequency domain defines the BT partial dynamic structure factors, $S_{NN}(q,\omega)$, $S_{CC}(q,\omega)$ and $S_{NC}(q,\omega)$.

Finally, note that the separation of the AL partials into self and distinct parts (Eq. 208), when taken to the definition of the BT partials leads in particular to

$$
\begin{aligned}
\frac{F_{CC}(q,t)}{x_1 x_2} &= x_2 F_1^s(q,t) + x_1 F_2^s(q,t) + \\
&\quad x_1 x_2 \left(F_{11}^d(q,t) - 2 F_{12}^d(q,t) + F_{22}^d(q,t) \right) \, .
\end{aligned}
$$

$$(212)$$

This is used in the main text to justify the relation between concentration-concentration dynamic properties and interdiffusion processes.

G

PUBLICATIONS

All the work presented in the present thesis has been or is in the process of being published.

Papers

Beatriz G. del Río, Johannes M. Dieterich, and Emily A. Carter, "Globally-optimized Local Pseudopotentials for (Orbital-Free) Density Functional Theory Simulations of Liquids and Solids", *in preparation* (2017)

B. G. del Río, L. E. González, L. Calderín, and D. J. González, "Local order and dynamic properties of liquid Ag_x-Sn_{1-x} alloys by ab initio molecular dynamics", *submitted* (2017)

B. G. del Río, O. Rodríguez, L. E. González, and D. J. González, "First principles determination of static, dynamic and electronic properties of liquid Ti near melting", *submitted* (2017)

B. G. del Río and L. E. González, "Longitudinal, transverse and single-particle dynamics in liquid Zn: ab initio study and theoretical analysis", *accepted* Phys. Rev. B (2017)

B. G. del Río, L. E. González, and D. J. González, "Ab initio study of several static and dynamic properties of bulk liquid Ni near melting", *J. Chem. Phys.* **146**, 034501 (2017)

Beatriz G. del Río, David J. González, and Luis E. González, "An ab initio study of the structure and atomic transport in bulk liquid Ag and its liquid-vapor interface", *Phys. Fluids* **28**, 107105 (2016)

Beatriz G. del Río and Luis E. González, "Orbital free ab initio simulations of liquid alkaline earth metals: from pseudopotential construction to strcutural and dynamic properties", *J. Phys.: Condens. Matter* **26**, 465102 (2014) (included in IOP Select)

Conference Proceedings

B. G. del Río and L. E. González, "Orbital-free ab initio molecular dynamics study of the static structure and dynamic properties of the free liquid surface of Sn", accepted for publication in the *16th International Conference on Liquid and Amorphous Metals Proceedings, European Physical Journal (EPJ) Web of Conferences* (2017)

B. G. del Río and L. E. González, "Structure and dynamics of liquid Zn: an analysis of ab-initio simulations", accepted for publication in the *16th International Conference on Liquid and Amorphous Metals Proceedings, European Physical Journal (EPJ) Web of Conferences* (2017)

B. G. del Río, J. Souto, M. M. G. Alemany, and L. E. González, "Ab initio study of intrinsic profiles of liquid metals and their reflectivity", accepted for publication in the *16th International Conference on Liquid and Amorphous Metals Proceedings, European Physical Journal (EPJ) Web of Conferences* (2017)

B. G. del Río, L. E. González, and D. J. González, "Dynamic properties of liquid Ni revisited", accepted for publication in the *16th International Conference on Liquid and Amorphous Metals Proceedings, European Physical Journal (EPJ) Web of Conferences* (2017)

B. G. del Río and L. E. González, "Liquid Be, Ca and Ba. An orbital-free ab-initio molecular dynamics study", *15th International Conference on Liquid and Amorphous Metals Proceedings, AIP Conf. Proc.*, **1673**, 020008 (2015)

BIBLIOGRAPHY

[1] P. Hohenberg and W. Kohn, Phys. Rev. **136**, B864 (1964).

[2] W. Kohn and L. J. Sham, Phys. Rev. **140**, A1133 (1965).

[3] R. G. Parr and W. Yang, *Density-Functional Theory of Atoms and Molecules* (Oxford University Press, New York, 1989).

[4] B. J. Alder and T. E. Wainwright, J. Chem. Phys. **27**, 1208 (1957).

[5] B. J. Alder and T. E. Wainwright, J. Chem. Phys. **31**, 459 (1959).

[6] A. Rahman, Phys. Rev. **136**, A405 (1964).

[7] L. Verlet, Phys. Rev. **159**, 98 (1967).

[8] L. Verlet, Phys. Rev. **165**, 201 (1968).

[9] J. R. D. Copley and S. W. Lovesey, Rep. Prog. Phys. **38**, 461 (1975).

[10] M. P. Allen and D. J. Tildesley, *Computer Simulation of Liquids* (Oxford University, Oxford, 1990).

[11] F. H. Stillinger and A. Rahman, J. Chem. Phys. **60**, 1545 (1974).

[12] M. Levitt and A. Warshel, Nature **253**, 694 (1975).

[13] M. S. Daw and M. I. Baskes, Phys. Rev. Lett. **50**, 1285 (1983); Phys. Rev. B **29**, 6443 (1984).

[14] R. Car and M. Parrinello, Phys. Rev. Lett. **55**, 2471 (1985).

[15] K. Laasonen, M. Sprik, M. Parrinello and R. Carr, J.Chem. Phys. **99**, 9080 (1993).

[16] M. J. Gillan, Contemp. Phys. **38**, 115 (1997).

[17] D. Marx and J. Hutter, *Ab Initio Molecular Dynamics* (Cambridge University Press, 2009).

[18] M. A. Abdou, The APEX TEAM, A. Ying, N. Morley, K. Gulec, S. Smolentsev, M. Kotschenreuther, S. Malang, S. Zinkle, T. Rognlien, P. Fogarty, B. Nelson, R. Nygren, K. McCarthy, M.Z. Youssef, N. Ghoniem, D. Sze, C. Wong, M. Sawan, H. Khater, R. Woolley, R. Mattas, R. Moir, S. Sharafat, J. Brooks, A. Hassanein, D. Petti, M. Tillack, M. Ulrickson, and T. Uchimoto, Fusion Eng. Des. **54**, 181 (2001).

[19] J. W. Coenen, G. De Temmerman, G. Federici, V. Philipps. G. Sergienko, G. Strohmayer, A. Terra, B. Unterberg, T. Wegener, and D. C. M. Van den Bekerom, Phys. Scr. **T159**, 14037 (2014).

[20] L. Yi and J. Liu, Int. Mater. Rev. **6608**, 1 (2017).

[21] B. J. Carey, J. Z. Ou, R. M. Clark, K. J. Berean, A. Zavabeti, A. S. R. Chesman, S. P. Russo, D. W. M. Lau, Z.-Q. Xu, Q. Bao, O. Kavehei, B. C. Gibson, M. D. Dickey, R. B. Kaaner, T. Daeneke, and K. K. Zadeh, Nat. Commun. **8**, 14482 (2017).

[22] J. W. Boley, E. L. White, and R. K. Kramer, Adv. Mater. **27**, 14 (2015).

[23] U. Balucani and M. Zoppi, *Dynamics of the Liquid State* (Clarendon, Oxford, 1994).

[24] J. P. Boon and S. Yip, *Molecular Hydrodynamics* (McGraw-Hill, Dover, 1980).

[25] U. Balucani, M. H. Lee, and V. Tognetti, Phys. Rep. **373**, 409 (2003).

[26] J. P. Hansen and I.R. McDonald *Theory of Simple Liquids* (Academic Press, New York, 1986).

[27] C.N.J. Wagner and H. Ruppersberg, At. Energy Rev. **1**, 101 (1981).

[28] R. L. McGreevy, A. Baranyai and I. Ruff, Phys. Chem. Liq. **16**, 47 (1986).

[29] J. Souto, M. M. G. Alemany, L. J. Gallego, L. E. González, and D. J. González, J. Nuc. Mater. **411**, 163 (2011).

[30] J. Souto, M. M. G. Alemany, L. J. Gallego, L. E. González, and D. J. González, Modelling Simul. Mater. Sci. Eng. **21**, 075006 (2013).

[31] N. H. March and M. P. Tosi, *Atomic Dynamics in Liquids* (Dover, New York, 1991).

[32] N. W. Ashcroft and D. C. Langreth, Phys. Rev. **156**, 685 (1967).

[33] G. E. Bacon, *Neutron Diffraction* (Clarendon, Oxford, 1975).

[34] J. Trullás and J. A. Padró, J. Chem. Phys. **99**, 3983 (1993).

[35] J. Trullás and J. A. Padró, Phys. Rev. E **50**, 1162 (1994).

[36] E. M. Adams, I. R. McDonald, and K. Singer, Proc. R. Soc. Lond. A 357 (1997) 37.

[37] T. Bryk, I. Mryglod, Phys. Lett. A **261**, 349 (1999); J. Phys.: Condens. Matter **12**, 6063 (2000).

[38] J. Blanco, D. J. González, L. E. González, J. M. López, and M. J. Stott, Phys. Rev. E **67**, 041204, (2003).

[39] D. J. González, L. E. González, J. M. López, and M. J. Stott, Phys. Rev. E **69**, 031205 (2004).

[40] D. J González, L. E. González, J. M. López, and M. J. Stott, J. Phys.: Condens. Matter **17**, 1429 (2005).

[41] D. J González and L. E. González, Condens. Matter Phys. **11**, 155 (2008).

[42] M. P. D'Evelyn and S. A. Rice, Phys. Rev. Lett. **47**, 1844 (1981).

[43] O. M. Magnussen, B. M. Oko, M. J. Regan, K. Penanen, P. S. Pershan, and M. Deutsch, Phys. Rev. Lett. **74**, 4444 (1995).

[44] M. J. Regan, E. H. Kawamoto, S. Lee, P. S. Pershan, N. Maskil, M. Deutsch, O. M. Magnussen, B. M. Ocko, and L.E. Berman, Phys. Rev. Lett. **75**, 2498 (1995).

[45] H. Tostmann, E. DiMasi, P. S. Pershan, B. M. Ocko, O. G. Shpyrko, and M. Deutsch, Phys. Rev. B **59**, 783 (1999).

[46] O. G. Shpyrko, P. Huber, A. Y. Grigoriev, P. S. Pershan, B. Ocko, H. Tostmann, and M. Deutsch, Phys. Rev. B **67**, 115405 (2003).

[47] O. G. Shpyrko, A. Y. Grigoriev, C. Steimer, P. S. Pershan, B. Lin, M. Meron, T. Graber, J. Gerbhardt, B. Ocko, and M. Deutsch, Phys. Rev. B **70**, 224206 (2004).

[48] P. S. Pershan, S. E. Stoltz, O. G. Shpyrko, M. Deutsch, V. S. K. Balagurusamy, M. Meron, B. Lin, and R. Streitel, Phys. Rev. B **79**, 115417 (2009).

[49] M. Zhao, D. S. Chekmarev, Z.-H. Cai, and S. A. Rice, Phys. Rev E **56**, 7033 (1997); D. Chekmarev, M. Zhao, and S. A. Rice, J. Chem. Phys. **109**, 1959 (1998).

[50] S. Iarlori, P. Carnevali, F. Ercolessi, and E. Tosatti, Surf. Sci. **211-212**, 55 (1989).

[51] E. Chacón, M. Reinaldo-Falagan, E. Velasco, and P. Tarazona, Phys. Rev. Lett. **87**, 166101 (2001); E. Velasco, P. Tarazona, M. Reinaldo-Falagan, and E. Chacón, J. Chem. Phys. **117**, 10777 (2002).

[52] H. Mo, G. Evmenenko, S. Kewalramani, K. Kim, S.N. Ehrlich, and P. Dutta, Phys. Rev. Lett. **96**, 096107 (2006).

[53] J. M. Bomont, J. L. Bretonnet, D. J. González, and L. E. González, Phys. Rev. B **79**, 144202 (2009).

[54] E. DiMasi, H. Tostmann, B. M. Ocko, P. S. Pershan, and M. Deutsch, Phys. Rev. B **58**, R13419 (1998).

[55] D. J. González, L. E. González, and M. J. Stott, Phys. Rev. B **74**, 014207 (2006).

[56] M. J. Regan, P. S. Pershan, O. M. Magnussen, B. M. Ocko, M. Deutsch and L. E. Berman, Phys. Rev. B **54**, 9730 (1996).

[57] E. Chacón and P. Tarazona, Phys. Rev. Lett. **91**, 166103 (2003).

[58] M. S. Daw and M. I. Baskes, Phys. Rev. Lett. **50**, 1285 (1983).

[59] M. J. Stott and E. Zaremba, Phys. Rev. B **22**, 1564 (1980).

[60] D. Levesque, L. Verlet, and J. Kürkijarvi, Phys. Rev. A **7**, 1690 (1973).

[61] W. E. Aller, B. J. Alder, and S. Yip, Phys. Rev. A **A**, 3174 (1983).

[62] R. Zwanzig, J. Chem. Phys. **33**, 1338 (1960); Phys. Rev. **124**, 983 (1961); H. Mori, Prog. Theor. Phys. **33**, 423 (1965).

[63] T. Scopigno, G. Ruocco, and F. Sette, Rev. Mod. Phys. **77**, 881 (2005)

[64] B. J. Berne and R. Pecora, *Dynamic Light Scattering* (Wiley, New York, 1976), Chap 10.

[65] R. D. Mountain, Rev. Mod. Phys. **38**, 205 (1966).

[66] U. Bafile, E. Guarini, and F. Barocchi, Phys. Rev. E **73**, 061203 (2006).

[67] J. R. D. Copley and S. W. Lovesey, Rep. Prog. Phys. **38**, 461 (1975)

[68] T. Scopigno, U. Balucani, G. Ruocco, and F. Sette, Phys. Rev. Lett. **85**, 4076 (2000)

[69] M. H. Ernst, E. H. Hauge and J. M. J. van Leeuwen, Phys. Rev. Lett. **25**, 1254 (1970; Phys. Rev. A **4** 2055 (1971); J. Stat. Phys. **15** 7 (1976).

[70] I. M. de Schepper and M. H. Ernst, Physica **98A**, 189 (1979)

[71] M. H. Ernst and J. R. Dorfman, Physica **61**, 157 (1972); J. Stat. Phys. **12**, 311 (1974).

[72] W. Götze, Cond. Matter Phys. **1**, 873 (1998).

[73] W. Schirmacher and H. Sinn, Condens. Matter Phys. **11**, 127 (2008).

[74] L. Sjögren and A. Sjölander, J. Phys. C: Solid St. Phys. **12**, 4369 (1979).

[75] L. Sjögren, Phys. Rev. A **22**, 2866 (1980).

[76] G. Wahnström and L. Sjögren, J. Phys. C: Solid St. Phys. **15**, 401 (1982).

[77] D. Levesque and L. Verlet, Phys. Rev. A **2**, 2514 (1970).

[78] L. Sjögren, J. Phys. C: Solid St. Phys. **13**, 705 (1980); Phys. Rev. A **22**, 2883 (1980).

[79] U. Balucani, R. Vallauri, T. Gaskell, and S. F. Duffy, J. Phys.: Condens. Matter **2** 5015 (1990); U. Balucani, A. Torcini, and R. Vallauri, Phys. Rev. A **46**, 2159 (1992); J. Non-Cryst. Solids **156-158**, 43 (1993); Phys. Rev. B **47**, 3011 (1993); U. Balucani, A. Torcini, A. Stangle, and C. Morkel, Phys. Scr. **T57**, 13 (1995).

[80] W. Gudowski, M. Dzugutov, and K.-E. Larsson, Phys. Rev. E **47**, 1693 (1993).

[81] F. Shimojo, K. Hoshino, and M. Watabe, J. Phys. Soc. Jpn. **63**, 1821 (1994); K. Hoshino, F. Shimojo, and S. Munejiri, J. Phys. Soc. Jpn. **71**, 119 (2002).

[82] L. E. González, D. J. González, and M. Canales, Z. Phys. B: Condens. Matter **100**, 601 (1996); J. Casas, D. J. González, and L. E. González, Phys. Rev. B **60**, 10094 (1999); J. Casas *et al*, Phys. Rev. B **62**, 12095 (2000); L. E. González, D. J. González, and J. Casas, J. Non-Cryst. Solids **312-314**, 158 (2002).

[83] M. Canales and J. A. Padró, J. Phys.: Condens. Matter **9**, 11009 (1997); Phys. Rev. E **63**, 11207 (2001).

[84] B. Schmid and W. Schirmacher, J. Phys.: Condens. Matter **23**, 254211 (2011).

[85] T. Gaskell and S. Miller, J. Phys. C: Solid St. Phys. **11**, 3749 (1978); Phys. Lett. A **66**, 307 (1978).

[86] H. Hellmann, Einführung in die Quantenchemie (Deuticke, Leipzig, 1937); R. P. Feynman, Phys. Rev. **56**, 340 (1939).

[87] U. von Barth, Phys. Scripta. **T109**, 9 (2004).

[88] S. H. Vosko, L. Wilkes, and M. Nusair, Can. J. Phys. **58**, 1200 (1980).

[89] J. P. Perdew and A. Zunger, Phys. Rev. B **23**, 5048 (1981).

[90] D. M. Ceperly, Phys. Rev. B **18**, 3126 (1978).

[91] D. M. Ceperly and B. Alder, Phys. Rev. Lett. **45**, 566 (1980).

[92] J. P. Perdew, K. Burke, and M. Ernzerhof, Phys. Rev. Lett. **77**, 3865 (1996).

[93] M. C. Payne, M. P. Teter, D. C. Allan, T. A. Arias, and J. D. Joannopoulos, Rev. Mod. Phys. **64**, 1045 (1992).

[94] M. Pearson, E. Smargiassi, and P. A. Madden, J. Phys.: Condens. Matter **5**, 3221 (1993).

[95] Y. A. Wang and E. A. Carter, *Theoretical Methods in Condensed Phase Chemistry* (Springer, 2002), pp. 117-184.

[96] D. J. González, L. E. González, J. M. López, and M. J. Stott, Phys. Rev. B **65**, 18420 (2002).

[97] L. H. Thomas, Proc. Cam. Phil. Soc. **23**, 542 (1927). Reprint in ref. [101].

[98] E. Fermi, Rend. Accad. Lincei. **6**, 602 (1927).

[99] E. Fermi, Z. Phys. **48**, 73 (1928). A translation into English appears in ref.[101].

[100] E. Fermi, Rend. Accad. Lincei. **7**, 342 (1928).

[101] N. H. March, *Self-Consistent Fields in Atoms.* (Oxford, Pergamon, 1975)

[102] D. A. Kirzhnits, Sov. Phys. JEPT. **5**, 64 (1957).

[103] C. H. Hodges, Can. J. Phys. **51**, 1428 (1973).

[104] D. R. Murphy, Phys. Rev. A **24**, 1682 (1981).

[105] M. Koivisto and M. J. Stott, Phys. Rev. B **76**, 195103 (2007).

[106] J. Shao, Mod. Phys. Lett. **B7**, 1193 (1993).

[107] C. F von Weizsäcker, Z. Phys. **96**, 431 (1935).

[108] J. M. Ziman, *Principles of the Theory of Solids* (Cambridge Univ. 1964).

[109] W. Jones and W. H. Young, J. Phys. C: Solid State Phys. **4**. 1322 (1971).

[110] L.-W. Wang and M. P. Teter, Phys. Rev. B **45**, 13196 (1992).

[111] F. Perrot, J. Phys.: Condens. Matter **6**, 431 (1994).

[112] E. Smargiassi and P. A. Madden, Phys. Rev. B **49**, 5220 (1994).

[113] M. Foley and P. A. Madden, Phys. Rev. B **53**, 10589 (1996).

[114] Y. A. Wang, N. Govind, and E. A. Carter, Phys. Rev. B **58**, 13465 (1998).

[115] A. E. DePristo and J. D. Kress, Phys. Rev. A **35**, 438 (1987).

[116] A. E. DePristo and J. D. Kress, J. Chem. Phys. **86**, 1425 (1987).

[117] B. Wang, M. J. Stott, and U. von Barth, Phys. Rev. B **63**, 052501 (2001).

[118] J. P. Perdew and L. A. Constantin, Phys. Rev. B **75**, 155109 (2007).

[119] E. Chacón, J. E. Alvarellos, and P. Tarazona, Phys. Rev. B **32**, 7868 (1985).

[120] P. García-González, J. E. Alvarellos, and E. Chacón, Phys. Rev. A **54**, 1987 (1996).

[121] P. García-González, J. E. Alvarellos, and E. Chacón, Phys. Rev. B **53**, 9509 (1996).

[122] P. García-González, J. E. Alvarellos, and E. Chacón, Phys. Rev. B **57**, 4857 (1998).

[123] D. J. Gonzalez, L. E. Gonzalez, J. M. López, and M. J. Stott, J. Chem. Phys. **115**, 2373 (2001).

[124] S. Gómez, L. E. González, D. J. González, M. J. Stott, S. Dalgiç, and M. Silbert, J. Non-Cryst. Solids **250-252**, 163 (1999).

[125] G. B. Bachelet, D. R. Hamann, and M. Schlüter, Phys. Rev. B **26**, 4199 (1982).

[126] N. Troullier and J. L. Martins, Phys. Rev. B **43**, 1993 (1991).

[127] L. Kleinman and D. M. Bylander, Phys. Rev. Lett. **48**, 1425 (1982).

[128] D. Vanderbilt, Phys. Rev. B **41**, 7892 (1990).

[129] B. Wang and M. J. Stott, Phys. Rev. B **68**, 195102 (2003).

[130] A. Aguado, J. M. Lopez, J. A. Alonso, and M. J. Stott, J.Chem. Phys. **111**, 6026 (1999).

[131] S. Watson, B. J. Jesson, E. A. Carter, and P. A. Madden, Europhys. Lett. **41**, 37 (1998).

[132] L. E. Gonzalez, A. Meyer, M. P. Íñiguez, and D. J. González, Phys. Rev. E **47**, 4120 (1993).

[133] L. Dagens, J. Phys. (Paris) **34**, 879 (1973).

[134] L. Hung and E. A. Carter, J. Phys. Chem. C **115**, 6269–6276 (2011).

[135] H. Zhuang, M. Chen, and E. A. Carter, Phys. Rev. Appl. **5**, 64021 (2016).

[136] D. J. González and L. E. González, J. Phys. Condens. Matter **20**, 114118 (2008).

[137] S. C. Watson and P. A. Madden, PhysChemComm **1**, 1–11 (1998).

[138] L. Hung and E. A. Carter, Chem. Phys. Lett. **475**, 163–170 (2009).

[139] M. Chen, X. W. Jiang, H. Zhuang, L. W. Wang, and E. A. Carter, J. Chem. Theory Comput. **12**, 2950–2963 (2016).

[140] S. Goedecker, Rev. Mod. Phys. **71**, 1085–1123 (1999).

[141] D. R. Bowler and T. Miyazaki, Reports Prog. Phys. **75**, 36503 (2012).

[142] J. Aarons, M. Sarwar, D. Thompsett, and C.-K. Skylaris, J. Chem. Phys. **145**, 220901 (2016).

[143] J. Da Chai, J. D. Weeks, Phys. Rev. B **75**, 205122 (2007).

[144] C. Huang and E. A. Carter, Phys. Rev. B **81**, 45206 (2010).

[145] C. Huang and E. A. Carter, Phys. Rev. B **85**, 45126 (2012).

[146] J. Xia and E. A. Carter, Phys. Rev. B **86**, 235109 (2012).

[147] I. Shin and E. A. Carter, J. Chem. Phys. **140**, 18A531 (2014).

[148] P. E. Blöchl, Phys. Rev. B **50**, 17953–17979 (1994).

[149] G. Kresse, Phys. Rev. B **59**, 1758–1775 (1999).

[150] B. Zhou, Y. A. Wang, and E. A. Carter, Phys. Rev. B **69**, 125109 (2004).

[151] C. Huang and E. A. Carter, Phys. Chem. Chem. Phys. **10**, 7109–7120 (2008).

[152] L. E. González, D. J. González, M. Silbert, and J. A. Alonso, J. Phys. Condens. Matter **5**, 4283–4298 (1993).

[153] B. G. del Rio and L. E. González, J. Phys. Condens. Matter **26**, 465102 (2014).

[154] S. C. Watson and E. A. Carter, Comput. Phys. Commun. **128**, 67–92 (2000).

[155] X. Cao, and M. Dolg, Rev. Comput. Mol. Sci. **1**, 200–210 (2011).

[156] Y. Ke, F. Libisch, J. Xia, L. W. Wang, and E. A. Carter, Phys. Rev. Lett. **111**, 1–5 (2013).

[157] Y. Ke, F. Libisch, J. Xia, and E. A. Carter, Phys. Rev. B **89**, 15511 (2014).

[158] J. Lehtomäki, I. Makkonen, M. A. Caro, A. Harju, and O. Lopez-Acevedo, J. Chem. Phys. **141**, 23410 (2014).

[159] J. A. Anta and P. A. Madden, J. Phys. Condens. Matter **11**, 6099 (1999).

[160] M. Chen, L. Hung, C. Huang, J. Xia, and E. A. Carter, Mol. Phys. **111**, 3448–3456 (2013).

[161] M. Chen, J. R. Vella, A. Z. Panagiotopoulos, P. G. Debenedetti, F. H. Stillinger, and E. A. Carter, AIChE J. **61**, 2841–2853 (2015).

[162] J. M. Ziman, Adv. Phys. **13**, 89–138 (1964).

[163] J. M. Ziman, Proc.Phys.Soc. **91**, 701–723 (1967).

[164] L. Dagens, J. Phys. C Solid State Phys. **5**, 2333–2344 (1972).

[165] F. Perrot and G. Chabrier, Phys. Rev. A **43**, 2879–2889 (1991).

[166] L. E. González, A. Meyer, M. P. Iñiguez, D. J. González, and M. Silbert, Phys. Rev. E **48**, 4120–4129 (1993).

[167] A. Delisle, D. J. González, M. J. Stott, Phys. Rev. B **73**, 64202 (2006).

[168] B. Zhou and E. A. Carter, J. Chem. Phys. **122**, 184108 (2005).

[169] J. M. Dieterich, G. H. Clever, and R. A. Mata, Phys. Chem. Chem. Phys. **14**, 12746–12749 (2012).

[170] J. M. Dieterich, S. Gerke, and R. A. Mata, J. At. Mol. Opt. Phys. **2012**, ID 648386 (2012).

[171] J. M. Dieterich and B. Hartke, Mol. Phys. **108**, 279–291 (2010).

[172] J. M. Dieterich and B. Hartke, J. Comput. Chem. **32**, 1377–1385 (2011).

[173] J. M. Dieterich, Appl. Math. **3**, 1552–1564 (2012).

[174] D. E. Goldberg, *Genetic Algorithms in Search, Optimization and Machine Learning* (1st ed.; Addison-Wesley Longman Publishing Co., Inc.: Boston, MA, 1989).

[175] B. Bandow and B. Hartke, J. Phys. Chem. A **110**, 5809–5822 (2006).

[176] B. Hartke, Rev. Comput. Mol. Sci. **1**, 879–887 (2011).

[177] Weise, T. *Why research in computational intelligence should be less inspired.* http://www.it-weise.de/thoughts/text/ecInspiration.html.

[178] K. Sörensen, Int. Trans. Oper. Res. **22**, 3–18 (2015).

[179] R. L. Johnston, Dalt. Trans. **22**, 4193 (2003).

[180] M. Powell, Dep. Appl. Math. Theor. Physics, Cambridge Univ. NA Rep. NA2009/06 **39** (2009).

[181] Apache Commons Math http://commons.apache.org (Accessed 1 February 2017).

[182] X. Gonze, J. M. Beuken, R. Caracas, F. Detraux, M. Fuchs, G. M. Rignanese, L. Sindic, M. Verstraete, G. Zerah, F. Jollet, M. Torrent, A. Roy, M. Mikami, P. Ghosez, J. Y. Raty, and D. C. Allan, Comput. Mater. Sci. **25**, 478–492 (2002).

[183] X. Gonze, B. Amadon, P. M. Anglade, J. M. Beuken, F. Bottin, P. Boulanger, F. Bruneval, D. Caliste, R. Caracas, M. Côté, T. Deutsch, L. Genovese, P. Ghosez, M. Giantomassi, S. Goedecker, D. R. Hamann, P. Hermet, F. Jollet, G. Jomard, S. Leroux, M. Mancini, S. Mazevet, M. J. T. Oliveira, G. Onida, Y. Pouillon, T. Rangel, G. M. Rignanese, D. Sangalli, R. Shaltaf, M- Torrent, M.J. Verstraete, G. Zerah, and J. W. Zwanziger, Comput. Phys. Commun. **180**, 2582–2615 (2009).

[184] G. Kresse and J. Furthmüller, Phys. Rev. B **54**, 11169–11186 (1996).

[185] G. S. Ho, V. L. Lignères, and E. A. Carter, Comput. Phys. Commun. **179**, 839–854 (2008); L. Hung, C. Huang, I. Shin, G. S. Ho, V. L. Lignères, and E. A. Carter, Comput. Phys. Commun. **181**, 2208–2209 (2010); M. Chen, J. Xia, C. Huang, J. M. Dieterich, L. Hung, I. Shin, and E. A. Carter, Comput. Phys. Commun. **190**, 228–230 (2014).

[186] M. Fuchs and M. Scheffler, Comput. Phys. Commun. **119**, 67–98 (1999).

[187] H. J. Monkhorst and J. D. Pack, Phys. Rev. B **13**, 5188-5192 (1976).

[188] F. D. Murnaghan, Proc. Natl. Acad. Sci. **30**, 244–247 (1944).

[189] L. Calderin, L. E. González, and D. J. González, J. Phys. Condens. Matter **23**, 375105 (2011).

[190] L. Calderín, L. E. González, and D. J. González, J. Phys. Condens. Matter **25**, 65102 (2013).

[191] M. Marqués, L. E. González, and D. J. González, J. Phys. Condens. Matter **28**, 75101 (2016).

[192] Y. Waseda, *The Structure of Non-Crystalline Materials: Liquids and Amorphous Solids* (New York: McGraw-Hill International Book Co., 1980).

[193] H. Olbrich, H. Ruppersberg, and S. Steeb, Z. Naturforsch. **38a**, 1328–1336 (1983).

[194] L. Löwenberg and A. Lodding, Z. Naturforsch. A **22**, 2077–2080 (1967).

[195] J. Sedlmeier, *Ph. D. Thesis* (Technische Universität München, Germany, 1992).

[196] P. Verkerk, P. H. K. de Jong, M. Arai, S. M. Bennington, W. S. Howells, and A. D. Taylor, Phys. B Condens. Matter **180–181**, 834–836 (1992).

[197] P. H. K. De Jong, *Ph. D. Thesis* (Technische Universiteit Delft, 1993).

[198] The ABINIT Group. *Norm-conserving pseudopotentials* www.abinit.org./downloads/psp-links (accessed Nov 1, 2014).

[199] D. R. Trinkle, R. G. Hennig, S. G. Srinivasan, D. M. Hatch, M. D. Jones, H. T. Stokes, R. C. Albers, and J. W. Wilkins, Phys. Rev Lett **91** 025701 (2003); D. R. Trinkle, D. M. Hatch, H. T. Stokes, R. G. Hennig, and R. C. Albers, Phys. Rev. B **72**, 014105 (2005).

[200] S. Pecker, S. Eliezer, D. Fisher, Z. Henis, and Z. Zinamon, J. App. Phys., **98**, 043516 (2005).

[201] A. K. Verma, P. Modak, R. S. Rao, B. K. Godwal, and R. Jeanloz, Phys. Rev. B, **75**, 014109 (2007).

[202] R. G. Hennig, T. J. Lenosky, D. R. Trinkle, S. P. Rudin, and J. W. Wilkins, Phys. Rev. B, **78**, 054121 (2008).

[203] Z. G. Mei, S. L. Shang, Y. Wang, and Z. K. Liu, Phys. Rev. B, **80**, 104116 (2009).

[204] V. Stutzmann, A. Dewaele, J. Bouchet, F. Bottin, and M. Mezouar, Phys. Rev. B **92**, 224110 (2015).

[205] U. Argaman, E. Eidelstein, O. Levy, and G. Markov, Materials Res. Express **2**, 016505 (2015).

[206] I. Balconyi, H. Ebert, and A. I. Liechtenstein, Phys. Rev. B **48**, 7841 (1993).

[207] M. Jafari, H. Jamnezhad, and L. Nazarzadeh, Iranian J. Sci. and Techn. A **4**, 511 (2012).

[208] Y. Waseda and S. Tamaki, Philos. Mag. **32**, 273 (1975).

[209] G. W. Lee, A.K. Gangopadhyay, K. F. Kelton, R. W. Hyers, T. J. Rathz, J. R. Rogers, and D. S. Robinson, Phys. Rev. Lett., **93**, 037802 (2004).

[210] T. Schenk, D. Holland-Moritz, V. Simonet, R. Bellisent, and D M Herlach, Phys. Rev. Lett. **89**, 075507 (2002).

[211] G. W. Lee, A. K. Gangopadhyay, R. W. Hyers, T. J. Rathz, J. R. Rogers, D. S. Robinson, A. I. Goldman, and K. F. Kelton, Phys. Rev. B **77**, 184102 (2008).

[212] T. H. Kim and K. F. Kelton, J. Chem. Phys. **126** 054513 (2007).

[213] N. Jakse and A. Pasturel, Phys. Rev. Lett. **91**, 195501 (2003); N. Jakse, O. Le Bacq, and A. Pasturel, J. Non-Crystall. Solids **353**, 3684 (2007).

[214] D. Holland-Moritz, O. Heinen, R. Bellissent, and T. Schenk, Mater. Sci. Eng. A, **449-451**, 42 (2007).

[215] A. H. Said, H. Sinn, A. Alatas, C. A. Burns, D. L. Price, M. L. Saboungi, and W. Schirmacher, Phys. Rev B **74**, 172202 (2006).

[216] J. Horbach, R. E. Rozas, T. Unruh, and A. Meyer, Phys. Rev. B **80**, 212203 (2009).

[217] J. R. Todd and J. S. Brown, Phys. Letters A **59**, 302 (1976).

[218] Ch. Hausleitner, G. Kahl, and J. Hafner, J. Phys.: Condens. Matter **3**, 1589 (1991).

[219] J. M. Wills and W. A. Harrison, Phys. Rev. B **28**, 4363 (1983).

[220] G. M. Bhuiyan, J. L. Bretonnet, L. E. Gonzalez, and M. Silbert, J. Phys.: Condens. Matter **4**, 7651 (1992).

[221] Y. Rosenfeld, J. Stat. Phys. **42**, 437 (1986); D. J. Gonzalez, D. A. Ng, and M. Silbert, J. Non-Cryst. Solids **117**, 469 (1990).

[222] A. F. Voter and S. P. Chen, *Characterization of Defects in Materials* (ed. R W Siegel, J R Weertman and R Sinclair, MRS Symposia Proceedings No 82, Materials Research Society, Pittsburg, 1987) p. 175.

[223] G. M. Bhuiyan, M. Silbert, and M. J. Stott, Phys. Rev. B **53**, 636 (1996).

[224] J.P. Perdew and Y. Wang, Phys. Rev. B **45**, 13244 (1992).

[225] T. Ishikawa and P. F. Paradis, J. Electron. Mater., **34**, 1526 (2005).

[226] D. Beeman, J. Comput. Phys. **20**, 130 (1976).

[227] P. Gianozzi, S. Baroni, N. Bonini, M. Calandra, R. Car, C. Cavazzoni, D. Ceresoli, G. L. Chiarotti, M. Cococcioni, I. Dabo, A. Dal Corso, S. de Gironcoli, S. Fabris, G. Fratesi, R. Gebauer, U. Gerstmann, C. Gougoussis, A. Kokalj, M. Lazzeri, L. Martin-Samos, N. Marzari, F. Mauri, R. Mazzarello, S. Paolini, A. Pasquarello, L. Paulatto, C. Sbraccia, S. Scandolo, G. Sclauzero, A. P. Seitsonen, A. Smogunov, P. Umari, and R. M. Wentzcovitch, J. Phys.: Condens. Matter **21**, 395502 (2009); S. Baroni, A. Dal Corso, S. de Gironcoli, P. Giannozzi, C. Cavazzoni, G. Ballabio, S. Scandolo, G. Chiarotti, P. Focher, A. Pasquarello, K. Laasonen, A. Trave, R. Car, N. Marzari, and A. Kokalj, http://www.pwscf.org/.

[228] L. Calderin, D. J. González, L. E. González, and J. M. López, J. Chem. Phys. **129**, 194506 (2008).

[229] L. Calderín, L. E. González, and D. J. González, J. Chem. Phys. **130**, 194505 (2009); M. M. G. Alemany, R. C. Longo, L. J. Gallego, D. J. Gonzalez, L. E. Gonzalez, M. L. Tiago, and J. R. Chelikowsky, Phys. Rev. B **76**, 214203 (2007).

[230] B. G. del Rio, D. J. González, and L. E. González, Phys. of Fluids **28**, 107105 (2016).

[231] B. G. del Rio, L. E. González, and D. J. González, J. Chem. Phys. **146**, 034501 (2017).

[232] S. Sachdev and D. R. Nelson, Phys. Rev. Letters **53**, 1947 (1984).

[233] S. Blairs, Intern. Materials Rev. **52**, 321 (2007).

[234] J. D. Honeycutt and H. C. Andersen, J. Phys. Chem. **91**, 4950 (1987).

[235] A. Torcini, U. Balucani, P. H. K. de Jong, and P. Verkerk, Phys. Rev. E **51**, 3126 (1995); M. M. G. Alemany, L. J. Gallego, and D. J. González, Phys. Rev. B **70**, 134206 (2004); M. M. G. Alemany, R. C. Longo, L. J. Gallego, D. J. González, L. E. González, M. L. Tiago, and J.R. Chelikowsky, Phys. Rev. B **76**, 214203 (2007).

[236] F. Shimojo, K. Hoshino, and M. Watabe, J. Phys. Soc. Jpn **63**, 141 (1994); S. Sengul, L. E. González, and D. J. González, J. Phys.: Cond. Matter **21**, 115106 (2009).

[237] S. Kambayashi and G. Kahl, Phys. Rev. A **46**, 3255 (1992); G. Kahl and S. Kambayashi, J. Phys.: Cond. Matter **6**, 10897 (1994).

[238] T. Scopigno, U. Balucani, G. Ruocco and F. Sette, J. Phys.:Cond. Matter **12**, 8009 (2000).

[239] M. Canales, L. E. González, and J. A. Padró, Phys. Rev. E **50**, 3656 (1994); T. Bryk and I. Mryglod, J. Phys.: Condens. Matter **12**, 3543 (2000); **13**, 1343 (2001); Phys. Rev. E **63**, 051202 (2001).

[240] S. Hosokawa, M. Inui, K. Matsuda, D. Ishikawa, and A. Q. R. Baron, Phys. Rev. B **77**, 174203 (2008).

[241] J. Casas, N. M. Keita, and S. G. Steinemann, Phys. Chem. Liq. **14**, 155 (1984).

[242] B.J. Palmer, Phys. Rev. E **49**, 359 (1994); U. Balucani, J. P. Brodholt, P. Jedlovszky, and R. Vallauri, Phys. Rev. E **62**, 2971 (2000); J. Blanco, D. J. González, L. E. González, J. M. López, and M. J. Stott, Phys. Rev. E **67**, 041204 (2003).

[243] A. D. Agaev, V. I. Kostikov, and V. N. Bobkovskii, Izv. Akad. Nauk, SSSR Met. **3**, 43 (1980).

[244] P. F. Paradis, T. Ishikawa, and S. Yoda, Int. J. Thermophys, **23**, 825 (2002).

[245] S. Hosokawa, M. Inui, Y. Kajihara, K. Matsuda, T. Ichitsubo, W.-C. Pilgrim, H. Sinn, L. E. González, D. J. González, S. Tsutsui, and A. Q. R. Baron, Phys. Rev. Letters **102**, 105502 (2009); Eur. Phys. J. Special Topics **196**, 85 (2011).

[246] S. Hosokawa, S. Munejiri, M. Inui, Y. Kajihara, W.-C. Pilgrim, A. Q. R. Baron, F. Shimojo, and K Hoshino, AIP Conf. Proc. **1518**, 695 (2013); S. Hosokawa, M. Inui, Y. Kajihara, S. Tsutsui, and A. Q. R. Baron, J. Phys.: Condens. Matter **27**, 194104 (2015).

[247] S. Munejiri, F. Shimojo and K. Hoshino, Phys. Rev. B **86**, 104202 (2012); S. Hosokawa, S. Munejiri, M. Inui, Y. Kajihara, W-C Pilgrim, Y. Ohmasa, T. Sutsui, A. Q. R. Baron, F. Shimojo, and K. Hoshino, J. Phys.: Cond. Matter, **25**, 112101 (2013).

[248] V. M. Giordano and G. Monaco, Proc. Natl. Acad. Sci. USA **107**, 21985 (2010).

[249] M. Marqués, L. E. González, and D. J. González, Phys. Rev. B **92**, 134203 (2015).

[250] M. M. G. Alemany, C. Rey, and L. J. Gallego, J. Chem. Phys. **109**, 5175 (1998); Phys. Rev. B **60**, 9208 (1999).

[251] S. O. Kart, M. Tomak, M. Uludogan, and T. Cagin, J. Non-Cryst. Solids, **337**, 101 (2004).

[252] J. L. Martins and M. L. Cohen, Phys. Rev. B **37**, 6134 (1988); R. M. Wentzcovitch and J. L. Martins, Solid State Comm. **78**, 831 (1991); N. Binggeli, J. L. Martins, and J. R. Chelikowsky, Phys. Rev. Letters **68**, 2956 (1992); J. R. Chelikowsky and N. Binggeli, Solid State Comm. **88**, 381 (1993).

[253] T. Iida and R. I. L. Guthrie, *The Thermophysical Properties of Metallic Liquids* (Oxford Univ. Press, 2015).

[254] V. M. Giordano and G. Monaco, PNAS **107**, 21985 (2010); Phys. Rev. B **84**, 052201 (2011).

[255] M. Zanatta, F. Sacchetti, E. Guarini, A. Orecchini, A. Paciaroni, L. Sani, and C. Petrillo, Phys. Rev. Lett. **114**, 187801 (2015).

[256] M. Marqués, D. J. González, and L. E. González, Phys. Rev. B **94**, 024204 (2016).

[257] T. Bryk, G. Ruocco, T. Scopigno, and A. P. Seitsonen, J. Chem. Phys. **143**, 104502 (2015).

[258] R. Zwanzig, *Boulder Lectures in Theoretical Physics* (ed. W. E. Brittin, B. W. Downs and J. Downs, Wiley Interscience, New York, 1961), vol. III, p. 106; H. Mori, Progr. Theor. Phys. **33**, 423 (1965).

[259] A. Aguado, A. Vega, A. Lebon, and B. von Issendorff, Angew. Chem. **54**, 2111 (2015).

[260] W. B. Pearson, *Handbook of Lattice Spacings and Structures of Metals and Alloys* (Pergamon Press, Oxford, 1958).

[261] D. M. North, J. E. Enderby, and P. A. Egelstaff, J. Phys. C: Solid State Phys **1**, 1075 (1968).

[262] H. Lou, X. Wanga, Q. Cao, D. Zhang, J. Zhang, T. Hu, H.-K. Mao, and J.-Z. Jiang, PNAS **110**, 10068 (2013).

[263] J.-F. Wax and T. Bryk, J. Phys.: Condens. Matter **25**, 325104 (2013); S. Bellissima, M. Neumannm, E. Guarini, U. Bafile, and F. Barocchi, Phys. Rev. E **92**, 042166 (2015).

[264] M. Ranganathan and H. C. Andersen, J. Chem. Phys. **121**, 1243 (2004).

[265] M. Ranganathan and H. C. Andersen, J. Phys. Chem. B **109**, 21437 (2005).

[266] N. H. Nachtrieb, E. Fraga and C. Wahl, J. Phys. Chem. **67**, 2353 (1963).

[267] B. G. del Rio, L. E. González, LAM16 Proceedings (2017).

[268] G. Kresse, J. Non. Cryst. Solids **312–314**, 52–59 (2002).

[269] T. Itami, S. Munejiri, T. Masaki, H. Aoki, Y. Ishii, T. Kamiyama, Y. Senda, F. Shimojo, and K. Hoshino, Phys. Rev. B **67**, 64201 (2003).

[270] S. Munejiri, F. Shimojo, and K. Hoshino, Phys. Rev. B **86**, 10 (2012).

[271] Y. Waseda and K. Suzuki, Phys. Status Solidi B **49**, 339 (1972).

[272] O. Genser and J. Hafner, Phys. Rev. B **63**, 14 (2001).

[273] K. Kawasaki, Phys. Rev. **150**, 1 (1966).

[274] W. Götze and M. Lücke, Phys. Rev. A **11**, 6 (1975).

[275] W. Götze, and L. Sjögren, Reports Prog. Phys. **55**, 3 (1992).

[276] M. Abtew and G. Selvaduray, Mater. Sci. Eng. **27**, 95 (2000); M. McCormack, S. Jin, G. W. Kammlott, and H. S. Chen, Appl. Phys. Lett. **63**, 15 (1993); C. M. Miller, I. E. Anderson, and J. F. Smith, J. Electron. Mater. **23**, 595 (2004).

[277] J. Gong, C. Liu, P. P. Conway, and V. V. Silberschmidt, Mater. Sci. Eng. A **427**, 60 (2006); C. M. L. Wu, D. Q. Yu, C. M. T. Law, and L. Wang, Mater Sci Eng R **44**, 1 (2004).

[278] I. Kaban, S. Mhiaoui, W. Hoyer, and J.-G. Gasser, J. Phys.: Condens. Matter **17**, 7867 (2005); M. Kucharski and P. Fima, Monatshefte für Chemie **136**, 1841 (2005); App. Surf. Science **257**, 3265 (2011).

[279] T. Gancarz, Z. Moser, W. Gasior, J. Pstrus, and H. Henein, Int. J. Thermophys. **32**, 1210 (2011).

[280] D. Yagodin, V. Sidorov, D. Janickovic, and P.Svec, J. Non-Cryst. Solids **358**, 2935 (2012).

[281] Z. Wei and W. BingBo, Chinese Science **58**, 938 (2013).

[282] R. A. Khairulin, S. V. Stankus, R. N. Abdullaev, Y. A. Plevachuk, and K. Y. Shunyaev, Thermophysics and Aeromechanics **17**, 391 (2010).

[283] Y. Plevachuk, V. Sklyarchuk, W. Hoyer, and I. Kaban, J Mater. Sci. **41**, 4632 (2006).

[284] M. L. Joshi and C. N. J. Wagner, Z. Naturforsch. A **20**, 564 (1965); C. N. J. Wagner and N. C. Halder, Adv. Phys. **16**, 241 (1967).

[285] I. Kaban, W. Hoyer, A. Ilinskii, O. Slukhovskii, and S. Slyusarenko, J. Non-Cryst. Solids **331**, 254 (2003)

[286] R. V. Gopala Rao and A. Satpathy, Phys. Rev. B **41**, 11938 (1990).

[287] G. M. Bhuiyan, Md. Saiful Alam, A. Z. Ziauddin Ahmed, Ishtiaque M. Syed, and R. I. M. A. Rashi, J. Chem. Phys. **131**, 034502 (2009).

[288] E. H. Bhuiyan, A. Z. Ziauddin Ahmed, G. M. Bhuiyan, and M. Shahjahan, Physica B **403**, 1695 (2008).

[289] P. Terzieff, J. Mater. Sci. **43**, 7203 (2008).

[290] T. Kato, J. Phys. Chem. **89**, 5750 (1985).

[291] K. Niwa, H. Nakajima, M. Tada, and N. Seo, J. Jpn. Inst. Met. **33**, 203 (1969).

[292] L. S. Darken and R. W. Gurry, *Physical Chemistry of Metals* (McGraw-Hill, 1953).

[293] M. Shimoji and I. Itami, *Atomic Transport in Liquid Metals* (Trans. Tech., 1986).

[294] A. Bruson and M. Gerl, Phys. Rev. B **21**, 5447 (1980).

[295] N. Anento and J. A. Padro, Mol. Phys. **99**, 275 (2001); J. Blanco, D. J. González, L. E. González, J. M. López, and M. J. Stott, Phys. Rev. E **67**, 041204 (2003); D. J. González, L. E. González, J. M. López, and M. J. Stott, Europhys. Lett. **62**, 42 (2003); Phys. Rev. E **69**, 031205 (2004); J. Phys.: Condens. Matter **17**, 1429 (2005).

[296] M. M. G. Alemany, L. J. Gallego and D. J. González, Phys. Rev. B **70**, 134206 (2004).

[297] E. Gebhardt, M. Becker and E. Tragner, Z. Metallkd. **44**, 379 (1953).

[298] A. Roll and H. Motz, Z. Metallk. **48**, 435 (1957).

[299] H. Nishikawa and N. Iwata, J. Mater. Process. Technol. **215**, 6 (2015)

[300] A.A. El-Daly, A.M. El-Taher, and S. Gouda, J. Alloys Comp. **627**, 268 (2015).

[301] G. Kresse and J. Hafner, , J. Phys.: Condens. Matter **6**, 8245 (1994).

[302] P. S. Pershan and M. L. Schlossman, *Liquid Surfaces and Interfaces. Synchrotron X-ray Methods*, (New York: Cambridge, 2012).

[303] G. Fabricius, E. Artacho, D. Sánchez-Portal, P. Ordejón, D. A. Drabold, and J. M. Soler, Phys. Rev. B **60**, R16283 (1999).

[304] B. G. Walker, C. Molteni, and N. Marzari, J. Phys.: Condens. Matter **26**, S2575 (2004).

[305] L. Calderín, L. E. González, and D. J. González, Phys. Rev. B **80**, 115403 (2009).

[306] L. Calderín, L. E. González, and D. J. González, Phys. Rev. B **87**, 014201 (2013).

[307] M. M. G. Alemany, M. Jain, L. Kronik, and J. R. Chelikowsky, Phys. Rev. B **69**, 075101 (2004); L. Kronik, A. Makmal, M. L. Tiago, M. M. G. Alemany, M. Jain, X. Huang, Y. Saad, and J. R. Chelikowsky, Phys. Status Solidi B **243**, 1063 (2006); M. M. G. Alemany, M. Jain, M. L. Tiago, Y. Zhou, Y. Saad, J. R. Chelikowsk, Comput. Phys. Comm. **177**, 339 (2007).

[308] M. M. G. Alemany, R. C. Longo, L. J. Gallego, D. J. González, L. E. González, M. L. Tiago, and J. R. Chelikowsky, Phys. Rev. B **76**, 214203 (2007).

[309] J. Souto, M. M. G. Alemany, L. J. Gallego, L. E. González, and D. J. González, Phys. Rev. B **81**, 134201 (2010).

[310] M. Inui, X. Hong and K. Tamura, Phys. Rev. B **68**, 094108 (2003).

[311] U. Dahlborg and M. Davidovič, Phys. Chem. Liq. **15**, 243 (1986).

[312] O. G. Shpyrko, R. Streitel, V. S. K. Balagurusamy, A. Y. Grigoriev, M. Deutsch, B. M. Ocko, M. Meron, B. Lin, and P. S. Pershan, Science **313**, 77 (2006).

[313] J. Penfold, Rep. Prog. Phys. **64**, 777 (2001).

[314] G. Ruocco and F. Sette, J. Phys. Condens. Matter **11**, R259 (1999).

[315] S. Iarlori, P. Carnevali, F. Ercolessi, and E. Tosatti, Europhys. Lett. **10**, 4 (1989).

[316] H. Reichert, F. Bencivenga, B. Wehinger, M. Krisch, F. Sette, and H. Dosch, Phys. Rev. Lett. **98**, 096104 (2007); B. Wehinger, M. Krisch and H. Reichert, New J. Phys. **13**, 023021 (2011).

[317] G. M. bhuiyan, L. E. González, and D.J. González, EPJ Web of Conferences **15**, 01011 (2011).

[318] F. Celestini, F. Ercolessi, and E. Tosatti, Phys. Rev. Lett. **78**, 3153 (1997).

[319] H. Reichert, O. Klein, H. Dosch, M. Denk, V. Hnkimaki, T. Lippmann, and G. Reiter, Nature (London) **408**, 839 (2000).

[320] J. Souto, M. M. G. Alemany, R. C. Longo, L. J. Gallego, L. E. González, and D. J. González, Phys. Rev. B **82**, 134118 (2010).

[321] B. G. Walker, C. Molteni, and N. Marzari, J. Phys. Condens. Matter **16**, S2575 (2004); J. Chem. Phys. **124**, 174702 (2006); **127**, 134703 (2007).

[322] S. Hosokawa, J. Greif, F. Demmel, and W.-C. Pilgrim, Chem. Phys. **292**, 253 (2003); S. Hosokawa, W.-C. Pilgrim, and F. Demmel, J. Non.Cryst. Solids **353**, 3122 (2007).

[323] R. Delgado-Buscaloni, E. Chacón, and P. Tarazona, J. Phys.: Condens. Matter **20**, 494229 (2008).

[324] R. B. Gordon, Acta Metall. **7**, 1 (1959).

[325] S. G. Louie, S. Froyen, and M. L. Cohen, Phys. Rev. B **26**, 1738–1742 (1982).

[326] Y. M. Juan and E. Kaxiras, Phys. Rev. B **48**, 14944–14952 (1993).

[327] M. Fuchs, M. Bockstedte, E. Pehlke, and M. Scheffler, Phys. Rev. B **57**, 2134–2145 (1998).

[328] M. Chen, J. R. Vella, F. H. Stillinger, E. A. Carter, A. Z. Panagiotopoulos, and P. G. Debenedetti, AIChE J. **6**, 2841 (2015).

[329] C. H. Ma and R. A. Swallin, J. Chem. Phys. **46**, 3014 (1962).

[330] T. Itami, T. Masaki, H. Aoki, S. Munejiri, M. Uchida, S. Matsumoto, K. Kamiyama, and K. Hoshino, J. Non-Cryst. Solids **177**, 312-314 (2002).

[331] M. Mouas, J. G. Gasser, S. Hellal, B. Grosdidier, A. Makradi, and S. Belouettar, J. Chem. Phys. **136**, 094501 (2012).

[332] C. Sun, H. Geng, Z. Yang, J. Zhang, and R. Wang, Mater. Charact. **55**, 383 (2005).

[333] E. V. Rozhitsina, S. Gruner, I. Kaban, W. Hoyer, V. E. Sidorov, and P. S. Popel, Russ. Metall. **2**, 118 (2011).